1 2 9 0

UNIVERSIDADE Ð
COIMBRA

Emanuel Gonçalves Marques

MITIGATE THE EFFECT OF COUPLING FACTOR VARIATIONS IN INDUCTIVE POWER TRANSFER SYSTEMS

PhD Thesis in Electrical and Computer Engineering, specialization in Energy, supervised by Professor Doctor André Manuel dos Santos Mendes and presented in the Electrical and Computer Engineering Department of Faculty of Sciences and Technology of the University of Coimbra.

January of 2023

"What the result of these investigations will be the future will tell; but whatever they may be, and to whatever this principle may lead, I shall be sufficiently recompensed if later it will be admitted that I have contributed a share, however small, to the advancement of science."

Nikola Tesla

Acknowledgments

This PhD dissertation is the culmination of an important life step and I would like to leave a few words of appreciation to the people who contributed to its success.

First of all, I would like to thank my parents for all the support throughout my academic journey, their advice and all the moments shared that helped me become a better person.

I would like to thank my supervisor, Professor André Manuel dos Santos Mendes, for the availability, guidance and support shown throughout this dissertation.

I also want to thank Professor Marina Mendes Sargento Domingues Perdigão for her support, availability and help.

I also would like to express my gratitude to all colleagues and friends from the laboratories, namely Luis Caseiro and Valter Costa for their friendship and moments spent while working.

To conclude, I would like to thank Instituto de Telecomunicações for accepting to be the host institution of this Thesis.

Abstract

Inductive power transfer (IPT) systems accomplishes power transfer between two sides across an air gap without the need of electric wires. Such systems eliminate the driver from the charging process and consequently, all risks associated to handling electrical equipment. The absence of physical contacts also offers the possibility of EV charging with the vehicle in movement. Such capability has the possibility to reduce the battery pack size and ensuring unlimited range capabilities. The power transfer capabilities of IPT systems are, however, limited by vertical and lateral displacements during the charging process.

The main work presented in this thesis addresses the effect of coupling factor variations due to displacements in different IPT configurations. New design methodologies are proposed to ensure load independent current and/or voltage source characteristics in extreme coupling factor variations. In addition, these design methodologies eliminate the need for an on-board controllable converter and a close loop off-board control strategy. The first problem addressed in this thesis was the impact of deviations in the self-inductance and capacitor values caused by displacements and aging, respectively. The analysis is carried out for the four series/parallel resonant configurations in two-coil systems. New generic equations of the circuit models are established for the reflected impedance values.

The magnetic coupler (MC) is the key element in IPT systems and is responsible for the energy transfer between the off-board and the vehicle's side. The magnetic coupler is formed by one or more coils and a ferromagnetic core and its coupling factor is directly affected by displacements. Their impact are, however, mitigated with a proper design and placement of the coils and ferromagnetic core. The extraction of both self and mutual inductance profiles, needed during the design of the overall IPT system, occurs mainly via finite element analysis (FEA) tools. Multiple simulations, ranging from several dozens up to a few hundred, are needed to fully assess the effect of different displacements and different combination of turns in the self and mutual inductance profiles. Unfortunately, each FEA simulation runtime ranges between a few minutes up to one hour, depending on the simulation model and computer specifications. Therefore, the full characterization of a magnetic coupling can be a cumbersome endeavor. A design methodology that minimizes the number of required FEA

simulations is then presented in this thesis. The presented design methodology uses adequate fitting curves to plot the effect of vertical and lateral displacements. This approach allows the extraction of minimum required charging positions and, consequently, has a positive impact on the required number of FEA simulations. The methodology is applicable to both non-polarized and polarized geometries in two and three-coils IPT systems and is validated through both FEA tools and experiments.

Pick-up or off-road vehicles with higher air gap values require MCs with larger sizes, even with optimized geometries. The power transfer capabilities are largely dependent on the VA ratings of the source and transmitter pads driven by large currents (above 150 A) are unavoidable for a reasonable power transfer. One way to boost the effective coupling factor of the MC is through the placement of an intermediate resonator between the transmitter and receiver coils. Unfortunately, the literature lacks design guidelines towards three-coil systems. Moreover, IPT solutions that don't require a communication link between the off-board and on-board sides are preferable since they are easier to implement, cheaper and with less components. Therefore, this work presents a design methodology to obtain a constant current charging mode and an estimation procedure to determine the coupling coefficients using off-board measurements. The realized prototype validates both the design methodology and estimation procedure under different load and charging conditions.

All the aforementioned solutions minimize the impact of displacements but they are still limited for large ground clearance vehicles like trucks or heavy-duty vehicles. This work explores the concept of in-wheel IPT systems to reduce the air gap to a minimum and independent of the vehicle class. A new double coupling resonant configuration is presented and use the wheel as an intermediary stage between the off-board and vehicle's side. The inclusion of a second magnetic coupler to accomplish power transfer between the wheel and the vehicle modifies the intrinsic characteristics of the resonant networks. Moreover, the curve shape of the receiver coils placed in the wheel and the effect of the wheel's rotation were never analyzed in the existing literature. Therefore, several magnetic coupler geometries were investigated and optimized together with a comparative study of different double coupling IPT resonant configurations. A real size in-wheel prototype validates the selected geometries and resonant configurations and the corresponding benefits against conventional IPT systems.

Globally, the thesis explored the effect of displacements in the coupling factor of IPT systems and proposed design methodologies in different components until culminating in a solution that minimizes displacements to a minimum and independent of the vehicle class.

Resumo

Sistemas de carregamento indutivo (IPT) permitem a transferência de energia entre dois lados através de grandes entreferros sem a necessidade de contactos. Estes sistemas eliminam a intervenção do condutor no processo de carga e todos os riscos associados ao manuseamento de equipamentos eléctricos. Os sistemas de carregamento indutivo permitem ainda que o processo de carga ocorra com o veículo em movimento. Desta forma, é possível reduzir a capacidade de armazenamento das baterias e garantir, simultaneamente, elevadas autonomias. Contudo, os elevados entreferros e os desalinhamentos laterais limitam a capacidade de transferência dos sistemas IPT.

Esta dissertação teve como principal objectivo a procura de soluções que mitigam os efeitos de variações de acoplamento, causados por desalinhamentos entre ambos os lados, em diferentes tipos de sistemas IPT atráves do uso de novas metodologias de dimensionamento. Este trabalho começou por analisar o impacto de desvios nos valores das indutâncias próprias e dos condensadores devido ao efeito de desalinhamentos e envelhecimento, respectivamente. Esta análise foi aplicada às quatro configurações ressonantes fundamentais e permitiu a identificação das equações genéricas de impedância reflectida.

A estrutura de acoplamento magnético (MC) é o componente responsável pela transferência de energia entre o transmissor (instalado no chão) e o receptor (instalado debaixo do veículo). O MC é formado por um ou mais enrolamentos e um núcleo ferromagnético. Os valores do entreferro e do desalinhamento lateral afectam o valor do acoplamento magnético entre o transmissor e o receptor. Este impacto pode, no entanto, ser mitigado através de uma disposição adequada dos enrolamentos e/ou núcleo ferromagnético. Neste contexto, é proposto um novo sistema de carregamento IPT vertical para veículos com elevadas distâncias ao solo. É realizado ainda um estudo de optimização de MCs para aplicações dinâmicas e sem a utilização de núcleos ferromagnéticos.

O mapeamento das indutâncias próprias e mútuas das estruturas de acoplamento magnético são imprescíndiveis durante a fase de dimensionamento de um sistema IPT. Neste sentido, é apresentada uma metodologia de mapeamento que minimiza o número de simu-

lações em elementos finitos. A metodologia apresentada ajusta o efeito do número de espiras em cada enrolamento e o efeito de desalinhamentos verticais e laterais em função de curvas lineares, exponenciais e Gaussianas, respectivamente. A metodologia é validada experimentalmente e através de um programa de elementos finitos.

A introdução de ressonadores entre o transmissor e o receptor melhora o factor de acoplamento e, consequentemente, a capacidade de transferência de energia. Contudo, não existe na literatura uma metodologia de dimensionamento de sistemas IPT com ressonadores sem a necessidade de comunicação entre o carregador e o veículo. Nesse sentido, foi desenvolvida no âmbito desta tese uma metodologia para seleção sa frequência de comutação e dimensionamento dos diversos componentes, de forma a garantir a operação do sistema como fonte de corrente e independente da carga. É ainda proposto um procedimento de estimação do nível de carga das baterias assim como dos valores das indutâncias mútuas com recurso exclusivo a grandezas eléctricas disponíveis no lado do transmissor. É realizada a validação experimental da metodologia e do procedimento de estimação em diferentes posições de carregamento e diferentes valores de carga.

As soluções acima apresentadas mitigam as variações no factor de acoplamento em sistemas IPT. No entanto, sistemas IPT continuam a apresentar limitições na presença de elevados entreferros. O trabalho realizado no âmbito desta dissertação explora a utilização da roda como meio intermediário de transferência de energia entre o carregador e o veículo. Deste modo, o entreferro é reduzido a um valor mínimo e independente do tipo de veículo, pelo que foi desenvolvido um sistema ressonante de duplo acoplamento. A introdução do segundo MC permite a transferência entre a roda e o veículo sem a necessidade de escovas. Foram também propostas diferentes geometrias para ambas as estruturas de acoplamento magnético, uma vez que o efeito curvilíneo do pneu e o impacto da rotação da roda nunca foram contemplados na literatura. Foram ainda analisadas diferentes malhas ressonantes com duplo acoplamento, culminando no desenvolvimento de uma metodologia de identificação da frequência de comutação e intervalo de variação das indutâncias mútuas. A validação das geometrias e da metodologia é feita através de simulação e de forma experimental num protótipo de escala real e uma jante de alumínio de 18 polegadas.

De forma global, o trabalho desenvolvido nesta dissertação explorou o impacto das variações no factor de acoplamento, causados por desalinhamentos entre ambos os lados, em sistemas IPT e propôs soluções em diferentes componentes até culminar numa solução que minimiza o valor de desalinhamentos, independentemente do tipo de veículo.

Acronyms

ABB Asea Brown Boveri

AC Alternate current

AGV Autonomous guide vehicle

AWG American wire gauge

BEV Battery electric vehicle

BPP Bipolar power pad

CAN Controller area network

CC Constant current mode

CCL Capacitor-Capacitor-Inductor resonant configuration

CFLP Concrete ferrite-less pad

CNFP Circular non-ferrite pad

CPT Capacitive power transfer

CV Constant voltage mode

CP Circular pad

DAB Dual-active bridge converter

DC Direct current

DDP Double-D pad

DDQP Double-D pad with quadrature coil

ETH Swiss Federal Institute of Technology

EU European Union

EV Electric vehicle

FEA Finite element analysis

FLBPP Ferrite-less bipolar pad

FLCP Ferrite-less circular pad

FLDDwR Ferrite-less double-D pad with reflective coil

FPGA Field programmable gate array

FOD Foreign object detection

IBPP Intermediate bipolar pad

IC Intermediate coupler

ICC Intermediary coupler circuit

ICE Internal combustion engine

ICNIRP International Commission on Non-Ionizing Radiation Protection

ICP Intermediate circular pad

IDDP Intermediate double-D pad

IGBT Insulated gate bipolar transistor

inWIPT In-wheel inductive power transfer

IPT Inductive power transfer

IRMC Inner rim magnetic coupler

HEV Hybrid electric vehicle

ICNIRP International commission on non-ionizing radiation protection

KAIST Korea Advanced Institute of Science and Technology

LCC Inductor-Capacitor-Capacitor resonant configuration

LCL Inductor-Capacitor-Inductor resonant configuration

MC Magnetic coupler

MIT Massachusetts Institute of Technology

MOSFET Metal-oxide semiconductor field effect transistor

MRC Magnetic resonance coupling

OCC One cycle control

OLEV On-line electric vehicle

ORNL Oak Ridge National Laboratory

ORMC Outer rim magnetic coupler

P Parallel configuration

PATH Partners for Advanced Transit and Highways

PFC Power-factor correction converter

PI Proportional-integral controller

PID Proportional-integral-derivative controller

PP Parallel-Parallel resonant configuration

PS Parallel-Series resonant configuration

PWM Pulse width modulation

Q Quadrature coil

RF Radio frequency

RLC Series resistance-inductor-capacitance load

RMS Root mean square

RP Rectangular pad

RT Real-time controller

S Series configuration

SAE Society of automotive engineers

SOC State of charge

SP Series-Parallel resonant configuration

SPP Solenoid power pad

SP-S Series-parallel configuration in the transmitter side and series configuration in the receiver side

SS Series-Series resonant configuration

SSE Sum of square errors

SSS Series-series-series double coupling resonant configuration

SSP Series-series-parallel double coupling resonant configuration

SS-IC Series-series configuration with an intermediate coupler

S-CLC Series configuration in the transmitter side and capacitor-inductor-capactior configuration in the receiver side

S/SP Series configuration in the transmitter side and series-parallel configuration in the receiver side

SUV Sport utility vehicle

THD Total harmonic distortion

TPP Tripolar pad

TTL Transistor-transistor logic

USA United States of America

VA Volt-ampere

V2G Vehicle-to-grid

WPT Wireless power transfer

ZCS Zero current switch

ZPA Zero phase angle

ZVS Zero voltage switch

x

Nomenclature

Symbol	Unit	Description
a_e		Constant of an exponential decay function
a_g		Constant of a Gaussian function
a_l		Slope of a linear function
$airgap$	mm	Distance between the transmitter and receiver coils
b_1		Relation factor between the operating and the natural transmitter resonant frequencies
b_2		Relation factor between the operating and the natural receiver resonant frequencies in two and three-coil systems and for the natural wheel resonant in inWIPT systems
b_4		Relation factor between the operating and the natural receiver resonant frequencies in inWIPT systems
b_e		Constant of an exponential decay function
b_g		Constant of a Gaussian function
b_l		Slope of a linear function
C_1	μF	Capacitor of the transmitter resonant tank
C_2	μF	Capacitor of the receiver resonant tank in two-coil systems and capacitor of the wheel resonant tank in inWIPT systems
C_4	μF	Capacitor of the receiver resonant tank in inWIPT systems
C_{int}	μF	Capacitor of the intermediate resonant tank
c_g		Constant of a Gaussian function
d	mm	Total diameter of circular geometries
d_{max}	mm	Maximum diameter of circular geometries
d_{min}	mm	Minimum diameter of circular geometries
f_s	Hz	Operating frequency
$G_{i_2 v_1}$		Transconductance gain function between the receiver and transmitter sides

$G_{i_2 i_1}$		Current gain function between the receiver and the transmitter sides in two and three-coil systems
$G_{i_3 i_1}$		Current gain function between the intermediate and the transmitter sides in three-coil systems
G_{iv_X}		Transconductance gain function between the on-board and off-board sides in inWIPT systems, where X takes the values of S and P for series and parallel compensations
i_1	A	Instantaneous transmitter current
i_2	A	Instantaneous receiver current
i_{int}	A	Instantaneous intermediate current
$\overline{I}_1$	A	Current phasor in the transmitter coil
$\overline{I}_{1,1}$	A	Fundamental current phasor in the transmitter coil
$|\overline{I}_1|$	A	RMS current in the transmitter coil
$|\overline{I}_1|$	A	Fundamental RMS current in the transmitter coil
$\overline{I}_2$	A	Current phasor in the receiver coil of two and three-coil systems and for the ORMC in inWIPT systems
$\overline{I}_{2,1}$	A	Fundamental current phasor in the receiver coil of two and three-coil systems and for the ORMC in inWIPT systems
$|\overline{I}_2|$	A	RMS current in the receiver coil of two and three-coil systems and for the ORMC in inWIPT systems
$|\overline{I}_{2,1}|$	A	Fundamental RMS current in the receiver coil of two and three-coil systems and for the ORMC in inWIPT systems
$\overline{I}_3$	A	Current phasor in the transmitter coil of the IRMC for inWIPT systems
$\overline{I}_{3,1}$	A	Fundamental current phasor in the transmitter coil of the IRMC for inWIPT systems
$|\overline{I}_3|$	A	RMS current in the transmitter coil of the IRMC for inWIPT systems
$|\overline{I}_{3,1}|$	A	Fundamental RMS current in the transmitter coil of the IRMC for inWIPT systems
$\overline{I}_4$	A	Current phasor in the receiver coil of the IRMC for inWIPT systems

$\overline{I}_{4,1}$	A	Fundamental current phasor in the receiver coil of the IRMC for inWIPT systems
$|\overline{I}_4|$	A	RMS current in the receiver coil of the IRMC for inWIPT systems
$|\overline{I}_{4,1}|$	A	Fundamental RMS current in the receiver coil of the IRMC for inWIPT systems
$\overline{I}_5$	A	Current phasor in the load of inWIPT systems
$\overline{I}_{5,1}$	A	Fundamental current phasor in the load of inWIPT systems
$|\overline{I}_5|$	A	RMS current in the load of inWIPT systems
$|\overline{I}_{5,1}|$	A	Fundamental RMS current in the load of inWIPT systems
$\overline{I}_{int}$	A	Current phasor in the intermediate coil
$\overline{I}_{int,1}$	A	Fundamental current phasor in the intermediate coil
$|\overline{I}_{int}|$	A	RMS current in the intermediate coil
$|\overline{I}_{int,1}|$	A	Fundamental RMS current in the intermediate coil
I_{bat}	A	Amplitude current in the batteries
$I_{cut-off}$	A	Minimum amplitude current in the batteries to stop the charging process
$|\overline{I}_{inv}|$	A	Rated current of the semiconductors used in the inverter
$\overline{I}_{oc}$	A	Current phasor in the transmitter coil during the open-circuit test
$|\overline{I}_{oc}|$	A	RMS current in the transmitter coil during the open-circuit test
$\overline{I}_{sc}$	A	Current phasor in the receiver coil during the short-circuit test
k_{12}		Coupling coefficient between the transmitter and receiver coils in two and three-coil systems and of the ORMC in inWIPT systems
k_{1int}		Coupling coefficient between the transmitter and intermediate coils
k_{int2}		Coupling coefficient between the receiver and intermediate coils
k_{34}		Coupling coefficient between the transmitter and receiver coils of the IRMC in inWIPT systems
k_{S1S2}		Coupling coefficient between to receiver pads
L_1	μH	Self-inductance of the transmitter coil in two and three-coil systems and of the ORMC in inWIPT systems
L_2	μH	Self-inductance of the receiver coil in two and three-coil systems and of the ORMC in inWIPT systems

L_3	μH	Self-inductance of the transmitter coil of the IRMC in inWIPT systems
L_4	μH	Self-inductance of the receiver coil of the IRMC in inWIPT systems
L_{int}	Self-inductance of the intermediate coil	
L_{12}	μH	Mutual inductance between the transmitter and receiver coils in two-coil systems and of the ORMC in inWIPT systems
L_{34}	μH	Mutual inductance between the transmitter and receiver coils of the IRMC in inWIPT systems
L_{1int}	μH	Mutual inductance between the transmitter and intermediate coils
L_{int2}	μH	Mutual inductance between the receiver and intermediate coils
L_{1S2}	μH	Mutual inductance between the transmitter and the second receiver pads
L_{S1S2}	μH	Mutual inductance between two receiver pads
l_t	mm	Lateral displacement
l_{tx}	mm	Lateral displacement along the x axis
l_{ty}	mm	Lateral displacement along the y axis
ldc	mm	Lower diameter of the pipe coil in the FLCP geometry
$lint$	mm	Diameter of the intermediate coil in the ICP geometry
luc	mm	Upper diameter of the pipe coil in the FLCP geometry
N_1		Number of turns in the transmitter coil
N_2		Number of turns in the receiver coil
N_{int}		Number of turns in the intermediate coil
$N_{x_{min}}$		Minimum number of turns in x coil, where x can take the designation 1,2 or int
$N_{x_{max}}$		Maximum number of turns in x coil, where x can take the designation 1,2 or int
$N_{x_{mean}}$		Average number of turns in x coil, where x can take the designation 1,2 or int

$N_{y_{min}}$		Minimum number of turns in y coil, where y can take the designation 1,2 or int
$N_{y_{max}}$		Maximum number of turns in y coil, where y can take the designation 1,2 or int
$N_{y_{mean}}$		Average number of turns in y coil, where y can take the designation 1,2 or int
N_{coil}		Total number of coils in the MC
P_{oc}	W	No-load active power during the open-circuit test
Pos		Specific charging position with a given $airgap$ and l_t values
P_{con_DIO}	W	Conduction losses of diodes
P_{con_MOS}	W	Conduction losses of MOSFETs
P_{in}	W	Input active power
$P_{L_{inv}}$	W	Conduction losses of the inverter
$P_{L_{rect}}$	W	Conduction losses of the rectifier
$P_{L_{AC-AC}}$	W	Joule and iron losses in the resonant tanks
P_{out}	W	Output active power
P_{su}	VA	Uncompensated apparent power
Q		Quality factor of the load
Q_1		Quality factor of the transmitter pad
Q_2		Quality factor of the receiver pad of two and three-coil systems and of the ORMC in inWIPT systems
Q_3		Quality factor of the transmitter pad of the IRMC in inWIPT systems
Q_4		Quality factor of the receiver pad of the IRMC in inWIPT systems
Q_{int}		Quality factor of the intermediate coupler
Q_{oc}		No-load reactive power during the open-circuit test
r_1	Ω	Resistance of the transmitter coil
$r_{1,1}$	Ω	Resistance of the transmitter coil at the fundamental frequency
r_2	Ω	Resistance of the receiver coil of two and three-coil systems and of the ORMC in inWIPT systems
$r_{2,1}$	Ω	Resistance of the receiver coil at the fundamental frequency of two and three-coil systems and of the ORMC in inWIPT systems
r_3	Ω	Resistance of the transmitter coil of the IRMC in inWIPT systems

$r_{3,1}$	Ω	Resistance of the transmitter coil at the fundamental frequency of the IRMC in inWIPT systems
r_4	Ω	Resistance of the receiver coil of the IRMC in inWIPT systems
$r_{4,1}$	Ω	Resistance of the receiver coil at the fundamental frequency of the IRMC in inWIPT systems
r_{int}	Ω	Resistance of the intermediate coil
$r_{int,1}$	Ω	Resistance of the intermediate coil at the fundamental frequency
r_D	Ω	On-state resistance of a diode
$r_o n$	Ω	On-state resistance of a MOSFET
r_{rim}	mm	Radius of the rim
R_{eq}	Ω	Equivalent resistance of the batteries before rectifier action
$Scenario$		Specific set of turns in a given Pos
Sad_1		Single coil configuration of the receiver pad of the ORMC
Sad_2		Two overlapped coils configuration of the receiver pad of the ORMC
v_1	V	Instantaneous voltage at the inverter output terminals
$\overline{V}_1$	V	Voltage phasor at the inverter output terminals
$|\overline{V}_1|$	V	RMS voltage at the inverter output terminals
$\overline{V}_{1,1}$	V	Fundamental voltage phasor at the inverter output terminals
v_{AK}	V	Instantaneous anode-cathode voltage of a MOSFET
V_{bat}	V	Amplitude voltage of the batteries
$V_{bat_{CC-CV}}$	V	Threshold voltage in the batteries to change from CC to CV mode
$V_{bat_{max}}$	V	Maximum amplitude voltage in the batteries
$V_{bat_{min}}$	V	Minimum amplitude voltage in the batteries
V_{DC}	V	DC voltage link
V_f	V	Threshold voltage of a diode
$|\overline{V}_{L1}|$	V	RMS voltage across the transmitter coil(s)
$|\overline{V}_{L1,1}|$	V	Fundamental RMS voltage across the transmitter coil(s)
$|\overline{V}_{L2}|$	V	RMS voltage across the receiver coil(s) in two and three-coil systems and of the ORMC in inWIPT systems
$|\overline{V}_{L2,1}|$	V	Fundamental RMS voltage across the receiver coil(s) in two and three-coil systems and of the ORMC in inWIPT systems

$\lvert \overline{V}_{L3} \rvert$	V	RMS voltage across the transmitter coil(s) of the IRMC in inWIPT systems
$\lvert \overline{V}_{L3,1} \rvert$	V	Fundamental RMS voltage across the transmitter coil(s) of the IRMC in inWIPT systems
$\lvert \overline{V}_{L4} \rvert$	V	RMS voltage across the receiver coil(s) of the IRMC in inWIPT systems
$\lvert \overline{V}_{L4,1} \rvert$	V	Fundamental RMS voltage across the receiver coil(s) of the IRMC in inWIPT systems
$\lvert \overline{V}_{Lint} \rvert$	V	RMS voltage across the intermediate coil(s)
$\lvert \overline{V}_{Req} \rvert$	V	RMS voltage across the load terminals
$\lvert \overline{V}_{Lint,1} \rvert$	V	Fundamental RMS voltage across the intermediate coil(s)
$\overline{V}_{L_{2-3coil}}$	V	Voltage phasor across the receiver coil for 3-coil systems
$\overline{V}_{oc}$	V	Voltage phasor in the receiver coil during the open-circuit test
ω	rad/s	Angular frequency of the inverter
ω_1	rad/s	Natural angular frequency of transmitter resonant tank
ω_2	rad/s	Natural angular frequency of receiver resonant tank in two and three-coil systems and of the wheel resonant tank in inWIPT systems
ω_4	rad/s	Natural angular frequency of on-board resonant tank in inWIPT systems
ω_{int}	rad/s	Natural angular frequency of intermediate resonant tank
Z_1	Ω	Impedance of the transmitter resonant tank
$Z_{1,1}$	Ω	Fundamental impedance of the transmitter resonant tank
Z_2	Ω	Impedance of the receiver resonant tank in two-coil systems and of the wheel resonant tank in inWIPT systems
$Z_{2,1}$	Ω	Fundamental impedance of the receiver resonant tank in two-coil systems and of the wheel resonant tank in inWIPT systems
Z_{4_X}	Ω	Impedance of the receiver resonant tank in inWIPT systems, where X assumes the values S or P for series and parallel configuration
$Z_{4_X,1}$	Ω	Fundamental impedance of the receiver resonant tank in inWIPT systems, where X assumes the values S or P for series and parallel configuration

Z_{int}	Ω	Impedance of the intermediate resonant tank
$Z_{int,1}$	Ω	Fundamental impedance of the intermediate resonant tank
Z_{in}	Ω	Impedance seen at the output H-bridge inverter terminals
$Z_{in,1}$	Ω	Fundamental impedance seen at the output H-bridge inverter terminals
Z_{int3}	Ω	Reflected impedance from the intermediate side in three-coil systems
$Z_{int3,1}$	Ω	Fundamental reflected impedance from the intermediate side in three-coil systems
Z_{rec}	Ω	Reflected impedance in two-coil systems
$Z_{rec,1}$	Ω	Fundamental reflected impedance in two-coil systems
Z_{rec3}	Ω	Reflected impedance from the receiver side in three-coil systems
$Z_{rec3,1}$	Ω	Fundamental reflected impedance from the receiver side in three-coil systems
$Z_{r_{ORMC},1}$	Ω	Fundamental reflected impedance from the wheel side onto the transmitter side in inWIPT systems
$Z_{r_{IRMC},1}$	Ω	Fundamental reflected impedance from the on-board side onto the wheel side in inWIPT systems
α	º	Phase-shift control angle
η_{AC-AC}	%	Resonant compensation networks efficiency
η_{inv}	%	Inverter efficiency
η_{rect}	%	Rectifier efficiency
η_{sys}	%	DC-DC system efficiency
$\Re$	H^{-1}	Equivalent reluctance of a given power pad
θ	º	Design parameter of the *saddle* coils
θ_1	º	Angle difference between θ_{11} and $\alpha/2$
θ_{11}	º	Angle difference between $\overline{I}_{1,1}$ and $\overline{V}_{1,1}$
λ_{coil}	mm	Length of a saddle coil

Contents

List of Figures

xxviii

List of Tables

Chapter 1

Introduction

The exponential growth of the world population and the current lifestyle is leading to historic global pollution levels. At the current rate, the planet risks a irreversible damage from climate change. As a result, there is a global initiative towards renewable and sustainable practices to reduce the human footprint in the planet. Electrical energy emerges as a desirable form of energy due to its numerous clean sources, like solar and wind, and ease of transportation in the existing global grid. New technological advancements lead to a reduction of the fossil fuels dependence and towards cleaner and friendlier solutions.

The transportation sector is responsible for 14 % of the global greenhouse emissions since 95 % of his energy comes from fossil fuels therefore, it is one major sector targeted for electrification. Electrified vehicles would then be powered by clean energy sources and reduce the pollution footprint in the process.

1.1 Electric vehicles

The concept of electric vehicles (EVs) is not new and the first prototypes dated from 1830s [1]. These early prototypes used small battery packs to supply the small direct current (DC) motors. The invention of rechargeable lead-acid batteries and other technological advancements in the late 19th century contributed to the widespread interest of EVs as a way of transportation. In London, there were Electric Cab Company's taxis. The low noise pollution, vibration and the low effort to operate an EV, in contrast with the hand cranking to start an internal combustion engine (ICE), make them suitable for short-distances like public transportation in large cities.

However, the advancements made in the late 19th and early 20th centuries regarding ICE vehicles contributed to a total disappearance of EVs since the 1930s. Inventions like the muffler by Hiram Percy Maxim in 1897 and the electric starter by Charles Kettering in 1912 make the use of ICE vehicles easier and bearable. Also, Henry Ford's assembly line and

Table 1.1: Battery specifications of different BEVs.

Model	Battery capacity (kWh)	Range (km)	Power consumption (kW/km)
BMW i3	33	200	0.165
VW Golf-e	35.8	190	0.188
Nissan Leak	39.5	240	0.165
Tesla Model 3	55	310	0.177
Chevy Bolt	65	417	0.156
Ford Transit	68	315	0.216
Toyota bZ4X	71.4	380	0.188
Cupra Born	77	450	0.171
Audi e-tron	95	360	0.264
Ford Mustang	99	539	0.184
Tesla Model S	100	510	0.196
Lucid Air	105	630	0.167
Mercedes EQS	107.8	640	0.168
Trucks			
Freightliner eM2	315	370	0.851
eCascadia	475	402	1.18
Tesla Semi	500	482	0.829
Volvo VNR	565	443	1.275
Nikola Tre	753	563	1.337

the discovery of large oil reserves in the United States of America (USA) caused a rapid drop of ICE vehicles costs, making them affordable to lower working classes. To fight the advancements of ICE vehicles, EVs manufacturers like Cleveland and Woods of Chicago offered hybrid electric vehicles (HEV). These new vehicles used an ICE together with an electric motor and Woods claimed that their HEV reached a top speed of 56 km/h and with a fuel efficiency of 4.9 liters per 100 km. However, the Woods HEV was more expensive and less powerful than existing ICE vehicles and therefore sold poorly.

The EVs faded away for nearly fifty years until the 1970s with the Arab oil embargo. A renewed interest around EVs by the U.S Department of Energy lead to numerous tests in various electric vehicles from different vehicle companies. The tipping point for EVs occurs in 1997 with the introduction of the first modern hybrid electric vehicle, the Toyota Prius. Since then, over 20 HEV have been offered by different automotive companies. Nowadays, the offer extends to full electric vehicles, also known as battery electric vehicles (BEVs), with the automotive company Tesla being the first company to have exclusively BEVs in its production lines. Table 1.1 shows some BEVs and EV truck models and their main battery properties, values obtained assuming average speed between 80 and 100 Km per hour. On average, a BEV consumes 185 W by kilometer whereas BEV trucks require 1250 W to travel the same distance. These values together with the battery capacity define the EVs mile range.

1.1.1 Charging electric vehicles

Electric vehicles have clear advantages over ICE vehicles like reduced noise, full torque capability of the motor from a standstill position and a smaller carbon footprint. However, they are still limited in range by the batteries storage capacity. The current state of EV lithium ion battery technology have a specific energy (energy per unit mass) that places them behind that of gasoline by a factor of almost 100. Manufacturers workaround this limitation using larger battery packs, as seen by the last entries of BEVs in Table 1.1. A costlier and bulkier solution to a limitation that follows EVs since their first appearance. Also, lithium ion batteries can take several hours to charge which will undoubtedly affect the driving habits of the users.

All current HEVs and BEVs models have in-built sockets that can charge the battery pack from a few kilowatts, in domestic chargers, up to 250 kW in supercharging stations [2, 3]. The vehicles can be charged from alternate current (AC) or DC power supply with different voltage and current values. According to Society of Automotive Engineers (SAE) standards, AC chargers can be divided into three different power levels, as depicted in Table 1.2 [4]. AC levels 1 and 2 are intended for domestic use. AC level 3 is permanently wired to the utility grids and they are usually found in commercial locations. The DC charging systems require a dedicated infrastructure and they are usually mounted at parking areas or public charging stations. DC chargers automatically adjust the voltage ratings according with the battery packs. Additionally, they are faster than AC chargers since they bypass the vehicle on-board battery controller and charge the battery pack directly. The supercharger of Tesla is one example where this strategy is adopted, allowing a maximum charging power of 250 kW.

Table 1.2: Power levels of EV chargers.

Operating level	Input voltage (V)	Maximum current (A)	Output power (kW)	Charging time (h)
AC Level 1	120	12-16	1.08-19	6-24
AC Level 2	208-240	16-80	3.3-19.2	1-3
AC Level 3	208/480/600	150-400	>19.2	0.5-1.5
DC Level 1	200-450	80	36	0.5-1.3
DC Level 2	200-450	200	90	0.3-1.3
DC Level 3	200-600	400	240	0.25-1

The high power rating of Level 3 AC/DC chargers require large power demands from the grid simultaneously. This scenario forces a restructuring of the electric power lines to accommodate several chargers. Unfortunately, the increase of EVs and the limited number

of chargers will provoke queues in the charging areas. In addition, the need of human intervention in the charging process increases the risk of shock hazard and electrocution. Alternative wireless charging technologies are then being studied as viable replacements to conductive chargers.

1.2   Wireless power transfer

Wireless power transfer (WPT) technology enables the energy transfer between two systems without any contact. The concept dates from the late 19th century where Prof. Heinrich Hertz demonstrated electromagnetic wave propagation in free space using a spark gap to generate high frequency power and to detect it at the receiving end. Nikola Tesla, in 1899, conducted a series of experiments in Colorado Springs where he devised the best approach for wireless power transfer [1,5]. During its stay in Colorado Springs, Tesla reported power transfer with distances over 18 m between the transmitter and receiver coils. Tesla accomplished such feats using one of his early inventions, known as Tesla coil, to operate the transmitter coil at higher frequencies and voltages levels. These apparatus would work with voltage levels of several hundred volts, making Tesla proposed systems potentially unsafe. Unfortunately, there is no evidence of a successful demonstration. In 1964, William C.Brown demonstrated the power transfer capabilities using microwaves to power a model helicopter. Later, in 1975, Brown and Robert Dickinson at NASA's Jet Propulsion Laboratory transmitted 30 kW DC output power using 2.38 GHz microwaves over a distance of 1.5 km. A renewed interest in wireless power transfer arose in 2007 when a group of researchers from MIT repeated Tesla experiment based on coupled mode theory using magnetic resonance over a distance of 2 m [6]. Since then, numerous studies have been carried out to incorporate wireless power transfer in EVs.

Wireless charging technologies can be grouped as far-field and near-field techniques, as illustrated in Figure 1.1. The first group includes Radio-frequency (RF)/microwave techniques that radiate energy isotropically or toward some direction through beamforming. The power transfer starts with a AC/DC conversion followed by a DC/RF conversion through a magnetron at the transmitter side. The energy is then captured in the receiver end by a rectenna and rectified into electricity again via a RF/DC converter. However, due to the high frequency spectrum (300 MHz to 300 GHz), the effect of electric fields in the human body are more dangerous and they are not widely used [7]. The near-field group includes the techniques that use variable magnetic or electric fields to accomplish power transfer between
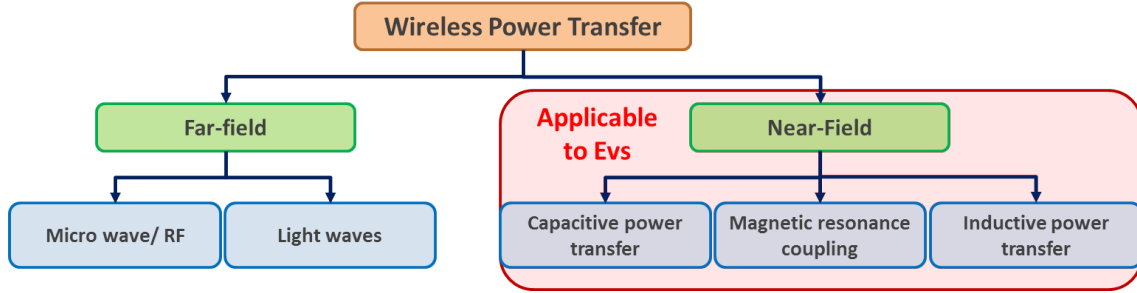
Figure 1.1: Classification of different WPT technologies.

two coupled sides. Electric field coupling, also known as capacitive power transfer (CPT), uses two pair of plates to form a capacitor for transferring power [8–12]. One advantage of CPT is the ability to transfer energy through metallic materials since a capacitor is formed between each conductor plate and the metallic surface. Furthermore, they are less sensitive to lateral displacements as the electric field between the plates "bends" with the displacement value. CPT systems are lightweight and cost-effective couplers when compared with magnetic coupling techniques. However, the capacitance between the two plates is low, limiting the power transfer capabilities in applications with high air gap distances. The increase of the operating frequency to the MHz range mitigates the large air gap values. Still, the power density of CPT is 5 to 9 times lower than magnetic coupled systems, meaning the capacitive coupler must be much larger than the air gap and it may not be practical.

Magnetic field coupling techniques use a varying magnetic field to achieve power transfer and it includes inductive coupling and magnetic resonance coupling (MRC) techniques. The second technique is based on evanescent-wave coupling that accomplishes energy transfer between two resonant coils through varying or oscillating magnetic fields [13–16]. The two resonant coils are strongly coupled and operate at the same resonant frequency, thus high power throughput is achieved with small leakage to non-resonant externalities. Several studies demonstrated the capabilities of power transfer over larger distances using MRC technique [17–20]. Another advantage of MRC is the simultaneous charging of multiple devices. However, the high operating frequency (range of MHz) [21–24] and the complex tuning of both sides is unsuitable for EVs charging applications.

Inductive coupling, also referred as Inductive Power Transfer (IPT) system, transfers energy between two coupled coils. The transmitter coil generates a varying magnetic field which induces a voltage across the receiver coil, according to Faraday's Law. To boost the quality factors of the coils at low operating frequencies (from 10 kHz to 250 kHz) compensation capacitors are added to the circuit [25–28]. IPT systems gain popularity and its applicability in EVs is being investigated by the scientific community since the early 21st

7

Table 1.3: Comparison of WPT technologies.

WPT technique	Advantages	Disadvantages
RF/Microwave	✓ Ultra-long transfer distance ✓ Potential transfer of several kW power	✗ High radiation and losses ✗ Complex equipment ✗ Antenna and rectenna orientation needed
Electric field coupling	✓ Better misalignment tolerance than IPT system ✓ Can transfer power through metallic materials ✓ Light and low-cost couplers	✗ Limited power due to low capacitance ✗ Very high electric field requirement
Magnetic field coupling	✓ Highest efficiency ✓ Some tolerance to displacements (although the efficiency decreases ✓ Can adapt to power transfer widely ranging from MW level to some Watts	✗ Small power transfer distance. ✗ Need for controlling the electromagnetic emissions

century. Since then, a lot of works present efficiencies as high as 97 % and equiparable to conductive chargers. Therefore, the work presented in this thesis addresses specific challenges of IPT systems. Table 1.3 summarizes the advantages and limitations of the different WPT technologies.

Inductive power transfer

IPT technology applied to EVs has the potential of similar charging capabilities as conductive chargers. Additionally, IPT technology offers new advantages and possibilities such as:

- **Autonomous operation**. The charge/discharge process occurs without the driver's intervention;

- **Safer operation**. Since the driver is not required in the charging process, there is no risk of electric shock. Furthermore, IPT systems accomplish power transfer in different weather conditions such as snow or rain;

- **Quasi-dynamic or dynamic charge**. IPT technology offers the possibility of EV charging while moving or in a stationary position for a short period of time. Such capability has the potential to reduce the battery pack size of an EV with a wide dynamic charging network.

- **Vehicle-to-grid (V2G) capabilities**. The electric market is shifting his power flow paradigm and IPT technology eliminates the driver from V2G tasks, allowing more

No	Institution/ Company	No	Institution/ Company
1	University of Auckland	6	University of Coimbra
2	Korea Advance Institute of Science and Technology	7	Witricity
3	Oak Ridge National Laboratory	8	Momentum Dynamics
4	Swiss Federal Institute of Technology	9	Plugless Power
5	Massachusets Institute of Technology	10	WAVE
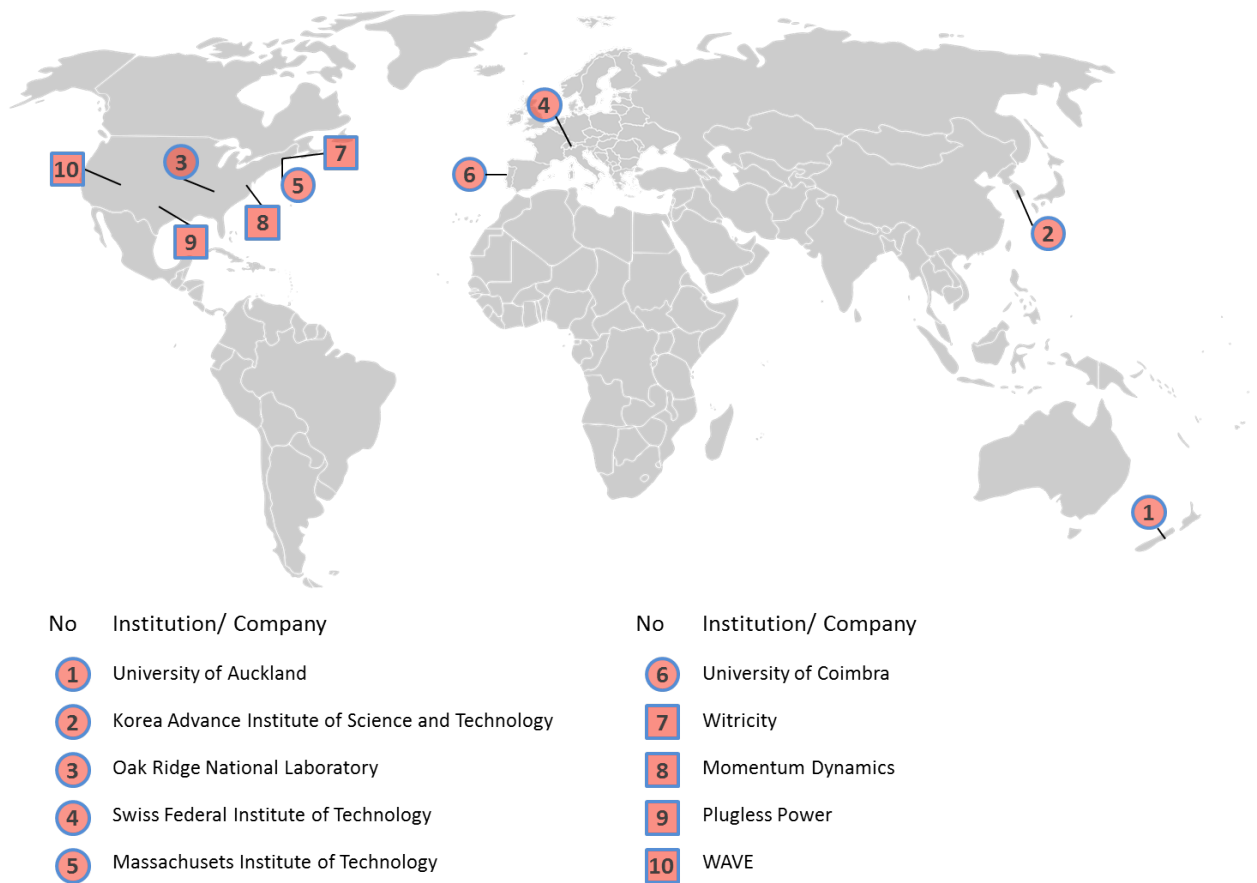
Figure 1.2: Geographical overview of IPT research groups and companies with IPT solutions for automotive sector.

complex grid adjustment algorithms.

The aforementioned advantages of IPT systems propelled a series of academic research groups around the world. Additionally, wireless EV technology companies spin-offs of academic research have several IPT products for different applications ranging from autonomous guide vehicles (AGVs) to electric buses. Figure 1.2 identifies geographically the main IPT research groups and companies whereas Table 1.4 enumerates the main parameters of IPT prototypes and commercial solutions.

Research groups within universities like the Massachusetts Institute of Technology (MIT), Auckland University [29] and Korea Advanced Institute of Science and Technology (KAIST) and national laboratories like the Oak Ridge National Laboratory (ORNL) are pioneers in IPT breakthroughs with main focus in dynamic IPT systems, magnetic coupler optimizations, high order compensation networks and control strategies with tolerance to displacements between the off-board and on-board sides of the vehicle. From these discoveries sprung spin-offs like HaloIPT and Witricity from Auckland and MIT, respectively. HaloIPT has IPT solutions in a power range between 3.3 and 20 kW and works in strict collaboration with

Table 1.4: Commercial and laboratory prototypes using IPT technology.

Company	Output power (kW)	Year	Application
Plugless	3.3-7.2	2012	Static: vehicle
Conductix	180	2013	Static: Bus
Bombardier	200	2013	Static: Bus
Halo IPT	3.3-22	2014	Static: vehicle
Chine ZTE	30	2014	Static: Bus
KAIST	180	2015	Dynamic: Bus
Witricity	3.6-11	2016	Static: vehicle
ETH	50	2016	Static: Bus
INTIS	30	2017	Static; vehicle
ORNL	120	2018	Static: Bus
Momentum	200	2018	Static: Bus
Japan NUT	22	2019	Static: vehicle
WAVE	250	2019	Static: Bus

Rolls Royce [30, 31]. Witricity also offers solutions with power levels up to 11 kW and their technology is licensed by Toyota to be integrated in new electric and hybrid vehicle models. Momentum Dynamics has solutions with power levels up to 300 kW for electric buses and with similar efficiencies of plug-in chargers. Conductix-Wampfler has demonstrators of stationary charging for electric buses in Torino with maximum output power levels of 60 kW [5, 32]. Plugless Power also offers static IPT solutions for the Chevrolet VOLT and Nissan Leafs EVs with power levels up to 3.3 kW.

The ORNL has focused its research in dynamic IPT with special emphasis on leakage field minimization, lateral displacement and interoperability between couplers with different geometries [33, 34]. The researchers presented a single-phase 120 kW system with maximum efficiency values around 97 % for a 127 mm air gap [35]. The KAIST team has successfully deploy several large-scale dynamic demonstrators on railway transit and EVs, where they propose different coil and core arrangements to improve power density [36–40]. The research group from ETH Zurich, in collaboration with the ABB group, provided a comprehensive design consideration regarding a Silicon Carbide (SiC)-based 50 kW charger. The demonstrator achieved maximum efficiency values around 96 % and considerations were made about leakage field, thermal and size constraints [41–43].

European Union is funding several research projects towards Eco solutions in the transportation sector with the inclusion of inductive chargers. The projects Fastincharge and UNPLUGGED, both started in 2012, carried out a comparative analysis of different charging methods including plug-in, static and dynamic IPT. Both projects concluded that the use of IPT systems is a feasible way to overcome the current limitation of EVs range. In addition, different static IPT configurations were presented with efficiency values above 90

% under perfect aligned conditions.

The IPT prototypes and commercial products identified in Table 1.4 show an increase of power levels to values comparable with plug-in fast chargers. The available solutions are mainly intended for static applications. Moreover, these systems are not applicable to every vehicle and the existing design methodologies take only into account the basic resonant configurations.

Taking all this into account, the main objectives of this work are the study, development and analysis of solutions that minimize the impact of displacements and, in the process, provide design guidelines that ease the construction of IPT prototypes based on real specifications and constraints. In addition, the new design guidelines will focus on resonant configurations that exhibit current and/or voltage source characteristics. In this way, the charging process of the batteries is regulated using the off-board controller with a open-loop control strategy. Therefore, the synchronization between both off-board and on-board controllers is avoided and the implementation costs are reduced.

1.3   Motivation

Sustainable electrical mobility is the way for a low carbon footprint in the transportation sector. Europe will meet its objectives in terms of greenhouse gas emission reduction only if it accelerates market uptake of EVs in the upcoming years. While electrically-chargeable cars accounted for 11 % of all new car registrations in the European Union (EU) in 2020, only 1.9 % of all vans sold in 2020 were battery-powered. Moreover, only 0.04 % of heavy-duty vehicles in the EU fleet are EVs. These values hardly change in the last two years.

Reluctance to EV adoption is related to the lack of charging stations (despite number increase) but especially to the limited ranged (up to 500 km). The large difference of energy density between the batteries and fossil fuels limits the storage capability in EVs. Additionally, plug-in chargers increase the risk of electric shock hazard, especially under wet environments. Also, it only allows the charging process with a parked vehicle and despite the increase in charging stations, larger queues can be discouraging for final users. IPT technology has the potential to solve all plug-in charger limitations and offer unlimited drive range. Therefore, the main motivation of this work was the search of affordable charging solutions that mitigate some of the current IPT limitations and accelerate the inclusion of IPT technology into EVs.

1.3.1   Outline of the Thesis

The effect of displacements can be mitigated in different components that form an IPT system. This work sought out solutions to the displacement problem in various research areas within IPT technology. The journey started with the analysis of the effect of displacements using the basic resonant configurations. Then, a magnetic optimization of different geometries is carried out to reduce the vertical displacement between the off-board and on-board sides. A new magnetic coupler with an intermediate network is also presented to provide better vertical tolerance with current source characteristics. Finally, a new IPT configuration and respective magnetic design that minimizes the vertical displacement, regardless of the vehicle class, is presented and analyzed.

To ease the reading and navigation throughout this work, a brief summary of each chapter is presented in this section. The content is divided into six chapters as follows:

- **Chapter 1** outlines the history of electric vehicles and the role of wireless power transfer technology to overcome the current EV charging limitations. A brief description of the existing WPT and the benefits of IPT technology over the remainder WPT technologies in EV battery chargers is carried out. The main contributions and publications of this work are presented, followed by a brief summary of the content in each chapter of this document.

- **Chapter 2** starts with a review of the IPT technology according with its main research areas. The fundamental concepts of IPT systems are also derived and key aspects of each topology like power transfer capabilities are discussed. The impact of manufacturer's tolerance and aging in the four basic compensation networks is analyzed. A summary of the main findings is presented at the end of the chapter.

- **Chapter 3** explores in detail the MC component. A new vertical double receiver IPT charger is presented for AGVs or heavy-duty vehicles. A design optimization of different ferrite-less geometries for dynamic applications is also carried out. To conclude, a new mapping methodology that minimizes the number of FEA simulations is presented and validated experimentally. The main findings are summarized at the end of the chapter.

- **Chapter 4** investigates the inclusion of an intermediate coupler in a conventional series-series IPT system. A design methodology of a open-loop constant current batteries charger is presented based on the steady-state circuital analysis. A set of selection metrics are proposed to identify the optimal solution. Furthermore, an estimation

procedure of the load and mutual inductance values, based only in the information available from the off-board side, is also presented. An experimental prototype that validates both the design methodology and identification method was built and assembled in a converted combustion vehicle. A summary of the main findings is presented at the end of the chapter.

- **Chapter 5** presents a new concept of inductive power transfer that minimizes the air gap, regardless of the vehicle class. The in-wheel IPT (inWIPT) concept is presented at the beginning of the chapter. A new double-coupling inWIPT is explored along with its constructive aspects. Several cylindrical shape MC designs with both non-polarized and polarized flux patterns are evaluated and optimized due to the lack of literature. Then, a comparative study is carried out using the series and parallel configurations since the inclusion of a second MC changes the intrinsic characteristics of a resonant circuit. A step by step guideline that identifies the operational range of the mutual inductance values, based on certain design specifications and constraints, is also presented. Experimental tests using a full scale wheel prototype validate the proposed inWIPT in different coupling charging scenarios and load conditions. A summary of the main findings is presented at the end of the chapter.

- **Chapter 6** summarizes the final conclusions of the presented work.

1.4   Main Contributions and List of Publications

The large number of admissible IPT configurations difficult the standardization of solutions based on certain specifications and constraints. Furthermore, the component's tolerance and aging effects are often ignored to simplify the system analysis. In this context, the first contribution of this work is the generic analysis of the four basic resonant configurations and equivalent model.

The magnetic coupler is the key element in IPT systems and is responsible for the energy transfer between the off-board and vehicle's side. Its constitution resembles a conventional 50/60 Hz transformer with a transmitter and receiver sides, each formed with one or more coils and a ferromagnetic core. The magnetic coupling between both sides depends directly on the direction and magnitude of the displacements [31, 44, 45]. Their impact are, however, mitigated with a proper design and placement of the coils and ferromagnetic core. The optimization of MCs and extraction of both self and mutual inductance profiles occur via finite element analysis (FEA) tools. The number of required FEA simulations range from several

dozens up to a few hundreds to assess the effect of different vertical and lateral displacements, and number of turns in the self and mutual inductance values. Unfortunately, each simulation runtime ranges between a few minutes up to 1 hour, depending on the simulation model and computer specifications. These execution times together with the numerous geometries available in the literature make it an unpractical approach in the profiling process of a MC. Therefore, this work also presents a framework that extracts the self and mutual inductance profiles with minimum FEA simulations. Several experimental coupling measurements in different magnetic coupler geometries validate the proposed framework.

One way to boost the power transfer capabilities in IPT systems with higher air gap requirements is to include an intermediate resonator between the transmitter and receiver coils. Unfortunately, the literature shows a lack of design guidelines towards three-coil systems. Moreover, IPT solutions that don't require a communication link between the off-board and on-board sides are preferable since they are easier to implement, cheaper and with less components. Therefore, this work presents a design methodology to obtain a constant current charging mode and an estimation procedure to determine the coupling coefficients using only off-board measurements. The realized prototype validates both the design methodology and estimation procedure under different load and charging conditions.

The air gap between the transmitter and receiver pads of the MC is reduced to a minimum and independent of the vehicle type if the wheels are used as an intermediary stage between the off-board and on-board sides of the vehicle. This work explores the in-wheel IPT concept and proposes a new double coupling resonant configuration. The main contributions regarding in-wheel IPT include the design and optimization of several MC geometries, comparative study of several double coupling IPT resonant configurations and a step-by-step guide to identify the minimum mutual inductance values based on specific specifications like output power, operating frequency and optimum efficiency. A real size in-wheel prototype validates the proposed configuration and corresponding benefits against conventional IPT configurations.

The aforementioned work resulted in a series of conference and journal articles, a chapter book and a financed project from Faculdade de Ciências e Tecnologia. The double coupling in-wheel configuration is currently under evaluation for patenting.

Journal Papers

- **E. G. Marques**, V. S. Costa, A. M. S. Mendes and M. S. Perdigão , "Double Coupling In-Wheel IPT System for Electric Vehicles," under R2 revision at IEEE Transactions on Vehicular Technology, 2022.

- V. S. Costa, A. M. S. Mendes, M. S. Perdigão and **E. G. Marques**, "Double-coupling impact on dynamic IPT systems for EV charging applications," under review at IEEE Transactions on Vehicular Technology, 2022.

- **E. G. Marques**, A. M. S. Mendes, M. Perdigão, and V. S. Costa, "Mapping methodology for self and mutual inductance profiles in ipt systems", Energies vol. 15, no. 17, 2022.

- **E. G. Marques**, A. M. S. Mendes, M. S. Perdigão, and V. S. Costa, "Design methodology of a three coil ipt system with parameters identification for EVs," IEEE Transactions on Vehicular Technology, vol. 70, no. 8, pp. 7509–7521, Aug 2021.

- **E. G. Marques** and A. M. S. Mendes, " Comparison of Magnetic Coupling Structures for IPT Systems ", COMPEL- the international Journal for Computation and Mathematics in Electrical and Electronic Engineering, vol. 34, pp. 514-530, March 2015.

Magazine Articles

- **E. G. Marques**, V. S. Costa, A. M. S. Mendes and M. S. Perdigão , "Inductive Power Transfer: Past and Future Trends," under review at IEEE Vehicular Technology Mag, 2022.

Conference Papers

- **E. G. Marques**, V. S. Costa, M. Torres, B. Rios, A. Mendes, and M. S. Perdigão, "Double coupling ipt systems for ev charging applications," in 2021 IEEE Vehicle Power and Propulsion Conference (VPPC), 2021, pp. 1–6.

- V. S. Costa, **E. G. Marques**, A. M. S. Mendes, and M. S. Perdigão, "Resonant converter topology impact on a dynamic IPT application," in 2021 Telecoms Conference (ConfTELE), 2021, pp. 1–6.

- V. S. Costa, **E. G. Marques**, A. P. Mendes, M. S. Perdigao, and A. M. S. Mendes, "Magnetic couplers for dynamic ipt systems," in 2019 IEEE Vehicle Power and Propulsion Conference (VPPC), 2019, pp. 1–6.

- **E. G. Marques**, C. Marques, J. V. N. Silva, S. V. da Silva, M. S. Perdigão, and A. M. S. Mendes, "Evaluation of intermediate coils in ipt systems under magnetic coupler displacements," in IECON 2017 - 43rd Annual Conference of the IEEE Industrial Electronics Society, 2017, pp. 5342–5347.

- **E. G. Marques**, S. V. da Silva, C. Marques, J. V. N. Silva, M. S. Perdigão, and A. M. S. Mendes, "A new ipt transmitter configuration tolerant to magnetic coupler displacements," in IECON 2017 - 43rd Annual Conference of the IEEE Industrial

Electronics Society, 2017, pp. 5307–5312.

- **E. G. Marques**, S. V. da Silva, and A. Mendes, "A new magnetic coupler for evs chargers based on plug-in and ipt technologies," in 2017 IEEE Energy Conversion Congress and Exposition (ECCE), 2017, pp. 2760–2766.

- **E. G. Marques** and A. M. S. Mendes, "Modelization and optimization of solenoid magnetic structures for ipt systems," in 2017 11th IEEE International Conference on Compatibility, Power Electronics and Power Engineering (CPE-POWERENG), April 2017,

- **E. G. Marques**, "Optimization of transmitter magnetic structures for roadway applications," in 2017 IEEE Applied Power Electronics Conference and Exposition (APEC), March 2017, pp. 959–965.

- **E. G. Marques**, , "Constant current controller for electric vehicles chargers based on ipt systems," in 2014 IEEE Vehicle Power and Propulsion Conference (VPPC), 2014, pp. 1–6.

- **E. G. Marques**, D. Abreu, M. S. Perdigao, J. P. Trovao, and A. M. S. Mendes, "Full-bridge topology for ipt system on-board charger," in 2014 IEEE Vehicle Power and Propulsion Conference (VPPC), 2014, pp. 1–6.

Book Chapter

- **E. G. Marques**, A. M. S. Mendes, M. S. Perdigão and V. S. Costa (2022) "Inductive Power Transfer: Past, Current and Future Research," in Hüseyin T. A. (Editor), The Dynamics of Vehicles - Basics, Simulation and Autonomous Systems, Intechopen.

FCT Project

- The project entitled "*inWheel Inductive Power Charging for Sustainable Mobility*" was approved in September 2022 by FCT foundation under the supervision of Prof. Dr.ª Marina S. Perdigão with the ID 2022.06192. PTDC. The project will explore the applicability of the inWIPT concept into dynamic charging applications.

Chapter 2

Inductive power transfer

This chapter starts with an overview of Inductive Power Transfer (IPT) system and its main research areas throughout Sections 2.1 to 2.5. A summary of the main conclusions is made in Section 2.6 and the adopted path of this work is made in Section 2.7.

2.1   System overview

Inductive power transfer (IPT) concept appeared soon after Ampère and Faraday propose their laws. The principle requires two or more coils magnetically coupled, where the current of one coil induces a voltage in the other. Figure 2.1 depicts a typical EV IPT system with its main components in the off-board and on-board sides. The off-board side comprises a high frequency power supply with a resonant compensation network connected to the transmitter pad of a magnetic coupling structure (MC). The on-board side includes the receiver pad of the MC, a resonant compensation network, the on-board converter and the batteries. The transmitter and receiver pads have degrees of freedom between one another, including air gap and lateral displacements. As a result, the coupling factor of the MC is drastically reduced to values between 0.05-0.35 [32,46,47]. To overcome this limitation, resonant compensations together with high operating frequencies are used to increase power transfer capabilities and, in the process, minimize the volt-ampere rating and commutation losses of the power supply. The mobility of the receiver pad together with the high frequency operation create additional concerns when compared with plug-in chargers like position detection, stray magnetic fields compliance and foreign object detection (FOD) between the transmitter and receiver pads. Figure 2.1 summarizes the main concerns in both off-board and on-board sides.

The power transfer capabilities and optimal operation of an IPT system depend on the proper selection of the resonant network configuration, off-board and on-board converters and, geometry of the magnetic coupler. Each component of the IPT system has several options, which means that the overall system can take up to several hundreds possibilities.
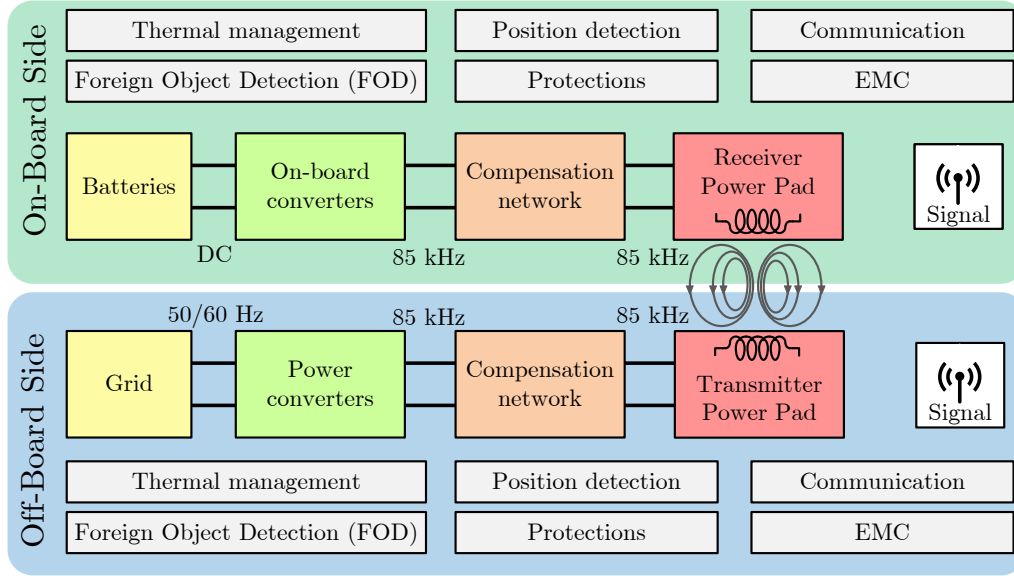
Figure 2.1: Overview of a typical IPT system with its main components.

Therefore, IPT systems are divided in four main research areas which include resonant configurations, circuitry analysis, design of magnetic coupling structures and off-board and on-board converters with their respective control strategies. Figure 2.2 illustrates the main research areas and sub-categories of IPT systems.

2.2   Static and Dynamic charging systems

IPT systems can be divided in two charging modes: static and dynamic. In the first mode, the vehicle is charged in a fixed position whereas in the second mode, the vehicle is moving along the roadway during the charging process [48, 49]. Figure 2.3 illustrates the typical conversion stages of a static IPT charger between the grid and the vehicle battery pack. In the off-board side, a full bridge rectifier with a power factor correction stage is often used to meet the harmonic requirements, as described in the EU directive IEC 61000-3-12. An output DC bus capacitor ensures a stable voltage that supplies the inverter. The high frequency AC signal generated by the inverter is filtered by the resonant tank to a sinusoidal current that flows through the transmitter coil. In the on-board side, the induced voltage across the receiver coil is boosted by the receiver resonant tank and then rectified into a DC voltage. The on-board converter regulates the charging process of the batteries.

Dynamic IPT systems were first employed in industrial materials handling applications using elongated transmitter coils, also known in the literature as track based IPT systems [50–55]. These applications use an elongated loop wire (e.g 100 m) as the transmitter coil, connected to an high-frequency power supply and resonant tank, as illustrated in Figure
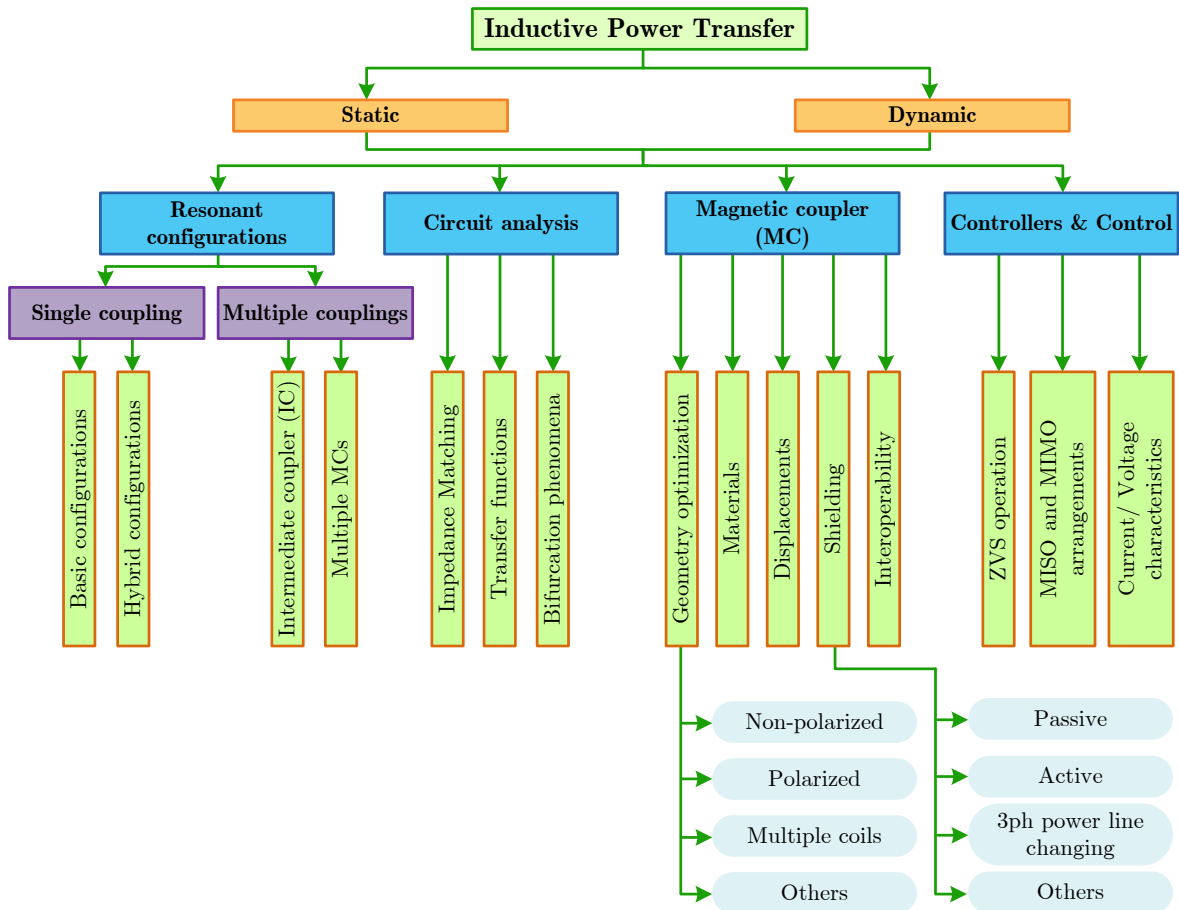
Figure 2.2: Main research areas of IPT systems.

2.4. Such configuration allows multiple receivers to be powered simultaneously and they are regulated individually. The same principle can be applied to EV dynamic chargers [56–58]. In 1992, Berkeley undertook the Partners for Advanced Transit and Highways (PATH) program to analyze the viability of dynamic EV IPT systems. The program prototypes achieved an efficiency of 60 % when transferring 60 kW with an air gap of 76 mm. Unfortunately, the limiting switching of power electronics set construction costs around 1 million doller per Km with track currents in the thousand range and low efficiency values.

The Korean Advanced Institute of Science and Technology (KAIST) has been conducted the on-line electric vehicle (OLEV) project with numerous prototypes across South Korea since early 2009 [36, 38, 39, 59, 60]. The first generations of prototypes solved most of the problems of the PATH project like high frequency current-controlled inverters, continuous power transfer, dynamic response analysis for high order resonant configurations and low EMF characteristics. Still, the construction cost and time of the power track should be reduced for a better adherence and commercialization.

The 5G OLEV uses a compact ferromagnetic with a S-type shape, as illustrated in
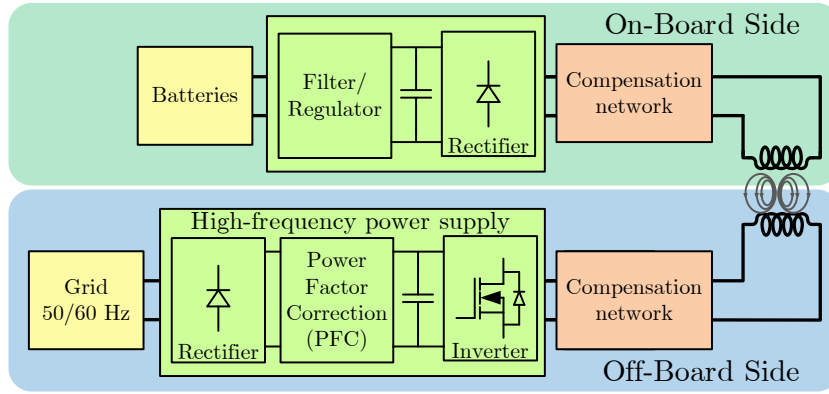
Figure 2.3: Overview of a typical static IPT configuration.
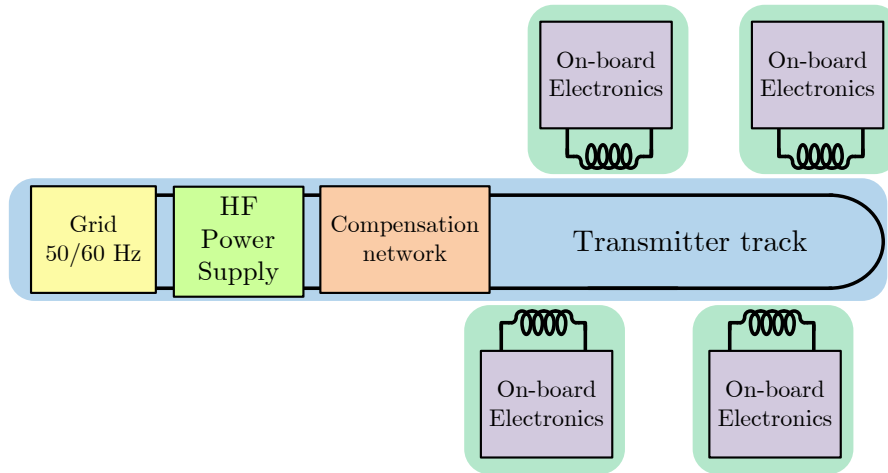
Figure 2.4: Overview of an elongated dynamic IPT configuration with multiple receivers.

Figure 2.5 [61–64]. This new design has a width of only 40 mm but at the expense of a large receiver pad of 1000x800 mm in order to ensure an air gap operation of 200 mm with a lateral tolerance of 300 mm. The system, in these conditions, can transfer a maximum power of 22 kW with an efficiency of 71 % [40, 62]. Other studies employ rectangular coil shapes at the expense of wider installation areas [65, 66].

The use of power tracks in IPT systems offer a continuous power transfer with a constant coupling factor but they have inherent limitations like the large self-inductance of the power track. The use of high inductance values reduce the overall coupling factor and require higher voltage levels to drive the necessary transmitter current. Additionally, most power track systems prototypes operate with frequencies around 20 kHz instead of the 85 kHz proposed by the SAE J2954 standard.

Segmented pads system, also referred in the literature as lumped systems, use discrete power pads placed along the road to transfer power to the vehicle [34, 67–69]. Figure 2.6 illustrates different segmented pad configurations studied in the literature. The configuration of Figure 2.6 (a) extends the DC bus from the roadside cabinet to each individual converter

(a)

(b)

(c)
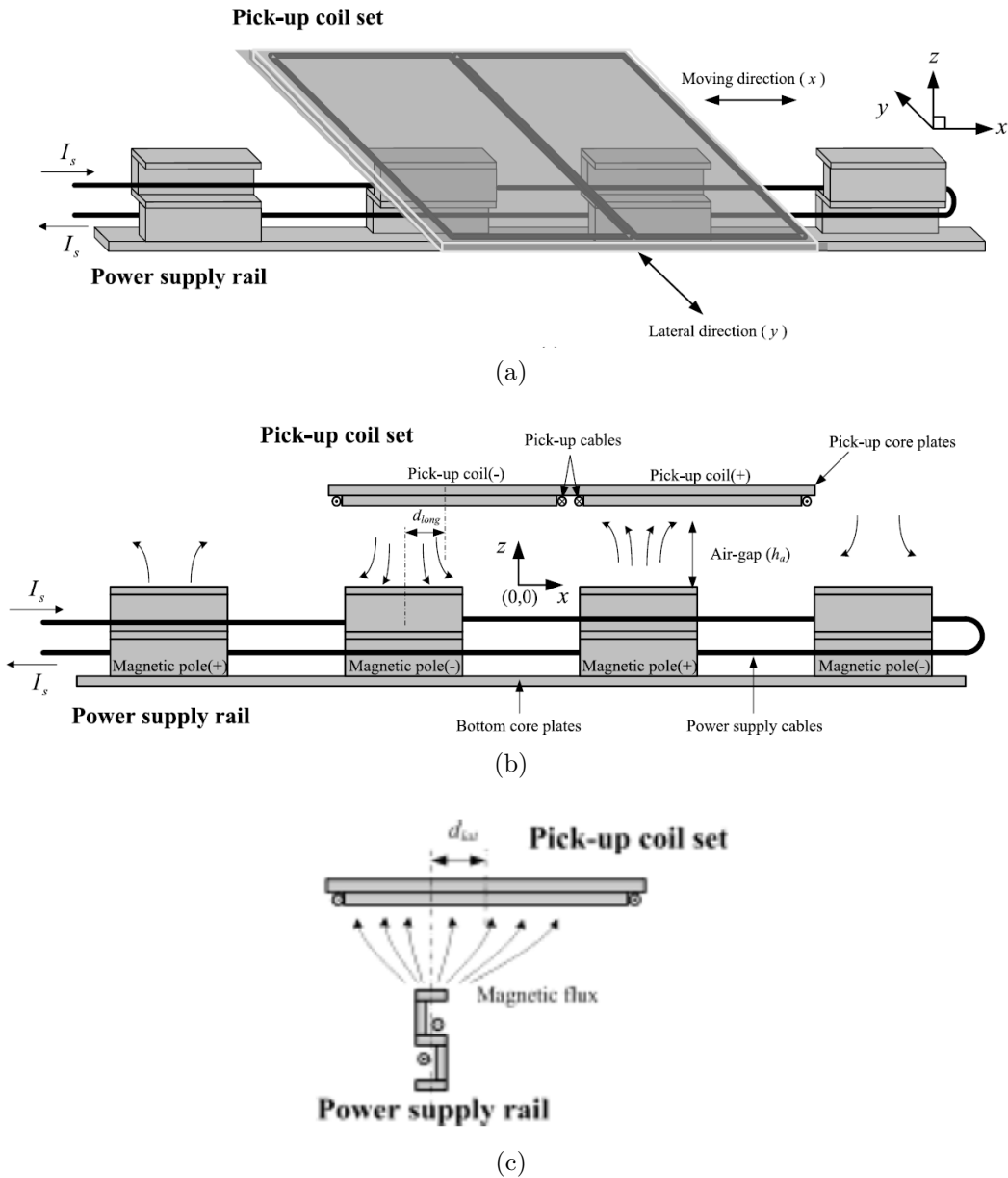
Figure 2.5: Overview of S-type power rail with receiver pad in: (a) 3D view, (b) side view and (c) front view [62].

and respective power pad [70,71]. This configuration is simple to implement but arises safety concerns as it uses high voltage and high power rating DC lines. The configuration from Figure 2.6 (b) overcomes the limitations of Figure 2.6(a) and the maintenance of the power converters, since they are all concentrated in the roadside cabinet [72]. Moreover, each converter can supply more than one transmitter pad simultaneously [73]. Unfortunately, the installation costs increase exponentially with the number of segmented power pads. In addition, the PFC module will vary in configuration, depending on the power levels of the overall system.

Figure 2.7 (a) depicts a segmented pad configuration that allows an independent operation of each segmented pad [74,75]. This feature is accomplished by using a magnetic coupler
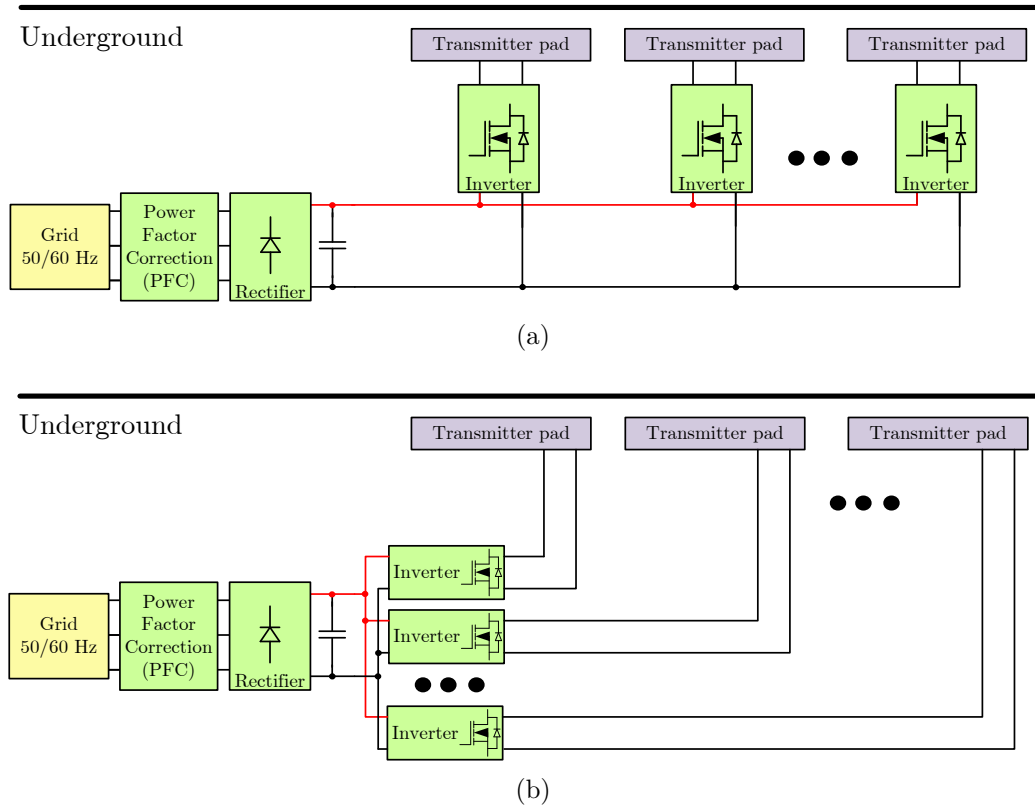
Figure 2.6: Overview of different segmented pad arrangements.

connected to a bidirectional AC switch to turn "on" or "off" the power pad. A benefit of such configuration is individual maintenance of each segmented pad without affecting the normal operation of the remaining system. The configuration illustrated in Figure 2.7 (b) uses two turns transmitter track configuration in which the current direction in one of the turns can be changed using the switch boxes to turn "on" or "off" the magnetic fields in a specific segmented pad. Since all switch boxes are connected in series, all components have to be rated for the nominal current of the transmitter pad.

Figure 2.8 illustrates a double coupling segmented pad system [76,77]. The system uses an additional intermediary coupler circuit (ICC) between the power track and the transmitter pad. The ICC is formed by the intermediary receiver coil with respective resonant tank, a semi-controlled full bridge rectifier with a large storage capacitor and a H-bridge inverter with respective resonant tank connected to the transmitter coil. The ICC has a strong coupling to the power track to cancel more self-inductance of the power track. In this way, the same voltage supply allows longer power tracks. The power is drawn from the power track to the ICC to charge the storage capacitor and then transferred to the vehicle using the H-bridge inverter at a higher operating frequency (85 kHz).

The configuration of Figure 2.8 has advantages towards the configurations illustrated in

(a)

(b)
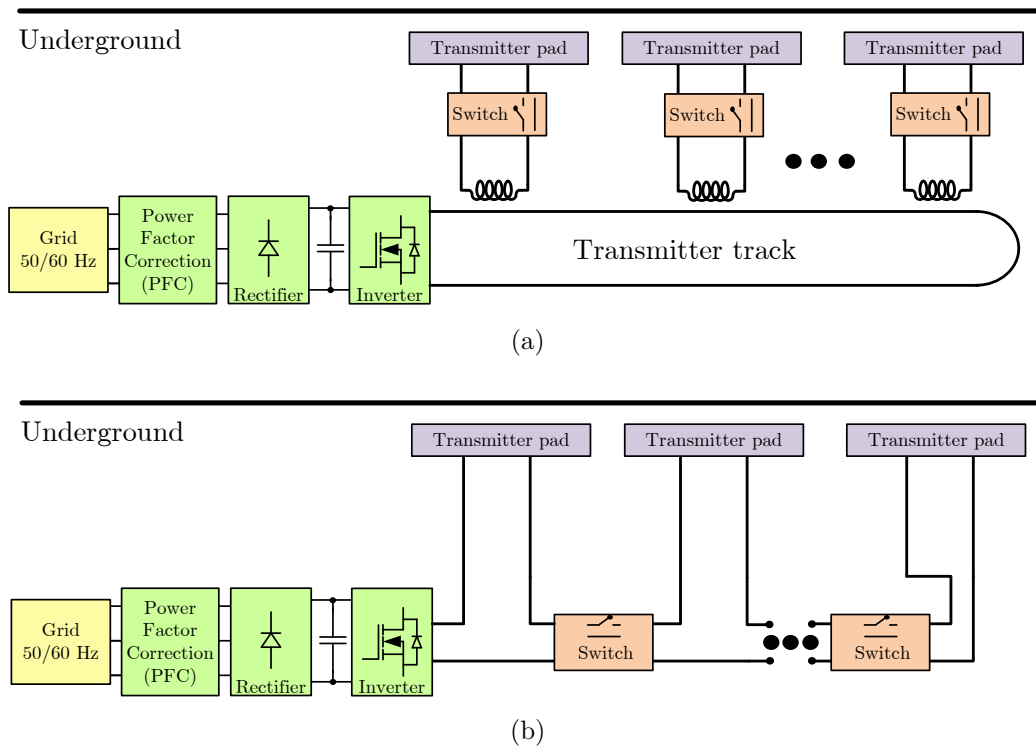
Figure 2.7: Overview of different segmented pad configurations with switch breaks.
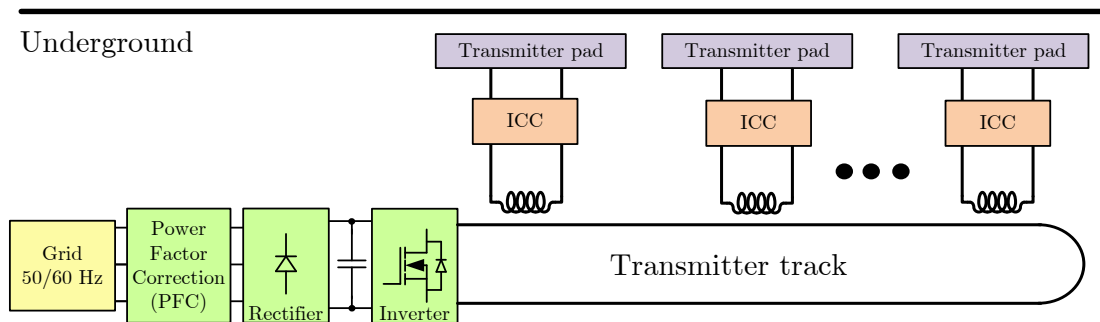
Figure 2.8: Overview of a double coupling segmented pad configuration.

Figure 2.6 and Figure 2.7. Firstly, the power track can run at a lower frequency (around 20 kHz) while the ICC runs at 85 kHz. Therefore, the safety concerns of installing DC lines are eliminated and the Joule losses in power tracks running at 85 kHz are also mitigated. Secondly, the storage capacitor reduces the power peaks drawn from the grid during rush hours since the storage capacitor can be discharged at a fast rate of 10-20 kW while the charging process occurs at a lower rate of 1-2 kW. Thirdly, each module can be controlled individually and maintenance can be performed in one segmented pad without interrupting the normal operation of the remainder. The downside of the proposed configuration is the larger number of components required and the lifespan and maintenance of the storage capacitors.

Other configurations have been presented in the literature that use additional MCs or
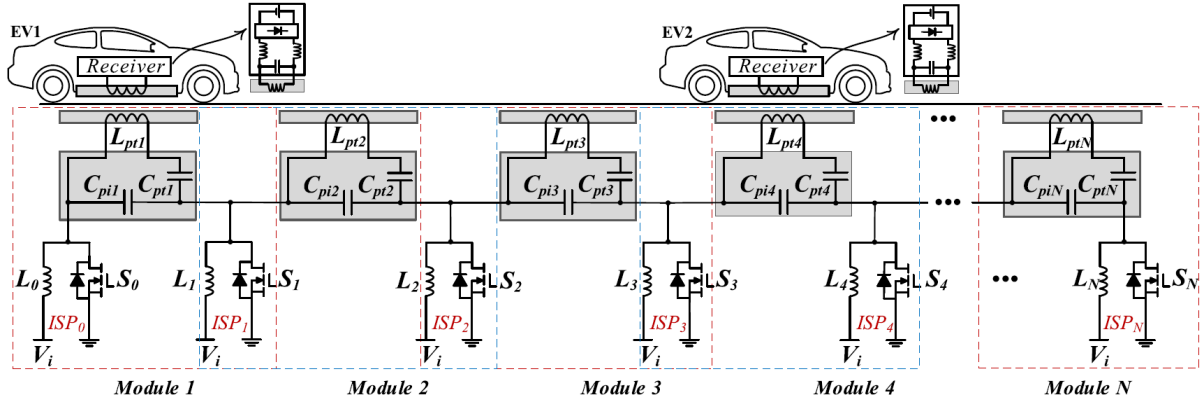
Figure 2.9: Overview of a push-pull driven coupler array [79].

that are modified arrangements of isolated DC-DC converts. The authors in [78] introduce a switchable inductively coupler that facilitates the system maintenance while ensuring, at the same time, a load-independent current in the main transmitter pad. On the other hand, [79] proposes a push-pull driven coupler array that minimizes the number of switches to N+1 required to drive N transmitter pads, as illustrated in Figure 2.9. Of all discussed topologies, the push-pull driven coupler array is the solution that requires less switches. Unfortunately, the current that flows through the transmitter pads can not be controlled electronically.

One advantage of segmented configurations over elongated tracks is the capability to turn-off the transmitter pad in the absence of a vehicle, in order to reduce losses and unwanted stray magnetic fields [80]. The ability to turn-on/off requires, however, a detection EV system. The authors in [81] propose a three-coil sensor system to detect the approach of vehicle. A similar approach is analyzed in [82] where several sensing coils are displaced before the transmitter pads to detect the vehicle passage. The authors in [83] propose instead, an orthogonal set of sensing coils placed in the transmitter pad. All the aforementioned techniques require a permanent energized circuit in the vehicle side. Therefore, this circuit is permanently consuming energy from the batteries. Alternatively, the authors in [84] propose a transmitter source coil formed by ferrite cores that have different magnetic flux shapes along the roadway. This solution though, increases the installation costs by using ferromagnetic cores.

One limitation of segmented pad configuration is the power fluctuation that occurs between two consecutive discrete pads and the amount of pads required to transfer a given quantity of energy [85]. One way to minimize the power fluctuation is two shorten the distance between two consecutive transmitter pads [67, 86]. This approach decreases the power fluctuation up to 80 % but has to take into account the coupling between the two discrete

transmitter pads during the design of the resonant compensation network. Alternatively, pads geometries with orthogonal flux patterns ensure a natural decoupling between two consecutive transmitter pads, thus avoiding the need for additional compensation capacitors [87]. A new resonant configuration with multiple coupling factors within the transmitter pad is proposed in [88]. The configuration enables a stable output power with a maximum fluctuation of 4%. The use of non-polarized geometries for the main coil will, however, limit the tolerance to lateral displacements.

Another difficulty associated with segmented pad configuration is the proper size selection of both transmitter and receiver pads together with the configuration of the power supply [89]. The authors in [90] explore different predefined Double-D pad (DDP) geometry configurations in both transmitter and receiver pads to assess the minimum admissible sizes compatible with both Sedan and SUV classes. An interoperability study of different transmitter pad designs with a DDP receiver pad geometry is carried in [91]. The authors show the benefits of using multi-segmented transmitter rectangular coils instead of a single wounded rectangular coil, especially under lateral displacement scenarios. In addition, durability tests showed a better temperature dissipation of segmented transmitter coils (temperature rising inferior to 4°C) when compared with traditional rectangular coils (temperature rising around 32°C). Other works focus on optimizing the energy transfer using generic coupling profiles rather than specific transmitter geometries [92, 93]. These design methodologies focus on the system constraints like admissible charging areas with minimum coupling values while both the power transfer and efficiency are maximized. The authors in [94] also propose a design methodology that maximizes power transfer for a series-series (SS) resonant configuration using non-polarized rectangular coils. Alternatively, [95] uses the length of a rectangular transmitter pad as a design parameter in the optimization that uses constraints like vehicle speed, system losses and minimum charging efficiency. The methodology consider transmitter and receiver air coils and their respective integral functions which in practical EV applications may not be feasible due to all magnetic materials like iron that form the vehicle.

The segmented pad configurations discussed above have benefits over track based configurations like higher efficiency values since only sections of the road are energized at a given time. Still, there is a long debate over the definitive solution for a global spread and both options have room for improvement in terms of costs, size and power transfer capabilities [96]. Table 2.1 summarizes the main advantages and limitations of both segmented and track based dynamic IPT systems.

Table 2.1: Comparison between elongated and segment dynamic configurations.

Type	Advantages	Limitations
Elongated pad	✓ Lower construction costs ✓ Easier to control ✓ Continuous power transfer ✓ Stable coupling factor	✗ Lower coupling factors ✗ High Joule and iron losses ✗ Unwanted exposure to stray fields ✗ High track self-inductance requires additional compensation
Segmented pad	✓ Easier maintenance and replacement ✓ High coupling profiles ✓ Better overall efficiency ✓ Capability to work as an elongated pad	✗ Requires EV detection systems ✗ Difficult to control ✗ Requires more components ✗ Optimization process complex

2.3 Resonant configurations

As discussed in Section 2.1, the power transfer capability of an IPT system is greatly affected by the reduced coupling between both sides of the MC. This limitation is mitigated with the use of resonant configurations that compensate the self-inductance of the MC. The simplest way to compensate an inductance is to place a capacitor in either series or parallel with the coil [51, 97, 98]. Over the years, several resonant configurations with multiple reactive components were proposed in the literature and they can be grouped according to the number of magnetic coupled coils and number of sides into: single coupling and multiple coupling resonant configurations. The first group comprises resonant configurations with two sides, the transmitter and receiver sides, and they are connected magnetically by a MC with one transmitter and one receiver pad. The second group includes configurations with multiple sides, i.e, one or more transmitters and/or receivers sides, multiple MC couplers connected in a cascaded way and configurations with intermediate couplers (IC).

The requirements and specifications of a given application dictate the most suitable resonant configuration. The basic requirements for resonant configurations are:

1. **Minimum VA rating:** The compensation of the transmitter leakage inductance increases the power factor closer to unity, while the receiver coil operates around the same resonant configuration.

2. **Maximum power transfer:** The system operates around the maximum value in the power function.

3. **CC or CV modes:** The operation in constant current (CC) or constant voltage (CV) modes depends on the application.

4. **High efficiency:** The system efficiency is closely related with quality factor of the coils, the coupling coefficient and soft switching of the inverter. The losses in the inverter depend on the resonant configuration.

5. **Displacement tolerance:** The system has to maintain the power transfer requirements in scenarios with lower coupling values. In such conditions, the VA rating of the power supply can be exceed or the inverter looses soft-switching operation due to bifurcation phenomenon. Bifurcation is the existence of multiple zero phase angle resonant frequencies in which the impedance seen at the inverter terminals may vary abruptly from capacitive to inductive, depending on the receiver quality factors. The input impedance depends on the resonant configuration.

2.3.1 Single coupling resonant configurations

Figure 2.10 illustrates the classification of resonant configurations in single coupling systems. The basic configurations place a single capacitor in series (S) or in parallel (P) with each coil into: series-series (SS), series-parallel (SP), parallel-series(PS) and parallel-parallel (PP). Hybrid configurations, on the other hand, use multiple reactive components to form high order resonant configurations like the LCL-LCL, LCL-S or CCL-S configurations. Figure 2.11 depicts the equivalent model of the basic and commonly used configurations.

2.3.1.1 Basic resonant configurations

Each resonant configuration offers different intrinsic characteristics and its selection depends on the application [51, 99]. A comprehensive analysis of the basic resonant configurations is made in [98, 100, 101]. A series compensation in the receiver side resembles a voltage source while the parallel compensation resembles a current source. In addition, the series compensation in the receiver side offers total independence from mutual coupling and load variation when the switching frequency of the power supply matches the natural resonance frequency of the receiver side. In other terms, the equivalent impedance from the receiver side seen by the transmitter resonant configuration is purely resistive. When coupled with a series configuration in the transmitter side to form SS configuration, the natural frequencies of both transmitter and receiver resonant circuits are unaffected by coupling variations that are caused by vertical and lateral displacements [102, 103]. One downside of the SS configuration is the high circulating currents in the transmitter side in the absence of the receiver
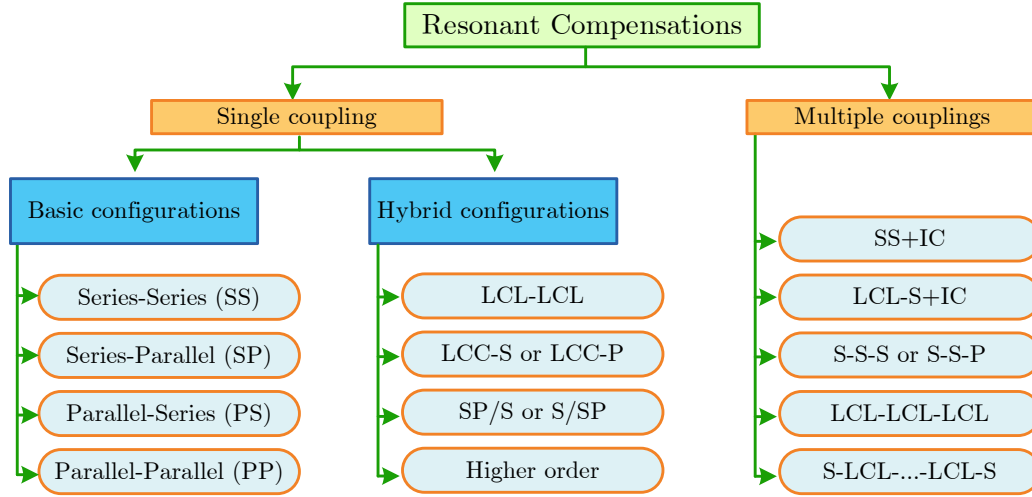
Figure 2.10: Classification of resonant configurations in IPT systems.

side (no vehicle). This characteristic limits the applicability of SS configuration to dynamic IPT systems without the use of fast EV detection systems and protection circuitry.

(a) series-series

(b) series-parallel

(c) parallel-series

(d) parallel-parallel
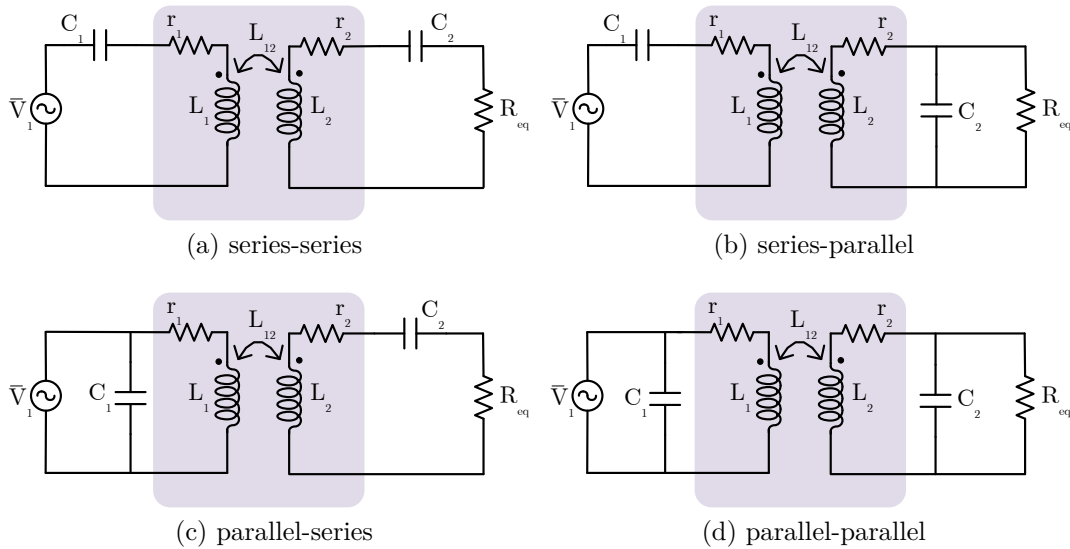
Figure 2.11: Equivalent circuits of the basic resonant configurations.

The parallel compensation in the receiver side originates a reflected reactance that depends on mutual inductance and switching frequency [98,104]. The tuning of the transmitter resonant circuit has to take into account this reflected reactance and the natural resonant frequency of transmitter network will only match the switching frequency of the power supply in one specific charging position. Therefore, the SP and PP configurations are highly sensitive to vertical and lateral displacements. Nevertheless, the current source characteristic of parallel compensation in the receiver side is suited for battery charging while parallel compensation in the transmitter side can generate a large transmitter current [51]. The
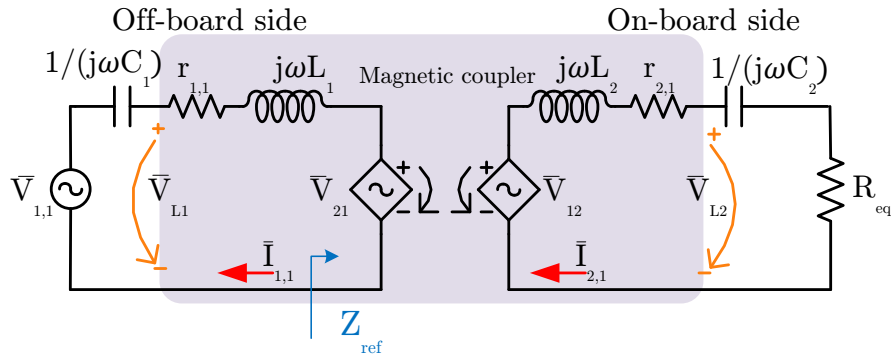
Figure 2.12: Equivalent circuit model of the SS configuration for the fundamental harmonic.

main advantages of PS and PP configurations include high efficiency and high power factor in low coupling charging scenarios and wide range of load and mutual inductance variation acceptance [65].

A comparison of the basic topologies in a 200 kW system was carried out in [9]. The authors shown that the SS requires less copper mass. The SP requires 4.6 % more, the PP 24 % and the PS 30 % more. Therefore, from a economical viewpoint, the SS and SP resonant compensation networks are more suitable for high power IPT systems. The PS and PP compensations are usually used for high power current source elongated cables [105]. The SP is also beneficial in bio-medical applications since is the resonant configuration with the lower self-inductance requirements in the receiver side [41].

2.3.1.2 Circuit analysis

This section derives the circuit analysis for the SS resonant configuration. The same principle analysis is then applied to the remaining basic resonant configurations to identify the generic reflect and input impedance functions. These functions are the result of the work conducted in this thesis to assess the impact of the components tolerance in the IPT system. Voltage and current transfer functions are derived as well for the basic resonant configurations.

The SS fundamental model, depicted in Figure 2.12, comprises the fundamental harmonic of the inverter's output voltage ($\overline{V}_{1,1}$) connected to the transmitter capacitor (C_1) in series with the self-inductance (L_1) of the transmitter coil. The receiver side comprises the self-inductance (L_2) of the receiver coil in series with the compensation capacitor (C_2). The parameter R_{eq} corresponds to the equivalent resistance of the batteries before a full diode rectifier with a filtering capacitor. The parameters $r_{1,1}$ and $r_{2,1}$ are the resistances from the transmitter and receiver coils, respectively. The first subscript number in the variables

indicate to which side the variable is related, where 1 and 2 stands for transmitter, and receiver sides, respectively. The second subscript number, separated by a comma from the first number, indicates the harmonic order of the corresponding variable. By applying Kirchhoff circuit laws to the circuit, the following equations are obtained

$$\overline{V}_{1,1} = r_{1,1}.\overline{I}_{1,1} + j.\omega((L_1 - 1/(\omega^2.C_1))\overline{I}_{1,1} - L_{12}.\overline{I}_{2,1}) \tag{2.1}$$

$$0 = (R_{eq} + r_{2,1})\overline{I}_{2,1} + j.\omega((L_2 - 1/(\omega^2.C_2))\overline{I}_{2,1} + L_{12}.\overline{I}_{1,1}), \tag{2.2}$$

where L_{12} is the mutual inductance between the transmitter and the receiver coils. The values of the capacitors are given by $C_1 = 1/(\omega_1^2.L_1)$ and $C_2 = 1/(\omega_2^2.L_2)$, where ω_1 and ω_2 are the angular resonant frequencies of its respective resonant tanks. The parameter R_{eq} is expressed as [106]

$$R_{eq} = \frac{8.V_{bat}}{\pi^2.I_{bat}}, \tag{2.3}$$

where V_{bat} and I_{bat} are the voltage and current values in the batteries, respectively. Solving (2.1) and (2.2) leads to equations (2.4)-(2.5) that accurately define the model shown in Figure 2.12 for the fundamental harmonic.

$$\overline{I}_{2,1} = \overline{I}_{1,1}.\frac{\omega^2.C_2.L_{12}}{\omega^2.L_2.C_2 - 1 - j.\omega.C_2.R_{eq}} \tag{2.4}$$

$$\overline{I}_{1,1} = \frac{\overline{V}_{1,1}}{Z_{1S,1} + Z_{rec,1}}. \tag{2.5}$$

The transmitter ($Z_{1S,1}$) and receiver ($Z_{2S,1}$) equivalent impedance equations, at the fundamental harmonic, are defined in (2.6) and (2.7), respectively. The parameter Z_{rec} is the impedance of the receiver side seen by the transmitter side and it is defined by (2.8) at the fundamental frequency.

$$Z_{1S,1} = r_{1,1} + j\left(\omega.L_1 - \frac{1}{\omega.C_1}\right) \tag{2.6}$$

$$Z_{2S,1} = r_{2,1} + j\left(\omega.L_2 - \frac{1}{\omega.C_2}\right) \tag{2.7}$$

$$Z_{rec,1} = \frac{\omega^2.L_{12}}{Z_{2X,1} + R_{eq}}. \tag{2.8}$$

The expression in (2.8) is independent of the resonant topology used in the transmitter side. The value of Z_{rec} increases at higher operating frequencies ($\uparrow \omega$) and/or with better coupling factors ($\uparrow Ł_{12}$), hence the use of high frequencies in IPT systems with optimized magnetic couplers. The equation of Z_{rec} for a series configuration in the receiver side can be found

Table 2.2: Reflected impedance for series and parallel configurations [107].

Top.	Series	Parallel
	Generic	
Real	$\dfrac{\omega^2.L^2.(R_{eq}+r_2)}{L_2^2.\omega^2.(1/b_2^2-1)^2+(R_{eq}+r_2)^2}$	$\dfrac{L_{12}^2.\omega^2.(R_{eq}+r_2)}{(R_{eq}+r_2)^2(1-1/b_2^2)^2+\omega^2.L_2^2}$
Im	$\dfrac{\omega^3.L_2.L_{12}^2.(1/b_2^2-1)}{L_2^2.\omega^2.(1/b_2^2-1)^2+(R_{eq}+r_2)^2}$	$\dfrac{L_{12}^2.\omega.b_2^2((R_{eq}+r_2)(1-1/b_2^2)-L_2^2.\omega_2^2)}{L_2((R_{eq}+r_2)^2(1-b_2^2)^2+\omega^2.L_2^2)}$
	Tuned	
Real	$\dfrac{\omega^2.M^2}{R}$	$\dfrac{M^2.R}{L_2^2}$
Im	0	$-\dfrac{\omega.M^2}{L_2}$

using (2.7) and replacing it into (2.8) to obtain

$$Z_{rec,1} = \frac{\omega^2.L_{12}^2.(R_{eq}+r_2)}{L_2^2.\omega^2(1/b_2^2-1)^2+(R_{eq}+r_2)^2} + j\frac{\omega^3.L_{12}^2.L_2(1/b_2^2-1)}{L_2^2.\omega^2(1/b_2^2-1)^2+(R_{eq}+r_2)^2}. \tag{2.9}$$

where b_1 and b_2 are relation factors between the resonant tanks frequencies (ω_1 and ω_2) with the switching angular frequency (ω) as

$$b_1 = \omega/\omega_1, \quad b_2 = \omega/\omega_2. \tag{2.10}$$

In a tuned system ($b_1 = b_2 = 1$), (2.9) is simplified into the equations shown in Table 2.2. As stated earlier, in tuned conditions the imaginary part of the reflected impedance is null and the real part depends on L_{12}, R_{eq} and ω. In light load conditions, $R_{eq} \to$ inf and $Re(Z_{rec}) \to 0$. Therefore, the SS configuration has larger transmitter currents under light load conditions to transfer the same amount of power when compared with the PS and PP configurations [104].

The reflected impedance for the parallel configuration is found by simply replacing the parallel receiver equivalent impedance, given in (2.11), into (2.8). Table 2.2 summarizes the reflected impedance equations for a series and parallel configuration in their tuned conditions and in their generic form. The tuned equations are already available in the literature whereas the generic equations are the result of this thesis work.

$$Z_{2P,1} = r_{2,1} + j\omega L_2 + \frac{R_{eq} - j\omega.R_{eq}.C_2}{1 + (\omega.R_{eq}.C_2)^2} \tag{2.11}$$
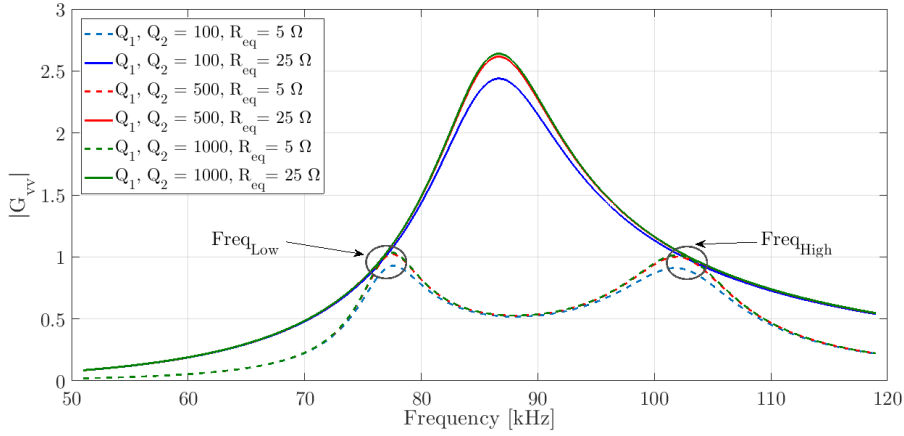
Figure 2.13: Voltage transfer function as a function of frequency for different load and coil's quality factors for the SS resonant configuration.

The load and coupling variations influence the equivalent impedance seen by the source (Z_{in}). In turn, it affects the inverter into operating in zero voltage switching (ZVS), zero current switching (ZCS) or zero-phase angle (ZPA). For instance, a decrease of L_{12} causes a decrease of Z_{in} for the SS and SP topologies. The opposite effect is identified for the PS and PP configurations, meaning that charging displacements provoke a drastic reduction in both supplied and absorbed currents.

At certain frequencies and compensation parameters, the resonant network configurations exhibit constant voltage (CV) and constant current (CC) modes. These modes guarantee an output voltage or current value independent of the load value and they are ideal for battery charging applications. For the SS resonant configuration, the output($\overline{V}_{Req}$) to input ($\overline{V}_{1,1}$) voltage transfer function can be determined by rearranging (2.1) and (2.2) into

$$G_{vv} = \frac{\overline{V}_{Req}}{\overline{V}_{1,1}} = \frac{j\omega.L_{12}.R_{eq}}{Z_{1S,1}.(Z_{2S,1} + R_{eq}) + \omega^2.L_{12}^2}. \tag{2.12}$$

Figure 2.13 shows the amplitude curves of (2.12) for two different load values using transmitter (Q_1) and receiver (Q_2) pads with different quality factors (only the resistance of the pads is changed). The plots show a load-independent voltage transfer function, marked with $Freq_{Low}$ and $Freq_{High}$, if the quality factors are high, i.e, r_1 and r_2 are neglected. A further manipulation of (2.12) results in

$$G_{vv} = \frac{1}{\frac{Z_{1S,1}}{j.\omega.L_{12.}} + \frac{Z_{1S,1}.Z_{2S,1}+\omega^2.L_{12^2}}{j.\omega.L_{12}.R_{eq}}}. \tag{2.13}$$

The voltage transfer function is independent of the load condition when $Z_{1S,1}.Z_{2S,1}+\omega^2.L_{12}^2 =$

Table 2.3: Load independent output conditions for the basic resonant configurations.

Condition	Transfer function
G_{ii} for SS	$\omega = \dfrac{1}{\sqrt{L_1.C_1}}$
G_{vv} for SS; G_{ii} for SP	$\omega_{Low} = \sqrt{\dfrac{\omega_1^2+\omega_2^2-\Delta}{2.(1-k_{12})^2}}$; $\omega_{High} = \sqrt{\dfrac{\omega_1^2+\omega_2^2+\Delta}{2.(1-k_{12})^2}}$
G_{vv} for SP	$\omega = \sqrt{\dfrac{1}{C_1.\left(L_1+\frac{L_{12}.L_2}{L_{12}+L_2}\right)}}$
G_{vv} for PS; G_{ii} for PP	$\omega = \dfrac{1}{\sqrt{L_2.C_2.(1-k_{12}^2)}}$

0. This expression can be further manipulated into

$$\omega^4(L_{12}^2 - L_1.L_2) + \omega^2(L_1.L_2(\omega_1^2+\omega_2^2)) - L_1.L_2.\omega_1^2.\omega_2^2 = 0, \tag{2.14}$$

The roots of (2.14) correspond to ω_{Low} and ω_{High} and they are identified in Table 2.3 [108]. A similar analysis can be conducted for the current transfer function. Table 2.3 identifies the frequency points that have load-independent voltage and/or current transfer functions for the basic resonant configurations. The SS has CC mode when the switching frequency equals the natural resonance of the transmitter network. The PS has CV mode in the same frequency as PP exhibits CC mode. This frequency, however, depends on the coupling factor and a variable frequency control is required to maintain these modes. Moreover, there are no frequencies for operating PS in CC mode and PP in CV mode [109, 110].

Table 2.4 summarizes the main characteristics of the four basic resonant configurations, their advantages and limitations. A petal diagram, illustrated in Figure 2.14, summarizes visually the findings from Table 2.4 [98]. The larger number in the diagram (further from the center) and the wider area in the figure, the better will be the resonant configuration in comparison with the others.

2.3.1.3   Hybrid resonant configurations

Hybrid resonant configurations insert several reactive components in series/parallel to form higher order resonant configurations [108, 111–115]. These new compensation networks

Table 2.4: Comparison of the four basic resonant configurations [98].

Parameter / Topology		SS	SP	PS	PP
Independence on L_{12} and R_{eq}	Transmitter	Yes	Yes	No	No
	Receiver	Yes	No	Yes	No
Zero coupling allowance		Not allowed	Allowed	Allowed	Allowed
Total impedance		Decreases with displacement	Decreases with displacement	Increases with displacement	Increases with displacement
Sensitivity to coil displacement		Low	Slightly larger than SS	High	High
Inverter voltage rating		Lower DC bus but higher than SP	Lower DC bus	Higher voltage is needed as compared to SS and SP	Higher voltage is needed as compared to SS and SP
Performance for low-power applications		Worse than parallel	Better than series	Worse than parallel	Better than series
Power transfer and efficiency with large air gaps		Relatively low	Relatively low	Relatively high	Relatively high
Load independent output		Voltage and current	Voltage and current	Only voltage	Only current
Other advantages		1) The output current does not depend on the load and resonance frequency. 2)Better efficiency and greater transmitted power at frequencies > 1MHz than in SP	1) Requires a smaller receiver coil self-inductance than SS. 2) The parallel resonant circuit supplies the stable current.	Not detected	Not detected
Other drawbacks		1) Load dependency of the voltage transfer ratio at partial-load condition. 2) Requires a larger receiver coil self-inductance than the SP. 3) High-frequency current through series capacitor results in high capacitor voltage	Lacking of DC component blocking	1)Requires a current source input to avoid instantaneous change in voltage. 2) Large input resistance requires a high driving voltage to transfer sufficient amount of power.	1) Low power factor. 2) A high load voltage of the parallel receiver. 3) Large current source requirements of the transmitter parallel. 4) Large input resistance requires a high driving voltage to transfer a sufficient amount of power
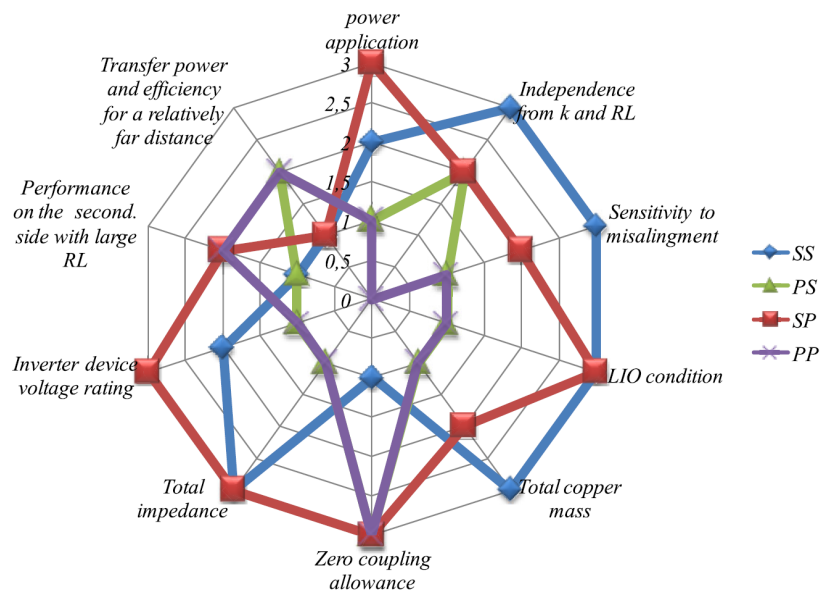
Figure 2.14: Petal diagram comparing the basic resonant configurations [98].

offer power transfer capabilities over wider coupling range, ZVS and ZPA operation and voltage/current source characteristics. Figure 2.15 illustrates some of the most common hybrid configurations. One of the first hybrid configurations used in IPT systems was the LCL configuration [116–118]. When applied in the transmitter side, the LCL configuration offers load-independent current source characteristics in the second L, if both values of L are the same [116, 119, 120]. Therefore, this configuration is often used in dynamic applications since the vehicle's absence does not compromise the integrity of the power supply [73, 121]. The LCL configuration is also employed in the receiver side to provide a smooth power transition between fully on and fully off [122] or to keep an unitary power factor in the transmitter side [123]. The authors in [124] use a LCL-S in a cascaded configuration to supply multiple receivers with different voltage requirements. This configuration uses only one control loop to control all receivers. Furthermore, this configuration is less sensitive to parameter variations and the system efficiency is steadier.

The use of the LCC configuration on both sides offers constant output RMS current once the input voltage is fixed [125–128]. A proper tuning of LCC can achieve ZVS mode [129]. Moreover, it exhibits load and mutual independence [130]. The authors in [131] propose a design methodology of an LCC-LCC configuration that achieves CC and CV modes with minimum frequency variation. A similar approach is carried out in [132, 133]. The works [134, 135] embody the inductor from the transmitter and resonant LCC resonant networks into the geometry of the magnetic coupler to minimize the impacts of displacements. The authors report power boosts under lateral displacements of 40 %. The transmitter LCC

(a) LCL-LCL   (b) LCL-P

(c) LCC-LCC   (d) SP-S

(e) S-SP   (f) S-CLC
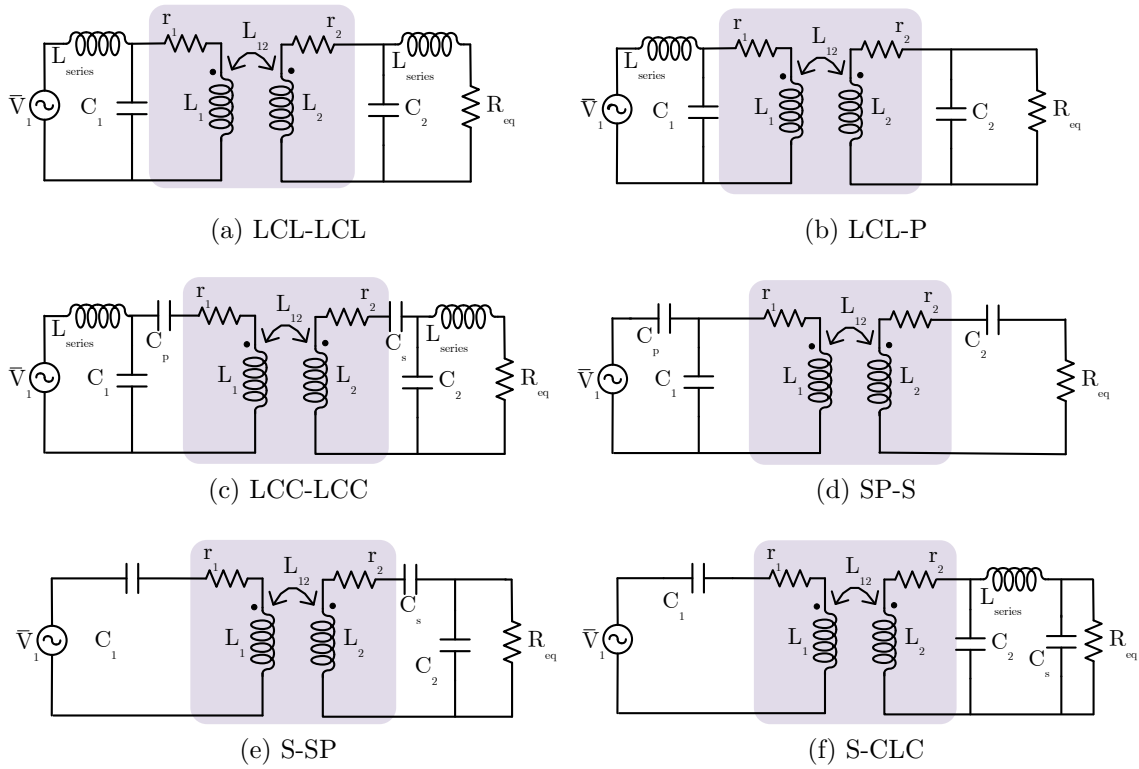
Figure 2.15: Equivalent circuits of hybrid resonant configurations.

can also be coupled with basic resonant configurations in the receiver side, either series or parallel. The parallel compensation confers robustness to load variations [130]. The series compensation requires a large bridge rectifier capacitor to ensure a continuous conduction and the pick-up voltage increases to a high value at larger power applications [136, 137]. A comparative study between the SS and double-side LCC is carried out in [138]. The LCC is less sensitive to variations of the self-inductance values caused by displacements between the transmitter and receiver pads. Furthermore, the voltage and current stresses on the series capacitors and main coils of the LCC configuration are smaller than those of the SS. A dual CLCL hybrid configuration with a dual-frequency is presented in [139]. This new resonant configuration extends the power transfer capabilities of 2.75 times in comparison with basic resonant networks.

The authors in [140] propose a S/SP hybrid configuration. This configuration has mutual coupling and load independent voltage gain. Additionally, it can realize good output voltage stability and low circulating losses under the condition of wide parameters variations [141]. The SP-S configuration was proposed in [101]. This configuration combines the characteristics of SS and PS configurations and allows higher displacement tolerances. The studies [108, 142, 143] evaluate high order configurations with different L and C arrangements in terms of soft-switching, system efficiency and zero-phase angle. The S-CLC compensation
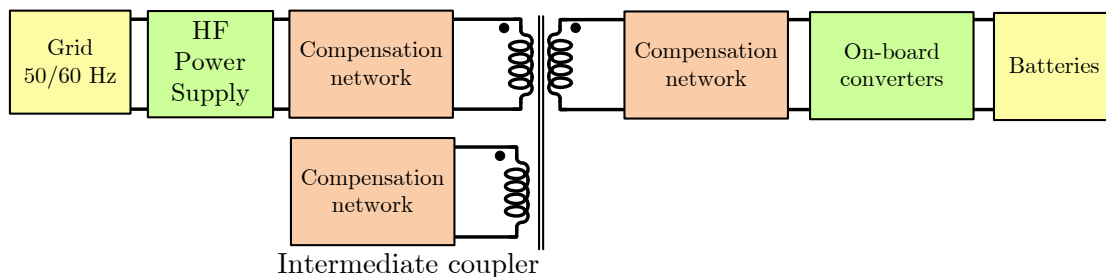
Figure 2.16: Equivalent diagram of an IPT system with an intermediate coupler.

network was proposed in [144]. The proposed configuration offers easier achievement of ZPA and ZVS [145]. In addition, it offers CC and CV modes and simplifies the control circuit design.

2.3.2 Multiple coupling resonant configurations

The efficiency of IPT systems is closely related with the coupling between the transmitter and receiver sides. This constraint is especially important in IPT systems with larger vertical and lateral displacements. The use of multi-coil resonators, also referred in the literature as intermediate couplers (IC), boost the magnetic link between the transmitter and receiver sides [146–152]. Figure 2.16 shows the equivalent circuit of an IPT system with intermediate couplers. A simplified comparison for a SS compensation between two and three coil systems is made in [153]. The authors verified that leakage field emissions for a three-coil system is met at smaller distances. The authors in [149] shown that a SS-IC configuration improves the efficiency of a SS since it reduces the source losses. On the contrary, the PP configuration does not benefit with the inclusion of the intermediate coupler. The SS-IC exhibits load-independent CV mode with almost ZPA operation mode [148]. The same configuration can operate in CC mode with ZPA when the intermediate coupler is tuned at a higher frequency than the switching frequency [154]. A S-LCC-IC configuration is proposed in [155] and realizes CC and CV modes with ZPA in both cases.

The use of multiple ICs is also verified in [156, 157]. The SS-IC-IC configuration shows load-independent CC and CV modes with ZPA mode. Since the proposed system operates at almost frequency in each CC and CV mode, the circulating currents are minimized. Experimental results show efficiencies between 95 and 97 % with transferred power in the range of 1-7 kW. However, the switching frequencies for CV and CC modes can be apart several kHz which will exceed the SAE J2954 frequency range.

The use of multiple couplers connected with one another is also investigated for delivering power to multiple loads or for dynamic applications. Figure 2.17 exemplifies a multi-coupler
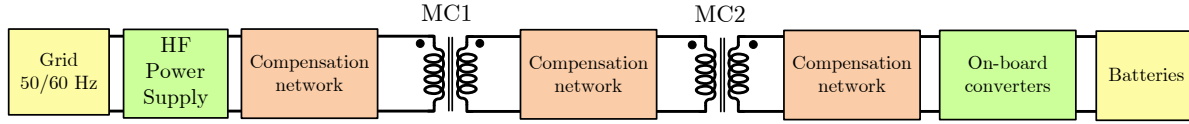
Figure 2.17: Equivalent diagram of a double coupling system.

configuration. The authors in [158] use a LCL-LCL-LCL configuration as a contactless interface for multiple transmitter and receiver sides. The use of a parallel compensation in the intermediate circuit minimizes the VAr requirements. A n-coupler S-LCL-...-LCL-S configuration is investigated in [159] to power multiple loads. This configuration ensures constant load current values regardless of load variations. The double coupling S-S-P and S-S-S configurations are analyzed in [160]. The S-S-S exhibits load independent CV mode if all natural resonant frequencies match the switching frequency. On the other hand, CC mode is achieved in the same conditions for the S-S-P configuration. In addition, both configurations exhibit ZPA during CC or CV modes. Moreover, S-S-X double coupling systems limit the transmitter current in the absence of the receiver, making them ideal for dynamic IPT applications.

2.4 Magnetic coupler

The magnetic coupling structure, also known in the literature as Magnetic Coupler (MC), is responsible for the energy transfer without physical contacts through a variable magnetic field. The MC resembles a conventional 50 Hz power transformer with a transmitter and receiver pads. Each pad comprises a coil (or set of coils), a ferromagnetic core and shield, as illustrated in Figure 2.18. In EV IPT applications, the transmitter pad, or pads, are placed in the ground or along the roadway while the receiver pad is placed under the vehicle.

A clear characteristic of IPT systems is the spatial freedom of the receiver pad towards the transmitter pad due the vehicle's movement. The relative positioning of the power pads will have a direct impact on the coupling factor and, subsequently, on the system power transfer capabilities [161–163]. Therefore, the degrees of freedom of the receiver pad can be classified as:

- **Vertical displacement:** Also referred in this work as air gap, it corresponds to the vertical distance between the transmitter and receiver pads;

- **Lateral displacement:** Corresponds to the lateral distance between the transmitter and receiver pads center point;

- **Rotation:** Corresponds to the rotational angle between the transmitter and receiver
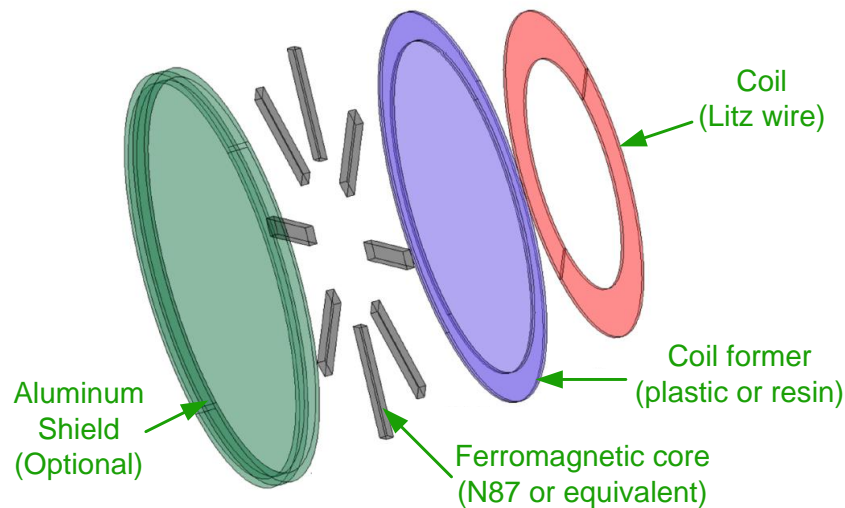
Figure 2.18: Typical components of a magnetic coupler pad.

pads along the horizontal plane (only applicable for rotary MC designs);

- **Tilt:** Corresponds to the inclination angle of the receiver pad.

Figure 2.19 illustrates the different degrees of freedom a 3D perspective.

The vertical displacement and tilt degrees of freedom depend on the vehicle's type (Sedan, SUV, etc) and, in normal operation, these values remain approximately constant. The lateral displacement and rotational degrees of freedom, on the other hand, depend on the driver ability to park the vehicle or driving it in a straight line. The guideline SAE J2954 suggests that a minimum lateral tolerance of ± 150 mm is sufficient for an average driver to drive/park the vehicle correctly.

Extreme charging positions with large vertical and lateral displacements reduce the coupling factor. Over the years, many researchers have address these issues by proposing new coil and core arrangements with better materials and shield techniques. These studies focused in one or more design principles like:

1. Maximize the coupling factor between the transmitter and receiver pads;

2. Minimize the leakage magnetic flux in the adjacent environment;

3. Maximize the vertical and lateral tolerances;

4. Enable the interoperability with different geometries.

2.4.1 Geometry

A magnetic pad, in its basic form, is formed by a single-coil. The physical placement of a coil within the pad determines the orientation of the generated flux. Figure 2.20 illustrates two distinctive flux patterns using different coil placements. The first scenario creates a
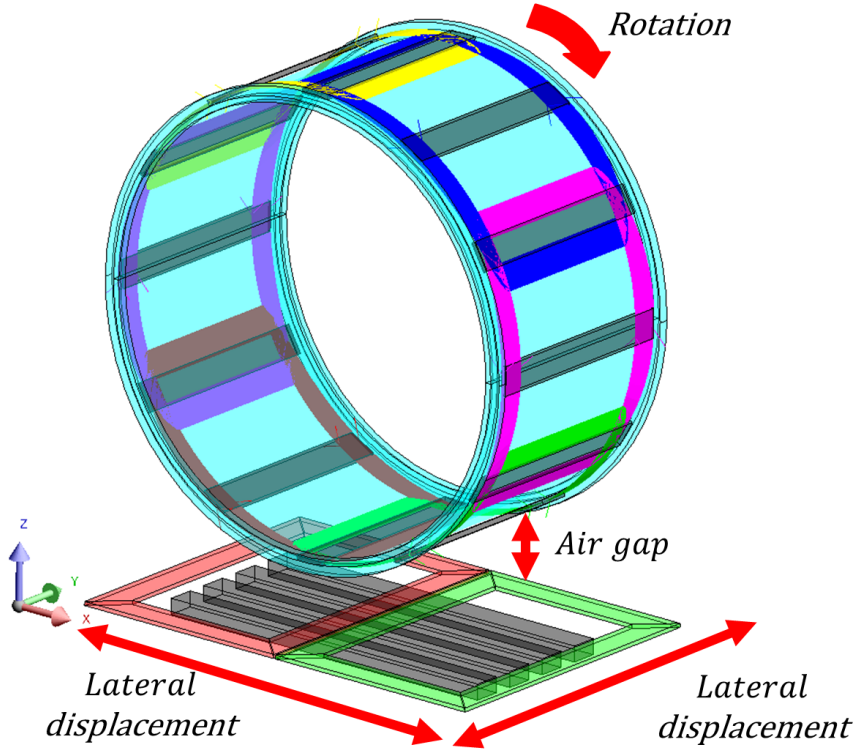
Figure 2.19: Degrees of freedom of a typical MC.

flux component perpendicular to the pad surface whereas the second scenario creates a flux component parallel to the pad surface. Additionally, the coil can be wounded in the top or around the ferromagnetic core, as illustrated in Figure 2.21(a) and (b), respectively. The first coil arrangement is also referred in the literature as single-sided geometries, whereas the second coil arrangement is known as double-sided geometries. Therefore, discrete MC geometries can classified in three major groups: non-polarized, polarized and omni-directional pads. The non-polarized groups includes the MC geometries that generate and couple either perpendicular or parallel flux component. Polarized pads, on the other hand, generate and couple both perpendicular and parallel flux components. Omni-directional pads generate and couples a flux pattern in every direction, thus ensuring a coupling profile in every position inside a volume [164–166]. The non-polarized and polarized groups are further divided into single-sided and double-sided groups, as illustrated in Figure 2.22.

2.4.1.1 Non-polarized pads

Non-polarized geometries are usually formed by a single coil. The most common geometries include the circular (CP) [167–169] and rectangular (RP) pads [42, 170]. These geometries produce high leakage magnetic fields, since one magnetic pole lies in the center
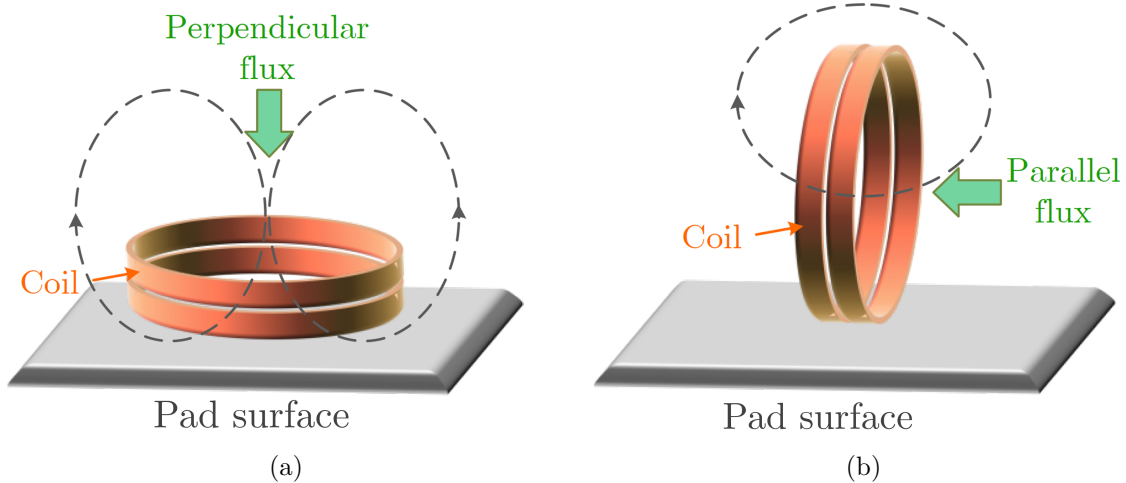
Figure 2.20: Flux pattern of a single-coil with different physical placement: (a) perpendicular and (b) parallel flux coupling.
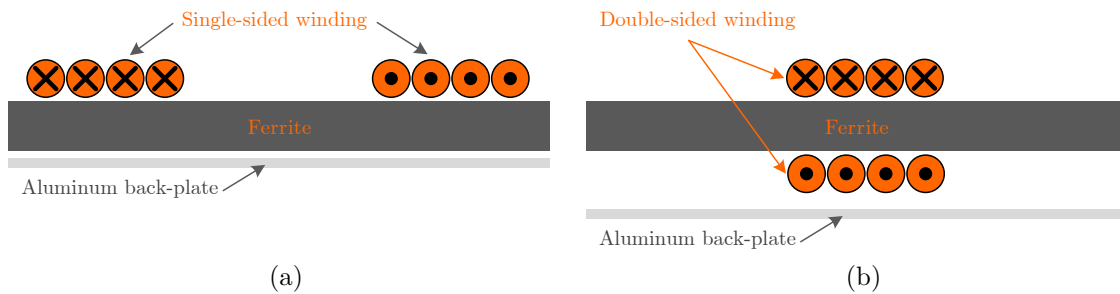
Figure 2.21: Wound coil configurations: (a) on top and (b) around the ferromagnetic core.

of the coil and the other in outside the coil limits. As a result, the fundamental flux path height is proportional to one quarter of the pad size thus, pads with larger sizes are required for applications with high air gap values. The coupling factor is increased by placing a ferromagnetic core in the back side of the coils. Optimization works show that a segmented core offers better ferromagnetic material usage than a full back plate core [171, 172]. Additionally, the leakage magnetic flux lines are reduced with longer ferromagnetic strips. CP provides a better magnetic coupling than square and rectangular pads with similar area [41].

The effect of lateral displacements in the coupling profile differs slightly for different geometries. The circular geometry can be displaced in any direction and only the magnitude of the displacement affects the coupling value [173, 174]. The rectangular geometry, on the other hand, has slightly different patterns according with the direction of displacement [175,176]. Pentagon and hexagon coils have similar displacement shapes as the CP [177,178]. The no-coupling scenario corresponds to a charging position where no flux lines generated by the transmitter coil are closed by receiver coil. For circular pads, this occurs for displacements equivalent to 40 % of the pad size and a similar result is found for rectangular pads [174].
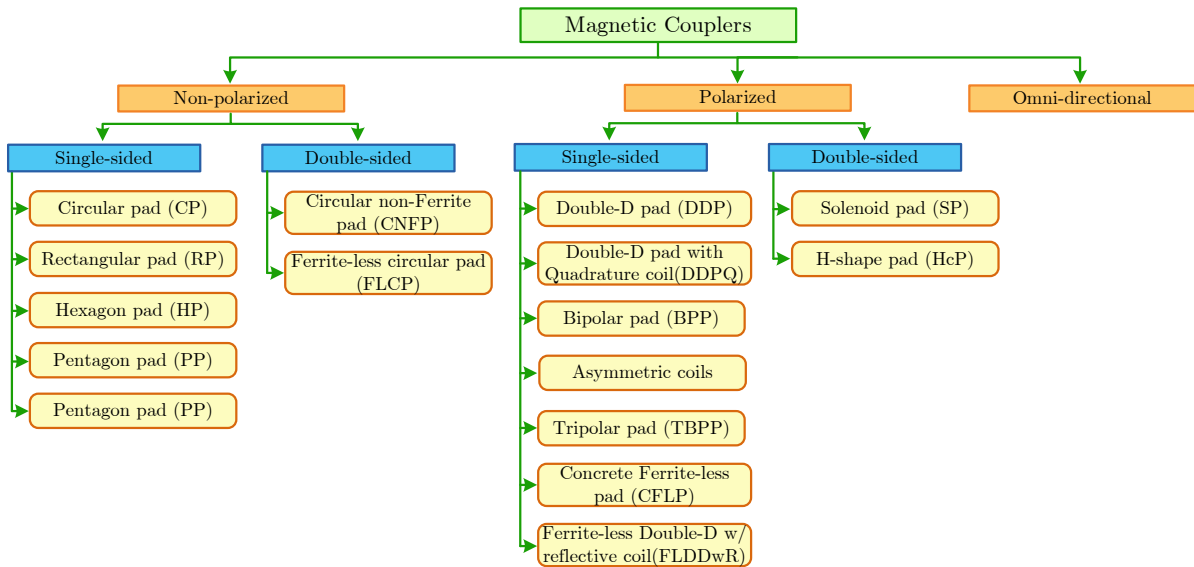
Figure 2.22: Classification of discrete magnetic couplers.
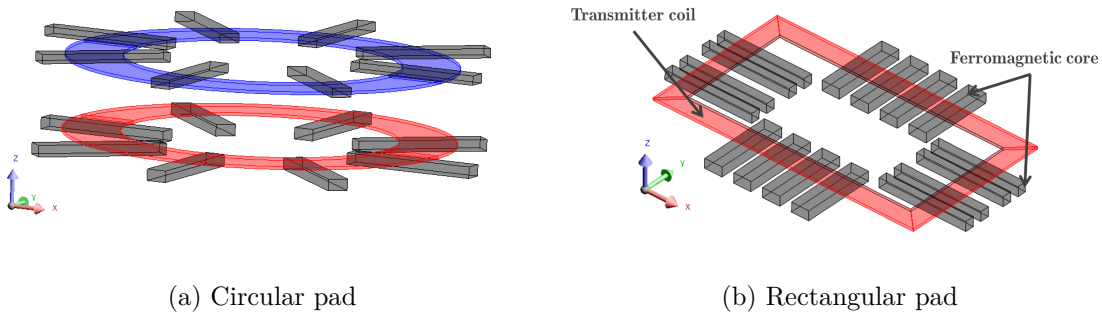
(a) Circular pad

(b) Rectangular pad

Figure 2.23: Illustration of non-polarized geometries.

This means that, from this charging position on, no power can be transfer between the transmitter and receiver sides. Figure 2.23 illustrates the CP and RP geometries.

2.4.1.2 Polarized pads

Polarized pads are composed by two or more coils with different electrical connection possibilities to produce/capture both perpendicular and parallel flux patterns. The solenoid pad (SPP) is one of the first polarized geometries proposed to EV IPT applications [179,180]. As the name suggests, the SPP resembles a solenoid with two coils wounded around a ferromagnetic core, as depicted in Figure 2.24(a). The SPP offers better coupling values for charging positions with higher air gaps and larger lateral displacements [181]. The authors in [182] study the interoperabilitiy between the SPP and the CP geometries. By connecting the two coils of a SPP either in series or in parallel produces a parallel or perpendicular flux pattern, respectively. However, the SPP generates a double-sided flux pattern and, as a

(a) Solenoid pad

(b) Double-D pad

(c) Double-D pad with quadrature coil

(d) Bipolar pad

(e) Tripolar pad [31]

(f) Concrete ferrite-less pad
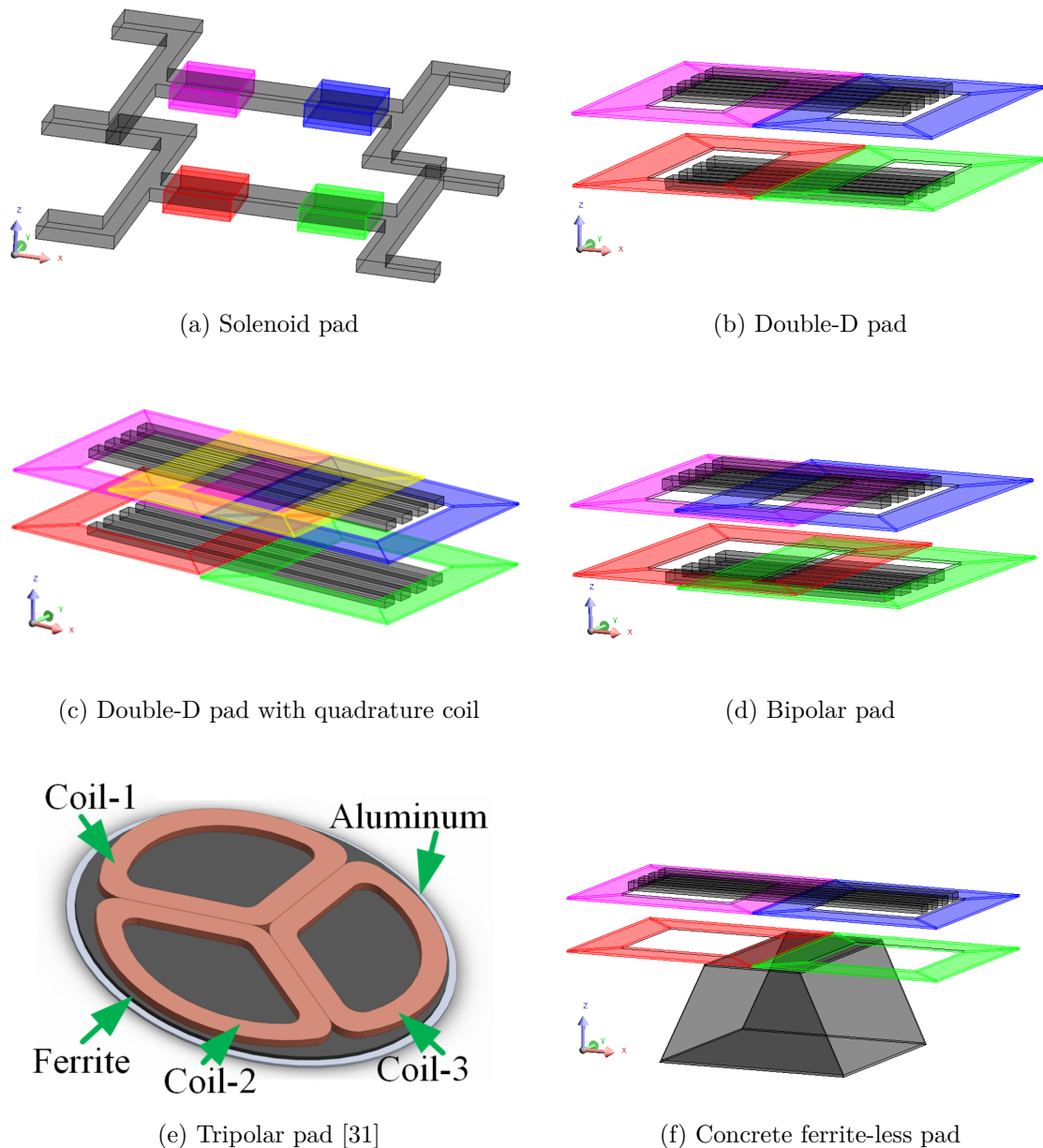
Figure 2.24: Illustration of polarized geometries.

result, the power pad has a lower quality factor and the use of a shield is essential to ensure the compliance with ICNIRP guidelines.

The Double-D pad (DDP) appeared as a substitute to the SPP geometry [183–185]. The DDP combines the advantages of both CP and SPP in a single-sided flux path geometry. The DDP geometry uses two planar coils, placed side-by-side over a set of ferromagnetic strips, as illustrated in Figure 2.24(b). The two coils are connected magnetically in series (flux from one coil passes through the other) and electrically in parallel, in order to lower the inductance seen by the power supply. The ferromagnetic core reduces the leakage flux in the backside of the geometry and the losses in the shield, created by Eddy currents,

are low [186]. The charging area of DDP is five times higher when compared to a square pad with similar size and cost [183]. The compliance with ICNIRP guidelines can be met for shorter distances to the center of DDP pad by extending the ferromagnetic core on both sides to capture additional leakage flux [186]. The authors in [187] replaced the ferromagnetic strips with a modified E-type ferromagnetic core and created a depressed transmitter coil to improve tolerance to lateral displacements and reduce leakage field in the surroundings of the geometry.

The DDP has two different coupling patterns for lateral displacements along the x and y axes. The DDP-DDP coupling along the x axis has a null coupling that occurs when the lateral displacement is approximately 34% of the pad length. At this charging position, the flux enters and exists the same coil, resulting in no induced voltage [183]. To overcome this limitation, a quadrature coil (Q) is placed over the two existing coils, as illustrated in Figure 2.24(c). The quadrature coil is magnetically decoupled from the DDP and independently tuned to couple the flux in the x axis direction. The use of a circular geometry over a rectangular geometry in the Q coil guarantees a constant coupling over a larger charging area [188].

The quadrature coil has an independent tuned circuit connected either to an inverter (if placed on the transmitter pad) or a rectifier (if placed on the receiver pad). Therefore, the Q and DD coils can be driven separately to produced a non-polarized perpendicular flux pattern or polarized parallel flux pattern depending on the geometry of the receiver pad, thus achieving interoperability with both polarized and non-polarized geometries [188]. A moving magnetic field is achieved by driving the Q coil with 90° out of phase compared to DD coils [173].

The Q coil is often used as the receiver pad with the DDP as the transmitter pad. This pad arrangement ensures a charging area 3 times larger than the DDP-DDP arrangement and 5 times larger than the CP-CP [173]. Furthermore, the DDQP is fully interoperable with a transmitter CP due to the Q coil and has a charging area 3 times larger than a CP-CP [173].

The Bipolar Pad (BPP) was initially proposed in [189] as a receiver pad for an under-floor IPT system. The BPP geometry comprises two mutually decoupled D coils that are partially overlapped, as illustrated in Figure 2.24(d). The overlap value is adjusted accordingly to ensure an almost null linkage value between the two coils [190]. Moreover, the optimal overlap value depends on the geometry of other pad (i.e BPP-CP, BPP-BPP, BPP-DDP, etc), as the ferromagnetic core and coils arrangements of the other pad influence the coupling of the coils

that form the BPP [190]. The BPP has equivalent output levels to DDQP while using 40 % less copper [191]. In addition, it is able to interact with both perpendicular and parallel flux patterns. Since the two coils are mutually decoupled, the BPP can be energized with different magnitudes and phases using two synchronized inverters, one in each coil. Different inverter operation modes produce different flux patterns. A non-polarized flux pattern is generated if the coils are driven in phase (mode 1) while a parallel field polarized along the length of the coil is produced if driven out of phase 180° (mode 2) [173]. A moving magnetic field is generated if driven out of phase 90° (mode 3). A fourth mode (mode 4) corresponds to an independent operation of each coil to produce a field neither perpendicular nor parallel. The BPP is also sensitive to tilt variations like the DDP or DDQP pads. The coupling factor drops by 13 % with a tilt of 30° [170]. The authors in [192] adapted a BPP transmitter pad to charge two receivers simultaneously. The design ensures a total decoupling between the two receiver pads.

Other designs have been presented in the literature for EV IPT applications. The tripolar pad (TPP), illustrated in Figure 2.24(e), is formed by three decoupled coils in a circular design and is intended for three-phase IPT systems [193]. The authors in [194] propose an asymmetric coil design formed by an U-shaped ferromagnetic core. The design offers large tolerance to vertical and horizontal displacements at the expense of large transmitter pads.

One major concern in dynamic IPT systems is the costs of manufacturing the transmitter pads. The ferromagnetic core weights more than 50 % in the total construction costs of the aforementioned geometries. The Auckland research group proposed in 2015 a Concrete Ferrite-less Pad (CFLP) geometry that uses a "pipe" coil instead of a ferromagnetic core to channel the flux in the backside of double-D coils, as illustrated in Figure 2.24(e) [195]. The design offers reasonable coupling profiles and lateral displacement tolerances with air gap variations between 150 and 200 mm. Moreover, high currents can be tolerated in ferrite-less geometries, since there is no ferromagnetic material that can be saturated. In [196], the authors used an additional coil, referred as reflection coil, below the double-D coils to help contain and shape the field. This geometry, designated as Ferrite-less Double-D pad with reflective coil (FLDDwR), differs from the CFLP geometry as the reflective coil is planar unlike the "pipe" coil of the CFLP. The size of the reflective coil influences the leakage control of the geometry. If the size of the reflective coil is the same as the DD coils, the geometry has similar or lower leakage flux per 1kVA in comparison with a DDP. A lower magnetic leakage is achievable when the reflection coil is placed with a depth of 80 mm, with a ratio of 6:1 (DD coils to reflection coil) turns and has approximately two times the area of
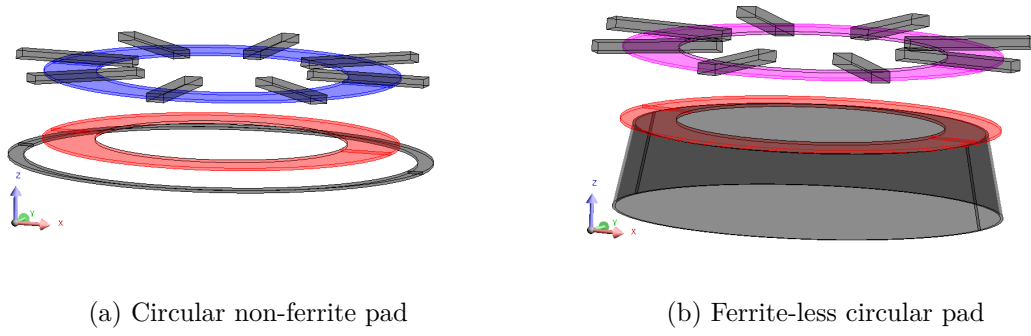
(a) Circular non-ferrite pad   (b) Ferrite-less circular pad

Figure 2.25: Illustration of ferrite-less non-polarized geometries in the transmitter side.
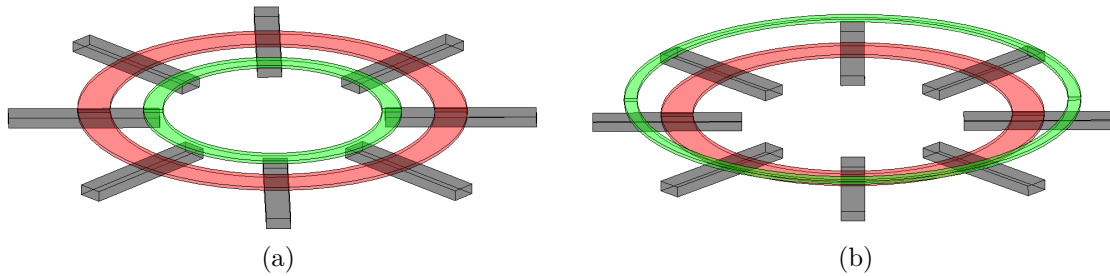
(a)   (b)

Figure 2.26: Illustration of different coplanar intermediate coil (depicted in green) arrangements with the transmitter coil (depicted in red) using the circular geometry.

the DD coils.

A similar approach for the FLDDwR was carried out in [197] for circular geometries, referred as Circular non-ferrite pad (CNFP). The authors placed a cancellation coil below the main circular coil, as illustrated in Figure 2.25(a), to reduce leakage flux around the geometry. The coils are wounded with one single wire in a series-opposing configuration that generates opposing magnetic fields. The turns ratio and height between the main and cancellation coils dictates effectiveness of the canceling field at a given lateral displacement. The coupling factors are lower than a CP but with reasonable values for dynamic operation. Another ferrite-less variant of circular geometries was proposed in [198], referred as Ferrite-less Circular Pad (FLCP). The authors placed a cone-shaped coil under the main circular coil to conduct the flux in the back of main coil, as illustrated in Figure 2.25(b). A slightly lower diameter in the base of the cone in comparison with the top cone offers the best coupling value with a CP geometry in the receiver pad. In addition, the coupling profiles under different vertical and lateral displacements are equivalent to the CP. The downside of the FLCP is the height of the cone-shaped coil, that varies between 80 and 140 mm [198].

2.4.1.3   Intermediate couplers

The power transfer capabilities of the aforementioned geometries are limited by the vertical displacement between the transmitter and receiver pads. The use of intermediate couplers, also known as multi-coil resonators relay coil IPT systems or multi-coil systems, enhance the magnetic link between the transmitter and receiver pads. Initial designs placed a solenoid coil between the transmitter and receiver pads [146, 147, 151, 152, 199]. However, the mid-air positioning of the solenoid coil is unfeasible for EV IPT applications. Works [148, 149, 154, 155, 200] place the intermediate coil closer to the transmitter pad, some in a coplanar arrangement with the transmitter coil. Figure 2.26 shows some coplanar arrangements using circular geometries. The mutual coupling between the transmitter and intermediate coils, in such position, is almost constant and independent of the receiver pad movement. The use of intermediate resonators closer to the transmitter side offers better power transfer capabilities [198] but the authors in [150] placed the intermediate resonator in the receiver side to constrain the leakage flux fields over large air gaps. The use of a smaller receiver coil reduces the intermediate current which, in turn, reduces the leakage fields. The use of multiple intermediate resonators is analyzed in [156, 201]. In [201], the intermediate couplers are placed in a coplanar arrangement with the transmitter coil, as depicted in Figure 2.26(a) (but with an additional coil). The overall coupling value doubles in comparison with the traditional two-coil magnetic coupler. In contrast, the authors in [156] placed an intermediate coupler in a coplanar fashion with both transmitter and receiver pads. The equivalent circuit offers constant current and constant voltage modes with fixed frequency. Additionally, the use of intermediate couplers can avoid the use of ferromagnetic cores in both transmitter and receiver pads.

2.4.2   Shielding

One major concern in IPT systems is the containment of stray magnetic fields to values devices and the human body can be subject to. The International Commission on Non-Ionizing Radiation Protection (ICNIRP) and the SAE J2954 guideline have set limits for both public and occupational exposure at 27 μT and 15 μT for persons with cardiac implantable electronic devices (CIEDs). Therefore, shielding techniques have been proposed in the literature to reduce the leakage flux produced by IPT systems [202].

The magnetic stray fields are affected by the vertical and lateral displacements between the transmitter and receiver pads. The guideline SAE J2954 defines 3 ground clearance

Table 2.5: Definition of the Z-classes.

Z-Class	Ground clearance (mm)
Z1	100-150
Z2	140-210
Z3	170-250
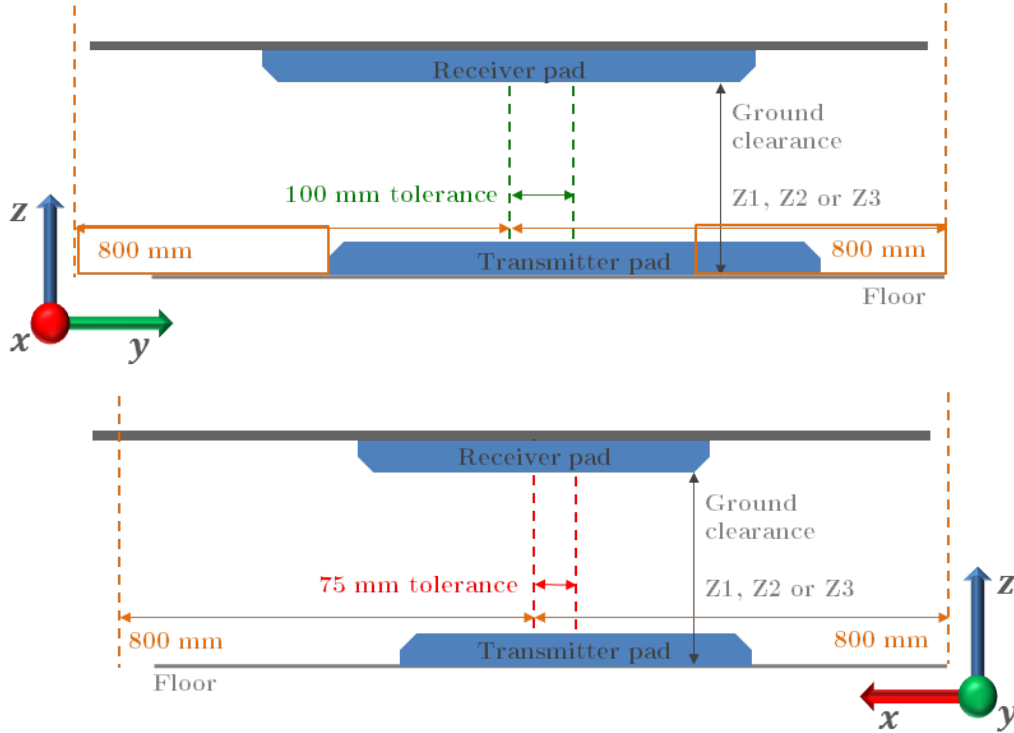
Figure 2.27: Definitions of ground clearance and leakage flux measurement.

classes, defined between Z1 and Z3 and specified in Table 2.5 [203]. In terms of lateral displacements, the guideline defines a ± 75 mm along the vehicle length (x axis) and ± 100 mm along the vehicle width (y axis). Figure 2.27 illustrates the vertical and lateral displacement tolerances. Therefore, IPT systems must comply with the magnetic stray field limits in worst charging positions (x=75 mm, y=100 mm,[Z1=150 mm, Z2=210 mm, Z3=250 mm]). The SAE J2954 guideline defines three physical regions, illustrated in Figure 2.28, to ease the electromagnetic field safety management. Region 1 comprises the underneath of the vehicle, including and surrounding the wireless power assemblies. This region does not extend beyond the lower body structure edges (e.g., rocker panels of lower edge of bumpers). Region 2 is the region around the periphery of the vehicle from the edge of the sheet metal. Finally, Region 3 is the vehicle interior.

Region 1 is subjected to exceeding electromagnetic fields and the manufacturer has to ensure human exposures using the following means:

- Active or passive access control;
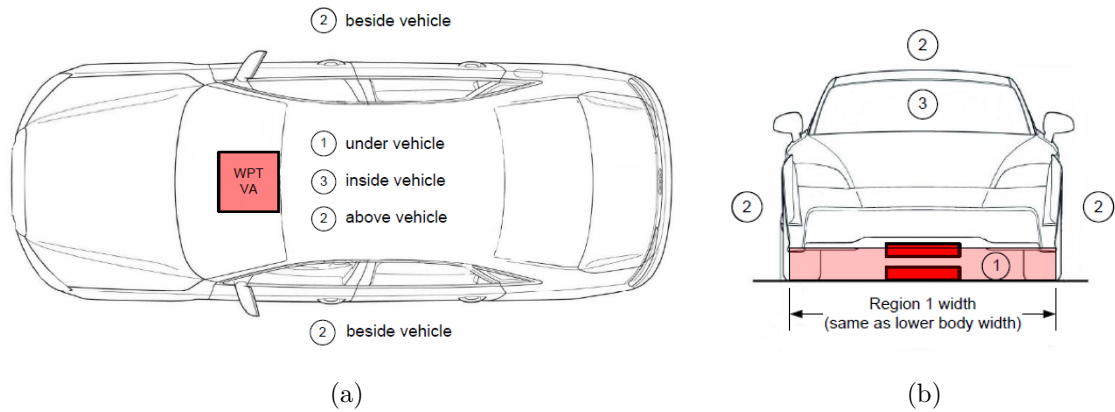
Figure 2.28: Definitions of electromagnetic regions in: (a) Top view and (b) Front view.

- Detection and shutdown before ingress into areas where such exposure could occur;
- By meeting the ICNIRP guideline limits.

On the other hand, regions 2 and 3 must comply with the 27 μT limit. This means the compliance in regions 2 and 3 are dependent on the vehicle dimensions and placement of the magnetic coupler. Most works assume a placement in the front of the vehicle and a vehicle width of 1600 mm. Consequently, measurement planes of 800 mm are used to assess the compliance in region 2 [204–206], as illustrated in Figure 2.27.

The simplest way to contain stray magnetic fields is by using passive shielding techniques through the use of high permeable materials like ferrites or by placing conductive materials like copper and aluminum in the back of the transmitter and receiver pads [204, 207–209]. The use of shielding materials with optimized geometries (both ferromagnetic core and coil form) met the ICNIRP guidelines at lower distances. The authors in [187] present a design optimization for the DDP with a E-shaped core instead of a strip ferrite core. Alternatively, active shielding techniques use canceling flux coils to shape the magnetic fields around the magnetic coupler. This technique adds turns to the coils but wounded with reverse polarity [210]. A canceling coil was presented in [197] to contain the magnetic field in the back side of a transmitter circular coil. A similar approach was conducted in [205] for the DDP using multiple canceling coils. The use of active shielding has, however, a negative impact on the original field and the system power transfer capability is worse.

Reactive shielding uses a coil with a resonant capacitor, similar to an intermediate coupler. One of the early applications of reactive shielding was carried out in the OLEV project by KAIST group [211, 212]. The authors placed several reactive shields on the side of the bus with magnetic field reductions up to 25 %. The work [150] investigates the best placement of a tuned intermediate pad that maximizes the air gap by assessing the leakage magnetic

fields and the apparent power effort. The main findings show a placement of the intermediate coupler closer to the secondary pad in order to lower the apparent power and stray magnetic fields. In addition, the receiver controller can be used to regulate the intermediate apparent power and reduce the leakage fields under lateral displacement scenarios. Results indicate that by shorting the receiver, the intermediate current dropped by 91 % and the leakage fields dropped by 52 %.

In summary, passive shields are appropriate for low and medium power IPT systems as they are able to bring the leakage magnetic fields to levels below the safe limits. In addition, they are cheaper, easier to implement and more robust. For high power applications, active and reactive shielding are more promising, specially under dynamic IPT applications.

2.5   Power converters and control strategies

Power electronic converters in IPT systems are highly dependent on the resonant topologies and selected geometries for the MCs. In early IPT systems, the IGBT semiconductor was applied in push-pull converters to complete the conversion but the evolution of MOSFET technology pushed the IPT technology to higher operating frequencies (around 85 kHz) [213]. The preferable configuration of the IPT power supplies employs a rectifier with power factor correction (PFC) a DC bus and a H-bridge inverter. The receiver side typically employs a full wave rectifier followed by a DC-DC converter.

Power converters can be grouped according to their placement into: off-board or on-board sides. Each side can be subsequently divided into unidirectional or bidirectional converters, as illustrated in Figure 2.29. Unidirectional power converters only allow power flow in one direction (source to load) [214] whereas bidirectional power converters allow power flow in both directions (source to load and load to source) [215–218].

2.5.1   Off-board side power converters

The off-board side converters are responsible for converting the AC 50/60 Hz voltage supply grid into a high-frequency supply [219]. The distinction between unidirectional and bidirectional power supply solutions is in the rectification stage of the grid. Unidirectional solutions employ single-phase or three-phase full-wave diode rectifier whereas bidirectional power supplies apply an active bridge rectifier. This stage of conversion precedes the DC link and the inverter. The most common types of inverter used in IPT systems are voltage source single [220,221], three [222,223] and multi-phase inverters, current push-pull and class EF structures, as illustrated in Figure 2.30.
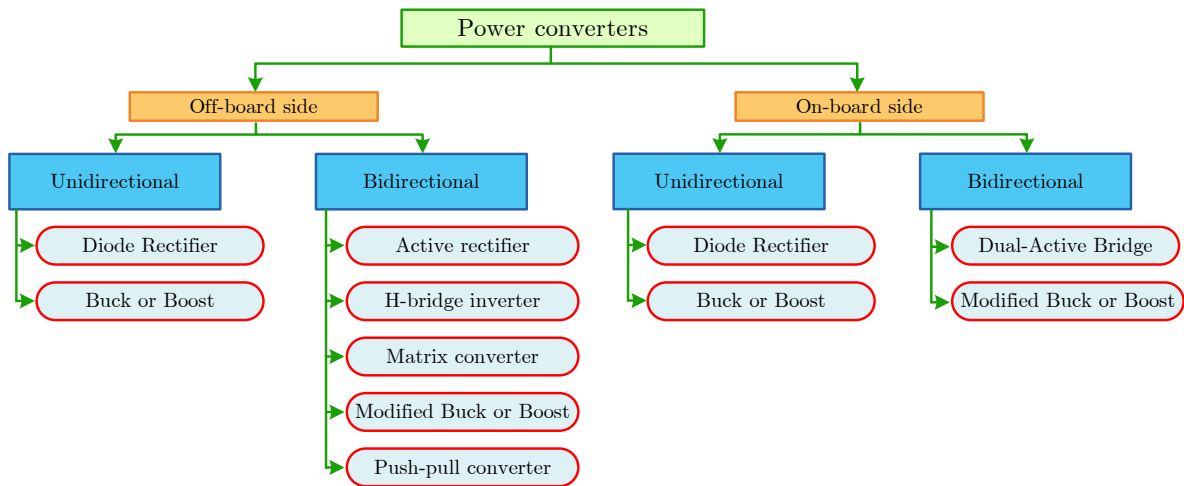
Figure 2.29: Classifications of power converter topologies used in IPT systems.

Single-phase inverter is the preferable solution for static IPT solutions that drive a single transmitter coil as a voltage or current source H-bridge, illustrated in Figure 2.30(a) [224, 225]. In addition, they can drive multiple coils, either in series or in parallel [226] in dynamic IPT systems, as illustrated in Figure 2.30(b) and 2.30(c). This solution reduces the number of inverters but increases the complexity of the control strategy. In alternative, multi-phase inverter topology can drive n transmitter coil using $n+1$ legs, as depicted in Figure 2.30(d). The complexity of the control increases but each transmitter coil can be controlled individually.

As stated earlier, inverters are associated with compensation networks to exhibit certain characteristics like voltage or current source characteristics. Figure 2.31 exhibits some inverter with resonant network configurations used in IPT systems. Parallel compensation is best suited using a current-fed converter, as illustrated in Figure 2.31(b), while series compensation is preferable with a voltage-fed converter, as illustrated in Figure 2.31(c) and Figure 2.31(d). Voltage-fed converters provide a faster dynamic response, with both high reliability and efficiency [121]. The voltage-fed LCL inverter, illustrated in Figure 2.31(e), offers load independent current source characteristics and is highly used in both static and dynamic applications [117–119, 227, 228].

A push-pull converter that uses the transmitter pads placed in an array, sharing a pair of DC inductor and switch with the neighboring transmitter pads, is presented in [79]. This topology minimizes the number of switches and only requires $n+1$ switches to drive n transmitter coils. In addition, each transmitter module can be activate individually while the remainder are disconnected, thus minimizing the losses in a dynamic charging system. However, the current through the transmitter coils can not be controlled electronically.

(a) Single pad configuration

(b) Multiple parallel pad configuration

(c) Multiple series pad configuration

(d) Multiple H-bridge configuration with single pads
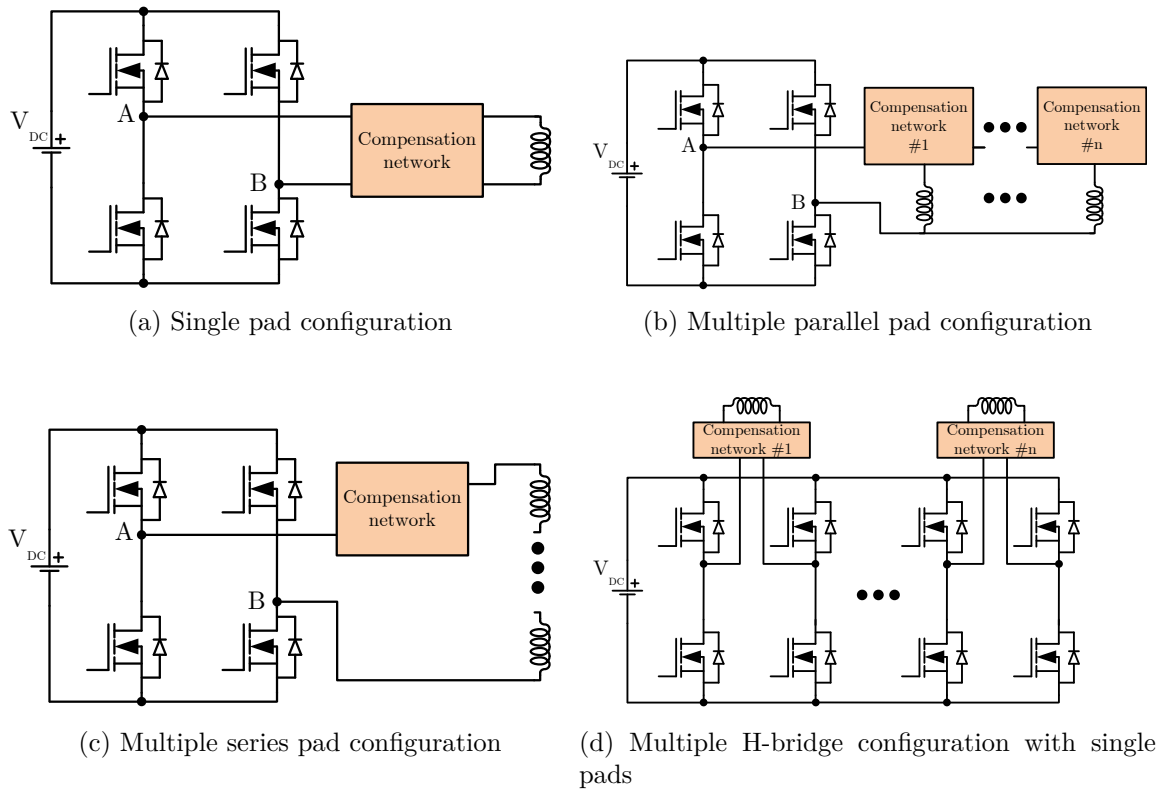
Figure 2.30: Classifications of power converter topologies used in IPT systems.

The aforementioned off-board topologies have two conversion stages: AC-DC and DC-AC. These stages of conversion are, however, interconnected by a large DC capacitor and a huge filter inductance in order to regulate voltage and frequency parameters in the output signals of the converters. The matrix converter converts an AC signal directly to another AC signal with a different frequency. The matrix converter comprises a set of bidirectional semiconductors that interconnect a source directly to the load. The semiconductors convert low frequency input signals (with fixed voltage and frequency) into high frequency output signals with variable voltage amplitude and frequency [229, 230]. The lack of bulky energy storage elements make matrix converters a more reliable and higher power density solution when compared with two-stage conversion solutions. In addition, they have inherently bidirectional capabilities that can be used in vehicle-to-grid (V2G) IPT connections [231].

Figure 2.32 illustrates a single-phase AC-AC matrix converter. The basic commutation strategy employed in a single-phase matrix dictates that only one switch from each bidirectional device is modulated at high frequency, and two switches from other bidirectional devices are entirely switched on or off for commutation purposes [121]. The authors in [230] proposed a modulation technique based on current direction commutation algorithms. Unlike voltage magnitude based commutation algorithms that typically require two accurate voltage readings, current direction commutation algorithms only require one precise current

(a) voltage-fed H-bridge inverter   (b) current-fed H-bridge inverter   (c) voltage-fed half-bridge inverter

(d) voltage-fed class D amplifier   (e) voltage-fed LCL inverter
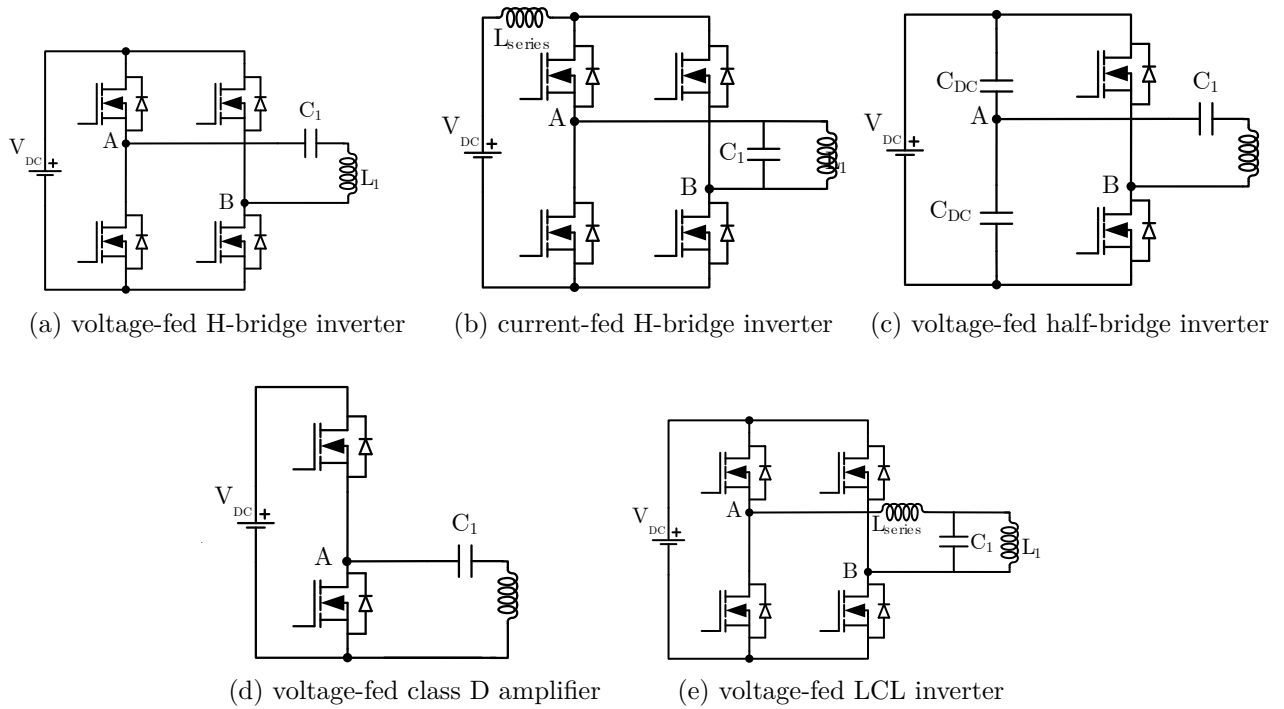
Figure 2.31: Types of off-board inverters.
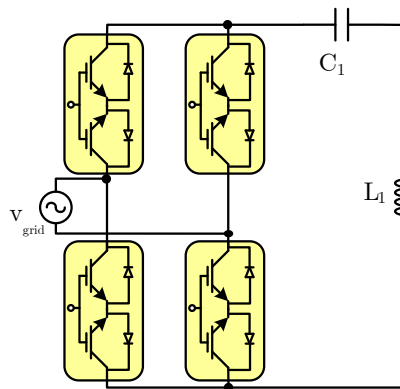
Figure 2.32: Illustration of a single-phase matrix converter.

measurement. The proposed modulation technique attenuates the harmonic distortion in the grid current. However, the converter is hard-switched and the efficiency is reduced as well as the system reliability. The authors in [231] proposed a soft-switching controller based on quantum energy injection/regeneration principle. The simplified controller can be implemented using simple logic components and avoiding entirely the need for FPGA platforms. Experimental results show efficiencies above 84 % in light load conditions.

2.5.2 On-board side power converters

The main function of on-board converters is to convert the high frequency AC signal from the on-board resonant network into a DC signal to charge the batteries. The simplest

approach is to use a full diode rectifier with a stabilization capacitor or LC filter, as illustrated in Figure 2.33(a) [232, 233]. However, the charging process of the batteries is regulated by the off-board power supply and a communication link between the EV charger and the vehicle is usually required. The use of controlled H-bridge converter, as illustrated in Figure 2.33(b), offers synchronous rectification capabilities to improve the efficiency in the power transfer at light loads [234, 235]. Additionally, when placed together with an off-board H-bridge converter to form a dual-active bridge (DAB), it offers bidirectional power transfer capabilities, but they require synchronization between both side converters [236, 237]. The authors in [234] proposed a synchronization method that uses an auxiliary coil to synchronize the voltage vectors of both converters instead of a communication link. The works [238, 239] use a semi H-bridge active rectifier to regulate the power transfer. The authors show the benefits of the proposed topology under large coupling variations and partial loads with reported efficiencies above 92 %.

The use of non-isolated DC-DC converters like the buck, boost or buck-boost together with a H-bridge diode rectifier is still the preferable approach for unidirectional IPT applications, as illustrated in Figure 2.33 (c)-(d) [50, 240, 241]. The selection of the DC-DC converter is affected by the resonant configuration. For example, a current-fed rectifier supplied by a LCL or SS resonant configuration is suitable for any of the three DC-DC converters whereas a voltage-fed rectifier supplied by a parallel resonant configuration is most suitable for a buck-boost or boost converter. The fundamental theoretical analysis on impedance matching is universal and valid for all wireless power transfer technologies. One of the early applications and stability analysis of boost converters in IPT systems was carried out in [50]. Since then, several variations have been proposed in the literature to address specific issues like smooth transition of the currents in the rectifier between the on and off-states [122].

Different topologies have been presented in the literature that address particular limitations of conventional topologies. A single-switch active rectifier is presented in [242]. One benefit of the proposed topology is the operation with a fixed frequency while providing a wide output voltage. The authors in [243] propose a poly-phase current-fed push-pull resonant converter for IPT applications with a rotating magnetic field. The system can generate sinusoidal current waveforms with low total harmonic distortion (THD). A novel multi-level phase-controlled resonant inverter is presented in [244]. The authors also present an asymmetrical phase-shift modulation that ensures a wide output voltage operation. A similar multi-level topology is presented in [245] but applied to both side of the IPT system. In this way, the presented topology has bi-directional power transfer capabilities. A new adapted

(a) H-bridge diode rectifier with filter   (b) H-bridge converter with filter

(c) Buck converter with series configuration   (d) Boost converter with parallel configuration
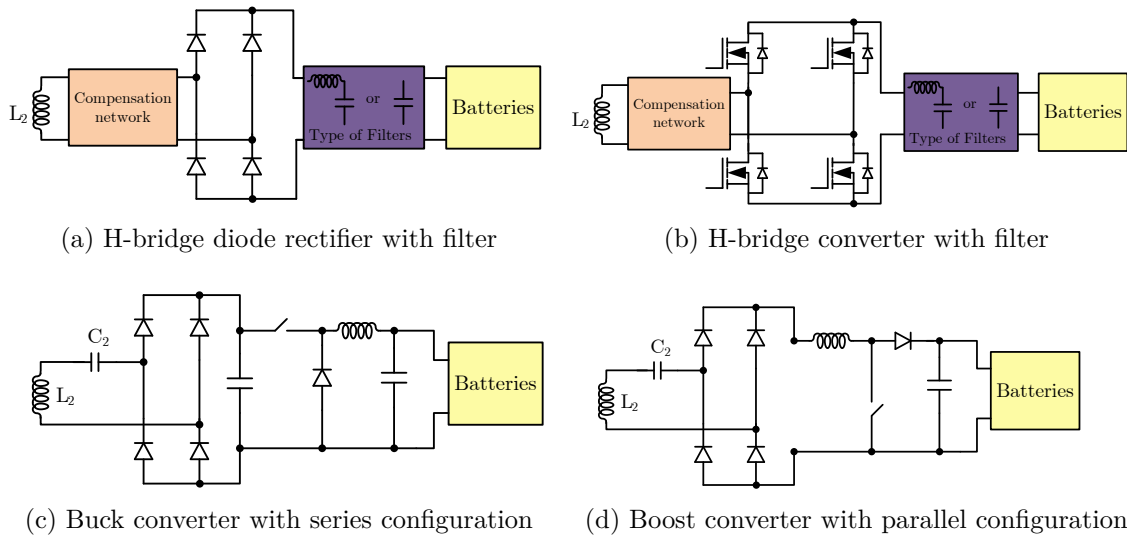
Figure 2.33: Overview of different on-board converter topologies.

fly-back converter is presented in [246]. The proposed converter achieves AC-AC with high output frequency regulation. A new transistor controlled variable capacitor is presented in [247]. The presented topology enables the adjustment of the effective capacitance in the off-board resonant network in order to maintain ZVS over a wider coupling range.

In recent works is discussed the integration of IPT solutions with the existing on-board battery chargers to reduce the number of on-board converters. Current commercial available solutions use DAB converters to regulate the batteries charging process. In this context, the work developed in this thesis replace the isolation transformer of the DAB converter by a modified magnetic coupler that integrates both plug-in as IPT charging capabilities, as illustrated in Figure 2.34 [248]. In plug-in mode, the modified magnetic coupler acts as an isolation transformer and in inductive charging mode the coupler acts as an IPT receiver pad. Simulation results show DC-DC efficiencies above 90 % using both charging modes. One drawback is the lower coupling factor of the modified magnetic coupler (≈ 0.93) when compared with a conventional isolation transformer (≈ 0.98), which leads to a reduction in the circuit's operating frequency. Moreover, the leakage fields in plug-in mode have to be contained using aluminum shields.

2.5.3   Control strategies to regulate the charging process of the batteries

Power converters are a central component of IPT systems as they increase the operating frequency and lead to higher power density systems with better efficiencies. In this context, the control strategies employed must minimize the system losses and ensure, at the same
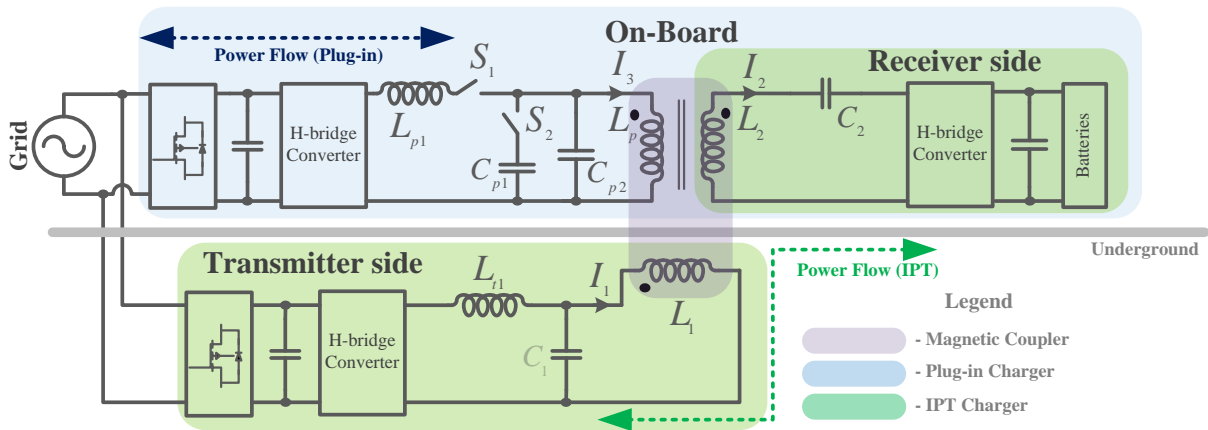
Figure 2.34: Hybrid plug-in and IPT topology with DAB converter [248].

time, constant current (CC) and/or voltage (CV) operating modes during the batteries charging process [249]. The existing control strategies for IPT systems can be grouped according with the placement of the power converter into: off-board, on-board and dual-side control, as illustrated in Figure 2.35.

The off-board control strategy of the batteries charging process requires knowledge of voltage and current measurements from the on-board side. On the other-hand, on-board control strategies have all the required information and do not need any communication link with the off-board side. Dual side control combines the best of both on-board and off-board control strategies to optimize power flow at higher efficiency values.

2.5.3.1   Off-board control

The regulation of the batteries charging process using only the off-board converters simplify the design, costs and complexity of the on-board circuitry. One downside is the communication link required to exchange information from the on-board side, namely the batteries voltage and current measurements. The wireless method usually involves radio-frequency emitters and receivers with high throughput to ensure a fast connection between the off-board charger and the vehicle [250, 251]. However, the additional hardware increase the costs and reduces the reliability of the IPT solution. Moreover, in dynamic IPT applications, the complexity of communications grows exponentially as the number of passing vehicles increase as well as the probability of interference and miscommunication between n vehicles and the off-board charger [252]. One way around this limitation is to estimate the state of charge (SOC) of the batteries and the mutual inductance values of the magnetic coupler using only off-board voltage and current measurements [253].
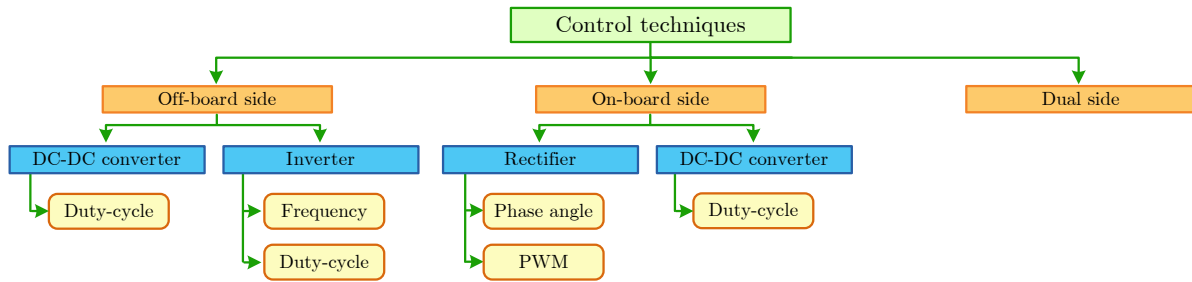
Figure 2.35: Different control techniques for IPT systems.

The works in [254, 255] use the reflected load theory in the IPT circuitry to estimate both load and mutual inductance values. However, the operating frequency of [254] as to be different from the resonant frequency of the receiver side. On the other hand, [255] is carried out under zero-phase angle conditions and the results are influenced by the current and voltage harmonics. The use of a frequency sweep method is proposed in [256] and can estimate simultaneously the mutual inductance, load and on-board side inductance or compensation capacitance. A systematic method is presented in [257] for multi-coil systems. The use of neural networks is investigated in [258] to ensure a constant output current under different coupling charging conditions using only off-board measurements. However, the training of the neural network requires large amounts of data to improve accuracy and its limited to a specific resonant compensation configuration. Other approaches have been proposed in the literature that use additional hardware but they reduce the power density of the IPT system or decrease the system stability. The authors in [250] introduce switches on the on-board side circuitry to create different operation modes: open-circuit, short-circuit and load connection. The data correlation of all modes allows the extraction of not only the mutual-inductance and load value but also the self-inductance, compensation capacitance and parasitic resistance of the on-board side. However, its applicability is limited to static IPT applications since is not feasible to emulate the three modes under dynamic conditions. The estimation procedure is extended to intermediate coupler IPT systems in [154]. The authors estimate the load and mutual-inductance values using the voltage and current measurements from the off-board and intermediate sides. The results show high accuracy but the method relies on predefined values such as self-inductance and compensation capacitance of the on-board side.

Regardless of the method to obtain the on-board measurements, the off-board control strategies are usually employed either to a DC-DC converter (whose presence is optional and placed after the rectification stage), or to the inverter. The use of a DC-DC converter

(a)

(b)
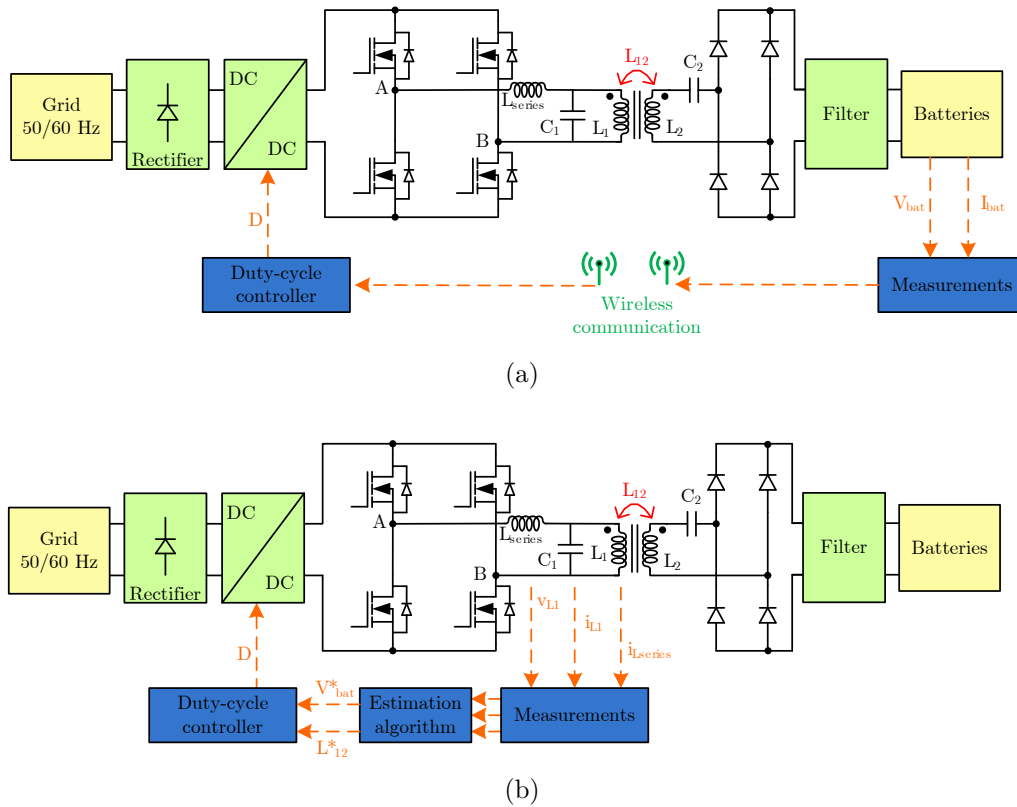
Figure 2.36: Overview of an IPT system with: (a) Wireless communication between the off-board and on-board sides and (b) estimation algorithm.

is usually adopted in resonant network configurations such as LCC and LCL, as illustrated in Figure 2.36. A fixed frequency and duty-cycle control is usually applied to the converter with these resonant configurations. Without the DC-DC converter, the current in the resonant network is kept with a constant value regardless of the load value, and the efficiency will decrease under light load condition. PI control, robust control [259] and sliding mode control [260] are common control strategies employed in DC-DC converters. PI control is the most widely implemented in industrial applications due to its simplicity. The sliding mode control, also referred as robust algorithm, is best suitable for dynamic IPT applications due to its diversity of the sliding surfaces and approaching laws. One cycle control (OCC) uses resettable integrators to perform pulse width modulators (PWM) [261]. OCC offers robustness with simple implementation. The authors in [262] apply a mixture of OCC and PI control strategies to obtain a rapid transient response of an static IPT system. The results show a faster transition to steady state using OCC-PD control when compared with OCC and PI controls. A cooperative control for multiple-excitation transmitter coils is presented in [263]. The control identifies the coupling value between the transmitters and the receiver coils and either optimizes the system efficiency or power transfer capability. In addition, the control offers great response speed since it only requires the DC current measurement.
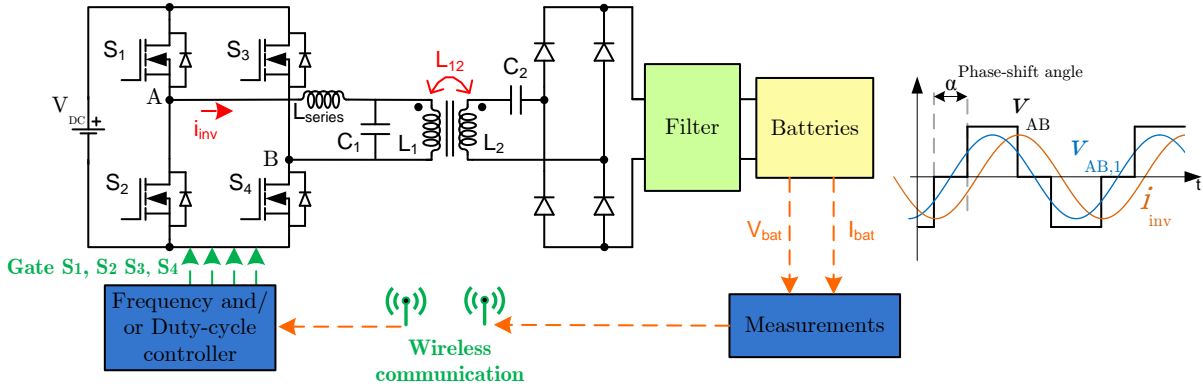
Figure 2.37: Overview of an off-board inverter control scheme for IPT systems.

The control strategies applied to inverters adjust duty-cycle and frequency [264, 265]. Phase-shift technique regulates the duty-cycle of the output inverter voltage by adjusting the shift angle between the inverter legs A and B, as illustrated in Figure 2.37. The drive pulses of the switches S_3 and S_4 overlap the drive pulses of S_1 and S_2 by a shift angle (α) to regulate the inverter output voltage and consequently, the amount of power transferred to the load. The authors in [266] propose a control strategy that adjusts the output voltage using only the off-board inverter and without direct on-board measurements feedback. A current controller based on phase-shift technique is proposed in [214] using only off-board measurements to estimate the batteries charging current. The control keeps the batteries current constant during the charging process even under coupling displacements or grid fluctuations. The authors in [267] propose an auto-resonant detection method that ensures a ZVS operation of the off-board inverter. The method extends the admissible charging area with improved efficiency. A decoupled control method based on PI controller is presented [268]. The control ensures a constant ZVS operation under both CC and CV modes.

Variable frequency control strategies adjust the switching frequency of the inverter to achieve zero-phase angle operation (ZPA) or avoid the bifurcation phenomena [269, 270]. As discussed in Section 2.2, each resonant network configuration behaves differently to mutual inductance or load variations. A variable frequency control strategy is presented in [271] for a SS configuration to obtain an constant and stable output voltage regardless horizontal displacements between the off-board and on-board pads. A phase-locked loop (PLL) is used to find the switching frequency that ensures a null phase difference between on-board current and the fundamental harmonic of the inverter output voltage. However, the efficiency is largely affected by switching commutation losses since the inverter has a power factor that oscillates between 0.6 and 0.8 inductive. In [33], the authors propose a frequency modulation

and phase-shift control strategy for the SP resonant compensation. The proposed control ensures the maximum power transfer capabilities of the system with almost zero reactive input power in the interface with the network, whilst ensuring the maximum efficiency. A variable frequency phase-shift control is proposed in [272] for the SP resonant configuration network. The authors use a current hysteresis comparator to suppress the noise in high IPT power applications. The control ensures ZVS operation whilst operating in CC mode, over a wide range of mutual inductance and load variations with high efficiencies.

New control strategies take advantage of the intrinsic characteristics of resonant network configurations to regulate the transmitter current and/or power transferred while the off-board inverter operates with a fixed phase-shift angle. An auto-tuning control system is presented in [273] for dynamic applications. The presented control uses the variation of the self-inductance of the transmitter pad caused by the ferrite core of the receiver pad to regulate the current in the transmitter pad. This configuration avoids the use of switches to turn on/off the multiple transmitter pads. The variation of the self-inductance can, however, be caused by extra ferromagnetic material over the transmitter pad like the vehicle chassis leading to an unwanted current increase. A similar approach is taken in [274]. The authors use, however, a saturable inductor to limit the current in the transmitter pads. Alternatively, [275] presents a ZVS control strategy based on a tuning capacitor. The variable capacitor is implemented using a MOSFET connected in series with the tuning capacitor. This series combination is then connected in parallel to the transmitter resonant capacitor. Therefore, the effective resonant capacitance is regulated by the duty-cycle applied to the MOSFET. The presented control reduces the switching losses in the H-bridge inverter by ensuring a ZVS operation over the total load range.

2.5.3.2   On-board control

The use of controllable power converters in the on-board side offers new possibilities of higher power transfer capabilities under displacement charging scenarios with better efficiencies as well as under light load conditions [276]. As stated earlier, the on-board control strategies are usually applied to a DC-DC converter or to a controlled H-bridge converter.

The non-isolated DC-DC converters have a relatively simple control without grand computational demands or sample frequency ratings [277]. In addition, with a careful design of the reactive components, these converters offer wide range of input voltage variations, ideal for compatibility across EV chargers from different manufacturers. Figure 2.38 illustrates
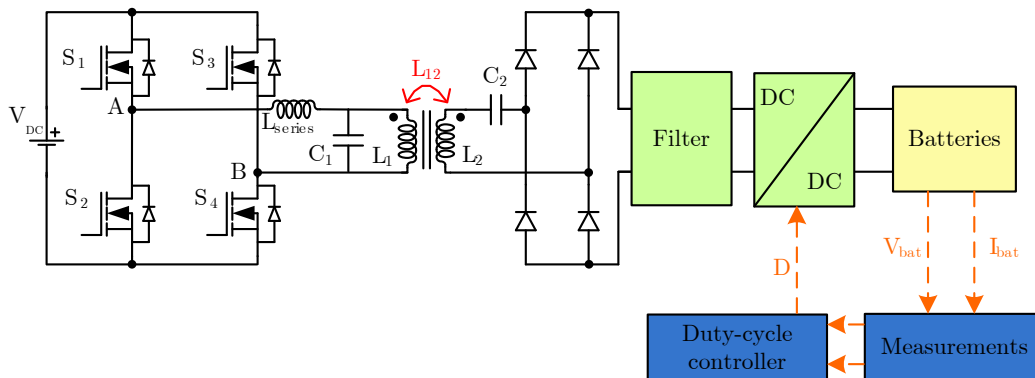
Figure 2.38: Overview of an on-board DC-DC control scheme for IPT systems.

the use of a H-bridge rectifier with a DC-DC converter on the receiver side [122]. A notable difference when compared with the off-board control strategies, depicted in Figure 2.37, is the absence of a communication link to the off-board side. Furthermore, unlike the switching frequency range of 81.2 kHz to 90 kHz imposed by the SAE J2954 for inverter operation, DC-DC converters can operate with lower switching frequencies. The work [278] operates the DC-DC converter at 10 kHz whereas the inverter operates at 100 kHz.

The selection choice of a boost or buck converter is largely dependent on the batteries nominal voltage value and the voltage gain function of the selected resonant configuration in the worst charging scenario. In [240], the authors develop a duty-cycle control strategy for a boost converter that ensures essentially a unitary power factor at the inverter output terminals. The control strategy reduces the power transfer capabilities of the system but it also reduces the size of the on-board coil. The non-linear effects of rectifiers were decreased using a Boost converter together with a LCL resonant compensation network [279]. A PID controller uses the errors of batteries current and voltage with the reference values to compensate lateral displacements under dynamic conditions. A control strategy for a Buck converter is proposed in [278] and is based on the maximum efficiency of a dynamic charging system. The control estimates the mutual-inductance values in real-time, which is essential for tracking the maximum efficiency condition.

The use of controllable H-bridge or semi H-bridge converters are also employed on the on-board side, as depicted in Figure. 2.39. The authors in [280] present an active H-bridge rectifier with a maximum efficiency tracking control. The control method shows efficiency improvements up to 10 % when compared with H-bridge diode rectifiers under light load conditions and natural resonance frequency variations on the receiver network.
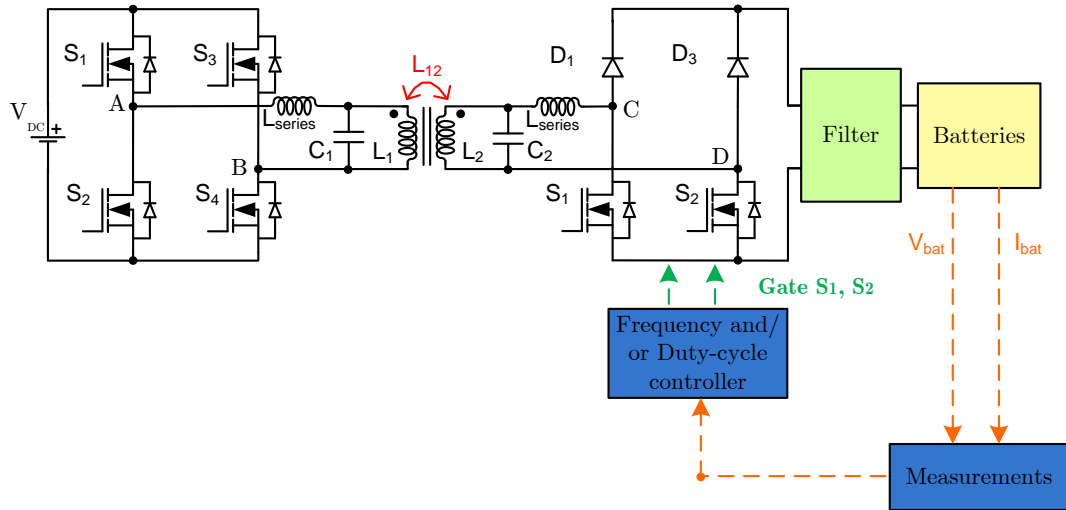
Figure 2.39: Overview of a semi H-bridge rectifier control scheme for IPT systems.

2.5.3.3   Dual-side control

Dual-side control strategies require controllable power converters on both off-board an on-board sides. Since the converters are synchronized, problems like over-currents are over-voltages are mitigated. Additionally, the system offers better performances under light-load conditions and large lateral displacements since both converters are adjusted to work in ZVS mode while exhibiting, under some load conditions, ZPA. Therefore, the commutation losses in the converters, one of the main causes for lower efficiencies, are mitigated. Figure 2.40 illustrates a DAB with dual-side control. In [239] a control strategy is proposed for a DAB configuration to improve the charging process in the worst coupling and load conditions. The synchronization of both sides occurs via wireless communication. A different dual-side control for a DAB converter with LCL-LCL resonant network configuration and without a communication link is presented in [216, 237, 281]. The control strategy takes advantage of the frequency versus power characteristic to create a step response, similar to PQ controller of synchronous generators. One downside of the proposed control strategy is the frequency deviation from the natural resonant point that may force the inverter to operate in ZCS, thus increasing the converter losses. The work in [282] also avoids a communication link and the estimation of the coupling value. The method estimates the voltage at the on-board parallel compensation capacitor to detect energy transfer.

An optimal PID controller for bidirectional IPT systems using DAB converter is presented in [283] using multi-objective genetic algorithm. The authors analyze different objective functions under different charging conditions to assess the best tuning function. When
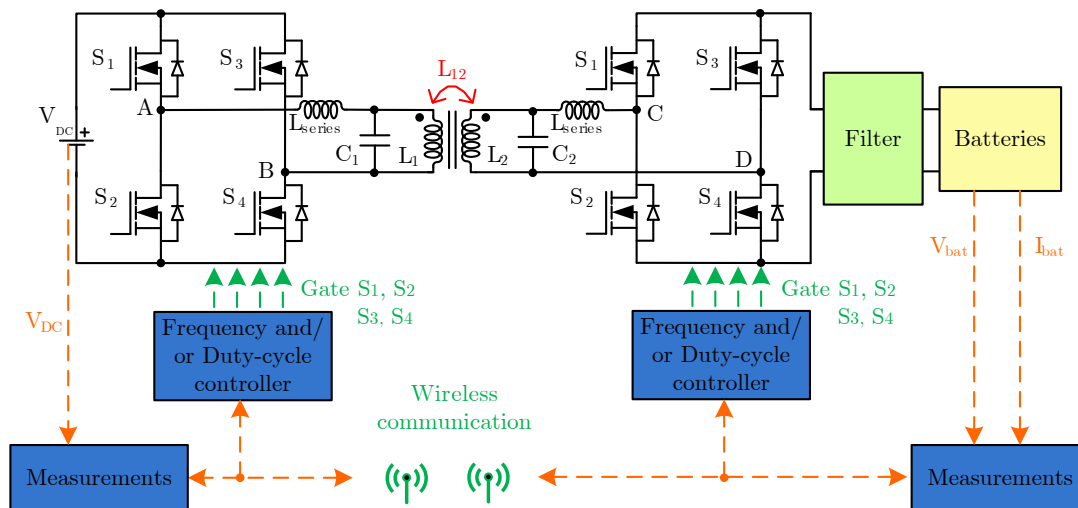
Figure 2.40: Overview of a DAB control scheme for IPT systems.

compared with the traditional Ziegler-Nichols method, the proposed controller exhibits faster response time. An optimized dual-side phase-shift control using a DAB converter with SS resonant configurations is presented in [220]. The control minimizes the coil losses by adjusting the DC voltage ratio to a value near to the square root ratio between the on-board and off-board coil resistances. The control presented in [284], on the other hand, tracks the maximum efficiency point using a predictive control model. When compared with PI control, the predictive control model exhibits faster response. The work in [285] uses a DAB converter with a CLC resonant network. The proposed topology and control reduces the current values in the converters and improves the power factor on both converters. A bidirectional DAB controller with multiple receiver sides is presented in [217]. The authors control the power flow through either phase and/or magnitude modulation of the voltages generated by each converter. A similar approach is carried out in [286] using a DAB topology with a LCL resonant network to create a bidirectional controllable current source.

In [287], the inverter output voltage is adjusted over a wide range by switching between different modes (full-bridge and half-bridge) to approach the optimal load impedance. The on-board semi-bridge-less active rectifier uses a modified phase-locked model to regulate the batteries current/voltage without the need for a communication link.

2.6   Summary

This chapter explores the main research areas in IPT systems and their current state of art. IPT systems can be divided into four main research areas: resonant configurations, magnetic couplers, controllers and respective controls and circuitry analysis.

The use of resonant configurations together with high operating frequencies boost the

power transfer capabilities of loosely coupled systems. The main intrinsic characteristics in a resonant configuration for IPT systems include operation in ZVS while exhibiting load-independent constant voltage and/or current modes. The basic SS an SP resonant configuration offer load-independent voltage and current but at distinct operating frequencies. In addition, ZVS is not ensured over the entire load variation. The use of higher order resonant configurations overcome the limitations of the basic resonant configurations while offering additional characteristics. The LCL resonant network exhibits a load-independent current source characteristic in the second inductor and is ideal for dynamic IPT applications. The SP-S resonant configuration, on the other hand, allows higher displacement tolerances. The use of intermediate couplers between the transmitter and receiver pads of a MC boosts the magnetic link for higher air gap values. A SS-IC exhibits load-independent CC and CV modes with minimal frequency variation. In addition, it also constrains the magnetic stray fields in the vicinity of the magnetic coupler.

The magnetic coupler is the key component that enables the energy transfer in IPT systems. There are numerous geometries in the literature and they are grouped according to the main flux path direction into: non-polarized and polarized geometries. The non-polarized geometries are easier to implement but they are limited in terms of power transfer capabilities and lateral displacement tolerances. Among the most promising polarized geometries are the DDPQ and the BPP. These geometries have been extensively optimized in the literature for both static and dynamic applications. The compliance of the geometries with the maximum admissible stray magnetic field levels is also imperative. The inclusion of aluminum plates in the back of the magnetic coupler is the simplest way to contain the stray magnetic fields. However, for large power applications, the magnetic couplers must also include active or reactive shield techniques to further contain the stray magnetic field.

The large number of admissible MC geometries difficult the characterization of the self and mutual inductance profiles needed during the design of the IPT system. The existing methodologies rely on extensive FEA simulations and they are usually applied for a given set of geometries. Moreover, the applicability of the current MCs to large ground clearance vehicles is made at the expense of MCs with larger sizes and limited power transfer capabilities.

The power converters in IPT systems are highly dependent on the resonant topologies and selected geometries for the MCs. They can be grouped according to their placement into: off-board and on-board topologies. The preferable off-board topology includes a rectifier with power factor correction, a DC bus and a H-bridge inverter. The receiver side typically

employs a full-wave rectifier followed by a DC-DC converter. The off-board inverter can be connected to a single MC or to multiple MCs, either in series or parallel. The on-board topology employs a H-bridge diode with a DC-DC converter for unidirectional power applications or employs a H-bridge converter for bidirectional applications.

The regulation of the batteries charging process can be made using the off-board, on-board or both converters. Off-board control strategies require information, like current and voltage measurements of the batteries, to properly adjust the frequency or phase-shift angle of the inverter. This on-board information can be transmitted via wireless communication or estimated using only off-board measurements. Off-board control strategies are often employed in static unidirectional IPT applications together with resonant configurations that exhibit load-independent CC and CV modes. On-board control strategies have all the information available on the vehicle side to regulate the charging process of the batteries. These control strategies, however, do not take into account the off-board operation of the converters and exhibit poorer efficiency profiles, especially under light load conditions. Dual-side control strategies synchronize both off-board and on-board converters to mitigate over-currents and over-voltages. Consequently, the power transfer capability versus efficiency is optimized in the entire load range while offering, at the same time, bidirectional capabilities.

2.7   Adopted path

The literature survey carried out in the previous sections showed different intervention areas to mitigate the effect of displacements. Figure 2.41 illustrates the adopted path of the work conducted in this thesis. Firstly, the impact of displacements was assessed in the four basic resonant configurations and the generic reflected impedance equations were derived in Chapter 2. In Chapter 3, a new vertical IPT charger with simultaneous double receiver charging capabilities is firstly presented for heavy-duty and autonomous guided vehicles. The vertical positioning of the transmitter pad reduces the air gap distance between the transmitter and receiver pads and eliminates, at the same time, the need for foreign object detection systems.

The employment of vertical IPT chargers is not feasible for passenger vehicles and the placement of the transmitter pad under the pavement is the preferable approach. The existing transmitter pad geometries take advantage of ferromagnetic materials to improve the magnetic coupling. However, these materials are expensive and easily breakable. Therefore, the next phase of this work consisted on the design and optimization of different ferrite-less
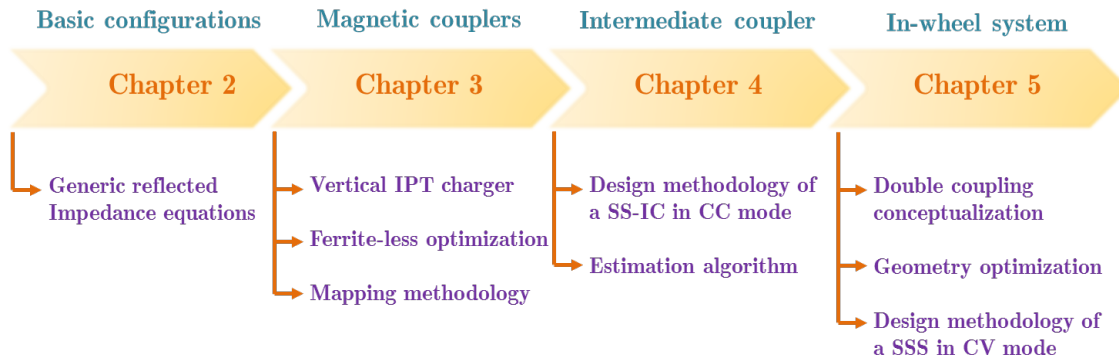
Figure 2.41: Adopted path of the work conducted in this thesis .

non-polarized and polarized geometries.

One difficulty found during the design of an IPT with given specifications and constraints was which values to use for the self and mutual inductances in different charging positions. The simplest way to determine these values involves 3D FEA simulations of the MC in the desired charging position. This approach, however, has to be repeated every time the vertical, lateral or number of turns is modified, increasing the overall design time. In this context, a mapping methodology of the self and mutual inductance profiles with minimum number of FEA simulations is also presented in Chapter 3.

As stated earlier, IPT systems benefit with the inclusion of ICs. Still, the literature lacks a design methodology of an IPT with an IC that exhibits current source characteristics. Such design enables the control of the batteries charging process from the off-board side, thus simplifying the on-board converter topology. Moreover, an estimation procedure of the batteries voltage and current would also eliminate the need for a communication link between the off-board and on-board sides. Therefore, a design methodology and respective estimation procedure is developed in Chapter 4 for a series-series with an IC system.

This work culminates in a novel double coupling configuration that uses the wheel as an intermediary stage between the off-board and on-board sides. The presented configuration keeps the air gap distance to a minimum and independent of the vehicle class. Moreover, the lateral displacement is also inferior since the driver can take advantage of the existing parking systems (like in-built vehicle cameras) to correctly park the vehicle over the transmitter pad. Chapter 5 firstly presents the conceptualization of the proposed double coupling system applied to a wheel. A design optimization of several curved geometries is then carried out using a FEA tool. Finally, a design methodology of a series configuration with voltage source characteristics is presented.

Chapter 3

Magnetic couplers

Magnetic coupler (MC) is the key component in IPT systems that enables the power transfer between the off-board and on-board sides of an EV. Chapter 2 explained the evolution of MC geometry since early 2000's and identified the prominent geometries chosen for EV charging applications. Magnetic couplers like the circular pad (CP), the Double-D pad (DDP) and the Bipolar pad (BPP) have been widely accepted both by the academic community and industrial manufacturers for traditional static EV IPT charging systems. Still, the vertical and lateral tolerances remain the same, despite the adopted MC geometry.

The initial work presented in this chapter places the transmitter pad in a vertical position to shorten the distance between the off-board and on-board sides of heavy-duty and autonomous guided vehicles. The solenoid pad (SPP) geometry was selected due to its double-sided flux pattern, allowing simultaneous charging of two receivers. The SPP ferromagnetic core is optimized using a 3D finite element analysis (FEA) tool. Other relevant magnetic properties like interoperability and compliance ICNIRP guidelines are also analyzed.

The employment of vertical IPT chargers is not viable for passenger vehicles and the traditional placement of the transmitter pad under the pavement is still the best approach. The aforementioned geometries e.g, CP, DDP and BPP, employ ferromagnetic cores to improve the magnetic coupler. These materials are, however, expensive and easily breakable. In addition, the use of ferromagnetic materials in dynamic IPT roadways would drastically increase the construction costs. Therefore, this chapter also presents a design optimization of different non-polarized and polarized ferrite-less geometries that use intermediate couplers (IC) or "pipe" coils as replacements to ferromagnetic cores. The study focus on assessing the best alternative to ferromagnetic cores with minimal coupling factor and power transfer capability losses. A new non-polarized geometry derives from this study and is named as ferrite-less circular pad (FLCP).

One difficulty in the design of IPT systems is which values for the self and mutual inductances to use in different charging positions. These values depend on parameters such as the number of turns, vertical and lateral displacements besides the geometry of MC. The use of 3D FEA tools is still the best way to determine these inductance values. This approach, however, has to be repeated every time one of the aforementioned parameters is modified. In this context, this chapter also presents a new mapping methodology for self and mutual inductance profiles with a reduced computational effort. The behavioral analysis of the self and mutual inductance profiles under different turns combinations, vertical and lateral displacements is done to identify adequate fitting curves. This allows extracting minimum number of required charging positions and consequently, has a positive impact on the required number of FEA simulations. In conclusion, it is possible to characterize a MC geometry with a specific size and ratio, and evaluate its applicability in different IPT systems with different power requirements and operational specifications.

The chapter starts with the fundamental analysis of two and three-coil MCs. The geometry optimization of the SPP is carried out in Section 3.2. The study of different geometries for dynamic applications, include the design and optimization of the FLCP is made in Section 3.3. The mapping methodology and respective validation is analyzed in Section 3.4. The summary of the chapter is drawn in Section 3.5.

3.1 Fundamentals

This section introduces the electric and magnetic concepts used in the optimization and comparison of magnetic coupler geometries. The presented concepts are derived for magnetic couplers in two-coil systems (one transmitter and one receiver pads) and in three-coil systems (includes an additional intermediate coupler).

3.1.1 Two-coil systems

The MC is a loosely coupled transformer with a transmitter and receiver pads. Each pad is formed by one or more coils, a ferromagnetic core and a shield (if necessary). Figure 3.1 illustrates the MC of a two-coil IPT system (represented by the color brown) and the flux lines that link the transmitter and receiver pads. The coupling coefficient (k_{12}) quantifies the magnetic link between both pads, in a scale from 0 to 1, and it determined according to

$$k_{12} = L_{12}/\sqrt{(L_1.L_2)}, \tag{3.1}$$
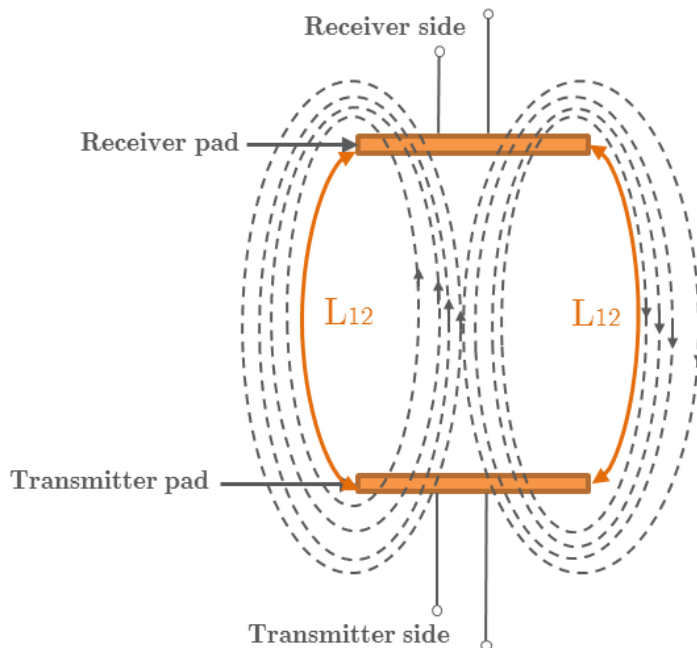
Figure 3.1: IPT system with a single transmitter and receiver pads.

(a)

(b)
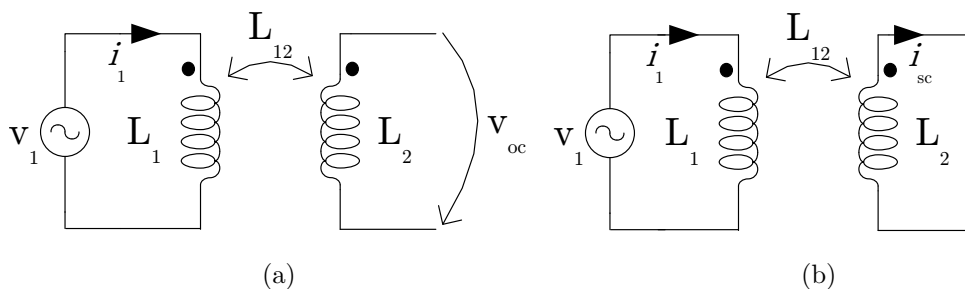
Figure 3.2: Experimental tests to determine: (a) open-circuit voltage and (b) short-circuit current.

where L_1 and L_2 are the self-inductance values of the transmitter and receiver coils and L_{12} is the mutual inductance. The subscript number in the variables indicate to which side the variable is related to, where 1 and 2 stands for transmitter and receiver sides, respectively.

The self and mutual inductance values and power transfer capabilities of a MC can be determined by the open and short-circuit tests, similar to a conventional 50 Hz transformer. The open-circuit test consists on supplying the transmitter coil with the nominal current $(\overline{I}_1)$ while receiver coil remains open, as depicted in Figure 3.2(a). In the short-circuit test, the receiver coil is shunted while the transmitter coil is supplied by the nominal current of the transmitter pad, as illustrated in Figure 3.2(b). Assuming a lossless circuit, the product of the RMS open-circuit voltage test $(|\overline{V}_{oc}|)$ with the RMS short-circuit current test $(|\overline{I}_{sc}|)$, described in (3.2) and (3.3), gives the uncompensated power (P_{su}) of the MC. Figure 3.2 illustrates the equivalent circuitry to measure $\overline{V}_{oc}$ and $\overline{I}_{sc}$.

$$\overline{V}_{oc} = j.\omega.L_{12}.\overline{I}_1 \tag{3.2}$$

$$\overline{I}_{sc} = \frac{\overline{V}_{oc}}{j\omega.L_2} = \frac{L_{12}.\overline{I}_1}{L_2}. \tag{3.3}$$

The output power (P_{out}) corresponds to the product result of P_{su} with the load quality factor (Q), as shown in

$$P_{out} = P_{su}.Q = |\overline{V}_{oc}|.|\overline{I}_{sc}|.Q = \omega.k_{12}^2.L_1.|\overline{I}_1|^2.Q. \tag{3.4}$$

The value of Q depends on the resonant topology used in the receiver side. For a series compensation, Q is defined as $Q = \omega.L_2/R_{eq}$ while for a parallel compensation, Q is given by $Q = R_{eq}/\omega.L_2$. In practical applications, the value of Q should be limited between 4-10 [50].

The self and mutual inductance values can be determined by the open-circuit test. The value of L_{12} is determined using (3.2). The value of L_x, on the other hand, can be determined using the no-load power (P_{oc}) and $\overline{I}_{oc}$ into

$$L_x = \frac{Q_{oc_x}}{\omega^2.|\overline{I}_{1_x}|^2}, x = 1,2 \tag{3.5}$$

where Q_{oc_x} is the no-load reactive power and it is determined by

$$Q_{oc_x} = \sqrt{(|\overline{V}_x|.|\overline{I}_{1_x}|)^2 - P_{oc_x}^2}, x = 1,2 \tag{3.6}$$

Therefore, the open-circuit test must be performed to each coil in order to fully characterize a MC.

3.1.2   Three-coil systems

The inclusion of an intermediate coupler (IC) in two-coil IPT systems, to form a three-coil system, boosts the magnetic link between the transmitter and receiver sides [288]. The IC is formed by an intermediate coil (L_{int}) connected in series with a capacitor (C_{int}) and is usually tuned with a frequency higher than the operating frequency [149]. The subscript word *int* identifies the variables from the intermediate side. Figure 3.3 illustrates the inclusion of an IC (represented in blue) between the transmitter and receiver pads. The intermediate coil creates two additional couplings between the existing transmitter and receiver coils: k_{int2} and k_{1int}. The first quantifies the magnetic link between the receiver and intermediate coils while the second quantifies the magnetic link between the transmitter and intermediate coils.
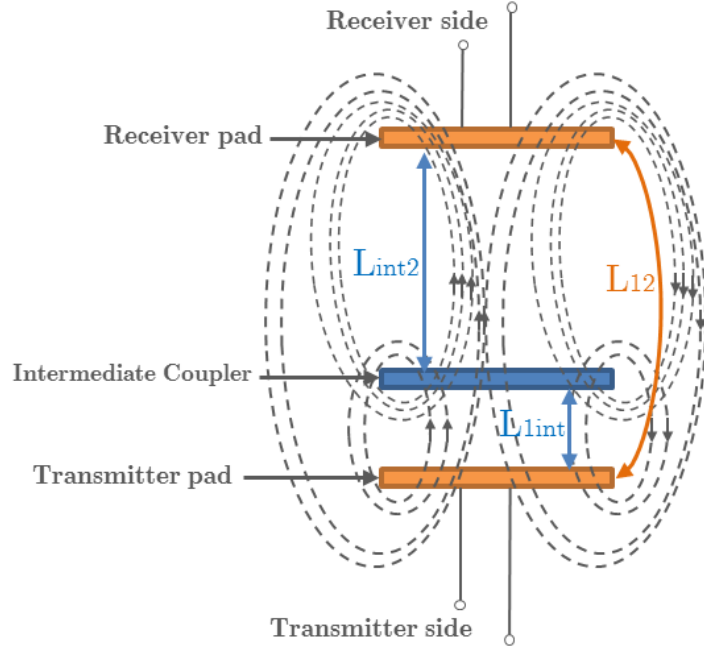
Figure 3.3: IPT system with the inclusion of an intermediate coupler.

The correspondent mutual inductance values, depicted in Figure 3.3, are given by

$$L_{int2} = k_{int2}.\sqrt{(L_2.L_{int})}, \tag{3.7}$$

$$L_{1int} = k_{1int}.\sqrt{(L_1.L_{int})}, \tag{3.8}$$

Analogously to two-coil systems, P_{su} can be used to quantify the power transfer capability of a three-coil system. The open and short-circuit tests in three-coil systems are performed with the transmitter and receiver coils connected in the same way as two-coil systems, illustrated in Figure 3.2, and with the intermediate coil shunted in both tests. In this way, there will be a circulating current in the intermediate coil ($\overline{I}_{int}$) and the voltage across the receiver coil ($\overline{V}_{L_2}$), assuming a lossless system, is then given by

$$\overline{V}_{L2-3coil} = j.\omega.L_2.\overline{I}_2 - j\omega(L_{12}.\overline{I}_1 + L_{int2}.\overline{I}_{int}), \tag{3.9}$$

The values $\overline{V}_{oc\_3coil}$ and $\overline{I}_{sc\_3coil}$ are determined using (3.9) and they are given by

$$\overline{V}_{oc\_3coil} = -j\omega(L_{12}.\overline{I}_1 + L_{int2}.\overline{I}_{int}) \tag{3.10}$$

$$\overline{I}_{sc\_3coil} = \frac{L_{12}.\overline{I}_1 + L_{int2}.\overline{I}_{int}}{L_2}. \tag{3.11}$$

The value of P_{out} is then determined by

$$P_{out} = \omega(k_{12}^2.|\overline{I}_1|^2.L_1 + k_{int2}^2.|\overline{I}_{int}|^2.L_{int} + 2.k_{12}.k_{int2}.k_{1int}.L_{1int}.|\overline{I}_1|.|\overline{I}_{int}|).Q \qquad (3.12)$$
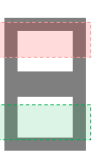
In a two-coil system the value of P_{out}, given by (3.4), only depends on $\overline{I}_1$, k_{12} and L_1. However, in three-coil systems, P_{out} depends on all coupling coefficients and both values of $\overline{I}_1$ and $\overline{I}_{int}$. The dependency of P_{out} on $\overline{I}_{int}$ difficult the comparison between two and three-coil systems since its value depends on the tuning of the IC.

3.2 Solenoid Pad

The solenoid pad (SPP) has been investigated in previous works for EV IPT charging systems [179, 182, 183, 289]. The design offers better k_{12} and P_{su} when compared with non-polarized geometries like the CP and RP. In addition, it offers interoperability with non-polarized and polarized geometries [182]. However, due to the double-sided flux pattern of a solenoid, just half of the flux lines contribute to the coupling between the transmitter and receiver pads. Moreover, the pad losses drastically increase with the inclusion of an aluminum shield required for the pad to comply with the human exposure limits to magnetic and electric fields [290]. Alternative designs based on the SPP were proposed in the literature, like the DDP and the BPP, to overcome this limitation. These new geometries are envisioned for placement under the EVs, offering both stationary and dynamic applicability. Nevertheless, vertical IPT chargers can be alternatives to use in cargo and heavy-duty EVs, as they reduce the distance between the transmitter and receiver pads. The same principle can be applied to Automatic Guided Vehicles (AGVs) in industry applications [191, 291, 292]. The use of elongated tracks is a common practice to charge AGVs in well established routes along the factory. Nevertheless, in some industries is not applicable the use of a buried elongated track or discrete transmitter pads due to factory or working constraints such as investment costs or dynamic routes for AGVs. The use of stationary chargers in different facility locations overcome these limitations. The double-sided flux pattern of a SPP enables simultaneous charging of two receivers using only a transmitter pad, thus reducing installation costs.

To evaluate the coupling of a solenoid magnetic coupling structure, a typical IPT system with one transmitter pad and one receiver pad is used. Table 3.1 shows several solenoid pad designs with different core arrangements to evaluate which one offers the best performance. A configuration with just half the ferrite volume (Core 6) is also analyzed for dynamic IPT charging applications. The pads were modeled in a 3D FEA software called Flux. The coils

Table 3.1: Comparison of different core arrangements of the SPP geometry.

Core	1	2	3	4	5	6
Layout						
Area [dm^2]	7.74	7.05	5.99	10.23	8.99	8.99
$P_{su}/Area$ [VA/dm^2]	115.76	89.2	60.6	123.36	152.17	34.93
$P_{su}/V_{Ferrite}$ [VA/dm^3]	1255	881	508	1767	1915	879
Air gap [mm] (perfectly aligned)						
50	2751, 0.37	1969, 0.33	1291, 0.30	3020, 0.38	3638, 0.39	835, 0.29
P_{su} [VA], k 100	896, 0.20	629, 0.20	363, 0.16	1262, 0.25	1368, 0.25	314, 0.22
150	391, 0.15	270, 0.13	144, 0.10	544, 0.17	635, 0.17	144, 0.12
Lateral displacement y [mm] (for an air gap = 100 mm)						
50	841, 0.21	590, 0.19	332, 0.16	1157, 0.24	1383, 0.25	731, 0.18
P_{su} [VA], k 100	702, 0.19	449, 0.16	261, 0.14	907, 0.22	1027, 0.22	513, 0.15
150	450, 0.16	296, 0.14	171, 0.11	603, 0.18	721, 0.18	323, 0.12

are represented in green and red and were modeled with the characteristics of a 1050 strands AWG 38 Litz wire with a cross section of 4.68 mm^2 and a DC resistance of 2.1 mΩ/m. All coils have 14 turns. Also, the position of the coils is equal for all pads, as seen in the figures of Table 3.1, in order to obtain a correct evaluation of all core configurations. The core is formed by N87 "I" ferrite bars from Epcos with the dimensions of 93x28x16 mm. The core material has an initial permeability of 2300 and a saturation level of 0.47 T. For a correct assessment of the analyzed geometries, the core volume is the same in all designs and corresponds to sixteen "I" bars with the aforementioned dimensions. Thus, rectangular core arrangements designs are proposed in this work. The air gap and lateral tolerances play an important role in the use of IPT systems in EVs or AGVs applications since a perfect alignment with the transmitter pad has a low probability of occurrence. Due to pad geometry, a lateral displacement of ±150 mm is deemed sufficient for vertical IPT chargers. The minimum air gap in vertical IPT chargers can be as small as 50 mm, contrary to the ground clearance range of EVs set between 150-350 mm. Consequently, an air gap range between 50 and 150 mm was considered with intervals of 25 mm.

Table 3.1 summarizes the values of P_{su} and k_{12} for all evaluated configurations at a frequency of 20 kHz and with a $|\bar{I}_1| = 20$ A in different air gap and lateral charging positions . The surface area and the power density (Area/P_{su}) are also indicated in Table 3.1. As expected, the core configuration with half the ferrite volume (Core 6) is the design with the
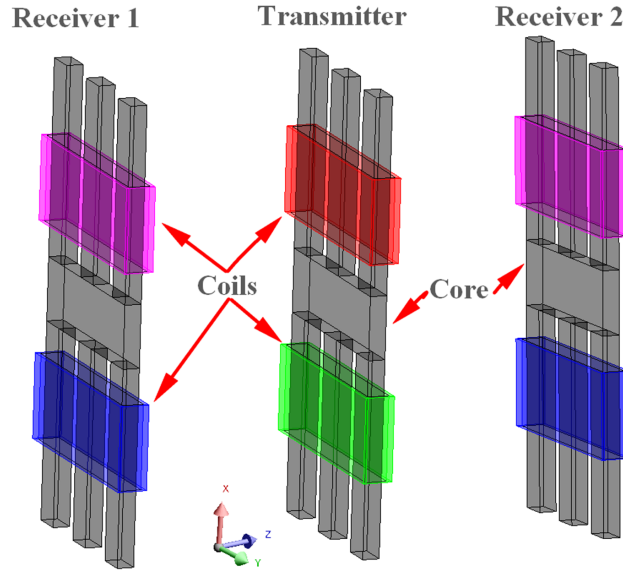
Figure 3.4: Proposed SPP pad configuration.

lower k_{12} and P_{su} values. However, the value of L_1 is approximately half when compared to the other configurations, reducing the value of P_{su}, according to (3.4). A higher P_{su} is achieved if more turns are added to the transmitter coils or if the working frequency is increased. The remainder pad configurations present large differences in magnitude of P_{su} and k_{12}, thereby, an optimal core design largely influences the flux lines orientation and the coupling between the transmitter and receiver sides. The core configurations 2 and 3 (Core 2 and 3) have lower coupling factors and uncompensated powers, when compared with the core configurations 1, 4 and 5. From the investigated core configurations, the Core 5 is the one that offers the best ratio $P_{su}/$Area, $P_{su}/$Ferrite and P_{su}. Assuming a receiver quality factor of 5, which is a valid assumption for EV IPT charging systems [100], the Core 5 is able to deliver approximately 18 kW with an air gap of 50 mm and without lateral displacements. This value drastically decreases for 6.8 kW for an air gap of 100 mm. In the presence of lateral displacements of 150 mm along the y axis, the value of P_{out} is 9.5 kW for an air gap of 50 mm and 3.6 kW for an air gap of 100 mm.

With a vertical charging system, the lateral tolerance is just critical in the axis of the pad parallel to the ground plane, since it is the one affected by the driver (axis y). The other axis corresponds to the vertical distance between the pad and the ground and it only suffers small displacements like different tire pressures in the EV. As seen by the results presented in Table 3.1, a variation of the air gap has more impact than a lateral displacement. On the other hand, conventional IPT charging systems would require a much larger surface area for the transmitter and receiver pads to transfer the same amount of power as the proposed
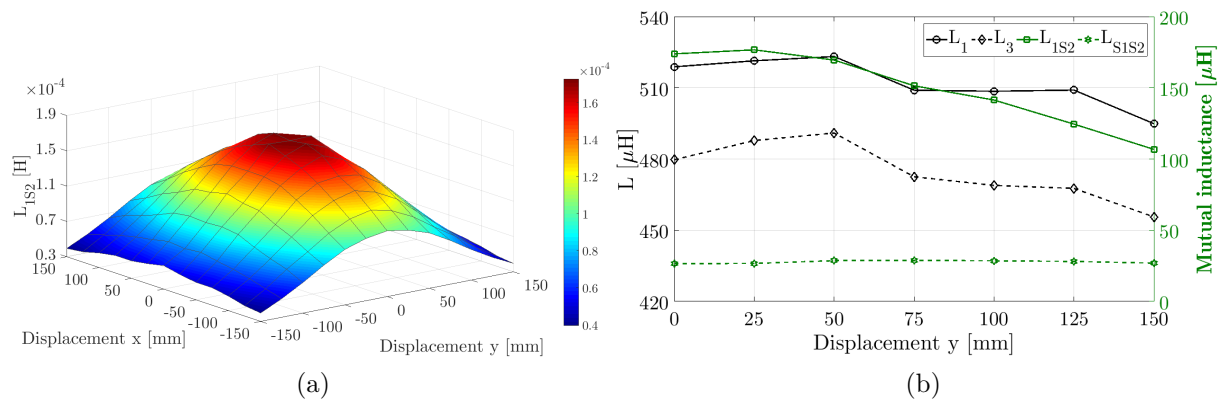
Figure 3.5: Profile of: (a) L_{1S2} and (b) self and mutual inductance values, as a function of lateral displacements for an air gap of 50 mm.

charging system, since the air gap with a vertical charging system is reduced. The Core 5 was chosen as a work basis pad configuration for further optimization in the following subsections.

3.2.1 Double-receiver SPP optimization

Figure 3.4 illustrates the 3D model of the proposed double-receiver SPP based IPT charging system. All the pads have the geometry of Core 5. The output power of each receiver pad is affected by the existing coupling between both receiver pads (L_{S1S2}). Ideally, this value should be zero or very close to it, in order to maximize the power transfer capabilities for each receiver. However, due to close proximity of both receivers with the transmitter pad, the coupling values can not be neglected. The self-inductance of each pad as well as the coupling between each receiver and the transmitter pad will be different than a conventional IPT system, due to the additional ferromagnetic material in the surroundings of each pad, increasing the values of the self and mutual inductance values. Figure 3.5(a) shows the profile of L_{1S2} for the second receiver with lateral displacements in the range ±150 mm in both axes and an air gap of 50 mm. The first receiver was placed at a distance of 50 mm, which is the worse scenario for the power transfer capabilities of each receiver. As expected, the profile of L_{1S2} depends on the direction of the displacement. The variation of L_{1S2} is steeper along the x axis due to the total decoupling of a transmitter coil in relation to the receiver coils.

Figure 3.5(b) represents the variation of the self and mutual inductance values of the transmitter and receiver 2 pads for an air gap of 50 mm. The value of L_1 has an increase of approximately 7 % when compared with the equivalent two-coil IPT charging system. The proximity with the ferromagnetic core of the receiver 1 leads to the increase of the

(a)   (b)
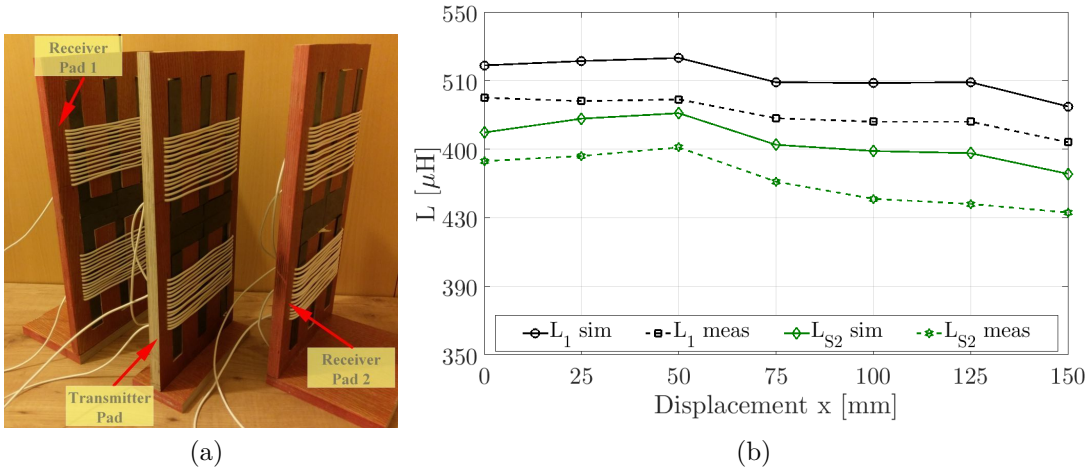
Figure 3.6: Practical assessment: (a) magnetic coupler with the dimensions of 372x242mm and (b) self-inductance measurements.

self-inductance of the transmitter pad. The variations of L_1 are more steeped in the event of lateral and air gap displacements, due to lower range for the air gap (50-150 mm), and must be accounted for during the design of the overall control. The coupling L_{S1S2} is another important factor which influences the output power of each receiver. Figure 3.5(b) depicts the curve of L_{S1S2} for lateral displacements. The variation is almost constant with a value of 22 μH and corresponds to a coupling factor (k_{S1S2}) of 0.04.

An experimental prototype was built to validate the proposed magnetic coupler, as shown in Figure. 3.6(a). The measured self-inductances L_1 and L_{S2} are shown in Figure 3.6(b). They present a maximum variation of 8%. The large difference is due to the small air gaps between the I-shaped ferrite bars and the different orientation of the ferrite core in the center, which are not considered in the simulation model. The difference between the simulation and practical results drops to a maximum of 2.8 % when small air gaps are introduced in the model, at the expense of longer simulation times.

3.2.2   Interoperability and Safety

The interoperability of a transmitter pad is a characteristic that indicates the coupling quality to other magnetic coupler geometries, both polarized and non-polarized. Higher coupling factors result in a better interoperable magnetic design. Figure 3.7 depicts k_{12} between the SPP transmitter and the DDP, BPP and CP geometries. The physical dimensions of the pads were ascertained using the optimizations made in [174, 183, 190] and all receiver pads have the same ferrite volume, for a fair comparison. The non-polarized shape of the magnetic field pattern of the circular pad is not fully interoperable with the polarized shape produced by the proposed solenoid pad due to the small ferrite area in the center of the
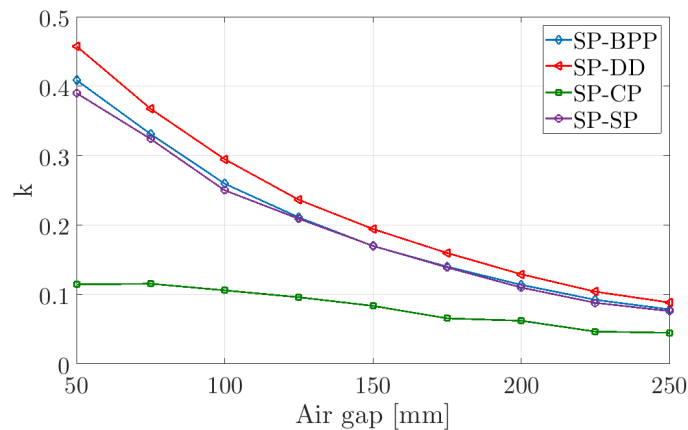
Figure 3.7: Coupling factor for different receiver designs.

proposed SPP, which does not couple the flux lines from the CP. However, the SPP coils can be driven separately in order to produce a non-polarized magnetic field pattern to couple with a CP receiver pad. Still, the coupling is much smaller when compared with the other pad configurations, as shown in Figure 3.7. The BPP and DDP pads produce polarized magnetic field patterns, hence the good coupling with the SPP transmitter pad. The DDP receiver pad offers the best coupling with a maximum value of 0.46 for an air gap of 50 mm. The area of the DDP is, however, 2.26 larger than the area of the SPP and the power density (P_{su}/dm^2) is smaller for the same dimensions. The BPP and SPP receiver pads have similar coupling factors, but with an area ratio of 1.87:1. The results represented in Figure 3.7 show the interoperability of the transmitter SPP with polarized geometries like the BPP and DDP pads. Also, the optimized SPP receiver pad offers better power density than the DDP and BPP when supplied by a SPP transmitter pad.

The compliance with the guidelines to human exposure of magnetic and electric fields has to be contemplated during the design. The International Commission on Non-Ionizing Radiation (ICNIRP) dictates that the general public should not be exposed to average RMS flux densities higher than 27 μT for frequencies of 85 kHz. Figure 3.8 shows the flux density levels along two planes, one parallel to the plane xoy and the other parallel to the plane xoz, and are equidistant of 500 mm from the geometric center of the magnetic coupler. A power of 6.3 kW is deliver to each receiver pad during the simulations with a RMS transmitter current of 20 A. The obtained results show flux density levels below the occupational limit in almost all charging area, except for a few localized points, as shown in Figure 3.8 by the colors above orange. An increase of the power transferred to 10 kW rises the minimum safe distance to 640 mm. On the other hand, when the air gap is increased to 150 mm and the power delivered corresponds to 6.3 kW, a minimum distance of 735 mm is required

(a)
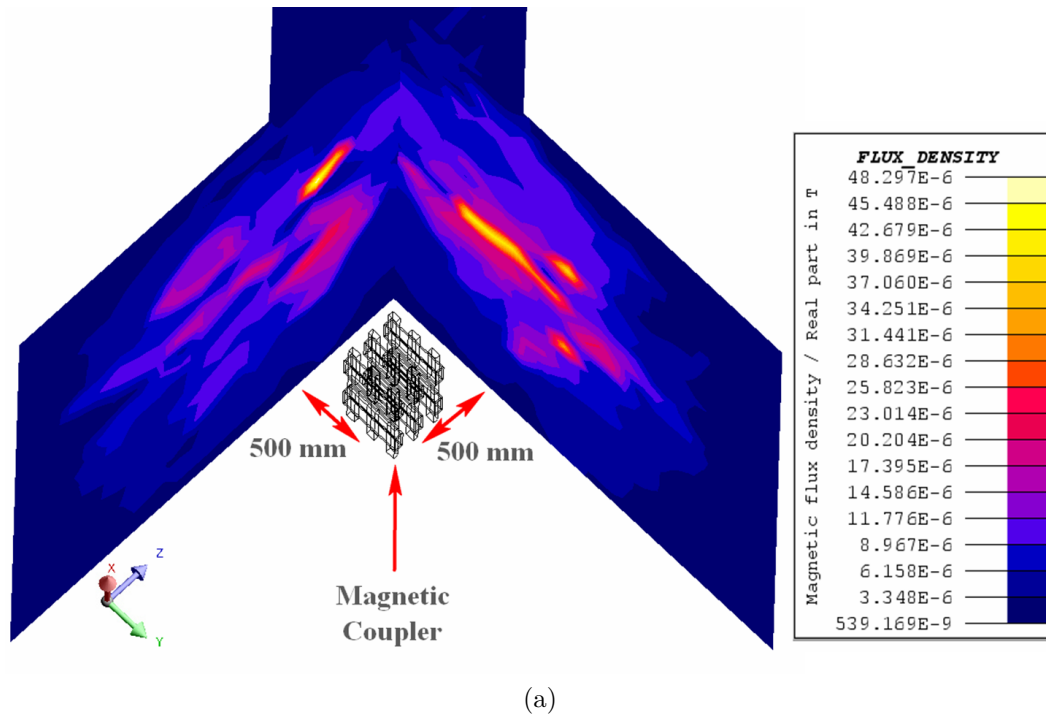
Figure 3.8: Distributed flux density levels at a distance of 500 mm.

for the magnetic coupler to comply with the occupational limits imposed by the ICNIRP guidelines, which corresponds to an increment of 26 % compared to an air gap of 50 mm. The aforementioned simulations do not consider an aluminum shield in the back of the receiver pads. An aluminum plate with 3 mm thickness decreases the stray magnetic fields in the *xoy* plane up to 30 %, at the expense of 14 % reduction in the coupling factor between the transmitter and receiver pads.

The minimum safety distances of the presented double-receiver SPP IPT charger are lower than traditional IPT systems. The works conducted in [174, 183] show minimum safe distances around 620 mm for CP-CP and DDP-DDPQ when transferring 2 kW. This means that a vertical charger reduces the air gap between the transmitter and receiver pads and power transferred almost triplicates within the same safe charging area. Moreover, risk of having small children or small animals between the transmitter and receiver pads is also mitigated, since the air gap is to narrow. Vertical IPT chargers also avoid the use of foreign object detection (FOD) systems to detect metallic objects between the transmitter and receiver pads [293, 294]. In summary, the presented double-receiver vertical IPT charger offers equivalent power transfer capabilities to traditional IPT charger while allowing a double charging scenario. In addition, the safety standards are met at lower distances and avoid the use of detection systems of children, animals and metallic objects.

3.3 Study of transmitter geometries for roadway applications

A distinct advantage of an IPT charger towards plug-in chargers is the ability to charge the vehicle in movement. As summarize in Chapter 2, dynamic charging systems can be formed by a continuous track or a set of discrete pads placed along the roadway. The second option offers better efficiency and controllability at the expense of higher material usage. One way to reduce the material costs of the transmitter pads is by removing the use of a ferromagnetic core. New ferrite-less designs were proposed in the literature including the Concrete Ferrite-less pad (CFLP) [195] and the circular non-ferrite pad (CNFP) [197]. The use of an intermediate coupler also boosts the magnetic link between the transmitter and receiver sides, resulting in an increase of the power transfer capabilities. Therefore, the study presented in this section investigates and models alternative transmitter pad geometries that do not require ferromagnetic cores as a function of both vertical and lateral displacements.

3.3.1 Modeling of transmitter geometries

The CP, BPP and DDP geometries were chosen as a work basis and their sizes along with the designation of certain optimization parameters are depicted in Figure 3.9 (a)-(c). The ferrite cores used in these designs were replaced by an intermediate coil(s) or a "pipe" coil that orients the flux lines in the back side of the transmitter pad. Figure 3.9 (d)-(f) shows the geometries with "pipe" coils and they are referred as Ferrite-less Circular Pad (FLCP), Ferrite-less Bipolar Pad (FLBPP) and CFLP, respectively. The geometries of the CP, BPP and DDP with intermediate coils are illustrated in Figure 3.9 (g)-(i) and they are designated as Intermediate Circular Pad (ICP), Intermediate Bipolar Pad (IBPP) and Intermediate Double-D Pad (IDDP).

The ferromagnetic core based geometries have the same ferrite volume, which corresponds to 16 N87 I cores with the dimensions of 93x28x16 mm. The coils were modeled with the same properties as the ones identified in Section 3.2. A lateral displacement between 0 and 250 mm was considered in intervals of 25 mm. The variables l_{tx} and l_{ty} denote the lateral displacements along the x and y axes. Air gap variations between 100 and 250 mm cover most of the ground clearance vehicles including SUVs and public transportation like buses. A total of 1446 simulations were conducted to assess all different possibilities and their impacts on the tolerance to lateral and vertical displacements as well as on the power

(a) Circular pad (CP)   (b) Bipolar pad (BPP)   (c) Double-D pad (DDP)

(d) Ferrite-less circular pad (FLCP) (e)   Ferrite-less   bipolar   pad (f) Concrete ferrite-less pad (CFLP)
(FPBPP)

(g) Intermediate circular pad (ICP) (h)   Intermediate   bipolar   pad (i)   Intermediate   Double-D   pad
(IBPP)   (IDDP)
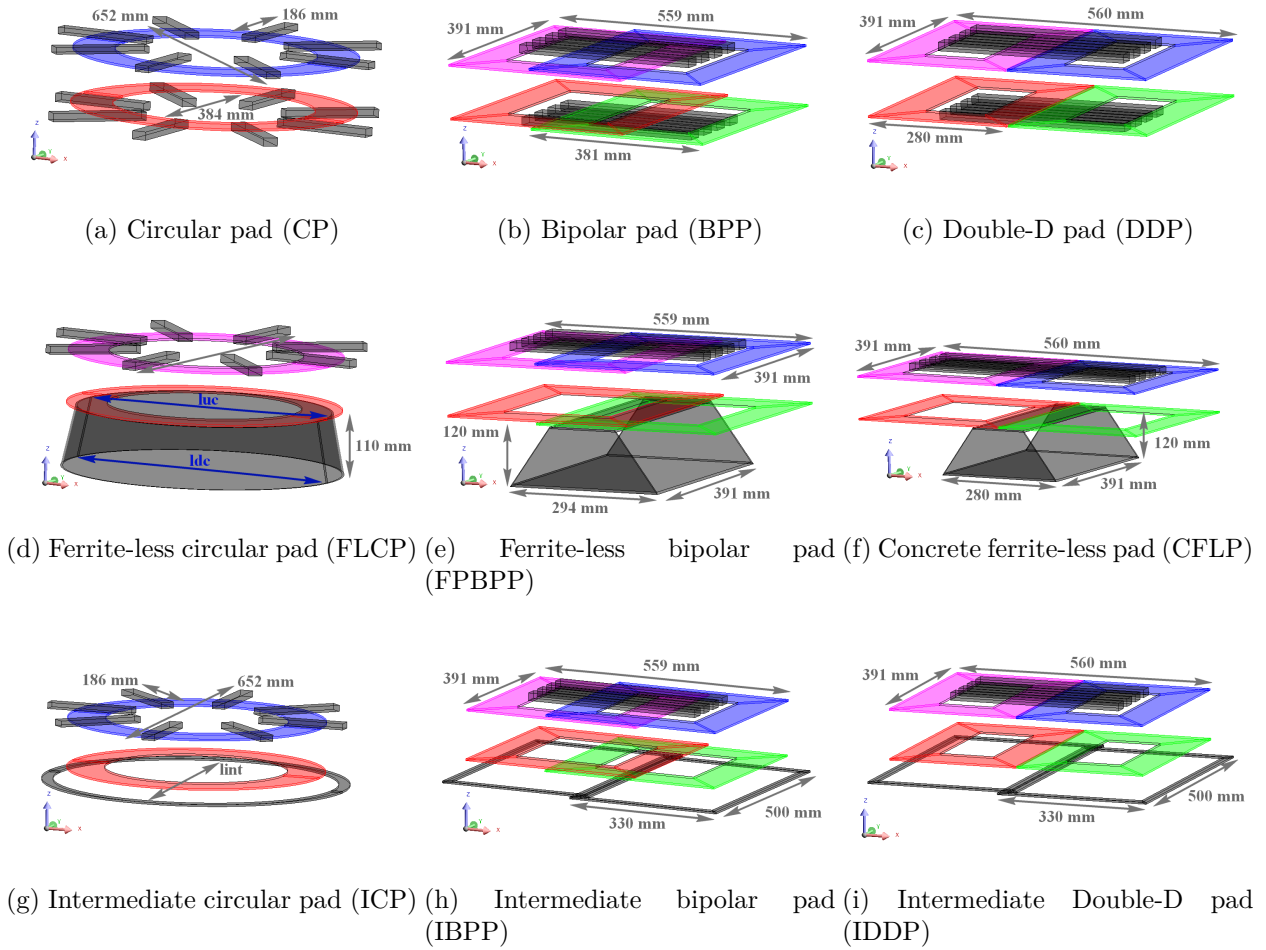
Figure 3.9: Portrayal of the modeled magnetic coupling structures.

transfer capabilities of the overall system.

The LCL compensation network was chosen for the transmitter resonant configuration since it exhibits load independent current source characteristics [116]. The second inductor of the LCL network is formed by the transmitter inductance (L_1). The sizing of the transmitter coils will take into account the maximum voltage levels admissible by the Litz wire, thus limiting the value of L_1 and avoiding the use of additional capacitors to reduce the "extra" inductance. The power supply operates at 20 kHz. The parallel compensation was chosen for the receiver side in order to evaluate the P_{su} for a three-coil IPT system.

The "pipe" coils of the FLBPP and CFLP were sized using the improvements made in [195]. The height and inclination of the pipe coil were 120 mm and 43°, respectively. Each pipe coil is wounded with 22 turns. In the case of the FLCP, several simulations were made to investigate the optimal size. Figure 3.10 shows the variation of the upper (luc) and lower (ldc) diameters of the pipe coil with a transmitter coil radius of 190 mm. The results show that larger diameters improve the coupling factor. The point (250 mm, 275 mm) was
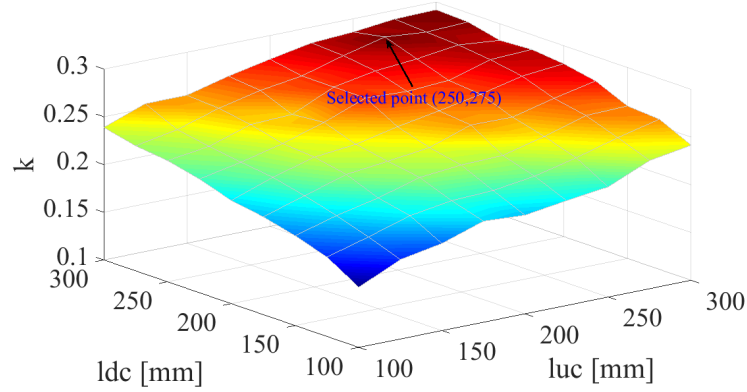
Figure 3.10: Coupling profile of FLCP for different pipe coil size arrangements.

(a) Circular pad   (b) Bipolar pad   (c) Double-D pad
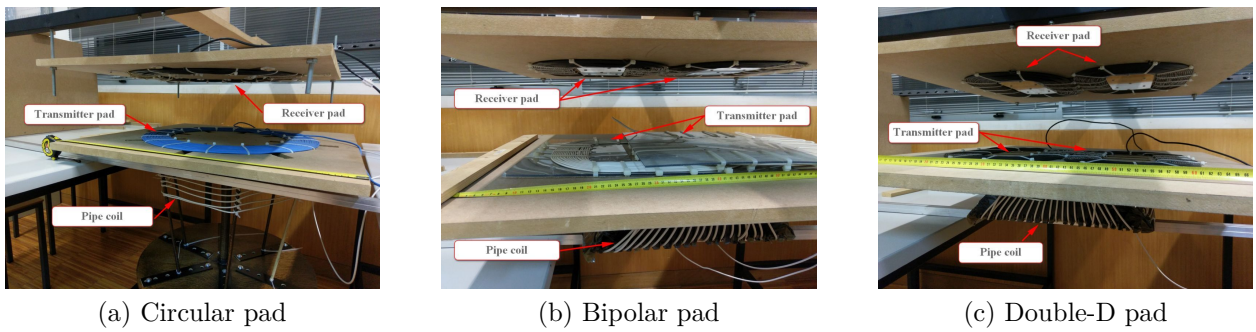
Figure 3.11: Developed prototypes of the transmitter pads with and without ferromagnetic cores.

selected as the optimal diameters for the pipe coil since larger diameters require more copper with little improvement in the coupling factor. The height of the pipe coil and the number of turns was also investigated. A height of 110 mm with 8 turns offers a good compromise between cost-effectiveness and efficiency.

(a)   (b)   (c)
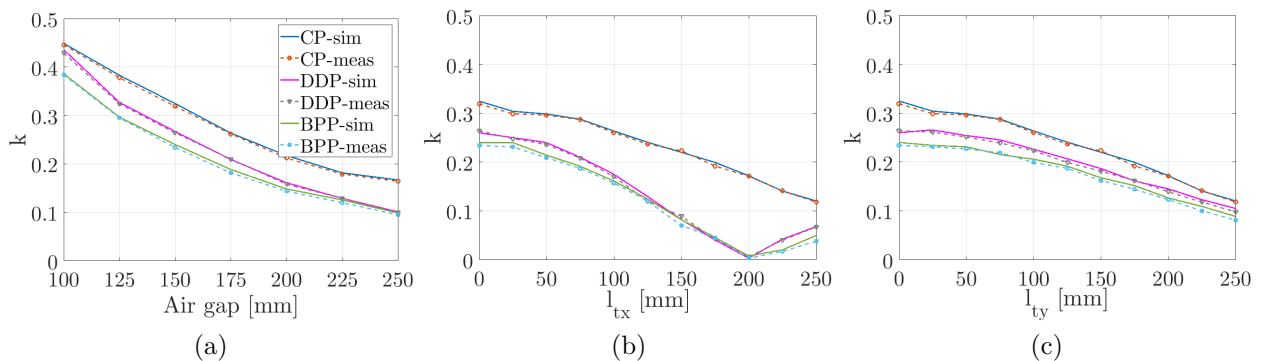
Figure 3.12: Coupling factors of the ferrite transmitter pads as a function of: (a) air gap, (b) lateral displacement along the x axis and (c) lateral displacement along the y axis.

Several prototypes were built to validate the 3D simulated models and they are depicted in Figure 3.11. Figure 3.12 shows the simulated and measured coupling factors for ferrite transmitter pads as a function of air gap and lateral displacements. Each transmitter pad
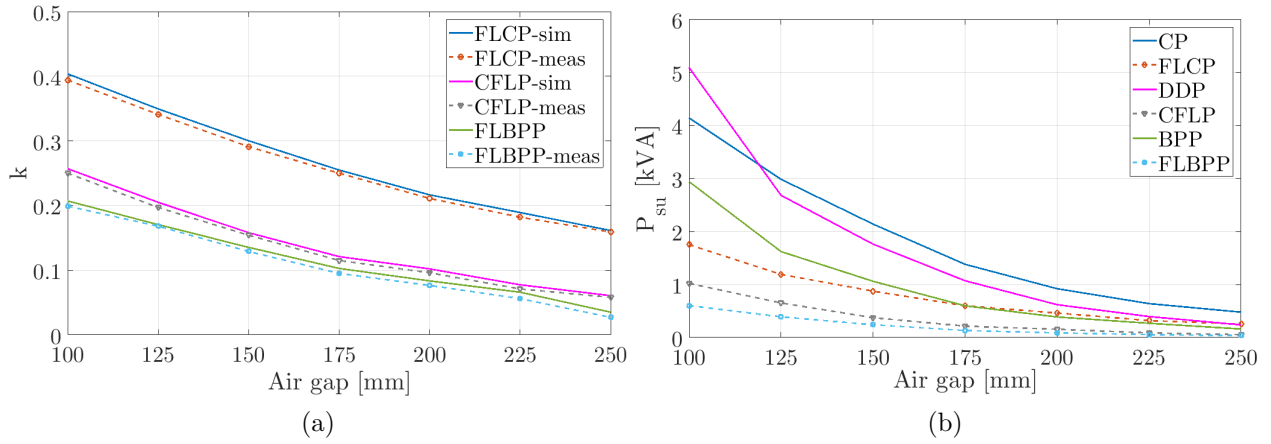
Figure 3.13: (a) Coupling factor and (b) uncompensated power of "pipe" coil transmitter geometries as a function of air gaps.

is coupled with a receiver pad with the same geometry and size, as illustrated in Figure 3.9. A maximum variation of 1.5 % was found between the simulated and experimental measurements. The CP has a higher k_{12} but its surface area is approximately one third larger than the DDP and BPP. As expected, lateral displacements along l_{tx} exhibit a null k_{12} around 200 mm for DDP and BPP due to the total decoupling of one of the two main coils that form the transmitter pads. On the other hand, the circular geometry exhibits the same pattern along both l_{tx} and l_{ty} directions due to its circular shape.

Figure 3.13 compares the values k_{12} and P_{su} of the ferrite pads with the geometries with pipe coils for different air gaps. The results show a decreasing in k_{12}, which is accentuated for the CFLP and FLBPP. In the case of the CFLP, the results are in agreement with the ones obtained in [195]. For air gaps up to 225 mm, k_{12}, for all transmitter pads, is within a reasonable range for a efficient power transfer. For higher air gaps, with the same dimensions, only the FLCP presents coupling characteristics for an efficient power transfer. The transmitter pads with pipe coil have lower P_{su} values, however, for an air gap of 150 mm and assuming a operational Q of 5, all transmitter pads enable the transfer of 1 kW.

Figure 3.13 (b) compares the P_{su} for different air gaps at a rated transmitter current of 20 A. The large values of P_{su} for the ferrite transmitter pads are related with the higher L_1 and k_{12} values, parameters which affects P_{su}, as seen in equation (4.18). The values of L_1 for all ferrite pads are in the range of 412-518 μH. At the rated value of $|\overline{I}_1| = 20$ A, the voltage level at the transmitter coil terminals would surpass the safety value of 1 kV imposed by the Litz wire manufacturer and SAE J2954 directives. Also, at higher working frequencies, the value of L_1 must be lower by reducing the number of turns in the transmitter coil(s). This power level can be maintained by the FLCP for air gaps superiors to 250 mm.
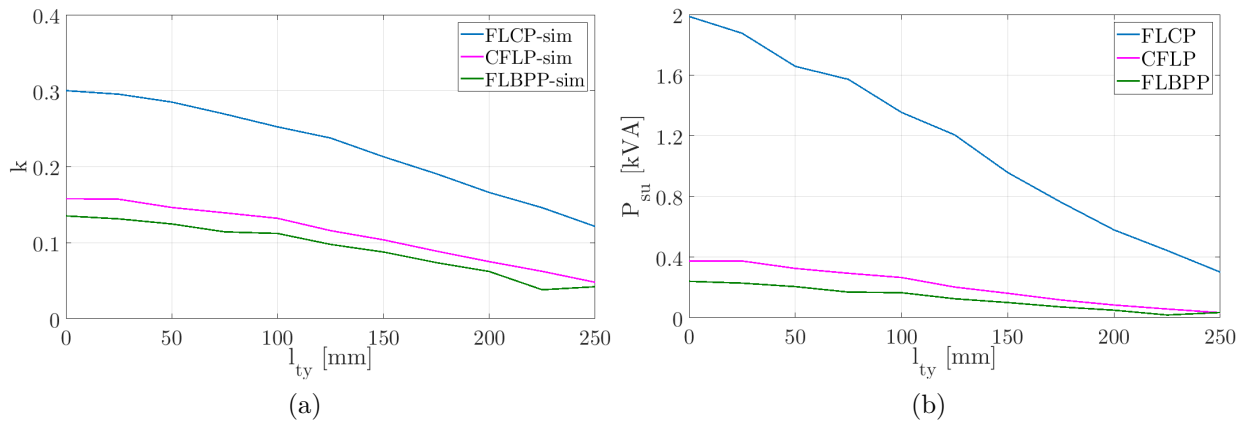
Figure 3.14: (a) Coupling factor and (b) uncompensated power of "pipe" coil transmitter geometries as a function of lateral displacements for an air gap of 150 mm.

In terms of lateral displacements, the FLCP has a higher power transfer capability with better coupling, as seen in Figure.3.14. However, and despite the higher power transfer capability of the FLCP, represented in Figure 3.14(b), the variation of P_{su} is more abrupt when compared with the CFLP or FLBPP and needs to be taken into account during the design of the controller in order to keep the same output power levels during displacement scenarios. From the results shown in Figure 3.13 and Figure 3.14, with the studied sizes, the FLCP is the transmitter pad that offers the best cost-efficiency relation, with transfer power capabilities in same order of magnitude of ferrite pads for air gaps above 200 mm.

The evaluation of the power transfer capabilities of a three-coil system is more complicated than a two-coil system, due to its dependency on some intermediate coupler parameters mainly the value of $|\overline{I}_{int}|$, which depends on the resonance frequency between C_{int} and L_{int}. For a correct assessment of P_{su}, the FEA simulation results were inserted in the software Matlab/Simulink to evaluate the overall efficiency of the IPT system using the parallel configuration on the transmitter and receiver sides. Firstly, it is necessary to evaluate the self and mutual inductance profiles between all three coils in order to determine the remaining elements of the IPT circuit. Figure 3.15(a) shows the coupling factors for different intermediate coil diameters ($lint$) in the ICP geometry, assuming a height of 30 mm between the transmitter and intermediate coils. The results show a decrease in k_{1int} at higher diameters while k_{12} and k_{int2} retain approximately the same values. The large disparity between L_{int} and both L_1 and L_2, is an important aspect because influences the output power transfer capability of each term in (3.12). The value $lint = 600$ mm was chosen as a study basis for the subsequent results presented in this section. Figure 3.15(b) depicts the profile of P_{su}, based on (3.12), for different values of $|\overline{I}_1|$ and $|\overline{I}_{int}|$. As seen in Figure 3.15(b), the
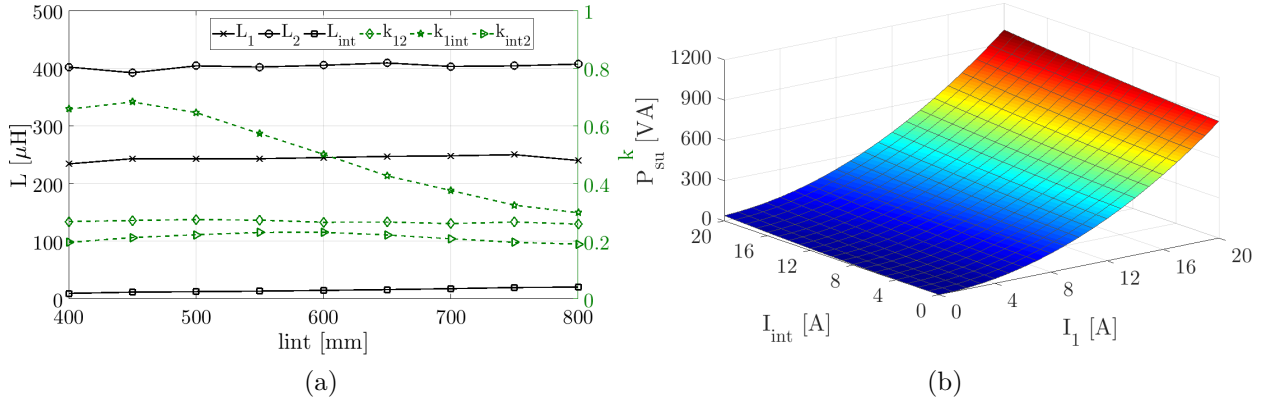
Figure 3.15: (a) Parameters of three-coil systems for different intermediate diameters and (b) profile of P_{su} for different $|\overline{I}_1|$ and $|\overline{I}_{int}|$ values.
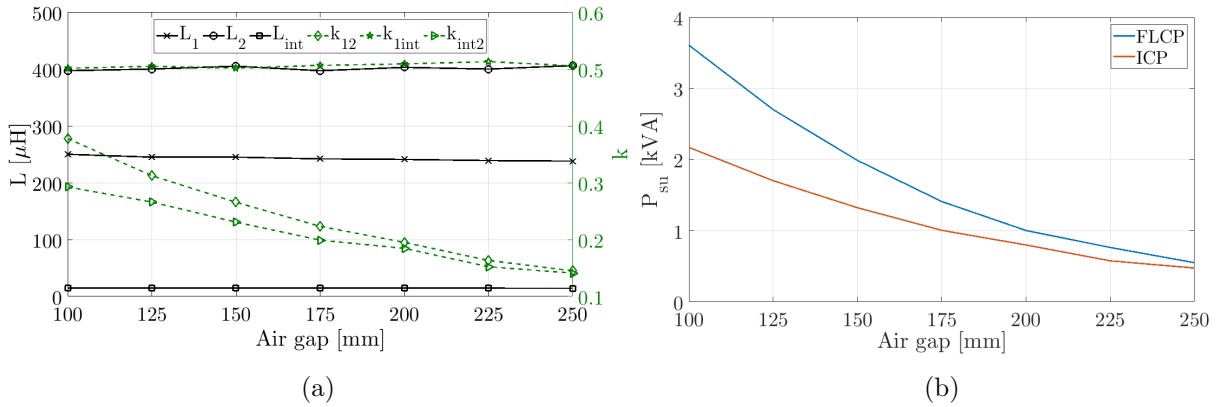
Figure 3.16: (a) Parameters of three-coil systems for ICP geometry and (b) profile of P_{su} as a function of air gap for different circular geometries.

first term of (3.12) ($\omega.k_{12}.I_1^2.L_1$) has the higher contribution for P_{su}, see the quadratic curve when $|\overline{I}_{int}|=0$. On the contrary, the second term of (3.12) is the one that less impacts the value of P_{su}. For example, a $|\overline{I}_1|$ and $|\overline{I}_{int}|$ equal to 10 A, the P_{su} is 250 VA and only 33 VA corresponds to the second and third terms. For the current design is then important to have high values of $|\overline{I}_1|$ to transfer large power levels. Figure 3.16(b) compares the P_{su} between the ICP and FLCP. The value of the P_{su} for the ICP was obtained through simulation of the equivalent circuit in Simulink and assuming a constant $|\overline{I}_1|=20$ A. The power transfer capability of ICP is lower than the FLCP. However, the difference of P_{su} between both pads decreases for higher air gaps. Also, the tuning frequency of the intermediate coupler impacts directly in the value of the reflected reactance, increasing or decreasing the P_{su} of the overall system. In this test, the natural resonant frequency of the intermediate coupler is 1.5 times higher than the inverter switching frequency. Figure 3.16 illustrates the variation of the self and mutual inductance values of the ICP for different air gaps.

Similar analysis is made for the DDP and BPP with intermediate couplers. To main-
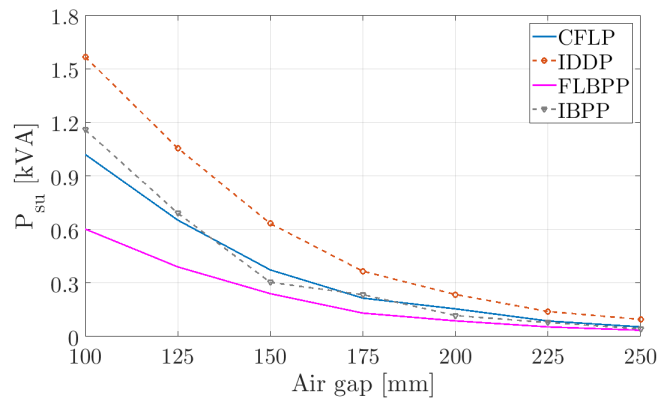
Figure 3.17: P_{su} as a function of air gaps for different ferrite-less geometries.

tain the interoperability of the DDP and BPP transmitter pads, two mutually decoupled intermediate couplers are place under the transmitter pad, as represented in Figure 3.9(h) and Figure 3.9(i). Figure 3.17 compares the values of the P_{su}. The intermediate coupler boosts the coupling between the transmitter and receiver (k_{12}), resulting in an increase of the contribution associated to the first term in (3.12).

In conclusion, ferrite-less geometries have reasonable power transfer capabilities and they are not constrained as ferrite geometries. The presented FLCP exhibits comparable coupling profiles to the CP, especially at high air gap values. The intermediate designs, on the other hand, have slightly lower P_{su} values but the intrinsic characteristics of three-coil systems make them ideal for dynamic IPT applications.

3.4 Mapping Methodology

The self and mutual inductance profiles in MCs are affected by the vertical and lateral displacements of the receiver pads and the number of turns in each coil that forms the MC. As a consequence, the power transfer capability depends on these parameters, for a given geometry and size. This means that the IPT specifications and constraints define the minimum self and mutual inductance admissible values, and a mapped geometry would simplify the design process. For example, an automotive manufacturer with a standardized geometry and size will have different specifications for vehicles with different classes and the geometry has to exhibit different magnetic properties for each class.

To avoid low coupling charging scenarios, optical positioning systems are usually employed to optimize the positioning of the receiver pad. Additionally, wireless communication between the off-board and the vehicle's side is often required to exchange information regarding batteries status and vehicle positioning. New mutual inductance and load estimation

algorithms have been presented in the literature using only measurements from the off-board side [154, 255, 295, 296]. Such algorithms, together with a mapped geometry, can be used as a guiding positioning system, thus eliminating the use of optical sensors.

Self and mutual inductance profiling as a function of different vertical and lateral displacements is usually performed using mathematical models or FEA tools. However, the mathematical models [297–300], are usually valid for a specific coil geometry and core arrangement, which limits the study of new MC geometries. FEA tools, on the other hand, offer unconstrained design capabilities [301–303]. The authors in [304] present a framework that evaluates different transmitter and receiver pad sizes in different charging positions and at different output powers using the DDP. The framework combines the mathematical model of an IPT system with the self and mutual inductance profiles of the MC obtained through a FEA tool. A total of 11648 FEA simulations were required to extract the profiles of the MC with a fixed number of turns in each coil. However, the computational effort and time consumption drastically increases if different turns arrangements are considered. On the other hand, a reduce order model that determines the coupling relation between the transmitter and receiver pads with minimum FEA simulations is present in [305]. The model, however, does not specify its applicability to three-coil systems as well as the relation between different number of turns in each coil. Therefore, a new mapping methodology for self and mutual inductance profiles for static IPT systems with a reduced computational effort is presented in this section.

3.4.1   Characterization of MC

This subsection explains the curve fitting based method that minimizes the number of FEA simulations required to create the self and mutual inductance profiles as a function of air gap ($airgap$), lateral displacement (l_t) and N_x.

3.4.1.1   Mutual inductance profiling

The mutual inductance quantifies the flux link between two magnetically coupled coils. This link is affected by the relative position of the coils but also by the number of turns in each coil. Two-coil IPT systems only have one mutual inductance (L_{12}) between the transmitter and receiver coils. On the other hand, three-coil systems have two additional mutual inductance values besides L_{12}: L_{int2} and L_{1int}. In three-coil IPT systems, the intermediate coil is placed in the same enclosure as the transmitter coil [148, 149, 198] and for that reason, the pattern of L_{1int} is unaffected by air gap and lateral displacements of the receiver coil,

especially in ferrite-less designs. On the other hand, the profile of L_{1int} as a function of the number of turns is identical to the profiles of L_{12} and L_{int2} in the same conditions and it will be explained later in this section.

The profiles of L_{12} and L_{int2} for different air gap, lateral displacement and set of turns values are identical in both three-coil and two-coil systems and they are illustrated in Figure 3.18. The colored areas show the effect of having different set of turns in the coils. The upper and lower boundary lines of the green and blue areas are determined for pair of turns ($N_{x_{max}}$ and $N_{y_{max}}$) and ($N_{x_{min}}$ and $N_{y_{min}}$), where x and y denotes the side of the respective coil: transmitter (1), receiver (2) and intermediate (int). The values of $N_{x_{min}}$ and $N_{y_{min}}$ are set to 1 while $N_{x_{max}}$ and $N_{y_{max}}$ are limited by the availability of space in the MC or by electric restrictions like maximum induced voltage at the coils terminals. The plots depicted in Figure 3.18 were obtained through several FEA simulation results and they are in compliance with the existing literature for both polarized and non-polarized pads [174, 176, 183, 197, 198]. Figure 3.18(a) shows the effect of air gap variations in L_{12} and L_{int2} and, for a given set of turns, it follows an exponential decay function given by

$$L_{xy}(airgap) = a_e . e^{b_e . airgap}, xy = 12 \quad or \quad xy = int2 \tag{3.13}$$

where a_e and b_e are constants that depend of N_x, N_y and $airgap$.

Similarly, the impact of l_t variations is identical across L_{12} in two-coil systems and L_{12} and L_{int2} in three-coil systems. The pattern of l_t, unlike the $airgap$ pattern, may differ along the x and y axes due to the shape of the MC and to its flux lines orientation (polarized or non-polarized MCs). Thus, Figure 3.18(b) illustrates the behavior of L_{12} for different lateral displacements along the y axis (l_{ty}) with different set of turns for a circular shaped MC like the FLCP and a polarized pad like the BPP. The behavior of L_{12} as a function of lateral displacements along the x axis (l_{tx}), with different set of turns, is depicted in Figure 3.18(c) for the BPP. Circular MC designs have the same behavior along the x and y axes and they only need to be characterized along one axis. The polarized pads have in turn distinct behaviors along both axes due to the total decoupling of one coil along the x axis, which corresponds to the inflection point of L_{12}, shown in Figure 3.18(c). Nevertheless, and up to the inflection point, all patterns of L_{12} or L_{int2} can be approximated using a Gaussian function defined as

$$L_{xy}(l_t) = a_g . e^{-((l_t - b_g)/c_g)^2}, xy = 12 \quad or \quad xy = int2, \tag{3.14}$$
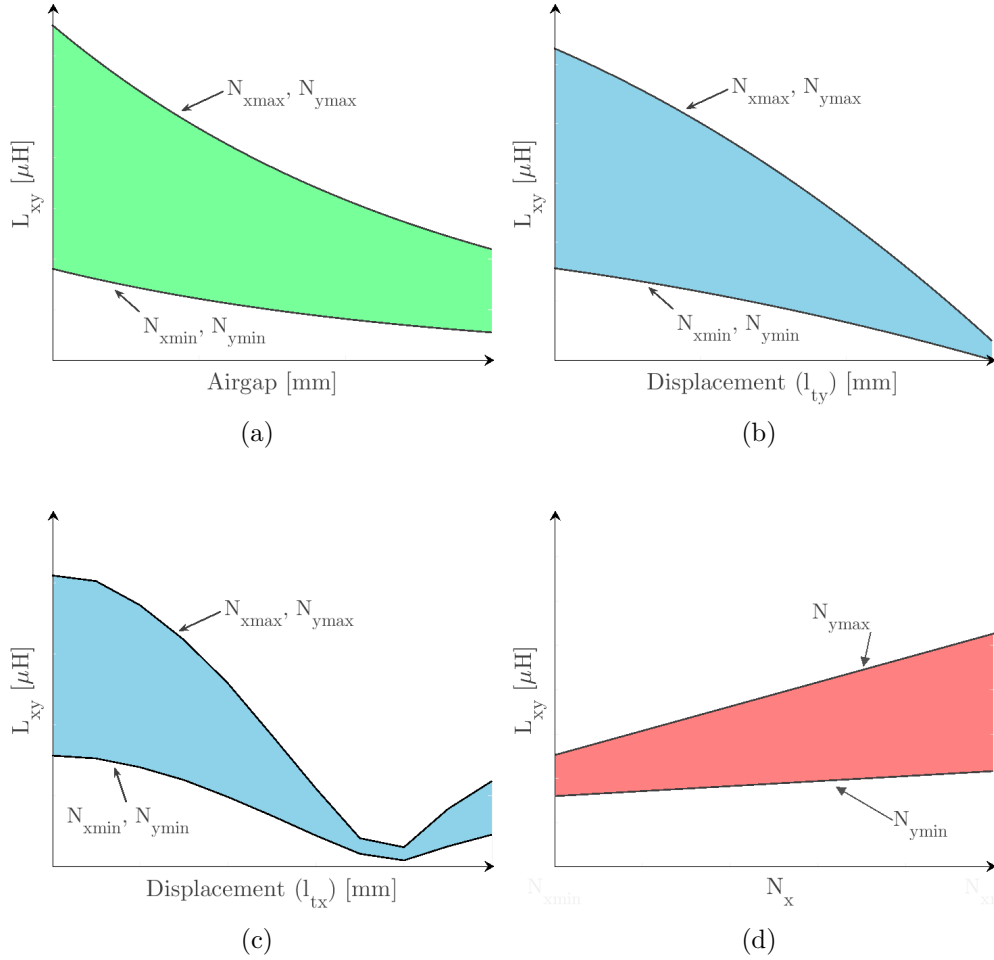
Figure 3.18: Profiles of L_{12} as a function of: (a) *airgap*, (b) lateral displacement along the x axis (l_{tx}), (c) lateral displacement along the y axis l_{ty} and (d) number of turns (N_x).

where a_g, b_g and c_g are constants that depend of N_x and l_t.

The set of turns in two mutually coupled coils also affect the value of the mutual inductance, as illustrated by the colored areas in Figure 3.18(a)-(c). At a given *airgap* and t_t charging position, the value of the mutual inductance exhibits a linear variation, described in (3.15), if one coil is set with a fixed number of turns (value set between N_{ymin} and N_{ymax}), while the other coil is winded between $N_{x_{min}}$ and $N_{x_{max}}$, as depicted in Figure 3.18(d).

$$L_{xy \to N_y}(N_x) = a_l . N_x + b_l, \tag{3.15}$$

where a_l and b_l correspond to the slope and intersect, respectively.

Figure 3.19 shows the volume of L_{12} and L_{int2} as a function of *airgap*, l_t, N_x and N_y for the FLCP. The proposed approach takes advantage of the identified patterns, represented in Figure 3.18, to minimize the number of required FEA simulations needed to create the volume in Figure 3.19.
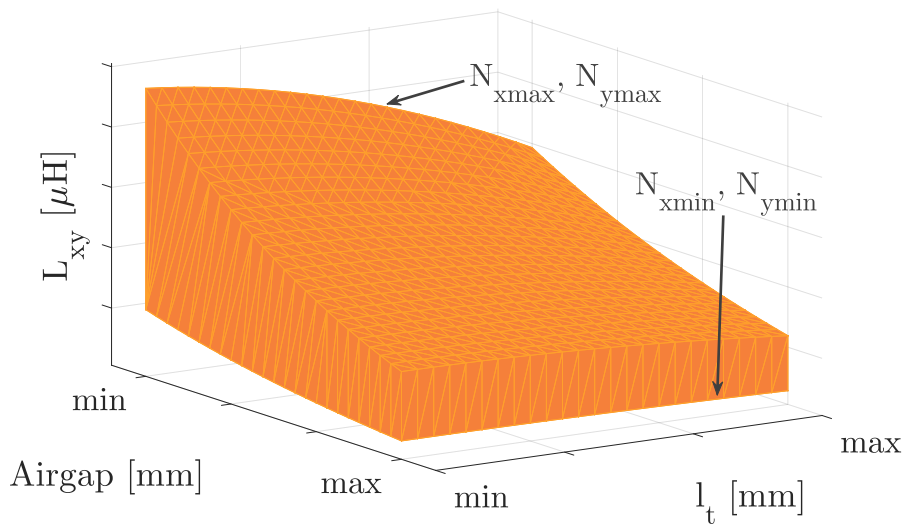
Figure 3.19: Volume of L_{xy}=f$(N_x, N_y, airgap, l_t)$.

3.4.2   Methodology

The proposed methodology builds the profile $L_{xy} = f(N_x, N_y, airgap, l_t)$ via an iterative way by varying one or two variables, like $L_{xy} = f(airgap)$ or $L_{xy} = f(N_x, N_y)$, while the remaining variables are kept constant. The unknown parameters of functions (3.13), (3.14) and (3.15) that model the effect of $airgap$, l_t and N_x, can be found using FEA simulation results. The total number of FEA simulation results required by the proposed approach will vary with the number and type of unknown variables. For example, a full characterization of a circular shaped MC has four unknown variables $(N_x, N_y, airgap, l_t)$ while the remaining MCs have five unknown variables since l_t splits into l_{tx} and l_{ty}. Also, the FEA simulation conditions differ according to the unknown variable. This work introduces the terms *Scenario* and *Pos* to differentiate positioning parameters like $airgap$ and l_t from construction parameters like set of turns in FEA simulations.

The term *Pos*, short for position, corresponds to a specific charging location with a given $airgap$ and l_t values. In each *Pos*, if the set of turns is unknown, the proposed approach needs to simulate additional *Scenarios*. Therefore, a *Scenario* accounts for a FEA simulation in the same *Pos* but with a different number of turns in each coil.

The effect of the number of turns, in one coil, can be modeled using (3.15), as depicted in Figure 3.18(d). The characterization of $L_{xy} = f(N_x, N_y)$, in a fixed charging position, can
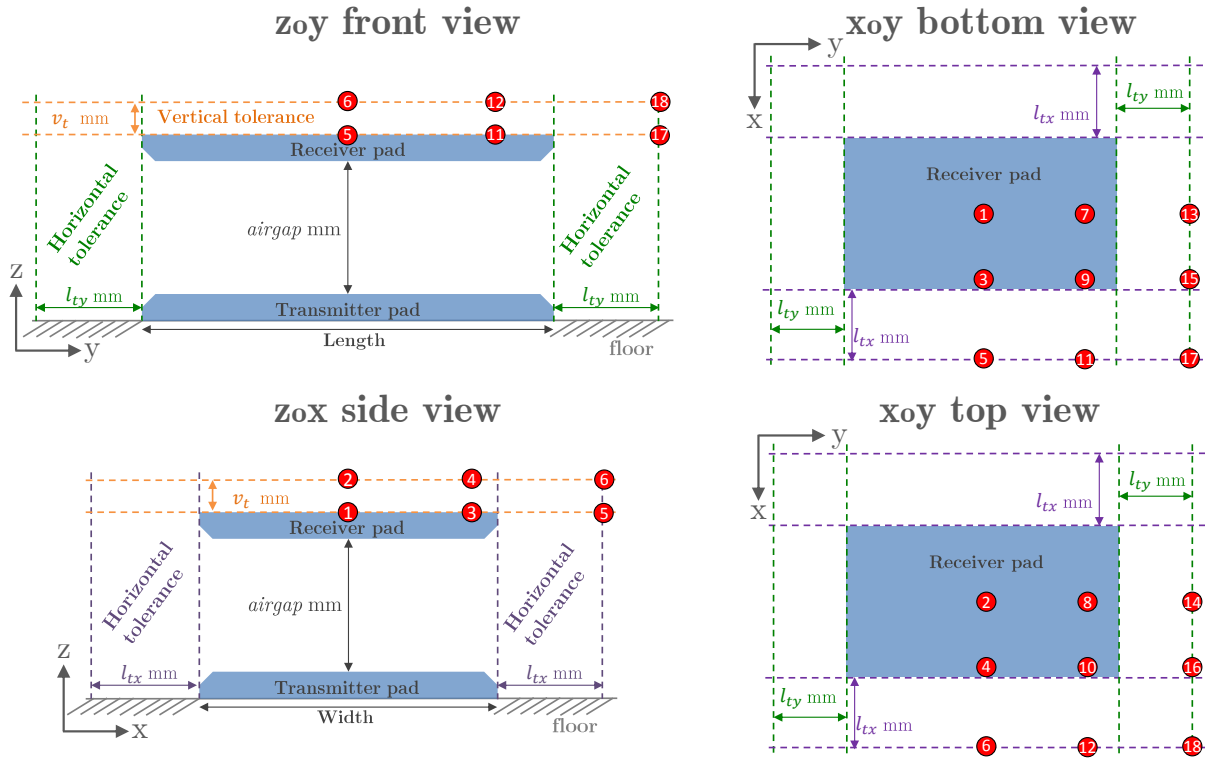
Figure 3.20: Operation area of the magnetic coupler.

then be made with resource to, at least, four *Scenarios* results given by

$$
\begin{aligned}
&Scenario\ A \rightarrow N_x = N_{x_{min}}, N_y = N_{y_{min}} \\
&Scenario\ B \rightarrow N_x = N_{x_{max}}, N_y = N_{y_{max}} \\
&Scenario\ C \rightarrow N_x = N_{x_{min}}, N_y = N_{y_{max}} \\
&Scenario\ D \rightarrow N_x = N_{x_{max}}, N_y = N_{y_{min}}.
\end{aligned}
\tag{3.16}
$$

These scenarios correspond to the four combinations between the maximum and minimum turn numbers. An identical approach is carried out for $L_{xy} = f(airgap)$ and $L_{xy} = f(l_t)$ (both l_{tx} and l_{ty}), depicted from Figure 3.18(a) to Figure 3.18(c). The first profile is extrapolated from an exponential decay function whereas the second and third profiles are found using a Gaussian function. The minimum number of points required to find the constant parameters in (3.13) and (3.14) are two and three, respectively. In other words, a minimum of two *Pos* results are needed to characterize $L_{xy} = f(airgap)$ and a minimum of three *Pos* results to identify $L_{xy} = f(l_t)$.

Figure 3.20 shows the operation area of an IPT system seen from different observation planes. The characterization of $L_{xy} = f(airgap, l_{tx}, l_{ty})$ is made with the FEA results from specific *Pos*, identified in Figure 3.20 with red numbered circles between 1 and 18. Circular

Table 3.2: Minimum number of *Scenario* and *Pos* that characterize L_{xy}.

MC	*Pos*	*Scenario*
N_x known		
CP	6	1
BPP	18	1
FLCP	6	1
N_x unknown		
CP	6	4
BPP	18	4
FLCP	6	6

shaped MCs only need six *Pos*, like *Pos* 1 to *Pos* 6, as depicted in $z_o x$ side view. The remaining twelve *Pos* are a consequence of different lateral displacements along x and y axes in non-circular shaped MCs, like the BPP. The profiling of L_{xy} as a function of the turns increases the total number of FEA simulations by a factor that corresponds to the number of *Scenarios*. For example, the CP requires only one FEA simulation result in each *Pos* if the number of turns is known. On the other hand, if the number of turns is unknown, the number of FEA simulation results in each *Pos* increases from 1 to 4, which corresponds to the number of *Scenarios*. Table 3.2 identifies the minimum number of *Pos* and *Scenarios* for different MCs. In short, after identifying the *Scenarios* and *Pos*, the following approach is applied :

1. **Profile of $L_{xy} = f(N_x, N_y)$**: Figure 3.21 illustrates the surface of $L_{xy} = f(N_x, N_y)$ with a fix value of *airgap* and l_t, using the FEA results from *Scenario* A to *Scenario* D, identified by the alphabetic numbered green squares. Figure 3.21(b) depicts a 2D plane, view from the N_x axis of Figure 3.21(a). The value of L_{xy} for specific values of N_x and N_y, exemplified by the red dot labeled as *Point* L_{xy} in Figure 3.21(b), can be identified by either linear functions $L_{xy}(N_x)$ or $L_{xy}(N_y)$, illustrated by the red dashed lines, which intersect at the desired L_{xy} value. The slope and intercept of $L_{xy}(N_x)$ are determined using points P_1 and P_2. The values of P_1 and P_2 are obtained using line equations $L_{xy \to N_{xmin}}(N_y)$ and $L_{xy \to N_{xmax}}(N_y)$ for the desired N_y, respectively. The desired value of L_{xy} is then found using equation $L_{xy}(N_x)$ for the desired N_x. This process is repeated $(N_{xmax} - N_{xmin}) * (N_{ymax} - N_{ymin})$ times to create the surface illustrated in Figure 3.21(a). The profiling of $L_{xy} = f(N_x, N_y)$ is replicated for all charging positions *Pos*.

2. Replace N_x and N_y with desired values in surface function $L_{xy} = f(N_x, N_y)$, determined in step 1, and repeat the process for all simulated *Pos*. The new values of L_{xy} already take into consideration the effect of the selected set of turns;
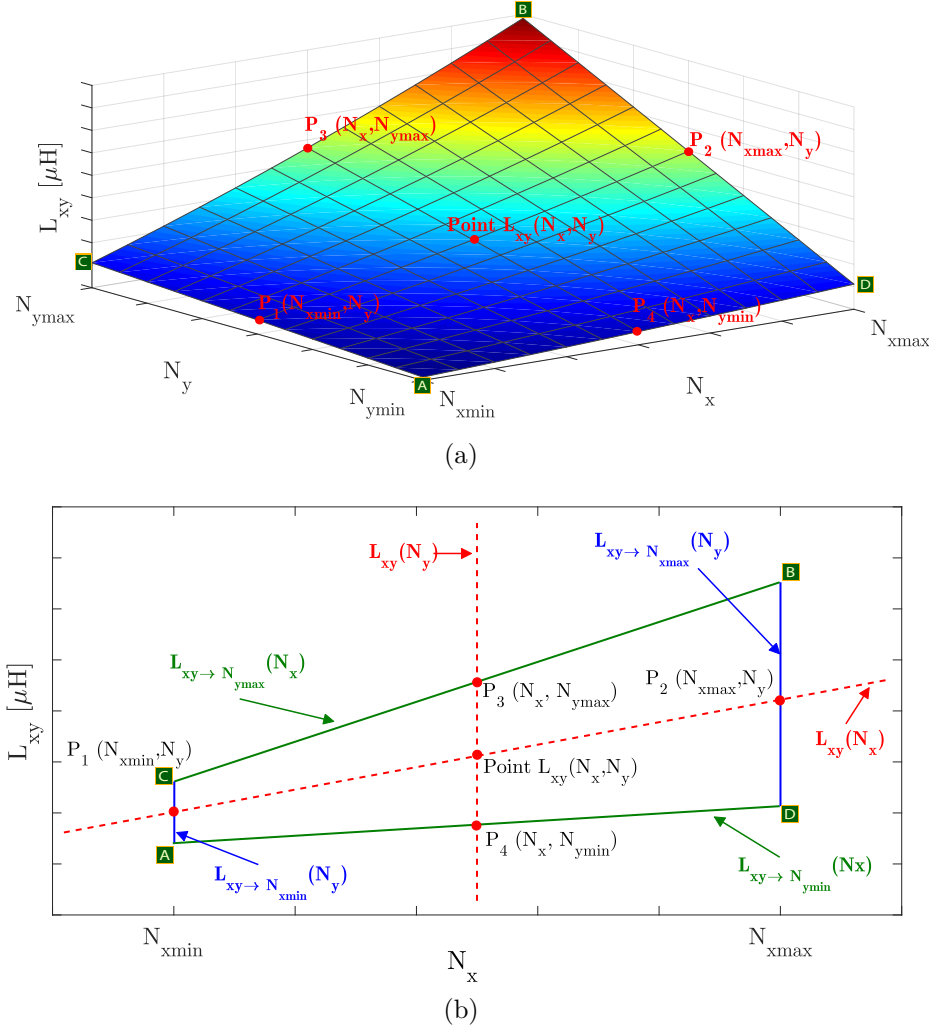
Figure 3.21: L_{xy} as a function of N_1 and N_2 in: (a) 3D view and (b) N_1 axis side view.

3. **Profile of $L_{xy} = f(airgap)$**: Use the values found in Step 2 for *Pos* 1 and *Pos* 2 to determine the constants a_e and b_e in (3.13). Repeat the process for the remaining *Pos* with the same lateral displacements but different air gap values, i.e, (*Pos* 3, *Pos* 4), (*Pos* 5, *Pos* 6), ... , (*Pos* 17, *Pos* 18). A total of three equations are determined for circular shaped MCs and nine equations for non-circular MCs. The equations are identified from *Exp*1 to *Exp*9 in Figure 3.22(a);

4. Replace *airgap* in equations *Exp*1 to *Exp*9 with the desired value to determine L_{xy} in points P_{x1} to P_{x9}, as illustrated in Figure 3.22(a). The new L_{xy} values take into account the effect of the selected set of turns and air gap values;

5. **Profile of $L_{xy} = f(l_{tx})$**: Use the values found in Step 4 that have the same *airgap* and l_{ty} values, like P_{x1} to P_{x3}, to determine the Gaussian constants a_g, b_g and c_g in (3.14). Repeat the process (if applicable) for the set of points P_{x4} to P_{x6} and P_{x7} to P_{x9}. A total of one or three equations are determined according with the shape of
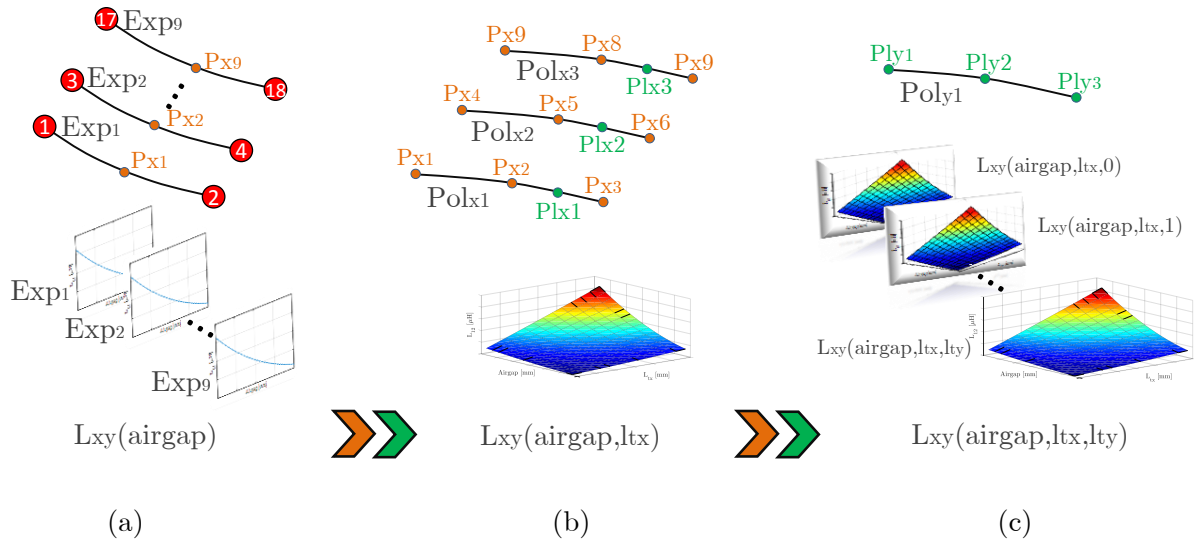
Figure 3.22: Illustration of the fitting methodology of $L_{12} = f(airgap, l_{tx}, l_{ty})$.

the MC. Circular shaped MCs are only evaluated in relation to l_{tx} or l_{ty} and only one equation is needed, whereas the remainingMCs require a total of three equations. Figure 3.22(b) illustrates the labeled equations from Pol_{x1} to Pol_{x3}.

6. Replace l_{tx} in equations Pol_{x1} to Pol_{x3} with the desired value to determine L_{xy} in the points P_{lx1} to P_{lx3}, represented in Figure 3.22(b) with color green. The new L_{xy} values already take into account the effect of the N_x, N_y, $airgap$ and l_{tx}.

7. **Profile of $L_{xy} = f(l_{ty})$**: Use the values found in Step 6 to determine the Gaussian constants a_g, b_g and c_g in (3.14). The new function is identified as Pol_{y1} and is illustrated in Figure 3.22(c);

8. Replace l_{ty} in equation Pol_{y1} with the desired value to determine L_{xy} for a set of turns, $airgap$, l_{tx} and l_{ty}values. Steps 7 and 8 are only required for non-circular shaped MCs;

9. **Profile of $L_{xy} = f(N_x, N_y, airgap, l_{tx}, l_{ty})$**: Repeat Step 2 to Step 8 for every combination of N_x, N_y, $airgap$, l_{tx} and l_{ty} to create the volume illustrated in Figure 3.19.

3.4.2.1 Self-inductance profiling

The self-inductance (L_x) of a coil corresponds to the quadratic number of turns (N_x) divided by the equivalent reluctance ($\Re$), as described in (3.17). Variations of N_x impact directly the value of L_x while $airgap$ and l_t variations affect $\Re$ and consequently, L_x. Figure 3.23 (a) shows the behavior of L_x as a function of N_x. As expected from (3.17), the pattern of L_x follows a quadratic function and the permeance ($1/\Re$) can be found using three FEA simulation results with different values of N_x.
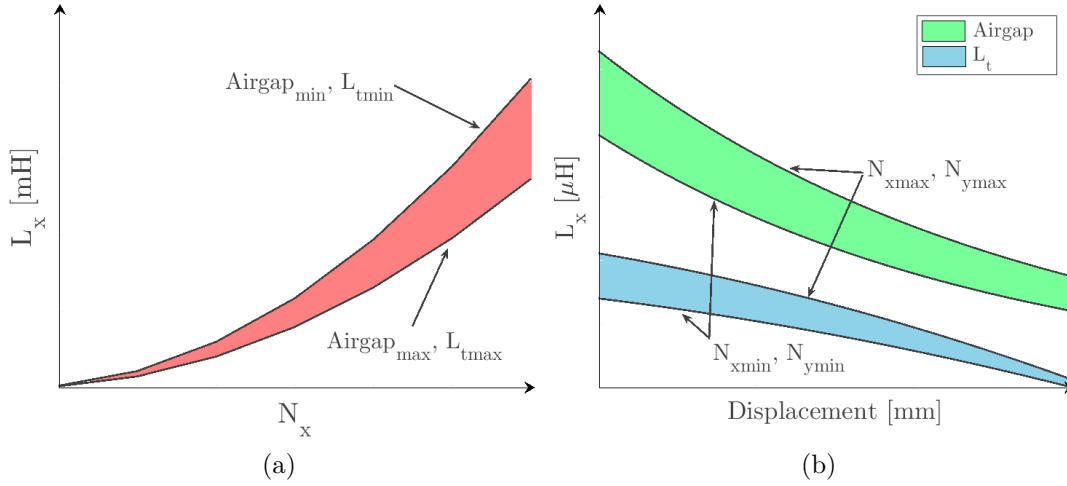
Figure 3.23: Profiles of L_x as a function of: (a) N_x and (b) *airgap* and l_t.

$$L_x = \frac{N_x^2}{\Re}, \ \ x = 1, 2, int \tag{3.17}$$

However, in scenarios A to D, listed in (3.16), only two different values for N_x, $N_{x_{min}}$ and $N_{x_{max}}$, are used. An additional scenario with a different set of turns is then needed and is given by

$$Scenario \ E \rightarrow N_x = N_{x_{mean}}, N_y = N_{y_{mean}}, \tag{3.18}$$

where $N_{x_{mean}}$ is the mean value between $N_{x_{min}}$ and $N_{x_{max}}$, and $N_{y_{mean}}$ is the mean value between $N_{y_{min}}$ and $N_{y_{max}}$.

Air gap and lateral displacements change the value of $\Re$ due to the presence and/or absence of ferromagnetic material from the opposite side pad. Figure 3.23(b) shows the impact displacements in L_x for different *airgap* and l_t values. Charging positions with smaller *airgap* values and $l_t = 0$ have higher values of L_x. However, in the event of lateral displacements, the variation of L_x is steeper when compared with charging positions at higher *airgap* values. The patterns of L_x as a function of *airgap* and l_t are identical to L_{xy} thus, the method described in Section 3.1 can be adapted to determine $L_x = f(N_x, airgap, l_{tx}, l_{ty})$ as follows:

1. **Profile of $\boldsymbol{L_x = f(N_x)}$**: Use the FEA simulation results from *Scenario* A to *Scenario* E, identified in (3.16) and (3.18), to determine the permeance $1/\Re$ in (3.17). Repeat the process for all *Pos*. A total of six equations are found for circular shaped MCs and eighteen equations for non-circular shaped MCs;

2. Replace N_x with the desired value equation $L_x = f(N_x)$, determined in step 1, and repeat the process for the remaining equations. The new values of L_x already take into

consideration the effect of the selected number of turns;

3. **Profile of $L_x = f(N_x, airgap, l_{tx}, l_{ty})$**: Replicate Step 3 to Step 9 of the methodology described in Section 3.1, to model the effect of air gap and lateral displacements in L_x.

3.4.2.2   Development to 3-coil systems

Three-coil systems use a third coil, also referred to as intermediate coil, in series with a capacitor to boost the link between the transmitter and receiver sides. As described earlier, the patterns of L_{12} and L_{int2} are identical and only differ by a scale factor. As for L_{1int}, since both transmitter and intermediate coils are installed in the same enclosure that forms the transmitter pad, its value is almost independent of air gap and lateral displacements. The effect off the number of turns, on the other hand, is the same as L_{12} and L_{int2} and it can obtained using Step 1 of the proposed approach (Profile of $L_{xy} = f(N_x, N_y)$). However, the scenarios listed in (3.16) are not sufficient to characterize L_{12}, L_{int2} and L_{1int} as a function of the number of turns. The new set of scenarios is given by

$$
\begin{aligned}
&Scenario\ A \rightarrow N_1 = N_{1_{min}}, N_2 = N_{2_{min}}, N_{int} = N_{int_{min}} \\
&Scenario\ B \rightarrow N_1 = N_{1_{max}}, N_2 = N_{2_{max}}, N_{int} = N_{int_{max}} \\
&Scenario\ C \rightarrow N_1 = N_{1_{min}}, N_2 = N_{2_{max}}, N_{int} = N_{int_{min}} \\
&Scenario\ D \rightarrow N_1 = N_{1_{max}}, N_2 = N_{2_{min}}, N_{int} = N_{int_{max}} \\
&Scenario\ E \rightarrow N_1 = N_{1_{mean}}, N_2 = N_{2_{mean}}, N_{int} = N_{int_{mean}} \\
&Scenario\ F \rightarrow N_1 = N_{1_{min}}, N_2 = N_{2_{max}}, N_{int} = N_{int_{max}} \\
&Scenario\ G \rightarrow N_1 = N_{1_{max}}, N_2 = N_{2_{min}}, N_{int} = N_{int_{min}},
\end{aligned}
\tag{3.19}
$$

where N_3 is the number of turns in the intermediate coil and $N_{int_{min}}$, $N_{int_{mean}}$ and $N_{int_{max}}$ correspond to the minimum, mean and maximum number of turns, respectively. The results from scenarios A to D characterize L_{12} and L_{int2} while scenarios A, B, F and G characterize L_{1int} as a function of the number of turns. Scenario E is used in the profiling of L_x, described in Section 3.4.2.

3.4.3   Case study

This section validates the proposed approach, step-by-step, using the FLCP illustrated in Figure 3.24 for a particular set of turns and in a specific charging position. Then, a prototype is built and the mapping profile of self and mutual inductances is validated experimentally under different vertical and lateral displacements. Estimation errors and computational time

Table 3.3: System specifications and physical constraints.

Specifications and constraints	Value
Normal frequency operation (f_s)	85 kHz
$airgap$	[100-250 mm]
Lateral tolerance (l_t)	[0-150 mm]
Maximum $|\bar{I}_1|$, $|\bar{I}_2|$, $|\bar{I}_{int}|$	30 A
Maximum MC size ($length$)	800 mm

gains of the proposed mapping methodology are evaluated.
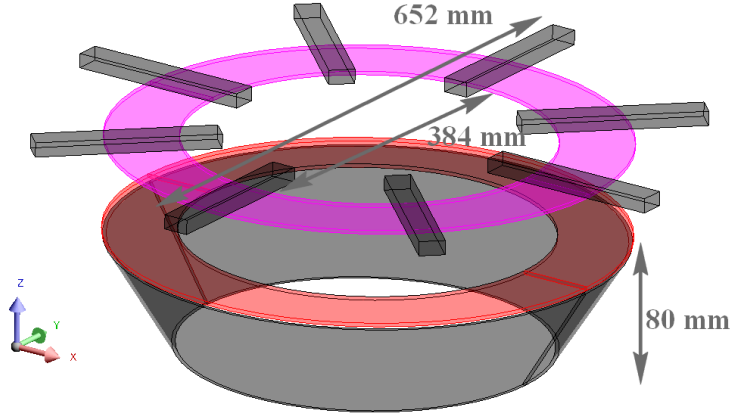
Figure 3.24: Illustration of the FLCP and respective dimensions.

3.4.3.1 Specifications and FEA simulations

Table 3.3 presents the operation specifications and some physical constraints of a typical IPT application. The installation area hinges the MC geometry and it imposes, inadvertently, the lateral tolerance limits and maximum size for the MC. On the other hand, the minimum admissible size for the MC depends on system specifications like output power levels, air gap and lateral displacement values. One characteristic of non-polarized pads is the total decoupling between the transmitter and receiver pads when the lateral displacements exceed around 40 % the total diameter (d) of the pads [174]. This means, the FLCP needs a minimum size of 400 mm to comply with the lateral tolerance of 150 mm, listed in Table. 3.3. A FLCP with a size of 650 mm was selected for evaluation and it respects the maximum size limit of 800 mm imposed by Table. 3.3. The transmitter and receiver pads of FLCP have the same size and its dimensions are shown in Figure 3.24.

The coils are wounded with Litz wire formed by 1050 strands, a cross section of 4 mm^2 and a rated current of 30 A. The value of $N_{x_{min}}$ is set at 2 whereas $N_{x_{max}}$ is set at 14 in order to avoid large induced voltage values at the coils terminals. The ferromagnetic core is modeled with the characteristics of the material N87 from Epcos.

Table 3.4: Minimum number of required FEA simulations needed to profile the self and mutual inductance values.

MC	N_{Pos}	N_x known Scenario	N_{coil}	N_{sim}
CP	6	1	2	12
BPP	18	1	2	36
FLCP	6	1	3	18
		N_x unknown		
CP	6	5	2	60
BPP	18	5	2	180
FLCP	6	7	3	126

A 3D model of the FLCP was simulated using the software Flux from Altair. Each simulation has a second order mesh with approximately 40000 mesh nodes. The use of second order mesh increases the simulation time but it provides accurate results, especially in ferrite-less geometries, like the FLCP. The open-circuit test is performed to each coil and the mutual and self-inductance values are determined using (3.2) and (3.3), respectively. This means that the same *Scenario* in each *Pos* has to be simulated with three different electric circuits. The total number of FEA simulations needed for a full characterization of a MC is then determined by

$$N_{sim} = N_{Scenario}.N_{Pos}.N_{coil}, \tag{3.20}$$

where N_{coil} is the total number of coils in the MC and it can take the values 2 or 3 for two or three-coil systems, respectively. The parameters $N_{Scenario}$ and N_{Pos} correspond to the total number of required *Scenarios* and *Pos*, respectively. Table. 3.4 lists the minimum number of simulations required for different MCs based on (3.20).

The runtime of each simulation ranges from 7 to 15 minutes, using a computer with a i7 4960X processor (max frequency of 4.00 GHz), 32 GB DDR3 at 2133 MHz and 2 TB HDD 7200 RPM Sata disk.

3.4.4 Self and mutual inductance profiling

This subsection explains in detail how to obtain the value of L_{12} and L_1 for an *airgap* = 185 mm and $l_t = 100$ mm of the FLCP with 650 mm. As identified in Section 3.4, the FLCP and CP require the simulation results in six *Pos* ($N_{Pos} = 6$) in order to extrapolate the mutual and self-inductance profiles. Since the number of turns is unknown, a total of seven *Scenarios* ($N_{Scenario} = 7$), identified in (3.19), have to be simulated for each *Pos*. A total of 126 FEA simulations, according to (3.20), are then needed to extract the mutual

Table 3.5: FEA simulation results of all *Scenarios* in each *Pos* for the 650 mm FLCP.

Scenarios	A		B		C		D		E		Unit
	L_{12}	L_1	L_{12}	L_1	L_{12}	L_1	L_{12}	L_1	L_{12}	L_1	
Pos 1	1.12	4.32	66.2	160	8.4	4.33	8.48	161	19.9	56.8	
Pos 2	0.34	4.23	21.9	155	2.7	4.23	2.73	155	6.3	55.3	
Pos 3	0.95	4.31	57.6	159	7.28	4.3	7.36	159	17.1	56.5	$[\mu\text{H}]$
Pos 4	0.31	4.22	20.4	155	2.51	4.23	2.53	155	5.84	55.2	
Pos 5	0.63	4.26	40.2	157	5.02	4.27	5.03	157	11.6	55.9	
Pos 6	0.24	4.22	16.5	155	1.99	4.22	2.01	155	4.63	55.3	

and self-inductance values. The charging positions are illustrated in *zox* side view of Figure 3.20 and they have the following coordinates (*airgap*, l_t): *Pos* 1=(100,0), *Pos* 2=(250,0), *Pos* 3=(100,75), *Pos* 4=(250,75), *Pos* 5=(100,150) and *Pos* 6=(250,150).

Table. 3.5 lists the FEA simulation results from *Scenarios* A to E, described in (3.19), in each *Pos* for the FLCP with a size of 650 mm. The first step in the fitting approach method is the identification of $L_{12} = f(N_1, N_2)$ in all six *Pos*. The method described in Section 3.4.2 is applied in detail to *Pos* 1. Figure 3.25 illustrates $L_{12} = f(N_1, N_2)$ in a 2D view for *Pos* 1 with all significant values. The corners of the geometric figure correspond to L_{12} values of *Scenario* A to *Scneario* D. The linear function between *Scenario* A and *Scenario* D corresponds to a fixed value of two turns (N_{2min}) in the receiver coil while the number of turns of the transmitter is varied, and it is given by

$$L_{12\rightarrow N_{2min}}(N_1) = 0.613 * 10^{-6}.N_1 - 0.107 * 10^{-6}. \tag{3.21}$$

The constants in (3.21) are found using a curve fitting tool, like the *fit* command of Matlab. The fitting process of a two-dimensional functions, like linear, exponential or Gaussian functions, requires the x and y point coordinates in two separate vectors. The curve fitting tool then applies linear or nonlinear parametric regression to the inserted vectors and retrieves the respective constants. For example, the x and y vectors used in (3.21) were $[2, 14]$ and $[1.12*10^{-6}, 8.48*10^{-6}]$, respectively. The x vector corresponds, in this particular case, to the values of N_1 in *Scenario* A and *Scenario* D, whereas the y vector is the correspondent L_{12} values in the same *Scenarios*. The same approach is also applied to discover the constant values in exponential and Gaussian functions.

Analogously, the linear function between *Scenario* C and *Scenario* B corresponds to a fixed value of 14 turns (N_{2max}) in the receiver coil while the number of turns of the transmitter
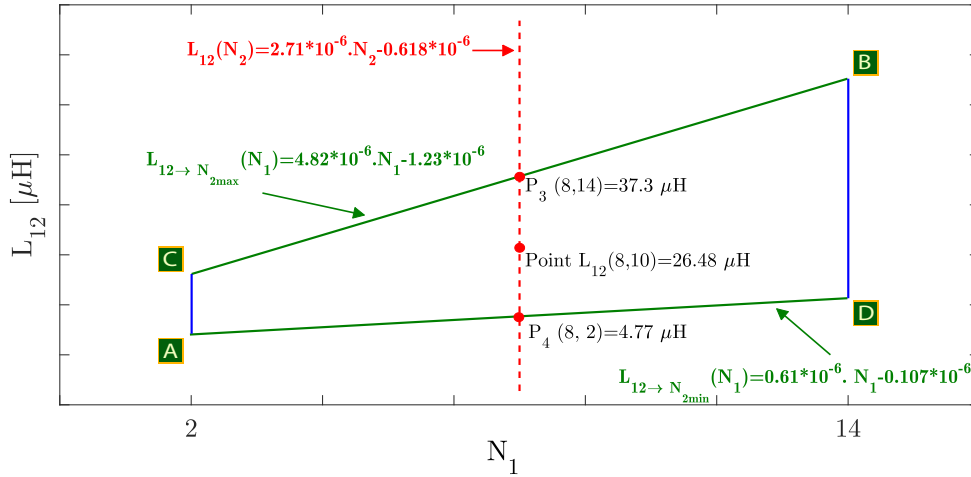
Figure 3.25: Profile of $L_{12} = f(N_1, N_2)$ in a 2D view for *Pos* 1.

Table 3.6: Estimation results of L_{12} in all six *Pos* for $N_1 = 8$ and $N_2 = 10$.

Pos 1	Pos 2	Pos 3	Unit
$L_{12} = 26.48$	$L_{12} = 8.71$	$L_{12} = 23.01$	μH
Pos 4	Pos 5	Pos 6	
$L_{12} = 8.11$	$L_{12} = 16.02$	$L_{12} = 6.5$	μH

is varied, and it is described as

$$L_{12 \to N_{2max}}(N_1) = 4.82 * 10^{-6}.N_1 - 1.23 * 10^{-6}. \tag{3.22}$$

All admissible L_{12} values for every combination of N_1 and N_2 are in between equations (3.21) and (3.22). To validate the methodology that finds L_{12} for a particular set of turns, the following conditions are assumed as an example: $N_1 = 8$ and $N_2 = 10$. First, the L_{12} values for points P_3 and P_4 are determined by replacing N_1 with the value 8 in (3.22) and (3.21), respectively. The impact of N_1 is already taken into account in P_3 and P_4 for N_{2max} and N_{2min}, respectively. The linear function between P_3 and P_4 infers the impact of N_2 in L_{12}, defined as

$$L_{12}(N_2) = 2.71 * 10^{-6}.N_2 - 0.618 * 10^{-6}. \tag{3.23}$$

The value $L_{12} = 26.48\mu H$ for *Pos* 1 is finally determined using (3.23) and replacing N_2 with 10. The same approach is applied to the remaining five *Pos* and the results are listed in Table. 3.6

Step 2 of the fitting approach method characterizes $L_{12} = f(airgap, l_t)$ using the values found in Step 1 for a particular set of turns. The estimated results of L_{12} for $N_1 = 8$ and $N_2 = 10$, listed in Table. 3.6, are used as an example to validate in detail Step 2 of the proposed approach. First, L_{12} is characterized as a function of the *airgap* for *Pos* with the

same l_t. The L_{12} results for *Pos* 1 and *Pos* 2, identified in Table. 3.6, are inserted in a curve fitting tool to discover the constant values in (3.13). In this particular case, the x vector used in fitting tool is equal to $[100, 250]$ whereas the y vector is equal to $[26.48 * 10^{-6}, 8.71 * 10^{-6}]$. The same approach is carried out for the L_{12} pair results (*Pos* 3, *Pos* 4) and (*Pos* 5, *Pos* 6) and they are defined as

$$L_{12_{Px1}}(airgap) = 55.5 * 10^{-6}.e^{(-7.41*10^{-3}.airgap)}$$

$$L_{12_{Px2}}(airgap) = 46.1 * 10^{-6}.e^{(-6.95*10^{-3}.airgap)} \tag{3.24}$$

$$L_{12_{Px3}}(airgap) = 29.1 * 10^{-6}.e^{(-5.97*10^{-3}.airgap)}.$$

To determine L_{12} at a particular air gap value, the variable $airgap$ is replaced in (3.24) by the desired value. Therefore, these three exponential equations determine three new L_{12} values in specific charging positions, labeled from P_{x1} to P_{x3}. As an example, the $airgap$ in (3.24) is replaced by 185 mm and the following L_{12} values are found: $L_{12_{Px1}}$=14.1μH, $L_{12_{Px2}}$=12.74μH and $L_{12_{Px3}}$=9.64μH. These L_{12} values are valid for $N_1 = 8$, $N_2 = 10$ and $airgap = 185$ mm, with lateral displacements of 0, 75 and 150 mm, respectively. The remaining values of L_{12} for charging positions with different lateral displacements are found using (3.14). The constants in (3.14) are obtained with the curve fitting tool, using the values of L_{12} from P_{x1} to P_{x3}. The vectors used in the fitting tool were $x = [0, 75, 150]$ and $y = [14.1*10^{-6}, 12.74*10^{-6}, 9.64*10^{-6}]$, respectively. The new equation, described in (3.25), determines L_{12} value as a function of l_t for a FLCP with a size of 650 mm.

$$L_{12}(l_t) = 14.08 * 10^{-6}.e^{-((l_t+111.4*10^{-19})/2.043)^2}. \tag{3.25}$$

To find L_{12} in a particular lateral displacement, the variable l_t is replaced in (3.25) with the desired value. As an example, l_t was replaced by 100 mm and the value of $L_{12} = 11.78\mu H$ was found.

The aforementioned process determined the specific value of L_{12} for $N_1 = 8$, $N_2 = 10$, $airgap = 185$ mm and $l_t = 100$ mm but the proposed approach extends beyond the estimation of L_{12} in a particular set of conditions. For instance, the results illustrated in Figure 3.25 show the profile of $L_{12} = f(N_1, N_2)$ in *Pos* 1 and it allows the immediate extrapolation of L_{12} for all possible combination of turns without additional FEA simulations. Furthermore, the exponential equations, listed in (3.24), characterize L_{12} for a particular set of turns and as a function of $airgap$. Consequently, they extrapolate L_{12} for different $airgap$

values even those that are outside the specifications listed in Table 3.3. In conclusion, the proposed approach profiles individually L_{12} as a function of different parameters and it combines all individual profiles in an iterative way to form, ultimately, the volume of L_{12} shown in Figure 3.19.

Concluded the validation process of the mutual inductance, the proposed approach is now applied to the self-inductance. The profiling of L_1 is explained step-by-step as a guide reference but the same fitting methodology extends to L_2 and L_{int}. As described in Section 3.4.2, the first step in profiling $L_1 = f(N_1, airgap, l_t)$ is the identification of $L_1 = f(N_1)$ in all Pos. The L_1 results from $Scenarios$ A, B and E, listed in Table 3.5, are inserted in the curve fitting tool to find the constants of a second order polynomial function, given by (3.17). A total of 6 equations are found for the $Scenario$ results of Pos 1 to Pos 6. The equations found for Pos 2, Pos 4 and Pos 6 are described in (3.26) and they were selected to show the impact of lateral displacement in L_1.

$$L_{1_{Pos2}}(N_1) = 803 * 10^{-9}.N_1^2$$
$$L_{1_{Pos4}}(N_1) = 802 * 10^{-9}.N_1^2 \quad\quad (3.26)$$
$$L_{1_{Pos6}}(N_1) = 803 * 10^{-9}.N_1^2.$$

As can be observed, the quadratic constants across all equations in (3.26) are similar and they correspond to the permeance of the transmitter pad. These results indicate that the presence of the receiver pad has small impact in the magnetic flux distribution of the transmitter pad, within the evaluated air gap and lateral displacement values. The value of L_1 for a particular N_1 is found by replacing N_1 in the corresponding second order polynomial equations of each Pos. As an example, the value of $N_1 = 10$ was assumed and the estimated L_1 values are listed in Table 3.7. The results show a maximum deviation of 3.2 % between minimum and maximum values and they are in line with the existing literature. Nevertheless, the impact of air gap and lateral displacements must be accounted for using the same approach as the identification of $L_{12} = f(airgap, l_t)$. The set of L_1 results with the same lateral displacements i.e, the set of L_1 values (Pos 1, Pos 2), (Pos 3, Pos 4) and (Pos 5, Pos 6) are used to find the constants in (3.13). These exponential equations model L_1 as a function of the air gap in three distinct lateral displacement values. As an example, using the same $airgap$ value of 185 mm the following L_1 values are found in the specific charging positions: $L_{1_{Px1}}=81.4\mu H$, $L_{1_{Px2}}=81.2\mu H$ and $L_{1_{Px3}}=80.8\mu H$.

To account the effect of lateral displacements, the obtained values of in L_1 in P_{x1}, P_{x2} and

Table 3.7: Estimation results of L_1 in all six *Pos* for $N_1 = 10$.

Pos 1	Pos 2	Pos 3	Unit
$L_1 = 82.9$	$L_1 = 80.3$	$L_1 = 82.4$	μH
Pos 4	Pos 5	Pos 6	
$L_1 = 80.3$	$L_1 = 81.4$	$L_1 = 80.3$	μH
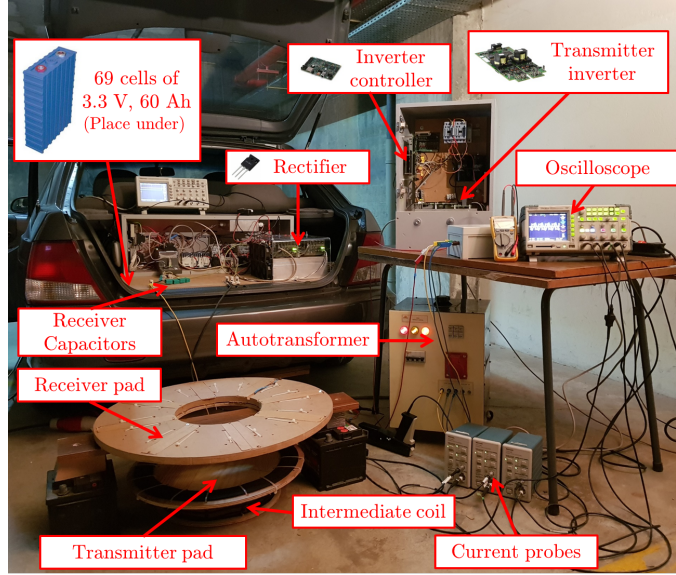
Figure 3.26: Experimental prototype built in a converted combustion vehicle.

P_{x3} are used to found the constants in (3.14) through a curve fitting tool. The new function characterizes L_1 as a function of l_t for an $airgap = 185$ mm and $N_1 = 10$. The variable l_t is then replaced with the desired value to find the final value for L_1. The process is repeated iteratively to build the profile $L_1 = f(N_1, airgap, l_t)$. The same approach is conducted for L_2 and L_{int}.

Figure 3.26 illustrates the built prototype of a FLCP and test bench with the following turns: $N_1 = 10$, $N_2 = 14$ and $N_3 = 6$. The FEA simulation results from Table 3.5 were used to extrapolate the fitting curves of L_{12} and L_1, illustrated in Figure 3.27. For each solid line, l_t is constant and the $airgap$ is varied. As such, the x axis corresponds to the vertical displacements. For dashed lines, the analysis is reversed i.e, the $airgap$ is constant and l_t is varied along the x axis. The experimental measurements correspond to square points and the FEA simulations correspond to circle points. From the figure analysis it is possible to confirm that both Gaussian and exponential decay functions can be used to mimic the behavior for L_{12} and L_1. Fitting based methods have inherent estimation errors that depend on number, quality and distance between the fitting points. Any difference can be mitigated by adjusting the fitting parameters of the curve fitting tool to reduce the square errors in the worst charging positions, i.e, for the highest vertical and lateral displacements.
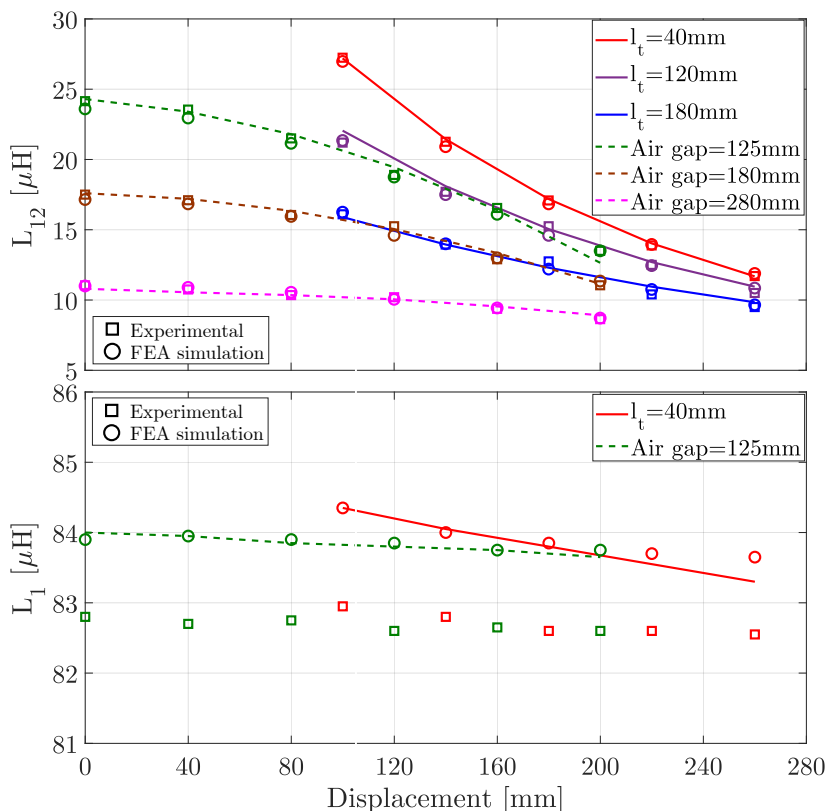
Figure 3.27: Comparison of the fitting approach with both experimental and FEA simulation data as a function of both vertical and lateral displacements.

3.4.5   Performance and Runtime

The estimation discrepancies of the proposed fitting approach method against FEA simulations and experimental data are quantified in this subsection as well as the time savings by the proposed mapping approach with the existing literature.

Figure 3.28 lists the errors between the fitting curves, the experimental data and FEA simulation results for L_{12} under vertical and lateral displacements. Within feasible displacements, the average error between the experimental data and the proposed fitting is below 3 %. The error difference is higher in scenarios where the value of l_t is higher. For example, a charging position outside the displacement specifications listed in Table 4.2 (($airgap$,l_t)=(280,200)), corresponding to a coupling factor of 0.06, has an error of 6.8 % between experimental and fitting curve (0.58μH). The estimation errors are higher (between 4.2 and 7 %) for charging scenarios that exhibit low coupling values (between 0.04 and 0.078). Such charging positions are unfeasible for an efficient high throughput energy transfer due to the high circulating currents required in the transmitter side. Similar error results are found for L_{int2} and for that reason they are not displayed.

The estimation errors for L_1 are comprised between 2.4 and 3.2 %. This error range is
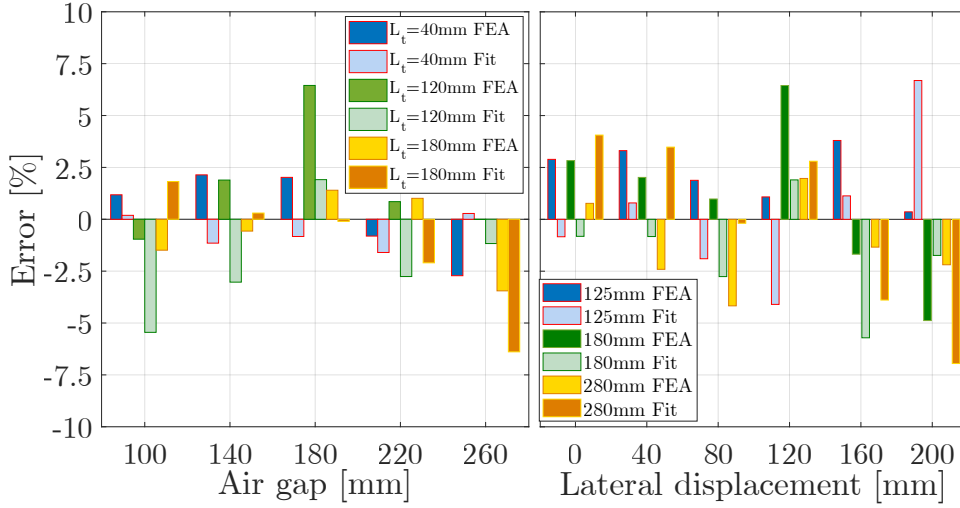
Figure 3.28: Errors between the experimental data and both FEA simulations and fitting approach methodology.

a consequence of an 1.4 μH offset between the experimental data and the fitting approach and FEA simulation results, as depicted in the second graph of Figure 3.27(b). Despite the offset value, the fitting curves follow the same pattern of the experimental data. Similar L_1 values are obtained in different vertical and lateral displacements with difference errors in the range of 0.8 to 3.4 %.

Figure 3.29 shows the error results between the fitting approach method and 3D FEA simulation results for L_1 and L_{12} with a FLCP size of 650 mm. The comparison is made with the FLCP in six different charging positions and with different set of turns, as identified in the top left corner of Figure 3.29. The results show an average error in L_{12} around 4 % whereas the average error of L_1 is inferior 1 %. The highest errors in L_{12} occur for higher lateral displacement values, like points 1 and 2. In these cases, the values of L_{12} are inferior to 10 μH and had a variation of just 0.5 μH in the fitting approach which lead to an error of 5 %. The estimation of L_1, on the other hand, has average errors inferior to 1 % and in some conditions, like point 2 and point 3, the error is negligible. This was due to the little effect of air gap and lateral displacements in the self-inductance values, which reduces the estimation errors. Similar error results were obtained for L_2, L_{int} and L_{int2} and for this reason are not depicted in Figure 3.29.

One benefit of the proposed approach is the reduced number of FEA simulations required to create the self and mutual-inductance profiles. As explained in subsection 3.4.2, the profiling of the self and mutual-inductance surfaces as a function of the number of turns requires the simulation of *Scenarios* in each *Pos*. The final number of required simulations in the unknown category is then affected by a factor that equals the number of *Scenarios*.
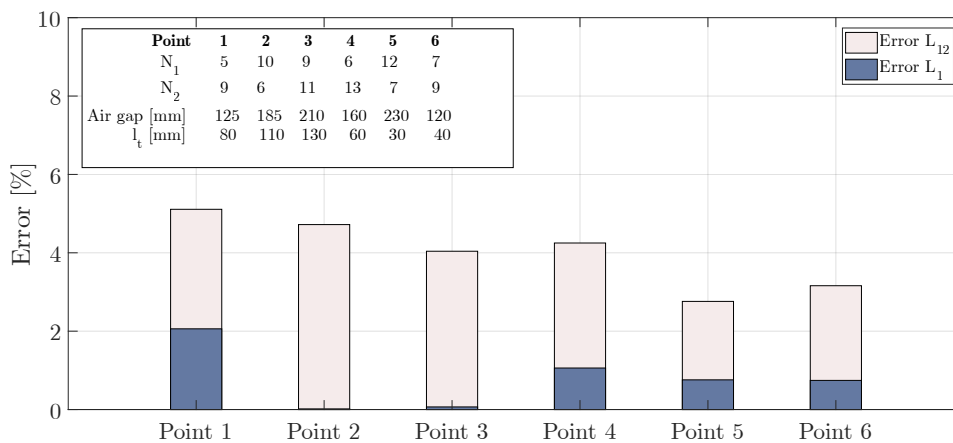
Figure 3.29: Estimation errors between the proposed fitting approach and FEA simulations.

Table 3.8: Benefits of the proposed fitting approach in the existing literature.

	Literature			Proposed work	
Work	MCs	N_x	N_{Sim}	N_{sim}	Time savings
*	1	unknown	270	126	$\approx 54\%$
[304]	64	known	11648	2304	$\approx 80\%$
[198]	9	known	1446	336	$\approx 77\%$

* Case study presented in this work.

Furthermore, non-circular shaped MCs require twelve additional *Pos*, like the BPP in Table. 3.4, to profile L_{xy} and L_x as a function of lateral displacements along the x and y axes. These types of MCs require a total of 180 FEA simulations, if the set of turns is unknown, and 36 FEA simulations, if the set of turns is known. On the other hand, circular designs like the CP only requires 6 *Pos* and the total number of simulations is reduced to one third when compared with the BPP. In overall, the total number of FEA simulations that fully characterize an MC are comprised between 12 (for the CP) and 180 (for the BPP).

Table 3.8 shows the benefits of the proposed fitting approach, taking into account the presented case study, in comparison with the typical approach. In addition, a benchmark comparison is also made in Table 3.8 with existing works in the literature. The table is subdivided into two groups: Literature and Proposed work. The first group shows the total number of evaluated MCs, whether the number of turns is known and the total number of simulations carried out in each work (N_{Sim}). The second group, identified in bold, shows the total number of simulations needed to characterize the MCs with the proposed fitting approach and the computational saving time in percentage. The first row in the table compares the profiling of the mutual and self-inductance values of the presented case study with the conventional approach and the proposed fitting methodology. To determine the number of simulations in the typical approach, it was established the analysis of 3 different air gap values and in 5 lateral displacements, making a total of 15 different charging positions.

In terms of turns, it were considered 6 FLCP with different set of turns making a total of N_{Sim} =3x5x6xN_{coils} = 270 FEA simulations. These assumptions are in line with the existing literature to profile L_x and L_{xy}. As can be observed, with the proposed fitting approach, for an unknown number of turns, the time savings are around 54%. This time savings only accounts for 6 different set of turns whereas the proposed approach takes into account all possible combination of turns between 1 and 14, which would increased the time savings by more than 90 %. The remaining rows of Table 3.8 compare the proposed approach with the existing literature. As expected, the total number of simulations considered in works [198] and [304] is drastically reduced using the proposed fitting approach with time savings around 80 %. Optimization works of MCs, like [65, 306], can also take advantage of the proposed fitting approach. However, the lack of information regarding the total number of simulations, the air gap and lateral displacement intervals difficult the saving time estimation. Still, if the simulation intervals for the air gap and lateral displacements are between 25 and 50 mm, the fitting approach could reduce the total number of simulations between 20 % and 50 % in the aforementioned works.

3.5   Summary

The MC is the component responsible for the air gap and lateral displacement tolerances in IPT systems. A proper design and optimization of the MC results in an improved power transfer capability under severe charging positions. This chapter investigates multiple MC geometries with ferromagnetic core or with a "pipe" coil to orient the flux lines in the back of the pads. A new ferrite-less circular pad is presented in this work for both static and dynamic applications. The new geometry exhibits coupling factor profiles equivalent to a ferrite circular geometry with a reduction inferior to 12%.

A new vertical double receiver static IPT system that reduces the air gap and lateral displacements in heavy-duty vehicles is also presented in this chapter. The vertical placement of the transmitter pad reduces the minimum air gap to values around 50 mm. In addition, the vertical placement of the transmitter pad allied with the low air gap values to the receiver pads eliminates the risk of metallic objects, small animals and people placed between the transmitter and receiver pads during the charging process. The solenoid SPP geometry with different core arrangements is investigated with two simultaneous receivers pads. In this way, the double-side flux pattern is harnessed simultaneously by the two receiver pads. The optimized SPP transmitter offers better power density when coupled with a similar SPP

receiver rather than a DDP or a BPP receiver pad. The compliance with ICNIRP rules is met at shorter distances. In comparison with traditional IPT systems, the proposed SPP configuration almost triplicates the power transfer capabilities using the same charging area.

The best approach to characterize a MC still resorts to FEA tools and is a time-consuming endeavor. This chapter presents a new mapping methodology of the mutual and self-inductance profiles in MC as a function of the number of turns, air gap and lateral displacements using a minimum number of FEA simulations. The methodology models the effect of vertical and lateral displacements with decay exponential and Gaussian functions, respectively. The effects of the number of turns are modeled using linear and second-order functions for mutual and self-inductance values, respectively.

The mapping methodology avoids new FEA simulations if the charging positioning or power requirements are modified. In addition, the use of fitting curves converts discrete FEA points in a continuous mapped volume. As an example, 60 FEA simulations are required to fully map the CP and 180 FEA simulations for the DDP and BPP. The proposed methodology can also be applied to MCs with an intermediate coupler. The method was compared with the FEA simulations and validated experimentally with an FLCP geometry. The fitted Gaussian and exponential curves exhibit a good correlation with the experimental data, and an average error below 3 % was found, even under charging conditions outside the design specifications. The fitted exponential curves can, however, exhibit larger errors (around 6%) if the air gap range is high (variations above 200 mm). This limitation can be mitigated with three or nine FEA simulations results with intermediary air gap values. The proposed approach can reduce up to 80 % the computational effort and simulation time when compared with the existing literature.

Chapter 4

Three-coil IPT system

The MC optimizations made in the previous chapter showed the benefits of an optimized geometry under different air gap and lateral displacement charging scenarios. Still, heavy duty and off-road vehicles exhibit high ground clearances between 250 and 500 mm. Consequently, the coupling factor is limited to values in the range 0.05-0.2.

The inclusion of an intermediate coupler (IC) between the off-board and on-board sides improves the magnetic link under different charging scenarios, as described in Chapter 2. In addition, the intermediate coupler offers off-board current limiting capabilities during the absence of vehicle. However, the literature lacks a design methodology to operate the overall system with current source characteristics. Therefore, this chapter starts with a design methodology of a series-series with an intermediate coupler. The design methodology takes advantage of the mapping methodology, presented in Chapter 3, to determine a set of size metrics of circular geometries with an intermediate coupler.

A system with current source characteristics is unaffected by load variations. In addition, the current value is adjusted using only the off-board inverter. This avoid the use of controllable converters in the on-board side and close-looped control strategies in the off-board side. The only requirement for the control is the knowledge of the mutual inductance values and the batteries state of charge in order to attain the system current gain and stop charging condition, respectively. Consequently, this work also proposes an estimation procedure of the equivalent load and mutual inductance values using only off-board voltage and current measurements. In this way, the presented system avoids entirely the need for a communication link between the off-board an on-board sides.

The chapter starts with the main overview of ICs followed by the circuit analysis of a series-series resonant configuration with an IC. Section 4.3 presents the estimation procedure of the mutual inductance and load values using only off-board measurements. A design procedure of an open-loop constant current controller with respective magnetic coupler is
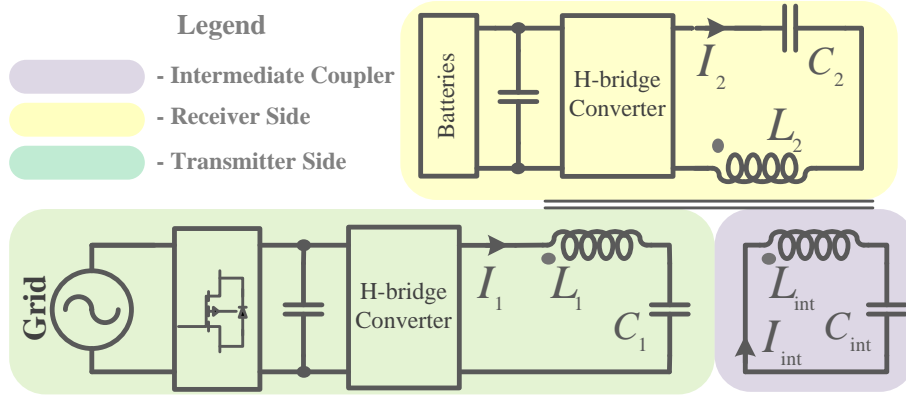
Figure 4.1: Placement of an intermediate coupler in conventional IPT systems.

introduced in Section 4.4. A case study that validates the proposed design is presented in Section 4.5 followed by experimental validation in Section 4.6. The main conclusions are drawn in Section 4.7.

4.1 Intermediate couplers

The intermediate coupler is an independent resonant tank circuit formed by a magnetically link inductor and a capacitor, as illustrated in Figure 4.1. The intermediate coil is magnetically linked with both the transmitter and receiver coils. Thus, two additional mutual coupling values are created: k_{1int} and k_{int2}. The subscript text 1, 2 and *int* in the variables denote the transmitter, receiver and intermediate sides, respectively. This additional magnetic link to the receiver coil boosts the power transfer capabilities of IPT systems [151, 156, 201, 288].

The benefits of intermediate couplers over conventional two-coil systems is analyzed in some works. The experimental results in [147] verify the efficiency of three-coil systems over two-coil systems. A 6.6 kW prototype is built in [148] to validate the applicability of intermediate couplers over longer air gap distances. Additionally, according to [153], the electromagnetic leakage field emissions are smaller for a three-coil system and the compliance with the ICNIRP guidelines is met at smaller distances. In [146], several configurations are analyzed with two, three and four resonators. The optimal positioning of the IC and the benefits of a three-coil system over a two-coil system is shown in [288].

The inclusion of the IC affects the power transfer capabilities. Figure 4.2 shows the output power of a three-coil system as a function of k_{1int} and k_{int2}. Although several combinations of k_{1int} and k_{int2} are merely theoretical hypothesis and only mathematically viable due to physical constraints of EV IPT charging applications, the surface represented in Figure 4.2
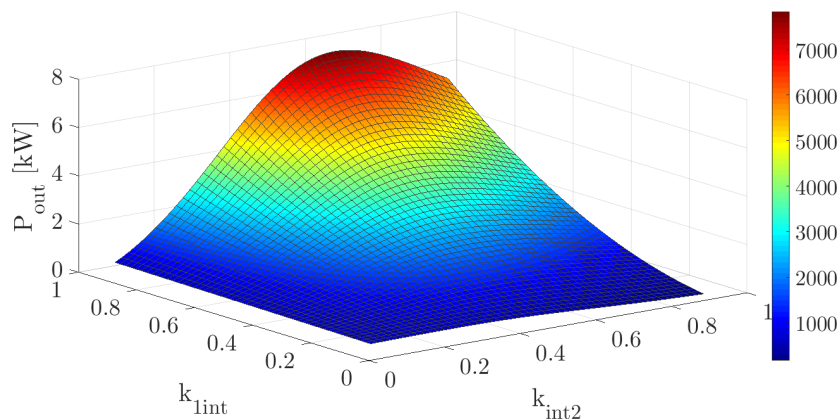
Figure 4.2: Output power as a function of k_{1int} and k_{int2}.

shows a higher output power is obtained when the intermediate coil is placed closer to the transmitter rather than the receiver coils (higher values of output power for values of k_{1int} closer to 1). This conclusion is corroborated by other existing works in the literature [147, 149]. However, the mid-air positioning of the intermediate coil is impractical for EVs batteries charging systems. Works [149,155,198,288] place the intermediate coil in a coplanar arrangement with the transmitter coil.

The placement of the intermediate coil in proximity or even in a coplanar fashion with the transmitter coil gives the possibility of connecting both coils and operating them at a single frequency or operating the intermediate coil independently. The first option is more suitable with parallel-parallel (PP) compensation whereas the second is preferable with a series-series (SS) compensation, as discussed in [149]. However, the analysis is performed in perfectly tuned conditions and the effects of lateral displacements and air gaps variations are not evaluated.

The shift of the transmitter current to the intermediate coupler reduces the losses in the inverter for a SS compensation. A quasi constant voltage (CV) mode is possible using a SS with an intermediate coupler (SS-IC) and the design procedure was discussed in [148]. However, the system does not achieve zero-phase angle (ZPA) in the entire load range and the effects of lateral displacements are not analyzed.

The aforementioned studies assume that all physical parameters are known to the controller. However, in a real EV application, the coupling coefficients depend on the relative positioning between the transmitter and receiver sides and a correct estimation of the position is needed by the controller [255]. Also, a single controller IPT system without any communication link with the receiver side must determine the current voltage level of the batteries to apply the correct charging mode.

4.2   Series-Series with Intermediate Coupler

4.2.1   Circuit analysis

A conventional SS-IC is illustrated in Figure 4.3(a). The transmitter side comprises a DC link (V_{DC}) followed by a high frequency H-bridge inverter and the transmitter resonant tank. The receiver side includes the resonant tank connected to a full-bridge diode rectifier with a filtering stage and the batteries. The IC is placed near the transmitter coil to improve the power transfer capabilities between the transmitter and receiver sides. A phase-shift control scheme is used to regulate the output voltage ($\overline{V}_1$) of the inverter, as shown in Figure 4.3(a). The drive pulses applied to the diagonals $\{S_1, S_4\}$ and $\{S_2, S_3\}$ are out of phase by a shift angle (α) between 0° and 180°. A full square wave is obtained when $\alpha = 0°$ and a null inverter output voltage when $\alpha = 180°$. The variable f_s corresponds to the operating frequency and ω to its respective angular frequency.

The root mean square (RMS) value of $\overline{V}_{1,n}$ is given by

$$|\overline{V}_{1,n}| = V_{DC}\frac{2\sqrt{2}}{n\pi}cos\left(\frac{n\alpha}{2}\right), \quad n = 1, 3, 5, 7, ..., \tag{4.1}$$

where n is the harmonic order. Figure 4.3(b) depicts the equivalent model for the n-th harmonic order. By applying Kirchhoff's circuit laws to the circuit, the following matrix form of the circuitry equations is obtained

$$\begin{bmatrix} \overline{V}_{1,n} \\ 0 \\ 0 \end{bmatrix} = \begin{bmatrix} Z_{1,n} & -jn.\omega.L_{12} & jn.\omega.L_{1int} \\ -jn.\omega.L_{12} & Z_{2,n} & jn.\omega.L_{int2} \\ jn.\omega.L_{1int} & jn.\omega.L_{int2} & Z_{int,n} \end{bmatrix} \cdot \begin{bmatrix} \overline{I}_{1,n} \\ \overline{I}_{2,n} \\ \overline{I}_{int,n} \end{bmatrix}, \tag{4.2}$$

where $Z_{1,n} = r_{1,n} + jn.\omega(L_1 - \frac{1}{n.\omega^2.C_1})$, $Z_{2,n} = (R_{eq} + r_{2,n}) + jn.\omega(L_2 - \frac{1}{n.\omega^2.C_2})$ and $Z_{int,n} = r_{int,n} + jn.\omega(L_{int} - \frac{1}{n.\omega^2.C_{int}})$. The variables L_1, L_2 and L_{int} are the self-inductances of the magnetic coupler. The parameters $r_{1,n}$, $r_{2,n}$ and $r_{int,n}$ denote the equivalent resistances of the inductors and capacitors that form the transmitter, receiver and intermediate resonant tanks at the n-th harmonic of f_s. Similarly, L_{12}, L_{1int} and L_{int2} are the mutual inductances between the transmitter, the receiver and the intermediate coils. The values of the capacitors are given by $C_1 = 1/(\omega_1^2.L_1)$, $C_2 = 1/(\omega_2^2.L_2)$ and $C_{int} = 1/(\omega_{int}^2.L_{int})$, where ω_1, ω_2 and ω_{int} are the angular resonant frequencies of its respective resonant tanks. The parameter
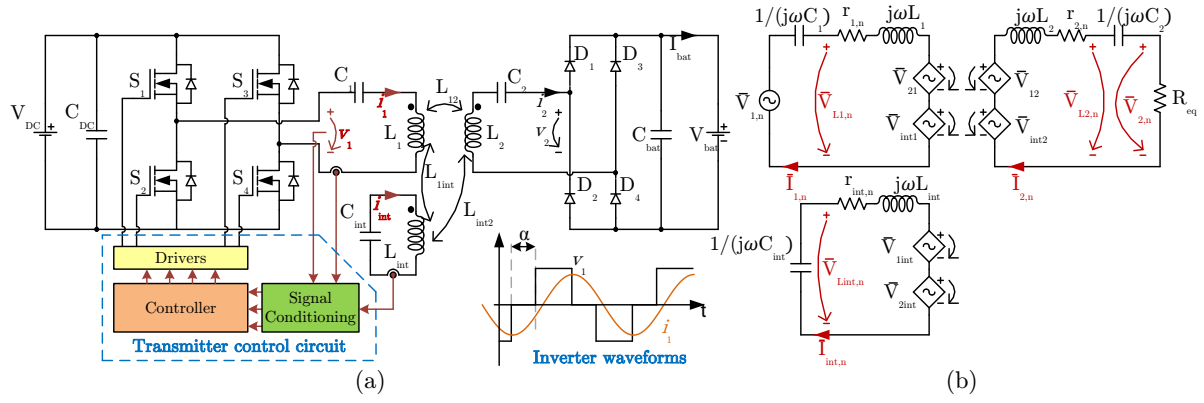
Figure 4.3: Proposed SS with an intermediate coupler system: (a) general representation and (b) equivalent circuit for n-th harmonic.

R_{eq} is the equivalent resistance of the batteries before the rectifier action, expressed as

$$R_{eq} = \frac{8.V_{bat}}{\pi^2.I_{bat}},$$ (4.3)

where V_{bat} and I_{bat} are the voltage and current values in the batteries, respectively. Solving (4.2) provides the current equations in the matrix form that accurately define the model shown in Figure 4.3(b) for the *n-th* harmonic

$$\begin{bmatrix} \overline{I}_{1,n} \\ \overline{I}_{2,n} \\ \overline{I}_{int,n} \end{bmatrix} = \begin{bmatrix} \frac{1}{Z_{1,n}+Z_{rec3,n}+Z_{int3,n}} & 0 & 0 \\ 0 & G_{i_2i_1} & 0 \\ 0 & G_{i_3i_1} & 0 \end{bmatrix} \begin{bmatrix} \overline{V}_{1,n} \\ \overline{I}_{1,n} \\ 0 \end{bmatrix}$$ (4.4)

where $G_{i_2i_1} = \frac{-p_2(L_{12}.L_{int2}-L_{1int}.p_1)+L_{1int}(L_{int2}^2-p_1.p_2)}{L_{int2}(L_{int2}^2-p_1.p_2)}$ and $G_{i_{int}i_1} = \frac{L_{12}.L_{int2}-L_{1int}.p_1}{L_{int2}^2-p_1.p_2}$. The variables p_1 and p_2 are constants given by

$$p_1 = \frac{L_2(b_{2,n}^2 - 1)}{b_{2,n}^2} - j\frac{R_{eq} + r_{2,n}}{n.\omega}, \quad p_2 = \frac{L_{int}(b_{int,n}^2 - 1)}{b_{int,n}^2} - j\frac{r_{int,n}}{n.\omega}.$$

The variables $b_{1,n}$, $b_{2,n}$ and $b_{int,n}$, described in (4.5), are relation factors between the system *n-th* harmonic angular frequency ($n.\omega$) and the resonant angular frequencies of the transmitter (ω_1), receiver (ω_2) and intermediate (ω_{int}) resonant tanks. A unitary relation factor at the fundamental frequency means $\omega = \omega_x$ while a relation lower than 1 means $\omega < \omega_x$.

$$b_{1,n} = n.\omega/\omega_1, \quad b_{2,n} = n.\omega/\omega_2, \quad b_{int,n} = n.\omega/\omega_{int}.$$ (4.5)

The parameters $Z_{rec3,n}$ and $Z_{int3,n}$ are the reflected impedances from the receiver and intermediate sides onto the transmitter side for the *n-th* and they are defined in (4.6) and (4.7).

The transmitter equivalent impedance ($Z_{1,n}$) is described in (4.2).

$$Z_{rec3,n} = \frac{jn.\omega.L_{12}.L_{1int}(\frac{L_{12}.L_{int2}}{L_{1int}}p_2 - L_{int2}^2)}{L_{int2}(L_{int2}^2 - p_1.p_2)} \tag{4.6}$$

$$Z_{int3,n} = \frac{jn.\omega.L_{1int}^2(p_1 - \frac{L_{12}.L_{int2}}{L_{1int}})}{L_{int2}^2 - p_1.p_2} \tag{4.7}$$

The impedance seen at the H-bridge inverter terminals is given by

$$Z_{in,n} = Z_{rec3,n} + Z_{int3,n} + Z_{1,n}. \tag{4.8}$$

The RMS values of the induced voltages across the MC coils at the fundamental frequency can be calculated by

$$
\begin{aligned}
|\overline{V}_{L_{1,1}}| &= |\overline{I}_{1,1}.(Z_{rec3} + Z_{int3} + j\omega L_1 + r_{1,1})| \\
|\overline{V}_{L_{2,1}}| &= |\overline{I}_{2,1}.(R_{eq} + 1/(j\omega.C_2))| \\
|\overline{V}_{L_{int,1}}| &= |\overline{I}_{int,1}/(j\omega.C_{int})|.
\end{aligned} \tag{4.9}
$$

Current regulations limit these values to 1000 Vrms in Europe and 400 Vrms in Asia. The use of capacitors in series with the coils is a common method to overcome this limitation by reducing the effective inductance of the coil.

The coupling factor k_{xy} quantifies the percentage of flux lines that couple the coil x and the coil y of the MC. The value of k_{xy} varies from 0 to 1 and is given by

$$k_{xy} = L_{xy}/\sqrt{(L_x.L_y)}, \quad x,y = 1, 2, int. \tag{4.10}$$

The transfer function between the output current ($\overline{I}_2$) and the input voltage ($\overline{V}_1$), also known as transconductance gain function ($G_{i_2 v_1}$), is described as

$$G\left(\left|\frac{\overline{I}_2}{\overline{V}_1}\right|\right) = \left|\frac{L_{1int}(L_{int2}^2 - p_1.p_2) - p_2(L_{12}.L_{int2} - L_{1int}.p_1)}{(Z_1 + Z_{rec3} + Z_{int3})(L_{int2}^2 - p_1.p_2.L_{int2})}\right|. \tag{4.11}$$

In typical IPT systems, the power transferred to the receiver is regulated through a phase-shift control in the transmitter inverter to modify the RMS value of $\overline{V}_1$. A load independent transconductance gain function would ensure a fixed phase-shift angle under the same physical conditions. Section 4.2.3 describes a selection method of the resonant tanks frequencies in order to obtain a quasi-load independent transconductance function.

4.2.2 Efficiency

The efficiency of the proposed system between the input DC bus and the batteries, commonly referred to DC-DC efficiency (η_{sys}), is given by

$$\eta_{sys} = \frac{P_{out}}{P_{L_{AC-AC}} + P_{L_{rect}} + P_{L_{inv}} + P_{out}}, \tag{4.12}$$

where $P_{L_{inv}}$, $P_{L_{rect}}$ and $P_{L_{AC-AC}}$ correspond to the conduction losses of the inverter, the conduction losses of the rectifier and the losses in the resonant tanks of the circuit, respectively. Assuming a continuous mode operation of the rectifier, the corrresponding conduction losses ($P_{L_{rect}}$) are given by [229]

$$P_{L_{rect}} = \frac{4\sqrt{2}}{\pi}V_f|\bar{I}_2| + 2r_D|\bar{I}_2|^2, \tag{4.13}$$

where V_f and r_D are the threshold voltage and equivalent on-state resistance of the diode, respectively. The value of $P_{L_{inv}}$ depends of the phase-shift angle (α) applied by the controller and is defined by [229]

$$P_{L_{inv}}(\alpha) = P_{con\_MOS}(\alpha) + P_{con\_DIO}(\alpha), \tag{4.14}$$

where $P_{con\_MOS}(\alpha)$ and $P_{con\_DIO}(\alpha)$ are the conduction losses of the MOSFETS and diodes of the inverter, respectively. The values of $P_{con\_MOS}(\alpha)$ and $P_{con\_DIO}(\alpha)$ are given by (4.15) and (4.16).

$$
\begin{aligned}
P_{con\_MOS}(\alpha) &= \frac{4}{2\pi}\int r_{on}i_1(\theta)^2 d\theta \\
&= \frac{1}{\pi}r_{on}|\bar{I}_1|^2(2\pi - \alpha + sin(\pi - \alpha)),
\end{aligned} \tag{4.15}
$$

$$
\begin{aligned}
P_{con\_DIO}(\alpha) &= \frac{1}{2\pi}\int v_{AK}(\theta)i_1(\theta)d\theta = \\
\frac{2\sqrt{2}}{\pi}V_f|\bar{I}_1|(1 - sin(\frac{\pi - \alpha}{2})) &+ \frac{1}{\pi}r_D|\bar{I}_1|^2(\alpha - sin(\pi - \alpha)).
\end{aligned} \tag{4.16}
$$

The variables v_{AK} and r_{on} are the anode-cathode voltage and the on-state resistance of one MOSFET, respectively. Regarding the commutation losses, it was verified in previous works that only 20 % of the total losses in a H-bridge inverter is due to switching losses [307], even with the transmitter side slightly mistuned. Also, [213] showed a proportional relation between switching losses and the amount of power being transferred by the H-bridge. Since

the comparisons made in this work assume the same amount of transferred power P_{out}, the value of the switching losses does not affect the analysis made.

The values of $P_{L_{AC-AC}}$ and P_{out} are defined as

$$P_{L_{AC-AC}} = r_{1,1}.|\bar{I}_{1,1}|^2 + r_{2,1}.|\bar{I}_{2,1}|^2 + r_{int,1}.|\bar{I}_{int,1}|^2, \tag{4.17}$$

$$P_{out} = |\bar{I}_{2,1}|^2.R_{eq}. \tag{4.18}$$

4.2.3 Selection of resonant frequencies

The tuning of the receiver and intermediate resonant tanks depend on the physical properties of the MC and have a great impact on the system efficiency and operating characteristics. Aforementioned works propose designs of the intermediate and receiver resonant tanks with frequencies different from the operating frequency (f_s). In [149], the intermediate and receiver frequencies are determined for the best efficiency results. The authors tuned the receiver tank with a frequency slightly above f_s whereas the intermediate resonant frequency is varied between 1.07-1.12 of f_s. However, no mention is made regarding the operating point of the current and voltage transfer functions. The authors in [148] propose a tuning method that achieves CV operating mode when the intermediate frequency is set approximately 10 % above f_s and the receiver frequency is placed between 10-20 % below f_s. The transmitter frequency is set around the receiver frequency but it depends on the value of L_{12} to achieve a high efficiency. Still, the effect of coupler displacements in the operating point of the voltage gain transfer is not addressed.

The transconductance function, described in (4.11), exhibits a quasi constant current (CC) mode when the reflected reactance of the receiver side ($Im\{Z_{rec3}\}$), given by (4.19), is zero at a specific load condition.

$$Im\{Z_{rec3}\} =$$
$$\frac{X_3.\omega^2.L_{12}^2(\omega^2.L_{int2}^2 + Re\{Z_t\}) + r_{int}.Im\{Z_t\}.\omega^2.L_{12}^2 - \omega^3.L_{12}.L_{int2}.L_{1int}.(\omega^2.L_{int2}^2 + Re\{Z_t\})}{(\omega^2.L_{int2}^2 + Re\{Z_t\})^2 + Im\{Z_t\}^2}$$
$$\tag{4.19}$$

The variable Z_t is the multiplication result between the receiver and intermediate resonant tanks impedance functions and is determined by

$$Z_t = r_{int}.(R_{eq}+r_2)-\omega^2.L_2.L_{int}(1-\frac{1}{b_2^2})(1-\frac{1}{b_{int}^2})+j\omega\left((R_{eq} + r_2)(1 - \frac{1}{b_{int}^2}) + r_{int}.L_2(1 - \frac{1}{b_2^2})\right).$$
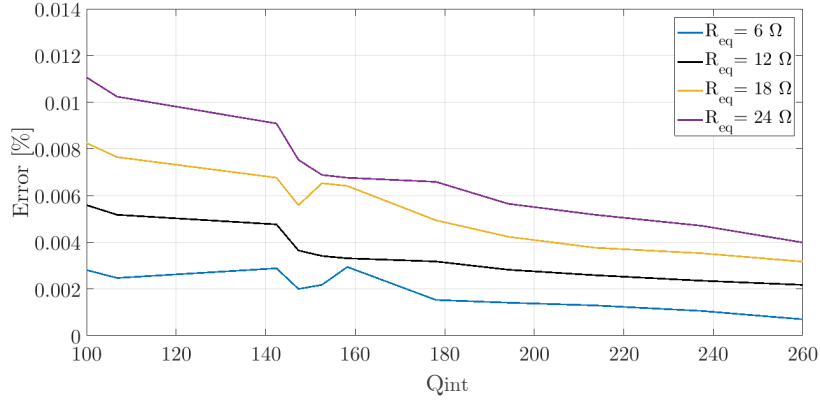
Figure 4.4: Error between theoretical lossless condition ($r_x = 0$) and real coils with different quality factors for different load conditions.

If the intermediate coil resistance (r_{int}) is neglected, the value of $Im\{Z_{rec3}\}$ is independent of the load value. The value of the desired f_s is then determined using

$$
\begin{aligned}
Im\{Z_{rec3}\} = 0 &\Leftrightarrow \omega^2(-\omega^3(L_{int2}^3.L_{12}.L_{1int} + L_{int}(1 - 1/b_{int}^2)) - \\
&- \omega.Re\{p_1.p_2\}(L_{int2}.L_{12}.L_{1int} + L_{int}.L_{12}^2(1 - 1/b_{int}^2))) = 0.
\end{aligned}
\tag{4.20}
$$

In practical applications, the intermediate resonant tanks losses may not be negligible. In this scenario, the frequency value for a null reflected reactance of the receiver side varies with R_{eq}. Figure 4.4 shows the error between the theoretical frequency ($r_{int} = 0$ Ω), and the practical frequency ($r_{int} \neq 0$ Ω) as a function of the quality factor of the intermediate coil ($Q_{int} = \omega.L_{int}/r_{int}$) for different values of R_{eq}. The value of r_{int} has almost no effect in the deviation between the theoretical and practical frequency, meaning the assumption of neglecting r_{int} in (4.19) is valid.

The relation factors b_2 and b_{int} are inversely proportional to the receiver and intermediate resonant frequencies, respectively. Several combinations of b_2 and b_{int} can meet (4.20) for the same MC properties. Therefore, the selection process depends on the requirements of the projected system. As an example, the selection of a b_2 closer to 1 increases the value of $|\bar{I}_1|$ while $|\bar{I}_{int}|$ decreases. Also, the value V_{DC} needed for the same P_{out} is smaller with higher values of b_2. In line with previous works it was verified that the receiver resonant frequency should be slightly higher than the operating frequency ($0.96 \leq b_2 \leq 0.99$) to achieve zero voltage switching (ZVS).

The value of the total reflected reactance $Im\{Z_{int3} + Z_{rec3}\}$ is almost constant and independent of the load conditions when equality (4.20) is verified. The value of C_1 can then be

determined using

$$C_1 = \frac{1}{\omega.(Im(Z_{int3}) + \omega.L_1)}, \tag{4.21}$$

where $Im(Z_{int3})$ is the reflected reactance from the intermediate side. This reactance appears inductive for values of b_{int} inferior to 1. The small reactance differences at different loads causes a variation in the phase angle between $\overline{V}_{1,1}$ and $\overline{I}_{1,1}$ in the range of 0-6°, depending on the system parameters. This characteristic allows the design of a ZPA system during the CC batteries charging mode.

Displacements of the receiver pad from the normal position reduce the coupling coefficients and detune the three resonant tanks. The new quasi-CC operation point is shifted from f_s to higher frequencies. If f_s is kept constant, ZPA is lost in almost the entire load range and increases the stress in the H-bridge inverter switches. This deviation of f_s can be taken into account during the resonant tanks design to comply with the SAE J2954 guideline as long as the magnetic properties of the MC are known in the entire area of operation.

4.3   Estimation procedure

The use of a single controller in the transmitter side without communication to the receiver side requires the value of the system parameters to correctly control the inverter. However, L_{12}, L_{int2} and R_{eq} depend on the vehicle positioning and batteries state-of-charge (SOC), and they cannot be directly measured. The value of L_{1int} also suffers slight variations due to the extra-ferrite of the receiver side. Therefore, Subsection 4.3.1 presents the estimation procedure to determine the mutual inductance values and the equivalent load resistance based on steady-state equations of the series-series with an IC circuit model.

The uncertainty of the passive components in the resonant tanks will alter the system transfer functions and operation mode and consequently, the estimation values of the mutual inductances and load. Subsection 4.3.2 discusses different alternatives of determining the self-inductance and capacitor values using only quantities accessible from the transmitter side. In this way, the values of the self-inductances and capacitors used by the estimation procedure are up to date every time a vehicle parks over the IPT charger. Furthermore, the estimated capacitor values can be used to schedule preventive maintenance and reduce downtime of the charger.

4.3.1   Mutual inductance and Load

The value of L_{1int} can be estimated using (4.22) if no current circulates in the receiver resonant tank. This state is achieved by driving the inverter with a large phase-shift angle to avoid conduction of the diodes in the receiver rectifier i.e, the amplitude of $\overline{V}_2$ is lower than V_{bat}.

$$L_{1int} = \left| \frac{\overline{I}_{int,1}}{\overline{I}_{1,1}} \cdot \left(\frac{L_{int}(b_{int}^2 - 1)}{b_{int}^2} - j\frac{r_{int,1}}{\omega} \right) \right|. \tag{4.22}$$

The set of independent equations formed by (4.17), (4.8) and (4.23) define the input power (the rectifier losses are neglected), the impedance seen at the output inverter terminals and the equivalent resistance as a function of $\overline{I}_1$ and $\overline{I}_{int}$. The signals v_1, i_1, and i_{int} can be measured and the corresponding RMS values (determined by software) matched in the aforementioned equations and solved in function of L_{12}, L_{int2} and R_{eq} (Please refer to Figure 4.3(a)).

$$R_{eq} = \frac{\overline{I}_1/\overline{I}_{int} \cdot (L_{12}.L_{int2} - L_{1int}.L_2(b_2^2 - 1)/b_2^2) - L_{int2}^2 + L_2.L_{int}(b_2^2 - 1)(b_{int}^2 - 1)/(b_2^2.b_{int}^2)}{r_{int}/\omega + j(L_{int}(b_{int}^2 - 1)/b_{int}^2 - L_{1int}.\overline{I}_1/\overline{I}_{int})}$$
$$- \frac{L_2.r_{int}(b_2^2 - 1)/(b_2^2.\omega)}{r_{int}/\omega + j(L_{int}(b_{int}^2 - 1)/b_{int}^2 - L_{1int}.\overline{I}_1/\overline{I}_{int})} \tag{4.23}$$

With all system parameters known, it is possible to estimate the value of V_{bat} and I_{bat}. The value of I_{bat} relates with $\overline{I}_{2,1}$ through

$$I_{bat} = \frac{\pi}{2\sqrt{2}} \cdot |\overline{I}_{2,1}|, \tag{4.24}$$

where $\overline{I}_{2,1}$ is determined using the gain function $G_{i_2i_1}$, described in (4.4). The value of V_{bat} is estimated by replacing (4.24) onto (4.3) and solving it in order to V_{bat}.

4.3.2   Passive components tolerance

There are six passive components that may vary in the studied three-coil system: L_1,L_2, L_{int}, C_1, C_2 and C_{int}. These values are needed in the estimation of mutual inductance and load values, described in section 4.3.1. While the self-inductance values have low variations (inferior to 4 %), the capacitor values can have manufacturing tolerances up to 10 %. Also, the capacitors have a life expectancy and they will lose capacitance over time. The evaluation and capacitance values in the proposed system is made in several steps with different working conditions.

4.3.2.1 Transmitter and intermediate parameters

The transmitter and intermediate resonant components can be identified through the following options:

1. Identification of the parameters using a voltage and current probes in the transmitter side and a current probe in the intermediate coupler (sensors used in the proposed work);

2. Addition of a voltage sensor at C_{int} terminals;

The first option does not need additional sensors and it is the preferable option. The identification of C_1 and C_{int} occurs in the absence of the receiver side (before or right after the last charging process occurs). In this way, the self-inductance values will not be affected by the additional ferromagnetic material of the receiver side and they will remain with a constant value (factory default). Also, the transmitter and intermediate sides are modeled as a series-series topology, as seen in Figure 4.5. By applying the Kirchhoff's circuit laws to the circuitry, the following equations are obtained

$$\overline{V}_1 = r_1.\overline{I}_1 + j.\omega((L_1 - 1/(\omega^2.C_1))\overline{I}_1 - L_{1int}.\overline{I}_{int})$$
$$0 = +r_{int}\overline{I}_{int} + j.\omega((L_{int} - 1/(\omega^2.C_{int}))\overline{I}_{int} + L_{1int}.\overline{I}_1). \tag{4.25}$$

Solving the aforementioned equations lead to equations

$$\overline{I}_{int} = \overline{I}_1.\frac{\omega^2.C_{int}.L_{1int}}{\omega^2.L_{int}.C_{int} - 1 - j.\omega.C_{int}.r_{int}}$$
$$\overline{I}_1 = \frac{\overline{V}_1}{Z_1 + Z_{int3}}. \tag{4.26}$$

In this condition, the values of Z_1 and Z_{int3} are given by

$$Z_1 = r_1 + j\left(\omega.L_1 - \frac{1}{\omega.C_1}\right)$$
$$Z_{int3} = \frac{\omega^2.L_{1int}^2.r_{int}}{L_{int}^2.\omega^2(1/b_{int}^2 - 1)^2 + r_{int}^2} + j\frac{\omega^3.L_{1int}^2.L_{int}(1/b_{int}^2 - 1)}{L_{int}^2.\omega^2(1/b_{int}^2 - 1)^2 + r_{int}^2}. \tag{4.27}$$

The impedance seen at the inverter output terminals (Z_{in}) is then given by

$$Z_{in} = r_1 + \frac{\omega^2.L_{1int}^2.r_{int}}{L_{int}^2.\omega^2(1/b_{int}^2 - 1)^2 + r_{int}^2} + j\left(\frac{\omega^3.L_{1int}^2.L_{int}(1/b_{int}^2 - 1)}{L_{int}^2.\omega^2(1/b_{int}^2 - 1)^2 + r_{int}^2} + \frac{b_1^2 - 1}{\omega.C_1}\right). \tag{4.28}$$

Figure 4.6(a) and Figure 4.6(b) illustrate the amplitude and phase of Z_{in} for different values of C_1 and C_{int}, respectively. The amplitude of Z_{in} shows similar values, regardless of the capacitors values, up to switching frequencies closer to the natural intermediate resonance
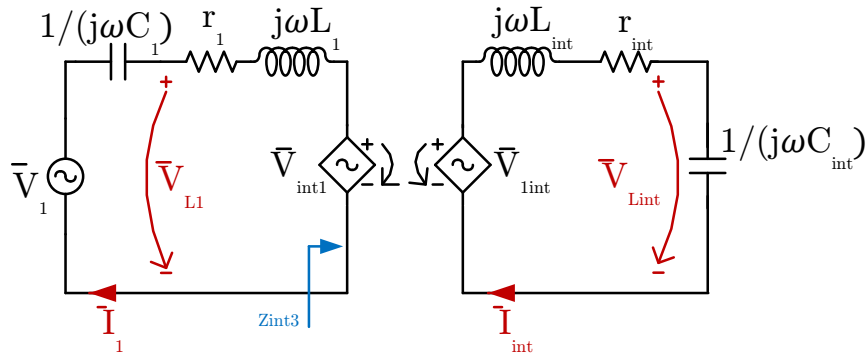
Figure 4.5: Equivalent circuitry of a series-series system.

frequency ($f_{int} \approx 145$ kHz). At this frequency, the system exhibits the maximum amplitude of Z_{in} in the original conditions (black dashed line). A deviation of C_{int} shifts the maximum amplitude to the right, if the value of C_{int} decreases from the original value, or to the left if the value of C_{int} increases. On the other hand, a variation of $\pm C_1$ almost has no effect in the amplitude of Z_{in}, with differences from the original value lower than 0.8%, as seen by the overlapped brown and blue lines over the original condition in Figure 4.6(a). Therefore, using only the amplitude analysis is not sufficient to assess the values of C_1 and C_{int}.

The phase characteristic of Z_{in}, illustrated in Figure 4.6(b), exhibits two colored regions: orange and green. The orange region depicts the impact of variations in C_1 whereas the green regions illustrate the impact of C_{int} variations. As expected, C_1 variations causes changes in the characteristics of Z_{in} (either inductive or capacitive) around the switching frequency of the inverter (82 kHz). The impedance of Z_{in} is inductive at higher switching frequencies if C_1 decreases from the original value (as seen by the brown line). This causes the system to operates in ZCS rather than ZVS. A similar behavior in Z_{in} occurs for a variation C_{int} (as seen by the green region between the red and green lines around the switching frequency). The main difference is the frequency adjustment needed to operate the system back in ZPA mode. In average, a variation of C_{int}, with a 10% tolerance, is almost identical to a variation of C_1 with a -1.4% tolerance, around the transmitter natural resonance frequency ($\omega = \omega_1$). However, around the intermediate natural resonance frequency, the impact of C_{int} variations causes a large shift in frequency value to operate the system in ZPA mode. The value of Z_{in} varies from a RL characteristic into a RC characteristic when

$$\frac{\omega^3.L_{1int}^2.L_{int}(1/b_{int}^2 - 1)}{L_{int}^2.\omega^2(1/b_{int}^2 - 1)^2 + r_{int}^2} + \frac{b_1^2 - 1}{\omega.C_1} = 0. \tag{4.29}$$

Moreover, these new ZPA switching frequencies are almost independent of variations in
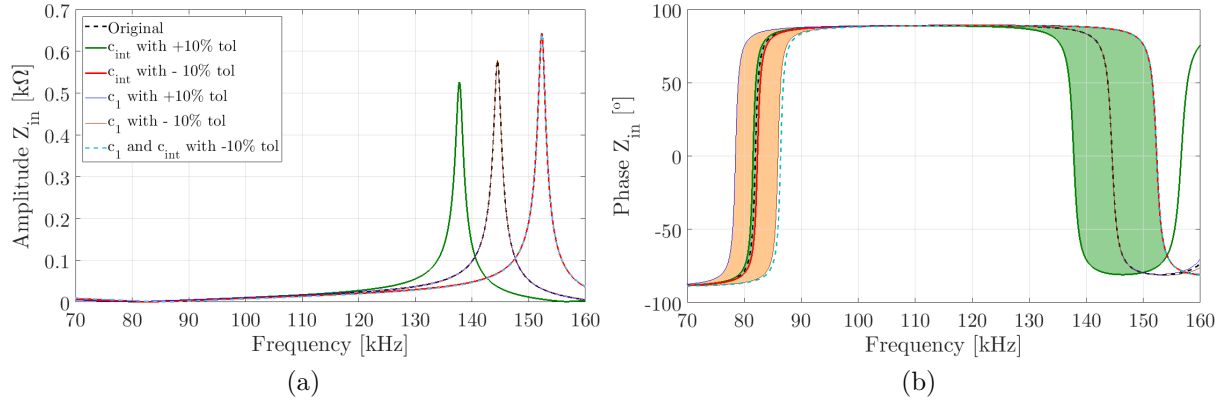
Figure 4.6: Characteristic of Z_{in} as a function of the frequency: (a) Amplitude and (b) phase, with different C_1 and C_{int} values.

C_1, as illustrated by the superimposed original line with the $\pm 10\%$ C_1 lines. Therefore, the identification of C_{int} can be made with a frequency sweep by the inverter to identify the ZPA frequencies around the natural intermediate resonant frequency together with the current gain function, given by (4.26). The identification of C_1 is then carried out using a frequency sweep around the natural transmitter frequency to determine the ZPA frequency and use this value, together with the newly found C_{int}, in (4.29) and solve it in order to C_1.

The values of L_1, L_{int}, r_1, r_{int} and L_{1int} are known from factory tests and they remain constant in the absence of the receiver. The values of L_1 and L_{int} will increase in the presence of the receiver and the new values can be determined by replicating the aforementioned process but in order to L_1 and L_{int} and using the new found values of C_1 and C_{int}.

4.3.2.2   Receiver parameters

The receiver resonant components can be identified from the transmitter (outside of the vehicle) or from the receiver side (inside the vehicle). In the second option, the vehicle controller executes a frequency sweep in a RLC circuit (it is assumed a H-bridge inverter for bidirectional applications) around its natural angular frequency (ω_2) to find C_2. Also, the frequency sweep is made without the transmitter side below the receiver side to ensure the value L_2 does not suffer any change. A new frequency sweep can be conducted with the transmitter side (the transmitter circuitry must remain opened) to infer the impact of the transmitter and intermediate coils in the value of L_2.

The estimation of L_2 and C_2 from the transmitter side is more challenging since the controller also does not know the values of L_{12}, L_{int2} and R_{eq}. The number of independent equations using only the information from the transmitter and intermediate sides is lower than the total number of unknown variables. A communication link between the transmitter

and vehicle's controller is a possible solution to reduce the number of unknown variables. In this way, the average voltage and current values in the batteries could be sent to the transmitter thus, a synchronization would not be required between both controllers.

4.4 MC Design for CC operation mode

An optimal IPT system rests on the selection of the MC and in the selection of the resonant tanks and operating frequencies. The first defines the MC geometry and corresponding dimensions while the second selects the resonant tanks frequencies to operate the IPT battery charging system as a load independent CC or CV modes. However, both designs are dependent on one another since the resonant frequencies depend on self and mutual inductance profiles, which in turn depend on the number of turns of the MC coils.

The proposed methodology provides a step-by-step approach to determine all possible combinations of resonant tanks frequencies, operating frequency range and number of turns for a list of user-defined specifications.

4.4.1 MC geometries

The non-polarized circular pad (CP), presented in Chapter 2, was modified to include the intermediate coil. Figure 4.7 shows the three proposed circular transmitter pads plus the receiver pad. Each transmitter has a unique coil arrangement to investigate the impact of having different coupling profiles between the intermediate coil and both the transmitter and receiver coils in the overall system. The intermediate coil is represented in green, the transmitter coil in red and the receiver coil in a blue color. The ferrite core is represented in dark grey. Transmitter 1 has the intermediate coil placed inwards the transmitter coil and in a coplanar fashion. The intermediate coil in Transmitter 2 is placed 30 mm above the core and with a larger diameter to increase the coupling to receiver. Transmitter 3 is a ferrite-less design. The ferrite core is replaced by an intermediate cone-shaped coil to channel the flux lines, similar to the Ferrite-less circular pad (FLCP) presented in Chapter 3. The height of the cone-shaped coil is set to 60 mm. The designs with ferrite cores are formed with N87 I 93x28x16 mm ferrite bars from Epcos and all coils are made of Litz wire with 1050 strands of 0.12 mm diameter wire.

4.4.2 Methodology

The MC design methodology is divided in three steps: pads sizing, self and mutual inductance profiling and number of turns selection.

(a) Transmitter 1

(b) Transmitter 2

(c) Transmitter 3
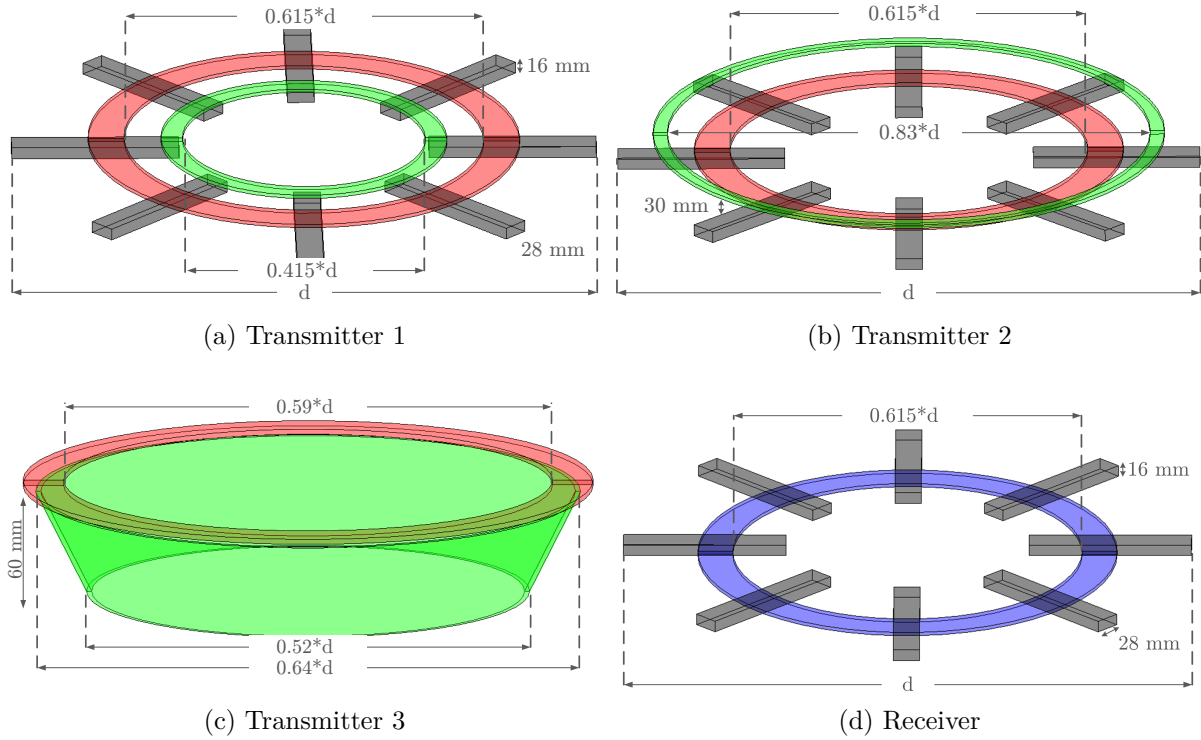
(d) Receiver

Figure 4.7: Layout of the transmitter and receiver geometries.

4.4.2.1   Pads sizing

The initial step of the MC methodology determines the minimum (d_{min}) and maximum (d_{max}) diameters for the transmitter and receiver pads. Previous studies show that if the ratio between the transmitter and receiver pads is greater than 1.6 the coupling between them is weakened. A unitary ratio between both transmitter and receiver pads was then considered as a work basis.

The value of d_{max} is set by the smallest available installation area of the transmitter and receiver pads. In most cases, d_{max} is set by the vehicle's width. On the other hand, the value of d_{min} depends on the working conditions of the IPT system. The normal height operation ($airgap$), vertical (v_t) and lateral (l_t) displacements and, the maximum value of P_{out} affect the minimum size admissible for the MC. Non-polarized circular geometries show a total decoupling between the transmitter and receiver coils if a lateral displacement of approximately 40 % of the total MC diameter (d) occurs [174]. It was found via 3D FEA tool that a maximum lateral displacement of approximately 31 % of the value d guarantees a safe operation and avoids a total decoupling scenario. This translates in a ratio between d and l_t of 3.25.

The power transfer capability of a three coil system, defined in Chapter 3, is written again in (4.30). The value of uncompensated power (P_{su}) is commonly used to assert the

quality of the MC designs. The load quality factor (Q) is set between 4 (Q_{inf}) and 10 (Q_{sup}) due to component VA ratios and tolerances [174,183]. The value of P_{su} in three coil systems depend on all coupling coefficients and self-inductance values which in turn vary with the number of turns in each coil, the *airgap* and l_t values. Therefore, the uncompensated power of the transmitter geometries, depicted in Figure 4.7, was investigated for multiple d sizes using 3D FEA simulations with the following specifications:

- Air gap (100-300 mm);

- Lateral displacement (0-350 mm);

- Number of turns in all coils (1-14);

- Diameter of the magnetic coupler (300-1000 mm);

- Value of $|\bar{I}_1|$ and $|\bar{I}_{int}|$ (0-35 A).

$$P_{out} = P_{su}.Q = \omega(k_{12}^2.|\bar{I}_1|^2.L_1 + k_{int2}^2.|\bar{I}_{int}|^2.L_{int} + 2.k_{12}.k_{int2}.k_{1int}.L_{1int}.|\bar{I}_1|.|\bar{I}_{int}|).Q \quad (4.30)$$

Figure 4.8 depicts P_{su} as a function of the air gap, for MCs with different diameters obtained, through several FEA simulations. Each colored area corresponds to a MC with a specific diameter. The lower boundary of each area is defined for $|\bar{I}_{int}| = 25$ A and $|\bar{I}_1| = |\bar{I}_{int}|/1.4$ A, whereas the upper boundary is defined for $|\bar{I}_1| = |\bar{I}_{int}| = 25$ A. The 1.4 factor between $|\bar{I}_1|$ and $|\bar{I}_{int}|$ is an average value found through Matlab simulations that compromises power transfer capabilities with the current shift from the transmitter resonant network into the intermediate resonant network to reduce the inverter losses. A higher factor would reduce even further the P_{su} of the MC, an undesired condition. The solid and dashed lines correspond to the quality factor of the load for the lower and upper boundaries of the colored areas, respectively. The MC with a 650 mm is able to transfer 5 kW, assuming the minimum load quality factor $Q = 4$, for air gap values up to 213 mm (Point 1) in the lower boundary and 237 mm in the upper boundary (Point 2). Similar values can be extracted for the remaining diameters: the 400 mm MC can transfer 5 kW up to 120 mm in the lower boundary and 142 mm in the upper boundary whereas the 850 mm MC can transfer up to 266 mm in the lower boundary and 289 mm in the upper boundary. Based on these values, the ratio between d and the *airgap* value (for a $Q = 4$) is comprised between 2.74 and 3.33 for Transmitter 1. On the other hand, for a maximum load quality factor $Q = 10$, the ratio between d and the *airgap* is reduced to values between 2.14 and 2.55 for the Transmitter 1. A similar analysis was carried out for Transmitters 2 and 3, and was found that a ratio of 2.9 between d and the *airgap* ensures an output power of, at least, 5 kW.
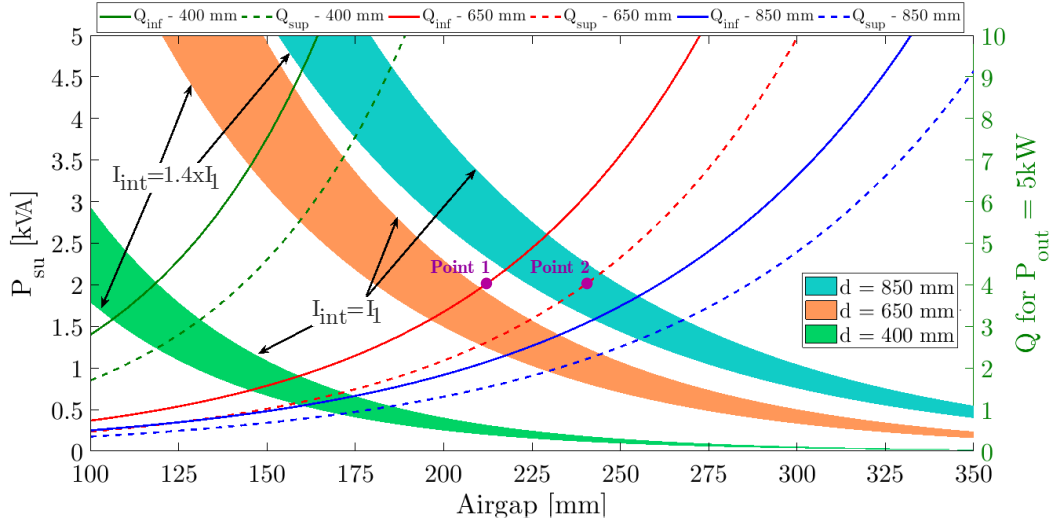
Figure 4.8: Simulated P_{su} as a function of the air gap for different MC dimensions and current values for Transmitter 1.

Figure 4.9(a) shows the impact of increasing the current limits from 25 A to 30 A while the MC properties remained the same. The air gap limit to transfer 5 kW is increased between 17 % and 27 % while the current value increases 20 %. In this scenario, the ratio of 2.9 between d and the *airgap* could be reduced to 2.5, however, the induced voltages at the coils terminals would surpass the 1000 V$_{RMS}$ limit. The number of turns of the coils also affects the power transfer capabilities since it alters the self and mutual inductance values. Figure 4.9(b) illustrates the impact of varying ± 2 turns in the receiver coil of the MC used in Figure 4.8 while the current values are kept constant at $|\bar{I}_1| = |\bar{I}_{int}| = 35$ A . The solid lines represent the quality factor for the MCs with minus two turns in the receiver coil whereas the dashed lines represent the quality factor for the MCs with two more turns. The results for the MC with a diameter of 400 mm only consider the scenario with minus two turns since the addition of two more turns would exceed the receiver limits. The variation of two turns increases/decreases, in average, the maximum air gap value by 11 %. Against this result, the air gap ratio of 2.9 would also suffer a variation of ± 11 %. Therefore, the ratio between d and the *airgap* can be set to 2.9 and it verifies most air gap and number of turns possibilities with output power levels up to 5 kW and current limits of 25 A.

The impact of lateral displacements depends not only of the current values and number of turns, but also of the air gap value in which the displacement occurs. This means that the ratio between d and the displacement, referred in this work as displacement ratio, has to be evaluated as a function of three variables. Figure 4.10(a) shows the pattern of P_{su} for several Transmitter 1 sizes at different air gap and lateral displacement values. The value of

(a)

(b)
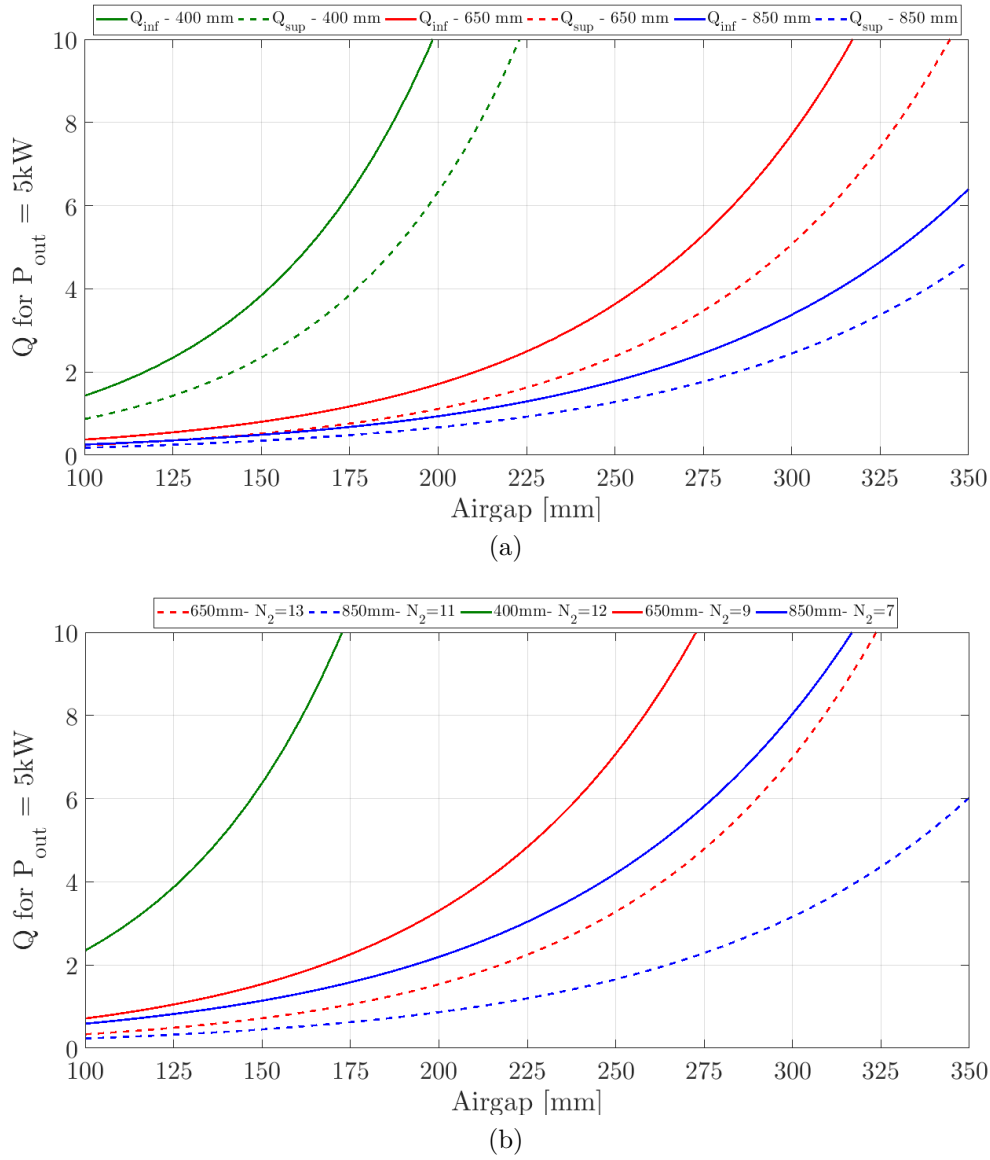
Figure 4.9: Quality factor as a function of the air gap for: (a) current limit of 30 A and (b) different turns in the receiver coil.

$|\overline{I}_1|$ and $|\overline{I}_{int}|$ is set to 30 A. As shown, the variation of P_{su} is highly affected by the air gap value at low displacement values but it tapers down for higher displacement values. As an example, the MC with a diameter of 650 mm has a P_{su} variation around 1.1 kVA at 100 mm and it decreases to 400 VA at 200 mm. In terms of ratio between d and lateral displacements, the value ranges between 2.75 and 3.33 for the MC 400 mm, 2.88 and 3.1 for the MC 650 mm and, 3.2 and 3.64 for the MC 850 mm. However, these displacement ratio ranges do not take into account the effect of different relations between $|\overline{I}_1|$ and $|\overline{I}_{int}|$. Figure 4.10(b) depicts the pattern of P_{su} for several MC sizes at different displacement and current values for a fixed air gap value. The results indicate that variations of $|\overline{I}_1|$ impacts the maximum displacement tolerance between 4 and 7 % when the air gap is set between 25 % and 30 % of the MC size. The displacement tolerance, however, increases between 7 and 13 % if the

(a)

(b)
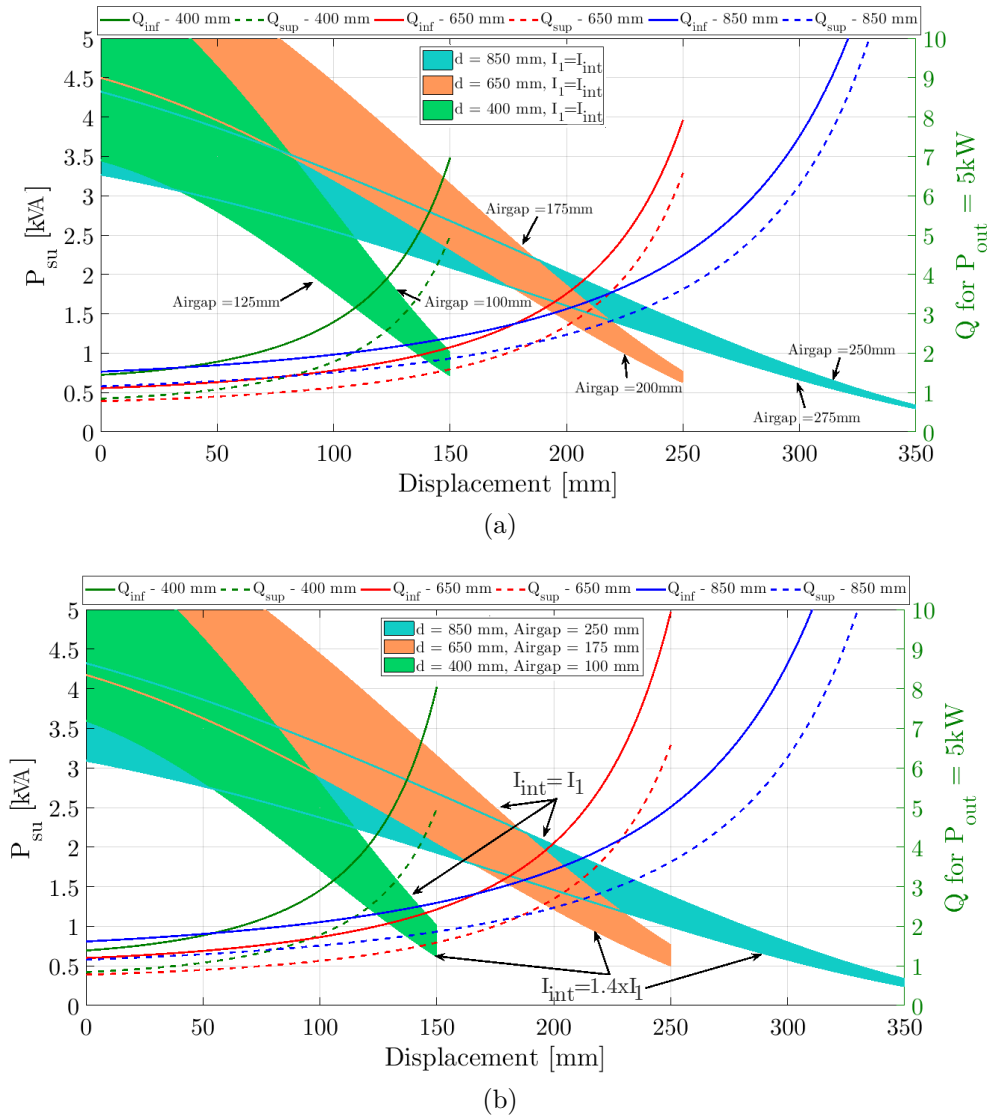
Figure 4.10: Simulated P_{su} as a function of lateral displacements for different Transmitter 1 sizes and: (a) air gap and (b) current values for Transmitter 1.

air gap is set between 20 % and 25 % of the MC size.

The combination of the results in Figure 4.10(a) and Figure 4.10(b) sets the displacement ratio ranges between 2.51 and 3.63 for the MC 400 mm, 2.58 and 3.48 for the MC 650 mm and, 2.97 and 3.98 for the MC 850 mm. These intervals guarantee an output power of 5 kW with $Q = 4$ and maximum current values of 35 A. A similar analysis was carried out for Transmitters 2 and 3. The displacement ratio of Transmitter 2 is comprised between 2.46 and 3.31 whereas the displacement ratio of Transmitter 3 is set between 2.8 and 3.79. The absence of a ferromagnetic core in Transmitter 3 together with the 35 A current threshold limits the tolerance to lateral displacements. Nevertheless, a displacement ratio of 3.25 was identified as a common ratio in all evaluated MC sizes that allows a power transfer capabilities of 5 kW, if the current limit is set at 45 A for the Transmitter 3.

To summarize, the ratios defined in (4.31) were identified under certain constraints (air

gap, lateral displacements, number of turns and maximum current values). These ratios can have variations that can exceed ± 25 % if the current and turns limits are changed. Nevertheless, these guidelines serve as a starting point in the design process and guarantee an output power of 5 kW within typical electric vehicles batteries charging applications.

$$
\begin{aligned}
& \bullet \quad d_{min} \geq 3.25 * l_t \\
& \bullet \quad d_{min} \geq 2.9 * (airgap + v_t) \qquad\qquad (4.31) \\
& \bullet \quad d_{min} \leq d_{max}
\end{aligned}
$$

4.4.2.2 Self and mutual inductance profiles

The second step of the MC methodology determines the self and mutual inductance profiles as a function of number of turns, air gap and lateral displacements. The MC characterization methodology, described in Chapter 3, is applied to the MCs shown in Figure 4.7. Table 4.1 summarizes the fitting equations that best characterize the self (L_x) and mutual (L_{12}, L_{int2} and L_{1int}) inductance profiles as a function of air gap, lateral displacements and number of turns. Table 4.7 also identifies the minimum required points to fit each equation. The unknown variables a_x, b_x and c_x are found using the fitting tool from Matlab. The self-inductance profiles (L_x), within the six charging position values, can be extrapolated as a function of the air gap and lateral displacements using a first order exponential function. On the other hand, the value of L_x follows a second order polynomial function for different number of turns.

The mutual inductance profiles of L_{12} and L_{int2} have the same pattern and only differ by a scale factor, since both the transmitter and intermediate coils are on the same side. These mutual inductance profiles follow a first order exponential function for different air gap values. In terms of lateral displacements, within the six charging positions defined in Figure 3.20 from Chapter 3, the mutual inductance profiles can be extrapolated using a Gaussian function. The Gaussian function represents the theoretical pattern of the mutual inductance between the transmitter and receiver sides from a total misaligned scenario to a perfect aligned scenario and again to a total misaligned scenario (characteristic curve in dynamic IPT systems). However, the fitting process of a Gaussian function can have a high sum of square errors (SSE) using only 3 points, especially if those 3 points do not start with a lateral displacement of 0. In alternative, second order polynomial functions can fit

Table 4.1: Fitting functions to extrapolate the self and mutual inductance profiles.

Variable	Air gap	Points	Displacement	Points	Turns	Points
L_x	$a_e.e^{b.x}$	2	$a_e.e^{b.x}$	2	$a_q.x^2$	3
L_{12}, L_{int2}	$a_e.e^{b_e.x}$	2	$a_g.e^{\left(-\left(\frac{x-b_g}{c_g}\right)^2\right)}$	3	$a_l.x + b_l$	2
L_{1int}	$a_e.e^{b_e.x}$	2	$a_e.e^{b_e.x}$	2	$a_l.x + b_l$	2

the scenarios where the Gaussian function has a poorer fitting. Both fitting processes are analyzed and it is selected the one with the best fitting results, but it is given preference to the Gaussian curve. All the mutual inductance values (L_{12}, L_{int2} and L_{1int}) vary linearly with the increase of the number of turns in one coil. For example, L_{12} increases linearly when N_1 is kept constant in the transmitter coil and N_2 is increased in the receiver coil. The previous example is valid for the remaining mutual inductance profiles. The mutual inductance value of L_{1int} suffers small variations with air gap or lateral displacements due to the presence of the ferromagnetic material of the receiver case. In either case, these variations can be fitted using a first order exponential function.

4.4.2.3 Frequencies and number of turns selection

The third step of the MC methodology determines all possible resonant tanks frequencies combinations that enable the operation of the IPT system as a quasi-load independent CC or CV modes. An iterative algorithm combines the estimated self and mutual inductance profiles, determined in step 2, with the circuit model presented in Section 4.2.

First, the algorithm determines all values of $b_{2,1}$ and $b_{int,1}$ that meet the condition defined in (4.20) for the desired operating frequency and load conditions. Then, the receiver and intermediate resonant frequencies are found using (4.5) and the capacitors determined accordingly. The value of the transmitter capacitor is obtained using (4.21). With all parameters known, the algorithm determines all electric quantities like voltage, currents, power and gain transfer functions. Finally, the solution is verified with the system constraints and added to a list of possible solutions. This process is repeated for every MC with a different set of turns and for all possible diameters.

Every system has constraints imposed by physical limitations, control restrictions, or even by government regulations. The main constraints included in the algorithm are:

- The guideline SAE J2954 proposes a operating frequency in the range of 81.38-90 kHz. The operating frequency under normal charging conditions is set to 85 kHz;

- The induced voltages in the coils are also limited by government regulations to 1000 V in Europe and 400 V in Asia;

- The maximum current values are imposed by the rated current of the Litz wire and resonant capacitors. In a series configuration, both the transmitter and receiver maximum current values are also limited by the rated current of the inverter switches and the rectifier diodes, respectively. The maximum current is then set by the smallest rated current of the components;

- The value of $\Delta G_{i_2 v_1}$ must be small to have a quasi CC mode. The load conditions and the self-inductance values affect the error difference. A difference between 2-4 % provides a good compromise between feasibility and operation.

- The capacitance range of the resonant capacitors is limited by the number of combinations between standard capacitor values. The resonant tank frequencies and/or the self-inductance values can be adjust to meet a list of available capacitance values since, it is easier to adjust an inductance rather than a capacitor.

- The operation in ZVS condition is critical for high power applications in order to reduce the switching losses of the inverter bridge as well as the stress from the commutations in the switches. The operation under ZVS is verified when the angle between the fundamental value of i_1 and the rising edge of v_1, defined as θ_1, is greater than zero (Please refer to Figure 4.3). Assuming a constant transconductance gain, for a desired value of $|\overline{I}_2|$, the value of $|\overline{V}_1|$ can be found using (4.11). The phase-shift angle (α) and the phase angle between $\overline{I}_{1,1}$ and $\overline{V}_{1,1}$, defined as θ_{11}, are then obtained using (4.1) and (4.4), respectively. Finally, the value of θ_1 corresponds to the difference between θ_{11} and $\alpha/2$. In this work, the value of θ_1 is used as an additional specification of the design methodology.

4.4.3   Optimization

The MC design methodology can provide multiple solutions that meet the list of requirements. The optimal solution depends on the metric used to sort out the solutions. The following list of metrics were used in this work:

Metric 1, Frequency - Operation in the tolerance region may require an adjustment in the operating frequency in order to maintain the system specifications. This metric selects the solution with the smaller operating frequency variation.

Metric 2, Efficiency - This metric determines the total system efficiency using (4.12), which includes the conduction losses of the inverter. The values of the coils resistances

are found using the Archimedean spiral formula to determine the total length of the Litz wire and considering a value of 0.0154 Ω/m. This value is the mean result of a series of experimental measurements made at the laboratory and considering different circular designs at a frequency of 85 kHz. This value includes the proximity, skin and core losses.

Metric 3, Cost - This metric selects the solution with less material usage. For a fair comparison between ferrite and ferrite-less geometries, it is assumed that one ferrite bar with the dimensions of 93x28x16 mm is equal to 6.5 m of Litz wire. This value was found for the current pricing rates of both materials.

Metric 4, Cost-effectiveness - The aforementioned metrics do not take into account the built-in tolerances of the capacitors as well as the presence of additional ferromagnetic material that may affect the self and mutual inductance values. As a consequence, the ZVS operation of the inverter may not be guaranteed in the entire region of operation. The cost-effectiveness metric combines the efficiency and cost metric in a weight function with the tolerance of the passive components.

The impact of each metric in the optimal solution will be addressed in Section 4.5.

4.5   Case study

This section applies the proposed methodology to an electric vehicle batteries charging system.

4.5.1   Specifications

Table. 4.2 presents the specifications and constraints of the case study. The charger has to supply a pack of 230 V batteries with a constant current in the range of 10-20 A. The minimum ($V_{bat_{min}}$) and maximum ($V_{bat_{max}}$) batteries voltage define the voltage range in which the batteries are being charged. These values are set to 193 and 230 V, respectively. The batteries voltage threshold to change from CC to CV modes ($V_{bat_{CC-CV}}$) is set at 227 V. The charging process terminates when the current in the batteries drops below 2 A. This variable is known as cut-off current ($I_{cut-off}$).

4.5.2   Methodology

4.5.2.1   Pads sizing

From the specifications in Table. 4.2, the value of d_{max} is set at 800 mm. The value of d_{min} must verify the conditions listed in (4.31). The first condition is verified for a

Table 4.2: System specifications and constraints.

System specifications	
Minimum batteries voltage ($Vbat_{min}$)	193 Vdc
Maximum batteries voltage($Vbat_{max}$)	230 Vdc
Threshold voltage from CC-CV ($Vbat_{CC-CV}$)	227 Vdc
Batteries current range (I_{bat})	10-20 A
Charging cut-off current ($I_{cut-off}$)	2 A
Normal frequency operation (f_s)	85 kHz
$airgap$	175 mm
SiC MOSFETs C2M0025120D (r_{on})	25 mΩ
Constraints	
Maximum MC diameter (d_{max})	800 mm
Maximum induced voltage in L_1($|\overline{V}_{L1}|$)	1000 Vac
Maximum induced voltage in L_2($|\overline{V}_{L2}|$)	1000 Vac
Maximum induced voltage in L_{int}($|\overline{V}_{Lint}|$)	1000 Vac
Operating frequency range SAE J2954 (Δf_s)	81.38-90 kHz
Height tolerance (v_t)	+25 mm
Lateral tolerance (l_t)	$\pm$200 mm
Maximum $|\overline{I}_1|$, $|\overline{I}_2|$, $|\overline{I}_{int}|$	35 A

diameter of 650 mm whereas the second condition is verified for a diameter of 580 mm. The value of d_{min} is then set to 650 mm. Since the maximum value of the output power is $P_{out} = Vbat_{max}.I_{bat_{max}} = 4.6$ kW and it is inferior to 5 kW, the conditions listed in (4.31) are valid.

4.5.2.2 Self and mutual inductance profiling

The self and mutual inductance profiles are estimated using MC characterization methodology from Chapter 3. A total of six charging positions, labeled from 1 to 6 in Figure 3.20, are necessary to characterize a circular geometry. The charging positions 1, 5, 2 and 6 correspond to the boundaries of the operation area, which in Cartesian coordinates ($airgap$, l_t) correspond to (175,0), (175,200), (200,0) and (200,200), respectively. Positions 3 and 4 are set to (175,80) and (200,80). In each position, the MC is modeled with two sets of turns: ($N_{1_{min}}$,$N_{2_{min}}$,$N_{int_{min}}$) and ($N_{1_{max}}$,$N_{2_{max}}$,$N_{int_{max}}$). The obtained results are then used to built the self and mutual inductance profiles. This process is repeated for each MC with a different diameter.

Figure 4.11(a)-(c) show the mutual inductance profiles as a function of lateral displace-

(a) Transmitter 1

(b) Transmitter 2
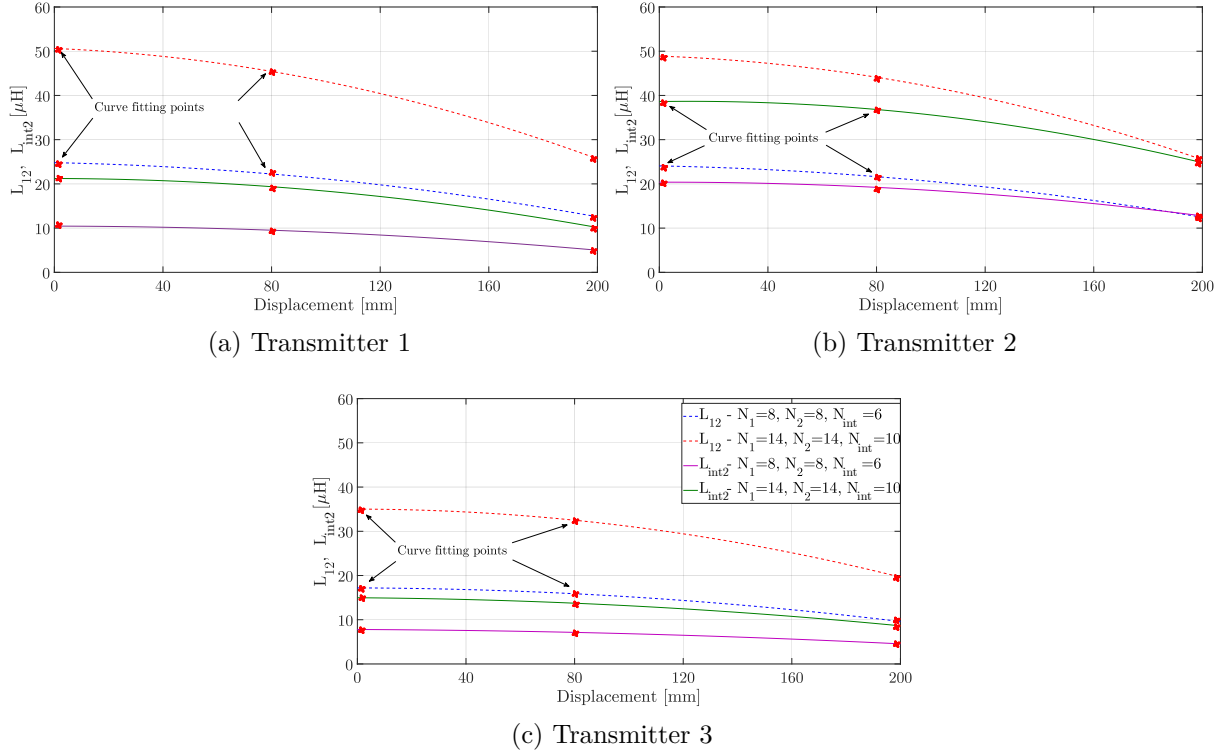
(c) Transmitter 3

Figure 4.11: Mutual inductance profiles of L_{12} and L_{int2} as a function of lateral displacements with an *airgap* of 175 mm and $d = 650$ mm.

ments. As expected, the ferrite-less Transmitter 3 shows lower mutual inductance profiles for the same number of turns, which reduces the coupling coefficient around 30% when compared with the Transmitters 1 and 2.

4.5.2.3   Frequencies and number of turns selection

The resonant tanks frequencies and the number of turns are selected using self and mutual inductance profiles, determined in the previous subsection, and the circuit model described in Section 4.2. In addition to the specifications listed in Table 4.2, the following constraints are used:

- $\Delta G_{i_2 v_1} = 2\%$ under normal operation and $\Delta G_{i_2 v_1} = 5\%$ under displacements;
- The value of the DC link (V_{DC}) is adjusted to maintain the $\alpha = 0$ in order to have a full square-wave in both charging positions 1 and 6;
- θ_1 can vary between $0°$ and $20°$.

A total of 1320 turns combinations were analyzed for each MC with a specific value of d which produce more than 20000 possible solutions.

Table 4.3: Optimization results using cost-effectiveness metric for different MC diameters.

Dia [mm]	650	675	700	725	750	775	800
Transmitter 1							
N_1 N_2	9 8 4	8 8 3	7 8 4	8 7 4	7 7 4	7 7 5	6 7 5
f_1 f_2 [kHz]	87 85.5	87 85.5	87 85.5	86.8 85.5	87 85.5	86.8 85.5	87.1 85.5
f_{int} [kHz]	148.8	145.6	142.6	148.8	142.6	145.6	137
Litz [m]	24	22.5	22.9	23.7	23	24.8	24
η	0.946	0.951	0.95	0.948	0.951	0.945	0.948
Transmitter 2							
N_1 N_2	7 8 4	8 7 4	7 7 3	6 7 4	6 7 4	7 6 4	6 6 4
f_1 f_2 [kHz]	89.8 86.8	89.6 86.8	90.3 87.3	90.1 87.3	90.1 87.3	89.7 87.3	89.7 87.3
f_{int} [kHz]	127	129.4	124.7	124.7	127	127	127.2
Litz [m] η	24.8	25.1	26.3	27.4	25.4	26.2	25.5
η	0.949	0.952	0.951	0.948	0.949	0.952	0.95
Transmitter 3							
N_1 N_2	9 11 6	10 10 6	9 10 5	9 9 6	9 9 6	8 9 6	7 9 6
f_1 f_2 [kHz]	88.6 85.5	88.4 85.5	88.3 85.5	88.5 85.5	88.4 85.5	88.7 85.5	89.1 85.5
f_{int} [kHz]	175	179.5	184.3	179.5	184.3	142.6	166.6
Litz [m]	31.9	33	31.3	32.3	33.3	32.8	32.3
η	0.946	0.948	0.949	0.948	0.948	0.946	0.944

4.5.3   Optimization

The optimal transmitter depends on the metric used to sort out all possible solutions. Table. 4.3 shows the optimal solutions for the three transmitters as a function of their diameters using the cost-effectiveness metric in the charging position 1 (175,0). All transmitters have an efficiency above 0.95 when transferring an output power of 4 kW. Regarding the resonant frequencies, all transmitters show an optimal resonant frequency of the receiver side in the range of 0.5% to 3% above f_s. The low mutual inductance values of Transmitter 3, depicted in Figures 4.11(c), are compensated with intermediate resonant tank frequencies in the range of 62% to 105% above f_s. The use of transmitters with larger diameters offer low improvements and material savings when compared with the 650 mm transmitter pads in the standard charging position 1. The use of larger transmitters increase the tolerance to lateral displacements above the specifications listed in Table. 4.2 at the cost of a larger installation area. Similar conclusions are drawn for transmitters in charging position 6.

In terms of material usage and installation requirements, Transmitter 3 requires a higher number of turns when compared with its homologous Transmitters 1 and 2 to meet the system

Table 4.4: Optimization results using the Transmitter 3 geometry with 650 mm for different selection metrics.

Metric	1	2	3	4
Charging position 1				
N_1, N_2, N_{int}	14, 13, 2	14, 14, 14	6, 13, 2	9, 11, 6
f_s, f_1 [kHz]	85, 90.9	85, 92.1	85, 88.6	85, 88.6
f_2, f_{int} [kHz]	85.4, 142.6	85.5, 142.6	85.5, 175	85.5, 175
Litz wire [m]	36.5	54.6	25.8	31.9
η	0.952	0.97	0.936	0.946
ΔG_{iv} [%]	2.42	0.623	1.97	1.94
θ_1 [°]	0	0	0	0
Charging position 6				
N_1, N_2, N_{int}	14, 13, 2	14, 13, 14	9, 14, 2	10, 14, 6
f_s, f_1 [kHz]	85.3, 90.9	85.7, 96.8	85.4, 88.6	85.4, 88.9
f_2, f_{int} [kHz]	85.4, 142.6	85.9, 122.5	85.5, 175	85.5 175
Litz wire [m]	36.5	53.1	31	37.5
η	0.926	0.94	0.905	0.909
ΔG_{iv} [%]	4.82	2.81	4.81	3.58
θ_1 [°]	3.1	5.6	2.6	2.2

specifications. As a consequence, Transmitter 3 uses, in average, 25 % more of Litz wire in comparison with Transmitters 1 and 2. Furthermore, the transmitter side is approximately 70 mm taller due to the intermediate's coil arrangement. However, the ferromagnetic core equivalence of Transmitters 1 and 2 is not being accounted for in Table. 4.3. In terms of material cost, Transmitters 1 and 2 far exceed the price of Transmitter 3. Only when assuming that 1 ferrite bar of 93x28x16 mm is equivalent to 0.7 m of Litz wire, Transmitters 1 and 2 are cheaper than Transmitter 3. At the current rates, 1 ferrite bar corresponds to 5-6.5 m of Litz wire. Also, the non-rigid configuration of the transmitter pad makes it suitable for both static and dynamic IPT charging applications. Based on the results from Table. 4.3 and the aforementioned conclusions, the Transmitter 3 with a 650 mm diameter was selected for further analysis.

Table 4.4 shows the optimal set of turns and resonant frequencies using different optimization metrics for the 650 mm Transmitter 3 in charging positions 1 and 6. All metrics provide solutions with similar efficiencies in the same charging position. Although the efficiency metric (Metric 2) has higher values, the material required to build the MC almost doubles when compared with the other metric solutions, whilst the efficiency increment is, in the best case, 3.5 %.

The frequency metric (Metric 1) solution can maintain the quasi CC mode if f_s is increased by 300 Hz while θ_1 has a maximum variation of 3.1°. The metrics 2, 3 and 4 can also maintain CC mode in charging position 6 with increases of f_s to 85.7 kHz and 85.4 kHz,

(a)

(b)
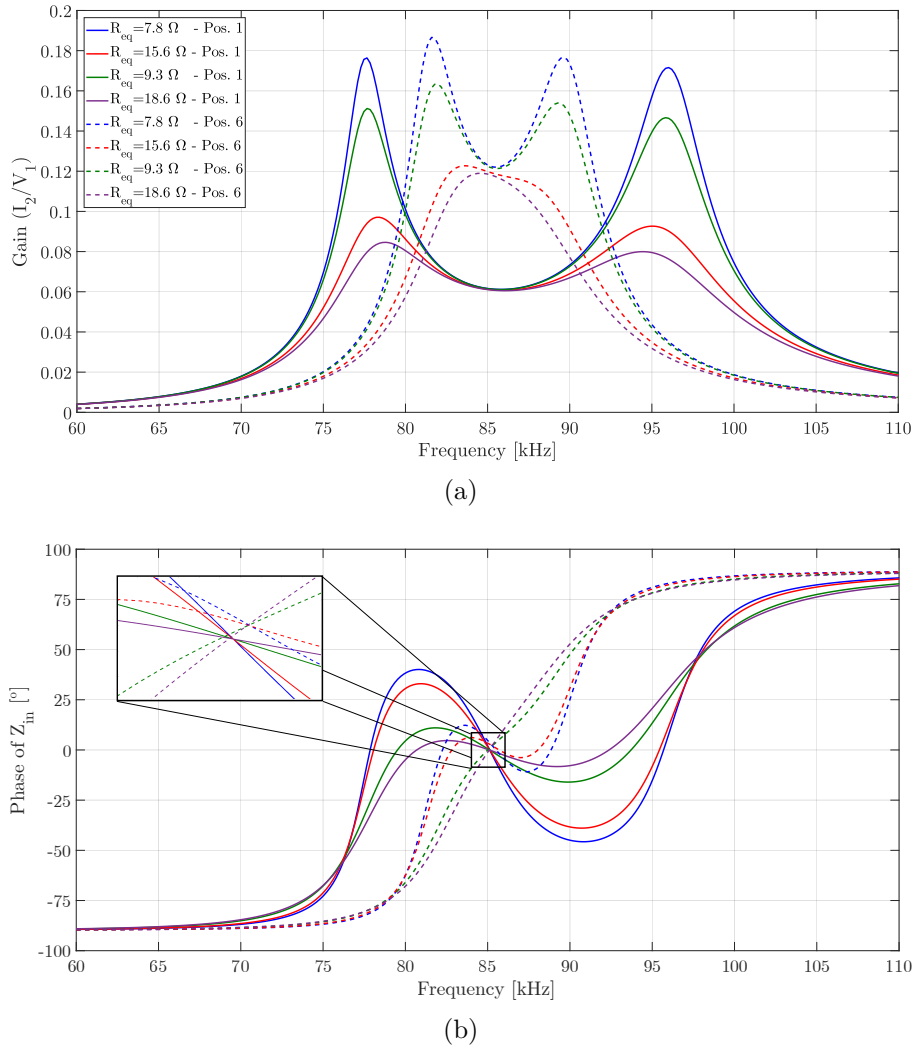
Figure 4.12: Characteristic curves of SS-IC for: (a) transconductance and (b) phase angle of Z_{in}.

respectively. In these cases, θ_1 varies between 1 and 5°, and ensures ZVS condition during the entire CC mode. However, the optimization results of metrics 1, 2 and 3 in charging position 6 can not maintain $\theta_2 < 20°$ and $\Delta G_{iv} < 6\%$ if the reactive components operate with 5 % tolerance. Only metric 4 solution compensates the built-in tolerances of the reactive components.

The results of Table. 4.4 also show the impact of vertical and lateral displacements in the copper usage of the MC. The lower couplings in charging position 6 are compensated with coils with higher number of turns to ensure that the specifications are met. The increments in copper usage vary in the range of 15-20 %, by comparing the results in Table. 4.4, between charging positions 1 and 6. It also shows the importance of having well-defined specifications to avoid unnecessary costs. The MC with the turns $N_1 = 10$, $N_2 = 14$ and, $N_{int} = 6$ from metric 4 solution was selected for experimental validation.

Figure 4.12 depicts the transconductance and the phase of Z_{in} plots as a function of the frequency in charging positions 1 (solid line) and 6 (dashed line) with the parameters of the

selected MC. The value of R_{eq} correspond to the batteries minimum and maximum voltages in CC mode over a charging current (I_{bat}) of 10 and 20 A, refer to (4.3).

Figure 4.12(a) shows a quasi CC mode in charging positions 1 and 6 with $\Delta G_{i_2 v_1}$ lower than 0.7% and 3.6%, respectively. These gain variations are even smaller if only the load values with the same I_{bat} are considered (difference between the blue and green lines or between the red and purple lines). The lateral displacements reduce the reflected impedance and increases the transconductance gain, that passed from 0.068 (solid line) to 0.123 (dashed line) in Figure 4.12(a). This patterns causes higher circulating currents in the transmitter circuit since the value of V_{DC} required to transfer the same amount of power is lower, which ultimately leads to higher losses in the inverter.

Figure 4.12(b) shows the phase of Z_{in} at the inverter terminals. The characteristic curves have crossings in the same point around 85 kHz for charging position 1 (solid lines) and, around 85.4 kHz for charging position 6 (dashed lines). As seen in the magnified rectangle of Figure 4.12(b), all load characteristics curves operate in ZPA or in the inductive region (phase of $Z_{in} > 0$), guaranteeing in both cases the ZVS condition. However, the operation in the tolerance region of the reactive components can cause a shift of the crossing point to the capacitive region. To avoid operation in ZCS, the transmitter resonant tank is designed to operate in the inductive region. The results show a compensated transmitter resonant tank with θ_{11} values lower than 4° in the entire charging operation area.

4.6   Experimental validation

The proposed design methodology was validated in a prototype built and assembled in the rear of a converted internal combustion engine vehicle, as illustrated in Figure 4.13(a). The H-bridge transmitter inverter is controlled using a real-time controller from National Instruments to generate the gate pulses to PT62SCMD12 drivers from Cree with C2M0080120D SiC MOSFETs. The receiver H-bridge rectifier includes anti-parallel diodes of the C2M0080120D Sic MOSFETs and it was placed in the vehicle's trunk, together with the protection relays, fuses and batteries. The bank of batteries is formed by 69 Lithium Iron Phosphate (LiFePo4) cells connected in series, each with a nominal voltage of 3.3 V and a capacity of 60 Ah. The AC voltage signal is measured using high-voltage differential probes P5200A from Tektronix. The transmitter (i_1) current signal is measured using the amplifier TCPA300 with the probe TCP303 whereas both the receiver (i_2) and intermediate (i_{inv}) current signals are measured using the amplifier TCP300 with the probe TCP312. All current/voltage probes have a
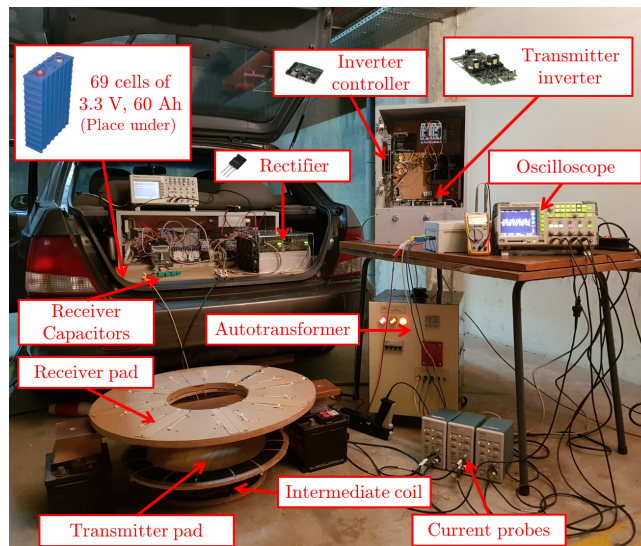
(a)
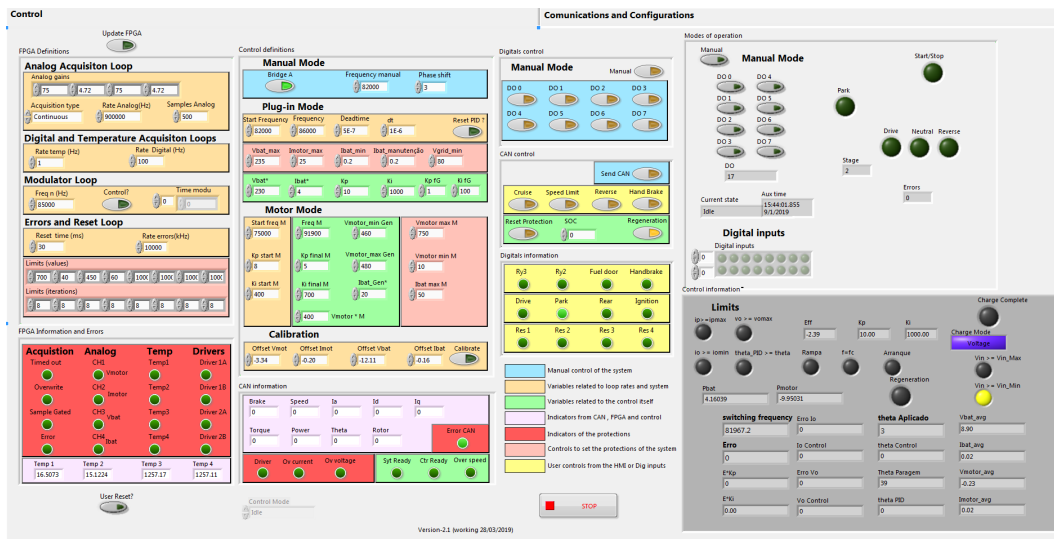
(b)

Figure 4.13: (a) Experimental setup and (b) dashboard of the Real-Time controller.

bandwidth superior to 15 MHz.

The signals are acquired by two different systems: the real-time controller (RT) and an oscilloscope. The real time controller used in this work is the CompactRIO with one C Module NI9223 and two C Modules NI9401 from National Instruments. This system has a maximum sampling rate of 1MS/s which is sufficient to determine the RMS values of the voltage and currents needed by the controller. The cRIO controller uses a Field Programmable Gate Array (FPGA) to acquire the analog signals at 1MS/s. The data is then sent via Direct Memory Access Fifos (DMA-FIFOs) to a real time Arm processor where the control is coded using the programming language Labview RT. The gate pulses resulting from the control are then sent to the FPGA which then generates a Transistor-Transistor logic (TTL) digital signal from the C Module NI9401. Figure 4.13(b) depicts the dashboard

of the RT controller that allows the user to configure not only charging parameters, but also vehicle protections and status/error messages of the motor controller using controller area network (CAN) communication. The validation of the estimation algorithm is carried out by acquiring the voltage and current signals using an oscilloscope Tektronix TPS 2014 with a sampling rate of 1Gs/s and a bandwidth of 100 MHz. The raw signals are then processed in either Labview or Matlab/Simulink.

4.6.1   Open-loop controller

One advantage of the proposed work is the operation in a quasi load independent constant current mode where the value of $|\overline{I}_2|$ is adjusted via the conduction angle (α) of the transmitter inverter. In this operation mode, the conduction angle only needs to be adjusted if the reference charging current value needs to be modified. The flowchart represented in Figure 4.14 depicts the procedure implemented in the cRIO controller to conduct the experimental tests. The system starts by identifying the mutual inductances (L_{12} and L_{int2}) and the equivalent resistance (R_{eq}) using the set of equations (4.8), (4.17) and (4.23). With all systems parameters known, it is possible to estimate the value of I_{bat} and V_{bat} using equations (4.24) and (4.3), respectively. The controller then determines the operating frequency that ensures a quasi-load independent transconductance mode using the condition given in (4.20). The transconductance gain is then determined using (4.11). With the transconductance gain known, it is possible to calculate the RMS value of the primary voltage ($|\overline{V}_1|$) needed to charge the batteries with a desired current (I_{bat}) using equation (4.24) and replaced it in equation (4.11). Finally, the phase shift angle is determined using equation (4.1). During the charging process, it is not necessary to adjust the phase-shift angle or the operating frequency, since the system operates in a quasi-load independent transconductance mode. The stop condition is set when the value V_{bat} reaches a certain threshold (depends on the type of battery). The aforementioned procedure is repeated each time the vehicle is parked to be charged or the system protections (over-current or over-voltage) go off.

4.6.2   Parameter estimation

The correct identification of L_{12} and L_{int2} is fundamental to operate the system in CC mode. Figure 4.15 compares the fitted curves of L_{12} and L_{int2} obtained in simulation with the values measured with an LCR meter (BK Precision 889A) and via the estimation algorithm described in Section. 4.3. The estimation process acquires the signals v_1, i_1 and i_{int} to estimate L_{12}, L_{int2} and R_{eq}. Figure 4.16 depicts the identification algorithm in different
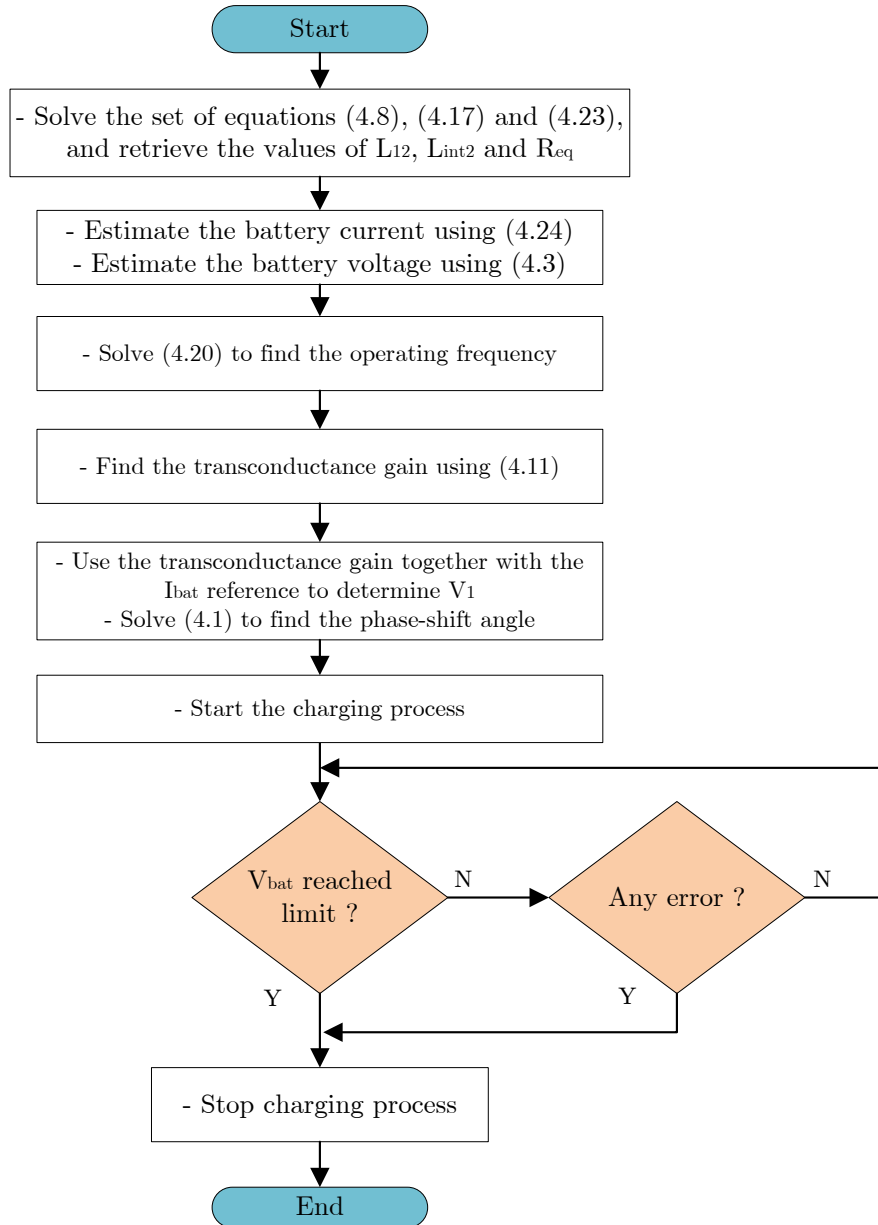
Figure 4.14: Open-loop controller implementation.

charging positions (identified using different colors). The estimation results are compared with the measured results of a LCR meter (marked with a circle). The estimation error is higher at low values of L_{12} and L_{int2} with maximum error values of 4.6 % in the identification of R_{eq}. One cause of the estimation errors is the variation of r_1, r_2 and r_{int} in different charging positions. These resistance variations occur between LCR measurements due to the tightening and loosening of the screws that connect the resonant tanks components. If the estimation algorithm contemplates a tolerance of 2 % in the values of r_1, r_2 and r_{int}, the estimation errors illustrated in Figure 4.16 would decrease to a maximum error of 3.2 %. The estimation errors will solely impact the estimation of $|\bar{I}_2|$ and R_{eq}, since the
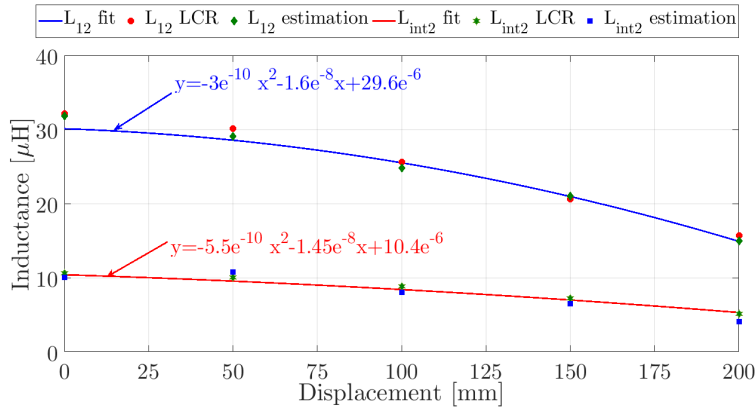
Figure 4.15: Comparison of the experimental values of L_{12} and L_{int2} using a LCR meter with fixed R_{eq} and air gap = 175 mm.

operation mode is guaranteed by the design methodology (assuming an operation within defined specifications). The measured signals in Figure 4.17 show the waveforms used to identify L_{12}, L_{int2} and R_{eq} in position 1 while charging a 224 V battery pack with $I_{bat} = 4$ A.

The non-linearity and measurement noise error introduced by the voltage and current probes also increase the estimation error values. A simulation analysis was carried out to investigate the impact of the non-linearity and measurement noise in the estimation algorithm. The voltage and current probes used in the experimental tests were characterized in terms of non-linearity and measurement noise and were cross-referenced with the simulation results.

Figures 4.18(a)-(c) depict the estimation errors of L_{12}, L_{int2} and R_{eq} for different values of phase mismatch between the current ($\overline{I}_1$ and $\overline{I}_{int}$) and voltage measurements ($\overline{V}_1$) in the charging positions listed in Table 4.5. The phase angles of $\overline{I}_1$ and $\overline{I}_{int}$ were varied in the range of $\pm 1°$ from their original values. It was assumed that both current probes are equal hence, they present the same non-linearity response towards the voltage probe. The results show that the variables L_{12} and L_{int2} have approximately the same estimation absolute errors whereas the variable R_{eq} shows a larger estimation error. The slope of the estimation error is also steeper if the values of L_{12} or R_{eq} are lower. This behavior indicates a higher sensibility of the estimation algorithm to a phase mismatch in charging positions with high air gap or lateral displacement values. Nevertheless, the estimation errors are inferior to 1 % (with the exception of condition 1), if the mismatch between the voltage and current measurements is in the range of $-0.5°$ to $0.5°$.

The existing noise in measurement signals also causes a variation in the amplitude value from its original value. Figures 4.19(a)-(c) illustrate the estimation errors of L_{12}, L_{int2} and
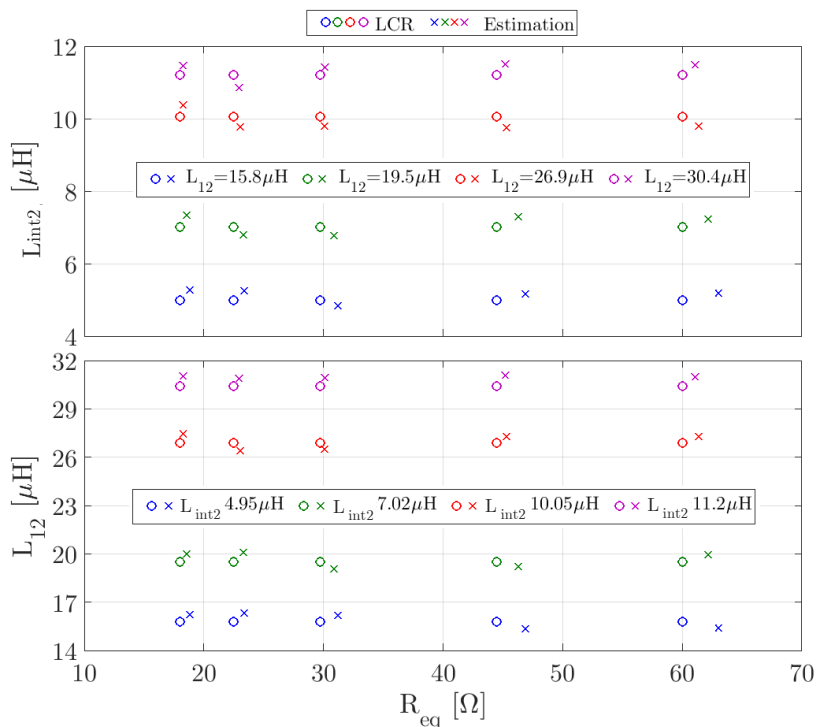
Figure 4.16: Comparison of the experimental values of L_{12} and L_{int2} using a LCR meter with different R_{eq} and air gap values.

Table 4.5: Charging conditions.

Condition	$L_{12}[\mu H]$	$L_{int2}[\mu H]$	$R_{eq}[\Omega]$
1	30.97	11.05	21
2	25.4	8.76	14
3	21	6.7	18.4
4	38	18	11.3

R_{eq} for different noise percentage values. The amplitude values of $\overline{V}_1$, $\overline{I}_1$ and $\overline{I}_{int}$ are varied in the range of $\pm 1\%$ of their original amplitude values. The difference in the estimation error between the original value (Tolerance $= 0\%$) and the worst value (Tolerance $= \pm 1\%$) is inferior to 0.5% in all charging conditions. Also, the estimation of R_{eq} is the least affected variable with an almost null slope variation in all evaluated charging conditions. Therefore, the impact of phase errors of the voltage and current probes in the estimation algorithm is greater than amplitude errors.

The current and voltage probes used in the experimental tests were characterized in terms of non-linearity and measurement noise. The probes were calibrated using the calibration equipment Omicron CMC 259 plus. The calibration is made at 3 kHz for voltage probes and at 1 kHz for current probes. The non-linearity between both voltage and current probes is also analyzed using the Omicron CMC 259 Plus. The equipment generates a sinusoidal
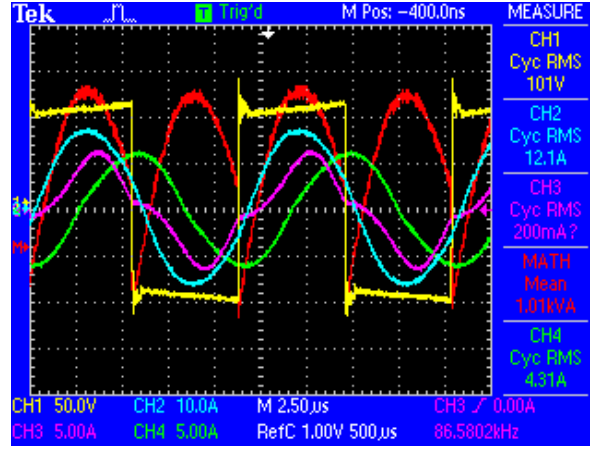
Figure 4.17: Waveforms of v_1 (yellow), i_1 (blue), i_2 (green), i_{int} (purple) and, inverter output instantaneous power (red) in charging position 1 while charging a 224 V battery pack with $I_{bat} = 4.1$ A. The fundamental phasors are: $\overline{V}_1 = 86.9\underline{/0°}$ V, $\overline{I}_1 = 11.18\underline{/-17.3°}$ A and, $\overline{I}_{int} = 3.35\underline{/-31.9°}$ A.
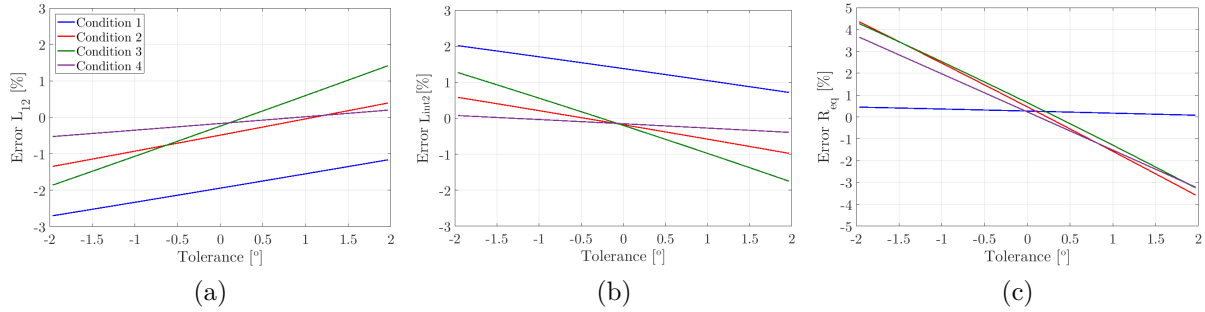
Figure 4.18: Estimation error as a function of phase mismatch in measurement acquisitions for (a) L_{12}, (b) L_{int2} and (c) R_{eq}.

current and voltage signal in phase at 1 kHz (maximum admissible frequency) and the phase difference was measured in an oscilloscope. A maximum difference angle of 0.15° was found for different voltage and current signal values. The current probes also show a maximum discrepancy between one another of 0.3° when measuring the same current signal at 85 kHz. Therefore, the selected voltage and current sensors introduce errors inferior to 1 % in the estimation algorithm.

4.6.3   Load operation

Figure 4.20(a) shows the voltage, currents and power waveforms in charging position 1, when supplying the batteries with a current of 10 A. The system achieved a maximum efficiency of 94.1 % between the inverter output and the batteries and, an overall efficiency of 88.9 %. Figure 4.20(b) illustrates the total efficiency under different air gap and displacement values and as a function of different load conditions. The low η_{sys} values are limited by the efficiency of the inverter. The operation of the inverter was set with a θ_1 around 9° to avoid the 250 ns dead-time zone of the gate drivers and ensure a ZVS operation.
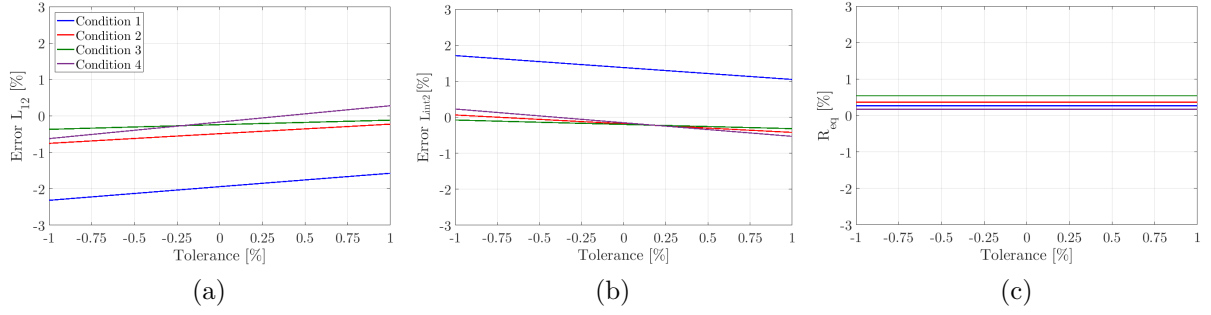
Figure 4.19: Estimation error as a function of different amplitude tolerance values for: (a) L_{12}, (b) L_{int2} and (c) R_{eq}.
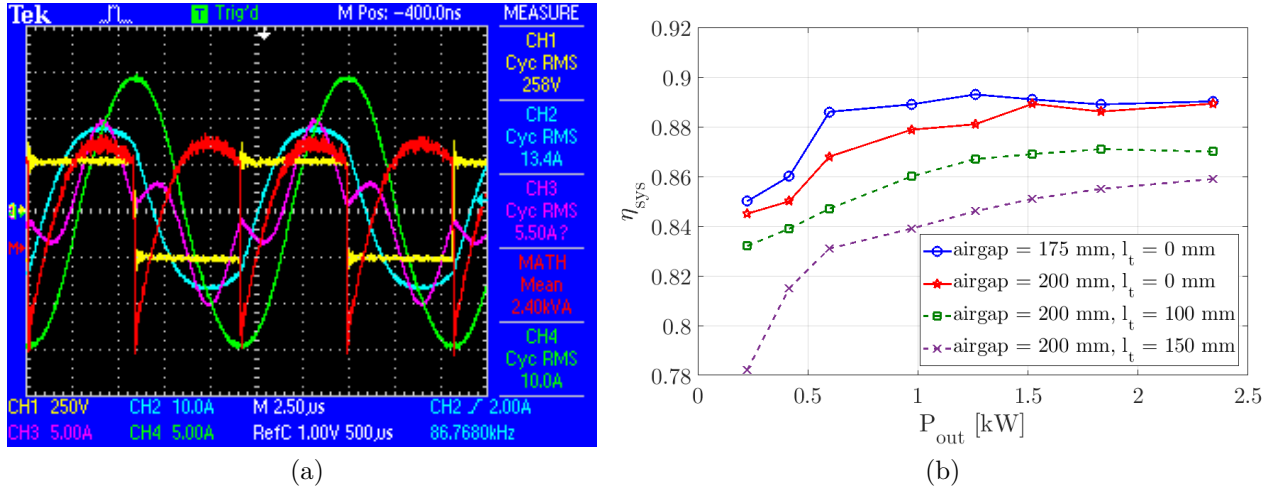
Figure 4.20: (a) Waveforms of v_1 (yellow), i_1 (blue), i_2 (green), i_{int} (purple) and, inverter output instantaneous power (red) in charging position 1 while charging a 223.5 V battery pack with $I_{bat} = 10.3$ A. (b) Total efficiency (η_{sys}) as a function of P_{out} in different charging positions.

Table 4.6 lists the experimental results from existing works in the literature together with the results from this work (last two lines). The majority of the works conducted experimental tests with air gaps in the range of 175-200 mm. One of the contributions of the proposed work is the experimental results under lateral displacements. The power deliver to the load ranges from 384 W to 6.6 kW while the total efficiency varies from 85.6 % to 95.57 %. The experimental results presented in [148] show the best efficiencies values between 94.27 % and 95.57 % when transferring power between 1.1 kW and 6.6 kW. The works [149] and [155] show similar efficiency values around 91 %. The efficiency of the experimental tests conducted in this work varies from 85.6 %, under displacement conditions, and 88.9 % under aligned charging position. The total efficiency (η_{sys}) can be deconstructed in the form of

$$\eta_{sys} = \eta_{inv} \cdot \eta_{AC-AC} \cdot \eta_{rect} \tag{4.32}$$

where η_{inv}, η_{AC-AC} and η_{rect} is the inverter, resonant tanks and rectifier efficiencies, respec-

Table 4.6: Comparison of experimental results with the existing literature.

Work	Charging Mode	Air gap [mm]	Displacement [mm]	MC	Freq [kHz]	P_{out} [kW]	η_{inv}	η_{AC-AC}* η_{rect}	η_{sys}
[148]	CV	200	0	Rectangular	100	2.2	-	-	94.72
[148]	CV	200	0	Rectangular	100	6.6	99.26	96.28	95.57
[149]	-	100	0	Circular	85	1.01	-	-	91.3
[155]	CC/CV	200	0	Circular	200	386	99.06	91.62	90.82
-	CC	175	0	Circular	86.7	2.2	92.5	95.92	88.9
-	CC	175	180	Circular	86.7	2.2	88.6	95.05	85.6

tively. The results listed in column 10 of Table 4.6 show aggregate efficiencies of $\eta_{AC-AC}.\eta_{rect}$ between 95.05 % and 95.92 % for the proposed work and in line with the remainder works. These efficiencies are the result of the high quality factors (Q) in the transmitter, receiver and intermediate coil designs, with values of $Q_1 = 210$, $Q_2 = 375$ and $Q_{int} = 130$, respectively. On the other hand, the efficiency of the inverter, listed in column 9 of Table 4.6, shows a range variation between 88.6 % and 99.26 %. The lower efficiency of the inverter in the presented work is caused by the phase difference between v_1 and i_1 to avoid the deadtime of the drivers. Consequently, the overall efficiency will be inferior to the inverter efficiency.

Table 4.7 compares the experimental results in charging positions 1 and 6. Charging position 6 exhibits larger Joule losses in the resonant tanks caused by the increase of $|\bar{I}_1|$. The value of η_{inv} decreased 2 %, highly due to shift of θ_1 from 9° to 13°. Nevertheless, the ZVS condition is kept between charging positions 1 and 6. The value of η_{sys} is similar in both charging positions. This means that a operation of the inverter with lower θ_1 would increase η_{sys} to values above 90 % in all charging areas.

Table 4.7: Experimental results in charging positions 1 and 6.

Variable	Charging Pos. 1	Charging Pos. 6
$|\bar{V}_1|$ [V]	258	171
$|\bar{I}_1|$ [A]	13.4	19.5
$|\bar{I}_{int}|$ [A]	5.7	6.5
I_{bat} [A]	10.3	10.5
P_{out} [kW]	2.3	2.35
η_{inv}	0.92	0.9
$\eta_{inv-bat}$	0.958	0.949
η_{sys}	0.889	0.856

4.7   Summary

This chapter presents a series-series resonant configuration with an intermediate coupler. A new design methodology is presented and determines the optimal magnetic coupler and resonant tanks frequencies to operate a series-series IPT system with an intermediate coupler in CC mode. The SS three-coil system exhibits a quasi CC mode when the reflected reactance from the receiver side is zero and the resonant tanks frequencies are determined accordingly. The methodology ensures a ZVS operation and a load-independent transconductance function within the desired system specifications. In this way, the battery charging process is controlled using only the off-board inverter with an open-loop control strategy, thus avoiding on-board controllable converters.

The design methodology determines multiple solutions that meet the list of specifications and constraints. The optimal solution depends on the metric used to sort out the solutions. A total of four metrics are proposed: Frequency, Efficiency, Cost and Cost-effectiveness. The first metric ensures that only the solutions that respect the frequency range imposed by SAE J2954 are admissible. The Efficiency and Cost metrics return the solution with the highest DC-DC efficiency or with the lower material usage in the magnetic coupler. The Cost-effectiveness metric combines the Efficiency and Cost metrics using a weighted weight function.

Three different intermediate coil arrangements in a modified circular MC geometry were investigated. A total of 2340 FEA simulations allow the extraction of a set of metrics that correlate the minimum pad diameter as a function of air gap and lateral displacements. A correlation of 2.9, between the maximum air gap and the MC diameter, and a correlation of 3.25, between maximum lateral displacement and the MC diameter, was found for output powers up to 5 kW.

The inverter open-loop control strategy requires the values of the mutual inductances and SOC of the batteries in order to determine the system current gain and the stop charging condition, respectively. An estimation procedure for L_{12}, L_{int2} and R_{eq}, using only the transmitter voltage and current signals together with the intermediate current signal is presented. Both design and estimation procedure were validated experimentally in a prototype assembled in a converted combustion engine vehicle. The cost-effectiveness metric offered efficiency values between 90.9 % and 94.6 % with material savings around 30 % when compared with Efficiency metric. The estimation algorithm shows maximum errors of 4.6 % in the identification of the load resistance in the worst charging positions. Moreover, the

estimation of the load resistance is the least affected variable by the existing noise in the measured signals. The proposed methodology ensures a ZVS operation in the entire operation range with an almost constant power factor and a maximum efficiency of 88.9 % when transferring 2.2 kW.

The proposed SS-IC IPT configuration with current source characteristics together with the estimation procedure creates a low-cost and reliable battery charger. In addition, it minimizes the commutation losses in the inverter with a ZVS operation in the entire load range. The presented configuration is applicable to charging scenarios with high air gap values at the expense of large driven currents. Still, the leakage magnetic fields pose significant concern in the vicinity of the magnetic coupler and additional detection systems are required to ensure no living organism or metallic object is placed between the off-board and on-board sides during the charging process.

Chapter 5

In-Wheel IPT system

The magnetic coupler (MC) optimizations, the proper selection of resonant networks and the introduction of intermediate couplers in conventional Inductive Power Transfer (IPT) systems, carried out in the previous sections of this document, mitigate the impact of large air gap values in the power transfer capability of IPT systems. Unfortunately, the air gap parameter varies from vehicle to vehicle and the applicability of IPT technology can be, ultimately, compromised in vehicles with higher ground clearance.

A new in-Wheel IPT (inWIPT) concept that uses the wheel as an intermediary stage between the off-board and the on-board sides of the vehicle is presented in this chapter. In this way, the air gap distance between the transmitter and receiver pads of the magnetic coupler (MC) is minimal and independent of the vehicle class. In addition, the power transfer requirements can be split, in the best case scenario, by the total number of wheels in the vehicle, thus reducing the overall magnetic couplers size. The chapter starts with a review of existing inWIPT configurations in the literature. The new double-coupling inWIPT concept along with its main advantages, limitations and constructive aspects is presented at the end of Section 5.1. The design and optimization of different non-polarized and polarized geometries is carried out in Section 5.2 and Section 5.3 for both magnetic couplers. The use of two consecutive MCs modify the intrinsic characteristics of resonant network configurations. Therefore, Section 5.4 derives the circuit model of double coupling IPT systems with different resonant configurations. A design methodology of the proposed inWIPT concept with voltage source characteristics is presented in Section 5.4. Experimental validation in a real-size prototype is carried out in Section 5.5 and the main conclusions are drawn in Section 5.6.

5.1 inWIPT system structure

Recent advancements in EVs traction show a trendline to incorporate the motors in the wheels [308]. The inclusion of IPT capabilities in the wheels just follows the tendency of

moving the powertrain and batteries charger from the vehicle into the wheels, leaving only the batteries itself within the vehicle [309, 310]. An early mention of inWIPT system was made in [311] and the authors envisioned the placement of several receiver coils in the rubber surface inside the tire, in replacement of the conventional IPT receiver pad placed under the vehicle. This configuration reduces the air gap distance to values that only depend on the height and/or thickness of the tire. In the best case scenario, the receiver coils are placed in direct contact with the inner rubber surface of the tire (or even within the tire), and both pads are only separated by the thickness of the rubber tire. The authors then connected each receiver coil in series with a capacitor and H-bridge rectifier to form a DC bus. All receiver coils are connected in parallel to guarantee that only the magnetically coupled coils have current during the charging process. A drawback in the proposed work is the use of slip rings to transfer the DC bus from the wheel to the on-board side. The low reliability and high maintenance of carbon brushes makes it an undesired solution. Furthermore, the placement of power electronic converters inside the tire makes them more prone to mechanical shocks. The authors in [312] also analyze an inWIPT system with main focus in the optimization of circular MCs for both transmitter and receiver pads. However, the circular design does not fully optimize the surface of a tire and no mention is made on how the power is transferred from the wheel to the vehicle.

One major concern in IPT systems is the possibility of small animals or children moving under the vehicle while its being charging wirelessly. The strong magnetic fields between the ground pad and the vehicle pad pose a significant health threat to living organisms and, as such, foreign object detection (FOD) systems are required to detect both living organisms and metallic objects in the vicinity of the IPT system. The air gap of the inWIPT system, on the other hand, is filled by the tire and there is no risk of a living organism going under the power pads. The only concern are the stray magnetic fields near the power pads, same as in traditional IPT systems. These stray magnetic fields must comply with ICNIRP guidelines and they often require the use of shielding materials like aluminum or copper sheets above the receiver pad (placed under the vehicle). The aluminum rim in inWIPT systems limits the magnetic stray fields and avoids the use of additional shield materials on the vehicle side.

The perfect positioning between the off-board pad and the vehicle's receiver pad is critical in order to achieve the highest energy transfer with optimum efficiency. Since each vehicle has different dimensions and the receiver pad can be placed in different positions below the vehicle, optical or magnetic positioning systems are installed together with IPT chargers to help the driver park the vehicle within a reasonable charging area. The inWIPT configuration
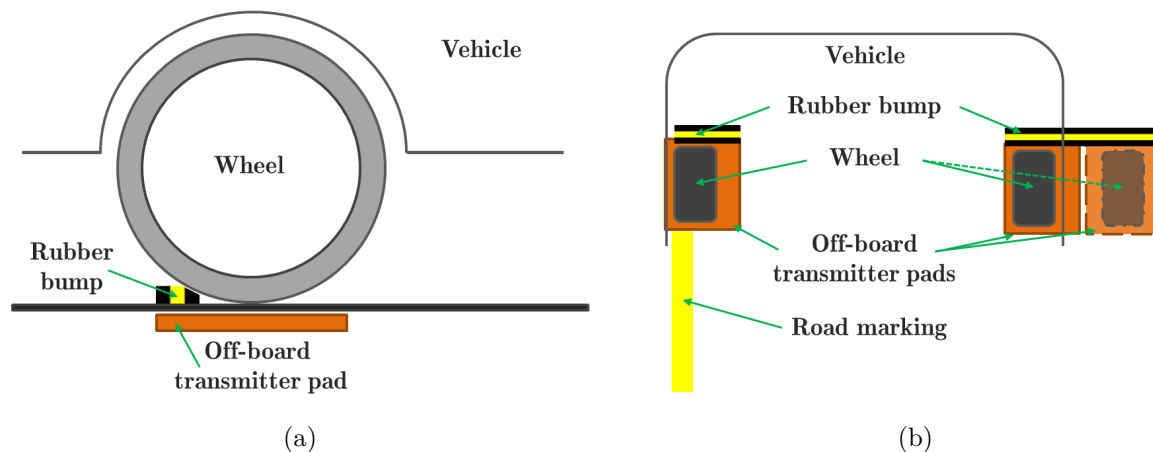
Figure 5.1: Illustration of a static inWIPT arrangement in: (a) side view and (b) top view.

avoids entirely the use of positioning systems since the optimum positioning can be met with a single rubber bumper placed above the transmitter pad. Figure 5.1 depicts the placement of the off-board transmitter pads to transfer energy using two wheels (from either front or rear axles). The driver aligns the vehicle using a road marking (illustrated in Figure 5.1 as a yellow strip) until it reaches the rubber bump placed on top of the transmitter pads. A small adjustment of the wheel may be required before the driver parks the vehicle. The adjustment consists on slightly moving the vehicle backwards until an estimation algorithm assesses the optimal positioning without additional hardware. With the vehicle in the park position, the other wheel is automatically in the correct position. Unfortunately, each vehicle has different widths that may exceed the width of the off-board transmitter pad (for the second wheel). This limitation is overcame using two off-board transmitter pads, next to one another, to increase the coverage area, as illustrated in Figure 5.1 by the dashed transmitter pad. This solution minimizes the magnetic stray fields since only the transmitter pad with the wheel over is activated.

The power transfer capabilities in traditional IPT systems depend on the component's rated current and voltage specifications (whose costs drastically increase for higher rated values). Moreover, some regulations impose limits to the induced voltage across the coils. The use of segmented coils with capacitors in series overcomes this limitation at the cost of additional components. One alternative is the use of multiple receivers to transfer the same amount of power. In this scenario, the VA rating of each receiver pad is n times lower than the desired output power, where n is the total number of receiver pads. Unfortunately, the number of receiver pads is limited by the available space area under the vehicle. The passenger compartment area is usually avoided, leaving only the front and rear sections of

the vehicle. The literature states the use of a single receiver placed in the front section of passenger vehicles, like sedans and SUVs, and several receivers in transportation vehicles like trucks or buses. The inWIPT can be inserted in every wheel without taking additional installation area. As such, the rated power of the receiver pad can be halved (if only the front or rear axle is used) or one quarter of the desired output power (if both axles are used). In transportation vehicles like trucks, the number of axles can vary between 4 and 6, each containing between two and four wheels. This means, the power rated of each receiver can be decreased up to 22 times (in 6 axles trucks). For example, a 200 kW IPT charger requires two 100 kW receiver pads (assuming a two receiver configuration as stated in the literature), or twenty 10 kW inWIPT receiver pads. The first option uses less components but they have to support higher voltage and current ratings. The induced voltages and the risk of arc between turns requires additional safety precautions in the manufacturing of the power pads. The second option uses more components but offers redundancy and lower risks of stray magnetic fields in each system.

One factor that limits the power transfer capabilities of inWIPT systems is the configuration of the tires. Steel belt tires are the most common tires in the market and, as the name suggests, they are formed by a series of steel wires in the surface of the tire to provide better adherence and stability to the vehicle. The steel wires difficult the magnetic flux passing using traditional double-D coils configuration since they offer better permeability than the air. As a consequence, they will heat up if exposed to strong magnetic fields over long periods of time. Alternatively, tires that use nylon wires instead of steel ones eliminate the risk of heating when exposed to magnetic fields [313]. The only concern is the risk of pressure increase caused by the rising of the air temperature within the tire. The temperature rising is caused by the Joule losses in the coils placed within the tire. This parameter can, however, be taken into account during the design of the inWIPT system in order to limit the maximum current in the coils. New airless tires designs are almost commercially available, namely the Uptis model from Michelin, illustrated in Figure 5.2. These new tires eliminate completely the aforementioned limitations to the inclusion of inWIPT technology into electric vehicles. Table 5.1 summarizes the main advantages and limitations of inWIPT systems for static applications.

The purpose of this work is then to improve the wheel to on-board sides energy transfer by proposing a second coupling structure. In this way, the energy transfer from the off-board to the on-board sides is made through two consecutive MCs without any physical contact. This will improve the feasibility and robustness of the proposed system in comparison with

Figure 5.2: Air-less Uptis tire from Michelin.

the aforementioned alternatives.

Table 5.1: Advantages and limitations of inWIPT systems.

Advantages
✓ Low air gap and almost independent of vehicle class
✓ Natural shield created by the aluminum rim
✓ Does not require vehicle positioning system
✓ Does not require Foreign Object Detection (FOD)
✓ Multiple receivers configuration
Limitations
✗ Limited power transfer capability with steel belt tires
✗ Lower power transfer capability (tens of kW)
✗ Multiple receiver configuration requires more components

5.1.1 Double coupling inWIPT

Figure 5.3 illustrates the proposed circuit where a common H-bridge inverter transfers energy through two consecutive MCs and respective resonant compensation networks to the batteries, using the on-board converter. The first MC, referred in this work as Outer Rim Magnetic Coupler (ORMC), enables the energy transfer between the off-board energy source and the wheel. The off-board energy system encompasses all components installed outside the vehicle, including the H-bridge inverter with respective resonant compensation and the transmitter pad of the ORMC. The wheel energy system, as the name suggests, is formed with the components attached to the wheel, including the receiver of the ORMC, the transmitter of the Inner Rim Magnetic Coupler (IRMC) and the resonant compensation that links both MCs. Finally, the on-board system includes the receiver pad of the IRMC with its respective resonant compensation, the on-board converter and batteries, as identified in Figure 5.3.
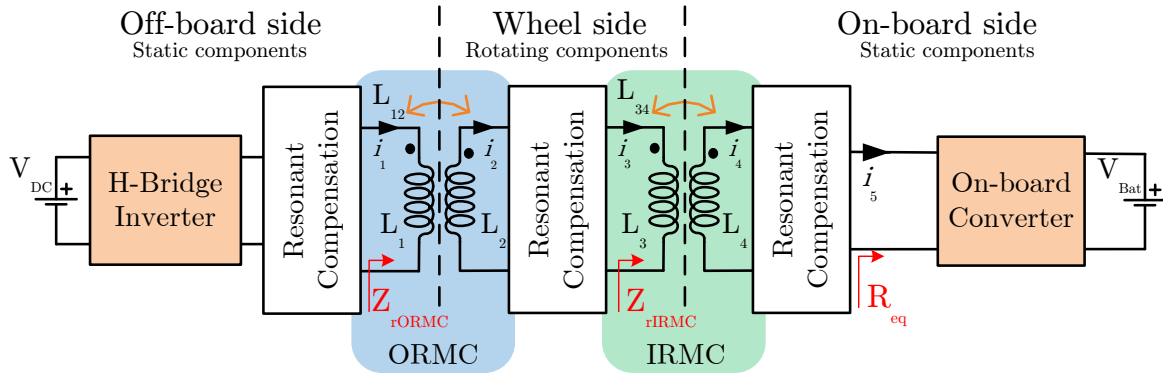
Figure 5.3: Proposed double coupling inWIPT.

The transmitter pad of the ORMC is placed underground, similar to a conventional IPT system, whereas the receiver pad is placed inside the tire, closer to the outer surface of the rim. The ORMC has the same degrees of freedom as a standard IPT system, including air gap and lateral displacements. The key difference in the inWIPT system is the lower air gap range that only depends on the height/thickness of the tire. Typical tire thickness ranges between 40 and 60 mm and an air gap variation between 20 and 40 mm will be considered in this work, assuming the placement of the receiver coils closer to the inner surface of the rubber tire. Figure 5.4 illustrates, in a exploded and assembly view, the placement of the coils within the tire (receiver pad of the ORMC) coupled to an array of transmitter pads (to illustrate dynamic charging along a roadway).

The second MC, referred in this work as IRMC, enables the energy transfer between a rotary component (wheel) and a fixed component (wheel hub and remaining vehicle) without any contact. The transmitter pad of the IRMC is fixed on the inner side of the rim whereas the receiver pad is fixed on the wheel hub assembly, which also supports the disk brakes. Both pads of the IRMC have an aluminum enclosure to mitigate the leakage flux lines while also acting as a protection barrier against intrusion, dust and water. The air gap between the transmitter and receiver pads of the IRMC, in such conditions, is constant and independent of any charging positions, thereby providing a constant coupling factor. Figure 5.4 illustrates the IRMC placement (without the aluminum case) in a wheel's hubs. The IRMC design has a cylindrical hollow shape in order to be incorporated between the breaking system of the vehicle and the inner side of the rim.

The connection between the receiver pad of the ORMC and the transmitter pad of the IRMC is made through a capacitor connected in series or parallel. In physical terms it means that the electrical terminals of the coil(s) that form the receiver of the ORMC have to cross
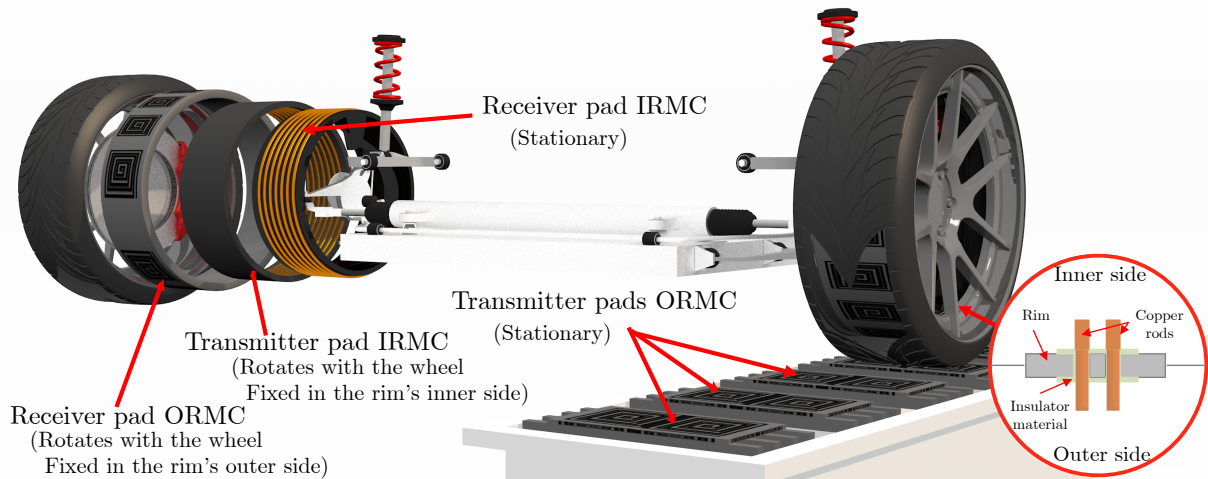
Figure 5.4: Proposed double coupling inWIPT.

the rim from the outer side to the inner side. This can be accomplished using two holes filled with a conductor material (like copper or aluminum) but electrically isolated from the rim using an insulator material (like plastic or a polymer). This physical connection is envisioned in the right lower corner of Figure 5.4. In electrical terms, the addition of a new resonant circuit between both MCs modifies the optimal charging conditions and a detailed analysis will be carried out later in this chapter. Table 5.2 summarizes the main characteristics of the ORMC and IRMC including the physical positioning, main MC geometries and degrees of freedom.

5.2 Outer Rim Magnetic Coupler

A distinctive factor in the ORMC design when compared with the conventional IPT systems is the placement of the receiver pad around the rim, as illustrated in Figure 5.5. The cylindrical shape of the rim forces the receiver coils to have a bending shape and they will be referred in this work as *saddle* coils. The cylindrical design together with the rotary movement of the wheels adds complexity to the mutual coupling analysis since it creates a new movement between the transmitter and receiver pads of the ORMC, besides the air gap and lateral displacements. Additionally, the geometry, disposition and number of coils in the receiver pad has direct impact in the coupling factor, interoperability between polarized and non-polarized transmitter pads and in the applicability of inWIPT to both static and dynamic charging applications.

An initial study was conducted to assess the best number of receiver coils and their respective size. A design angle parameter θ is introduced in this work and it relates the length of a *saddle* coil (λ_{coil}) with the radius of rim (r_{rim}), through $\lambda_{coil} = 2.\pi.r_{rim}/\theta$.

Table 5.2: Main characteristics of the ORMC and IRMC.

ORMC

- The transmitter pad is placed under the road using typical geometries like the Double-D, Bipolar, Rectangular and Circular;
- The receiver pad is installed between the inner surface of the tire and the outer surface of the rim with a cylindrical shape (not studied in the literature) ;
- The degrees of freedom between the transmitter and receiver pads include:
    Air gap: Variations between 30 and 60 mm, depending on the height of the tire;
    Lateral displacement: Typical variations between 0 and 100 mm;
    Rotation: 360° degrees coverage of the wheel;

IRMC

- The transmitter pad is placed in the inner side of the rim, inside an aluminum enclosure and with a cylindrical hollow shape (similar to a solenoid geometry);
- The receiver pad is fixed in the structure that holds the disk brakes with a cylindrical hollow shape (similar to a solenoid geometry);
- The air gap between the transmitter and receiver pads is fixed between 4 and 10 mm;
- The degrees of freedom between the transmitter and receiver pads include:
    Rotation: 360° degrees coverage of the wheel;

The range of θ is comprised between 0 and 360°, which corresponds to a full circle. Two coil arrangements for the receiver pad were studied in this work with non-polarized and polarized flux path characteristics. The first, labeled as Sad_1 configuration, is formed by a single *saddle* coil, as illustrated in Figure 5.5. The second configuration, labeled as Sad_2, consists on two overlapped *saddle* coils, similar to a Bipolar pad (BPP) design. Previous studies show the optimal overlap angle in typical IPT systems varies with the size of the coils and geometry of the transmitter pad [173, 191]. The bending shape of the *saddle* coils also affect the overlap angle. Yet, an overlap of 20° was considered as a work baseline since it provides deviations from the optimal operation point inferior to 7 % and this value has little influence in the comparison of Sad_1 and Sad_2.

The impact of θ in the coupling factor using Sad_1 and Sad_2 receiver configurations is also affected by the transmitter pad geometry. Three transmitter pad designs were selected for this assessment: a rectangular coil, the circular pad (CP) and the Double-D pad (DDP). The sizing of the CP and DDP took into account the optimizations made in [174, 183] while the rectangular pad has a size of 460 by 220 mm. All transmitter pads are comprised in a square of 460 mm and with a fixed air gap of 40 mm. The receiver pad, on the other hand, is inserted in a 18 inches rim ($\approx$ 460 mm) by 220 mm, a common wheel size. The effect of the aluminum rim, similar to conventional IPT systems, reduces the leakage magnetic flux lines and, as a consequence, also reduces the mutual coupling. However, the coupling pattern is
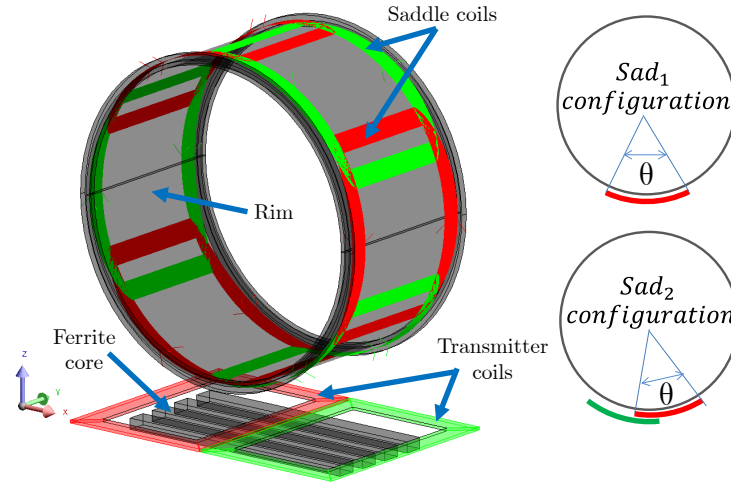
Figure 5.5: Geometry of the ORMC using the transmitter DD pad.

not modified and for that reason the rim effect is not taken into account in the comparison of Sad_1 and Sad_2 as a function of θ.

The bending shape of the receiver coils reduce the capabilities of interoperability between non-polarized and polarized pads. Thereby, the assessment of the best θ value will only consider the ORMC configurations with the same flux patterns: CP-Sad_1, Rectangular-Sad_1 and DDP-Sad_2 configurations. Figure 5.6 shows the coupling factor (k_{12}) as a function of θ with the aforementioned ORMC configurations. Maximum coupling profiles of 0.32 and 0.39 were found for the Sad_1 and Sad_2 geometries, respectively. These values are obtained for a θ of 65°, when using the Sad_2 geometry, and for a θ of 110° for the sad_1 geometry with the CP transmitter pad. Additionally, k_{12} decreases for higher values of θ thus, the analysis is limited to $\theta = 180°$.

When comparing non-polarized configurations i.e, rectangular and CP pads, they both exhibit similar peaks of k_{12}, with a difference smaller than 3 %, however, the rectangular pad does not have a ferromagnetic core. In terms of coil(s) surface area versus coupling factor, the Sad_2 configuration also has the best ratio when compared with the Sad_1 configuration. As an example, a coverage of one third of the rim corresponds to $\theta = 120°$ when using Sad_1 configuration, and to $\theta = 70°$ in the Sad_2 configuration, since the total size of Sad_2 is equal to the sum of both *saddle* coils size minus the 20° of overlap considered in this work. This analysis shows that, in the total considered range for θ, a wheel's coverage of 180° using the Sad_2 configuration ($\theta = 100°$) outperforms the Sad_1 configuration ($\theta = 180°$) by 31.5 %.

The surface coil(s) area versus coupling factor ratio is an important metric to identify the best number of coils around the rim, for a given inWIPT application. Using solely this metric, the optimal size of each *saddle* coil would correspond to $\theta = 65°$ for the Sad_2
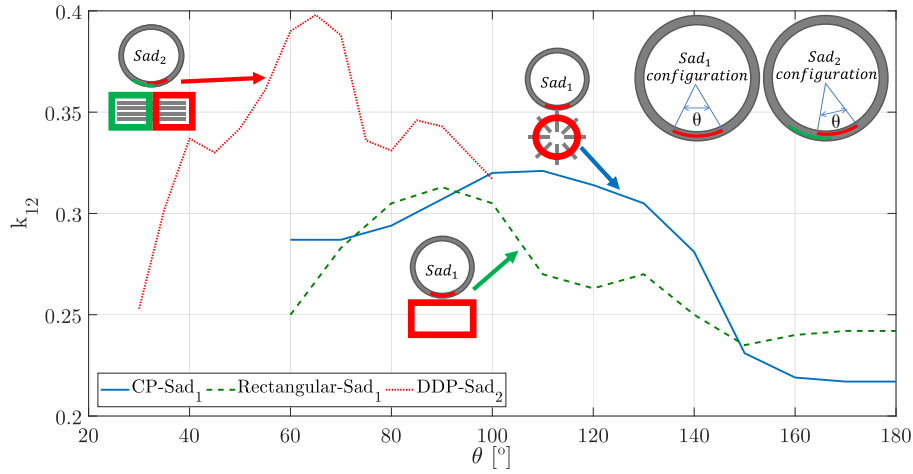
Figure 5.6: k_{12} as a function of θ using different transmitter pads.

geometry. This means, a total of 6 coils (corresponding to 3 Sad_2) would be required to have a full 360° coverage. The Sad_1 geometry, on the other hand, requires a total of 4 coils with $\theta = 105°$. This θ angle creates a slight overlap between consecutive Sad_1 coils to reduce the coupling between them.

The results from Figure 5.6 identify the best θ value for Sad_1 and Sad_2. Still, the impact of lateral displacements together with the rotary movement of the wheel has to be analyzed. The sizing of MCs in conventional IPT systems assume a unitary ratio between the transmitter and receiver pads. Furthermore, the pre-established lateral tolerance of 150 mm for IPT systems is usually attained by enlarging both transmitter and receiver pads. Unfortunately, the receiver pad of ORMC is constrained by the rim size and a unitary ratio between the transmitter and receiver pads of the ORMC may not be feasible. Therefore, and due to the lack of existing literature on the subject, a comparison of different transmitter and receiver geometry combinations with different size ratios is carried out. Figure 5.7 illustrates different admissible transmitter geometries and they are divided into two groups: ferrite and air designs. The first group, as the name suggests, includes the geometries with ferromagnetic cores like the rectangular pad ($Rect_{ferr}$), the DDP_{ferr_x} and DDP_{ferr_y}. The subscript $ferr$ in the acronym identifies the geometries with ferrite cores. The subscript letters x and y in the DDP geometries indicate the direction of the main flux path between both D-coils. The second group, on the other hand, enlists air coil designs including a single rectangular coil with ($Rect_{air_{pp}}$) or without ($Rect_{air}$) a pipe coil, the DDP_{air_x} and DDP_{air_y}. The subscript air in the acronym stands for air geometries.

Figure 5.8 depicts several receiver pad designs with different coil arrangements. For a fair comparison, all receiver designs are encompassed in an 18 inches rim with a 220 mm width.

(a) $Rect_{air}$

(b) $Rect_{ferr}$

(c) $Rect_{air_{pp}}$

(d) DDP_{air_x}

(e) DDP_{air_y}

(f) DDP_{ferr_x}

(g) DDP_{ferr_y}
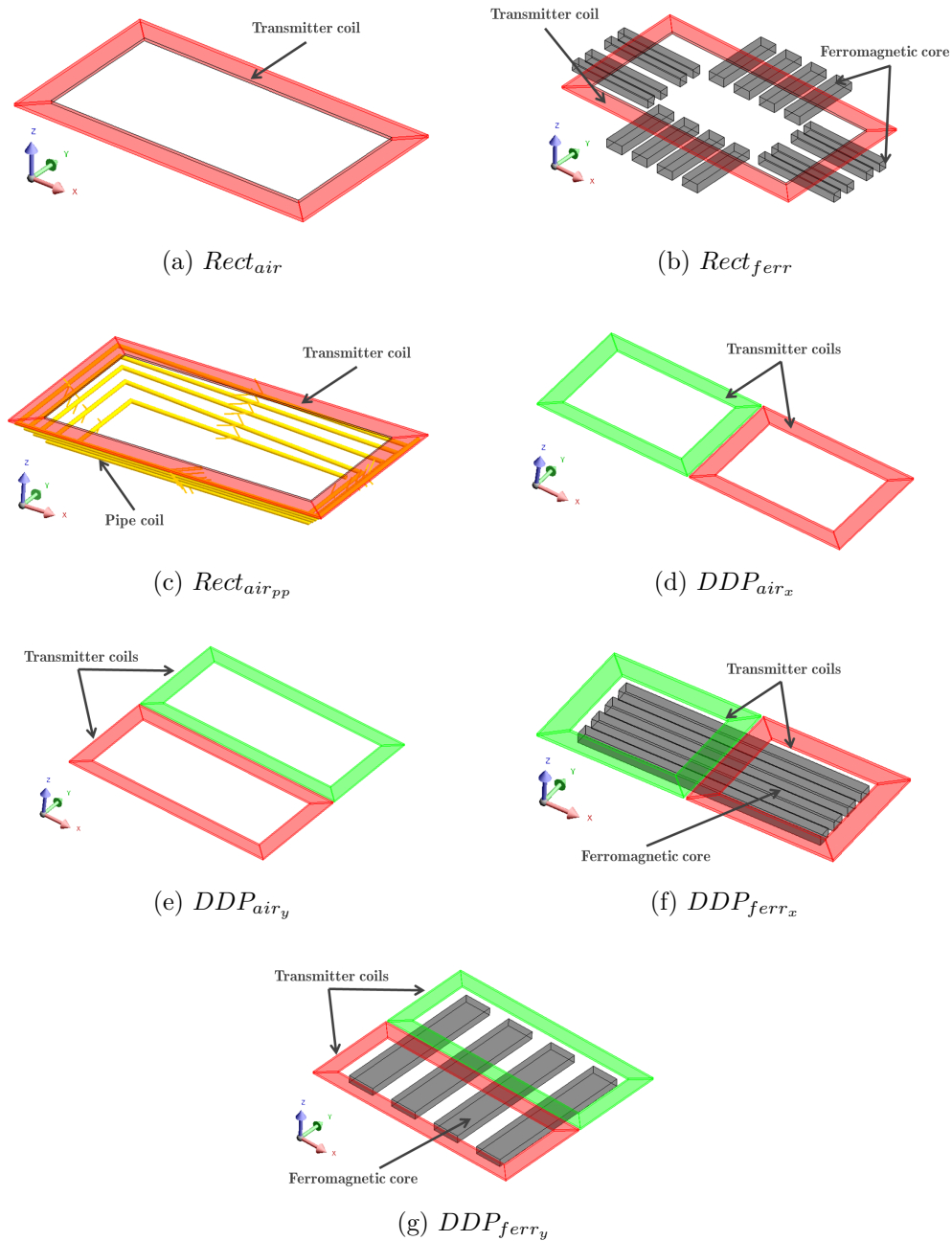
Figure 5.7: 3D view of different transmitter geometries for inWIPT systems.

Additionally, 12 ferrite bars are displaced equally around the rim to boost the coupling factor. The aluminum rim is not considered at this stage. The Sad_1 geometry, identified in Figure 5.8(a), is formed by 4 *saddle* coils equally spaced, decoupled from one another with $\theta = 105°$. The Sad_2 geometry is subdivided into Sad_{2x} and Sad_{2y}, as illustrated in Figures 5.8(b) and (c), respectively. This division is related with the positioning of the coils and the direction of the main flux path. The Sad_{2x} geometry has the main flux path along the x axis which also corresponds to the wheel's rotation. The geometry is composed by 6 *saddle* coils, overlapped and decoupled from one another with $\theta = 75°$, based on the results from Figure 5.6. The coils are connected in series in sets of 2, forming a total of 3 BPP configurations.

(a) Sad_1

(b) Sad_{2x}

(c) Sad_{2y}

(d) Sol
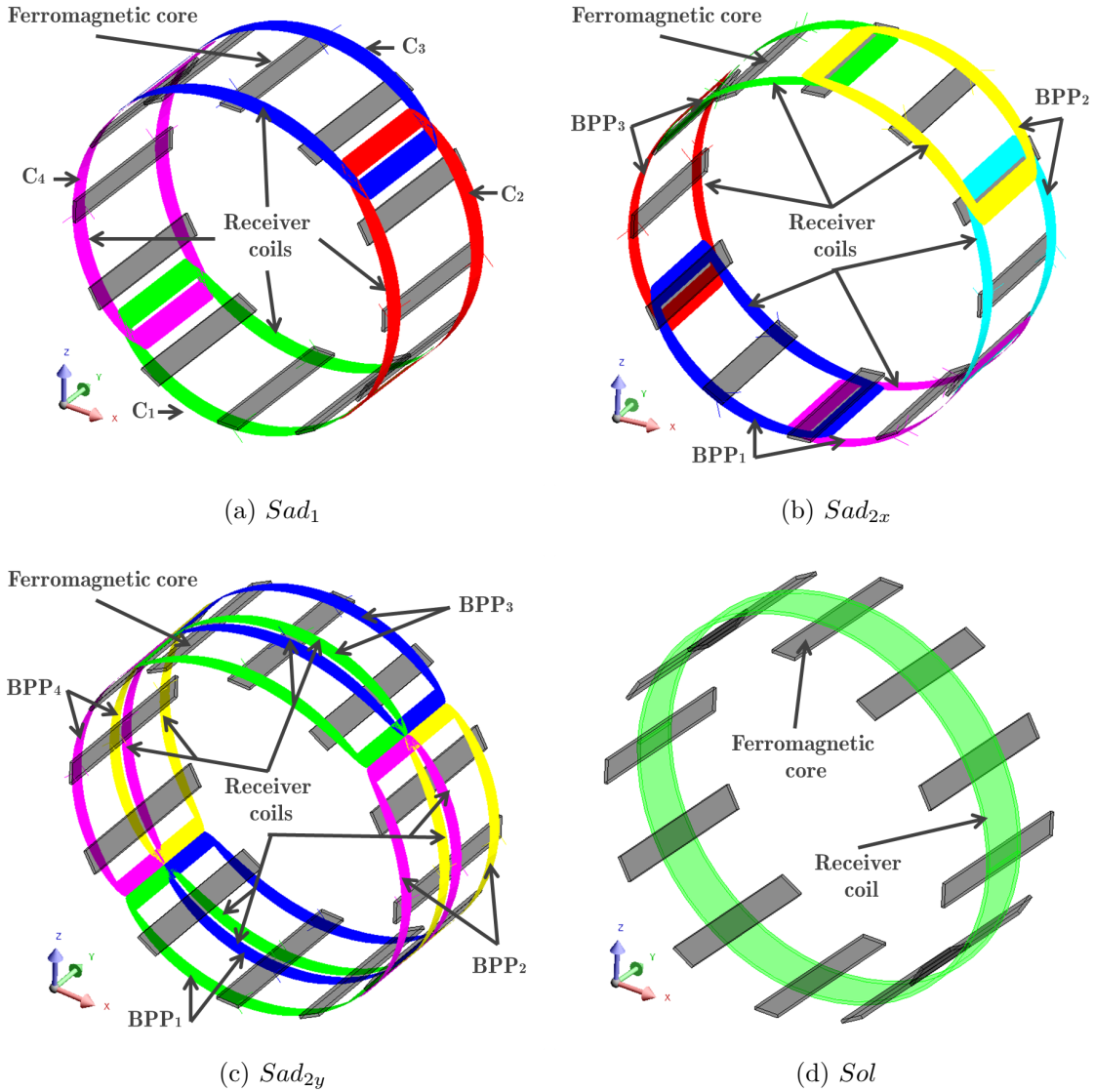
Figure 5.8: 3D view of different receiver geometries for inWIPT systems.

The Sad_{2y}, on the other hand, has the main flux path along the y axis which corresponds to lateral displacements of the inWIPT. A total of 8 coils, side by side in groups of 2, each with $\theta = 90°$, are required to fully encircle the rim. The coils are overlapped along the y axis, which means the width of each coil corresponds to half of the rim width (≈ 110 mm) plus the overlap value (≈ 30 mm). The coils are connected in series to form a total of 4 BPP configurations. Finally, the solenoid geometry (Sol), illustrated in Figure 5.8(d), is formed by a single coil that envelops the rim. As stated earlier, the curved shaped of the wheel affects the interoperability between non-polarized and polarized geometries. Table 5.3 shows the transmitter and receiver geometries with the same flux patterns.

The coupling profiles under different charging conditions are obtained via 3D Finite Element Analysis (FEA) software called Flux from Altair. The results discussed in Chapter 3 showed a good accuracy between simulation results and experimental validation, with errors

Table 5.3: Admissible combinations between different transmitter and receiver geometries with similar flux patterns.

	Geometries	$Rect_{air}$	$Rect_{air_{pp}}$	$Rect_{ferr}$	DDP_{air_x}	DDP_{air_y}	DDP_{ferr_x}	DDP_{ferr_y}
					Transmitter			
Receiver	Sad_1	✓	✓	✓	✗	✗	✗	✗
	Sad_{2x}	✗	✗	✗	✓	✗	✓	✗
	Sad_{2y}	✗	✗	✗	✗	✓	✗	✓
	Sol	✗	✗	✗	✗	✓	✗	✓

inferior to 7% in the worst case scenarios. Thereby, the comparison process of the Rect with the DDP_{ferrx} is carried out using 3D models of the ORMC geometries. Furthermore, it is assumed a constant 20 A_{RMS} sinusoidal current source working at 85 kHz.

5.2.1   Rectangular transmitter

The base dimensions of all $Rect$ transmitter geometries are identified in Table 5.4. The coil width (C_w) and length (C_l) are varied while the receiver pad remains constant. The ferromagnetic core parameters of $Rect_{ferr}$, listed in Table 5.4, are varied proportionally to the parameters of C_w and C_l. Figure 5.9(a) and Figure 5.9(b) illustrate the coupling profiles (k_{12}) of $Rect_{air}$ and $Rect_{ferr}$ as a function of C_w in multiple lateral displacement values, respectively. All transmitters with low C_w values have little or no coupling values for a lateral displacement (m_y) of 150 mm. In these charging scenarios, only 20 % receiver coil is inside the transmitter coil area and the flux created by the transmitter coil can not link the receiver coil. The increase of C_w boosts k_{12} in lateral displacement scenarios at the expense of a lower peak in a perfect aligned scenario (illustrated by the solid red line). Also, both geometries exhibit a C_w zone comprised 420 and 480 mm in which the deviation of k_{12} between different lateral displacements is minimum and inferior to 11 % and 17 % for $Rect_{air}$ and $Rect_{ferr}$, respectively. In terms of ferrite usage, k_{12} is boosted between 11 and 20 % for $Rect_{ferr}$, for a lateral displacement of 150 mm.

The type of inWIPT application, whether static or dynamic, influences the best value of C_w. In dynamic applications, the tolerance to lateral displacements is essential with the highest k_{12} possible. Additionally, a k_{12} profile as a function of lateral displacements with low variations would simplify the off-board controller and, at the same time, increase the energy transfer. The combination of these requirements results in a C_w zone between 420 and 480 mm, as illustrated by the green area in Figures 5.9(a) and (b). In static applications, system must comply with the ICNIRP rules of stray magnetic fields in the vicinity of the ORMC. This requirement is met at lower safe distances if compact MCs

Table 5.4: Dimensions of the *Rect* transmitter geometry.

Parameter	Value [mm]
C_w	220
C_l	460
F_{1l}	30
F_{2l}	150
F_{1w}	120
F_{2w}	15
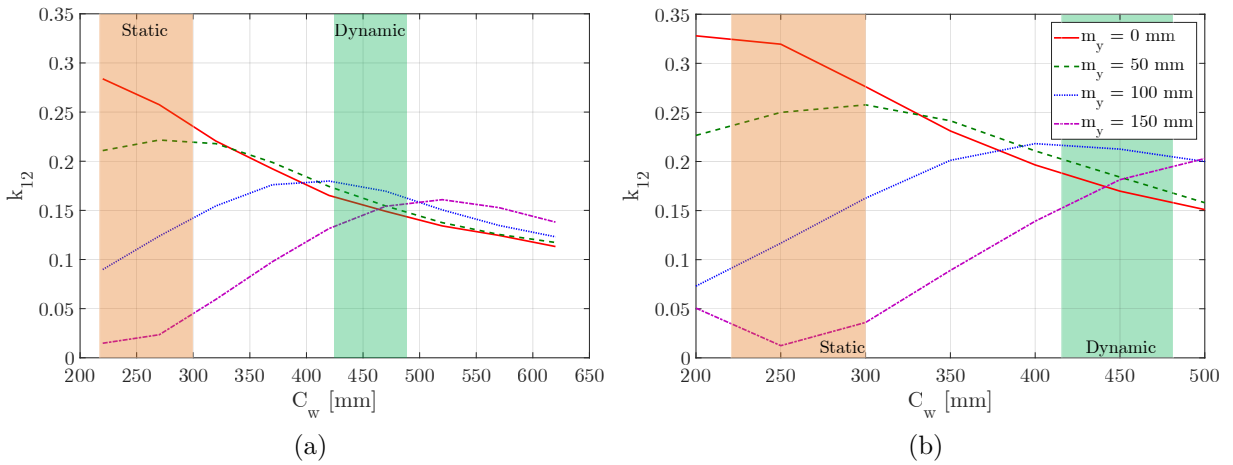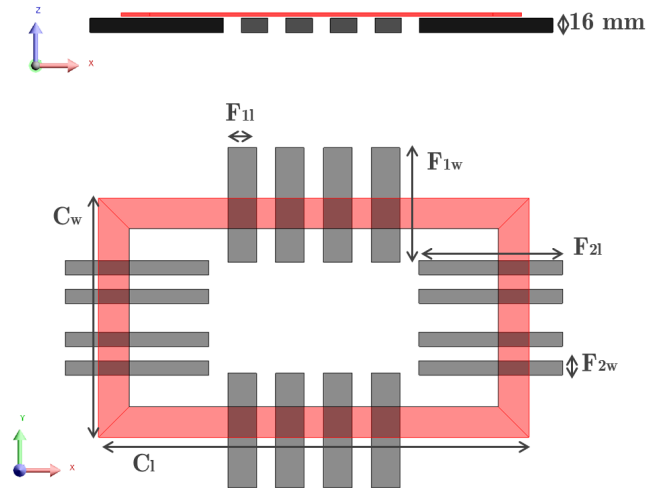
Figure 5.9: k_{12} as a function of C_w for: (a) $Rect_{air}$ and (b) $Rect_{ferr}$.

are employed. This means lower C_w are preferable with the benefit of higher k_{12} values. Moreover, as discussed in Section 5.1, a ± 50 mm lateral tolerance is sufficient for static inWIPT applications. Therefore, the C_w zone between 200 and 310 mm offers the best coupling profiles in the entire charging range. This zone is illustrated in Figure 5.9 by the orange area. The value $C_w = 470$ mm was selected as a working basis in the study of C_l, a parameter with large impact in the power transfer capabilities of dynamic applications.

The use of elongated tracks reduce the coupling, but an assessment of C_l is still needed because of the wheel's curvature. Figure 5.10 depicts k_{12} as a function of C_l for $Rect_{air}$ and $Rect_{ferr}$, in a perfect aligned scenario ($m_y = 0$ mm). Both geometries have similar decay patterns with a difference in coupling around 17 % due to the ferromagnetic core. A consequence of larger C_l values is the increase of the transmitter coil self-inductance (L_1). However, this increase is steeper for $Rect_{ferr}$ than $Rect_{air}$. As an example, and considering
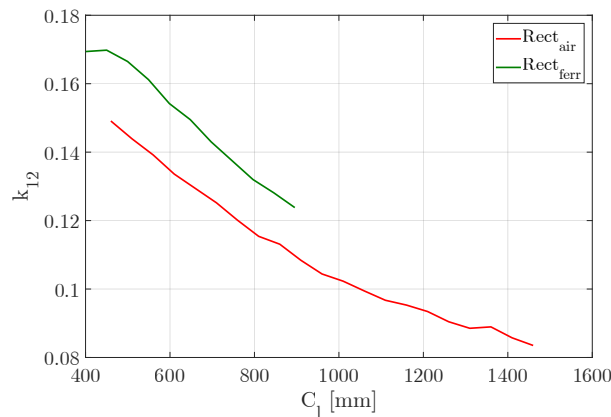
Figure 5.10: k_{12} as a function of C_l for the $Rect_{air}$ and $Rect_{ferr}$ geometries.

the same number of turns in each geometry, the value of $L_1 = 100 \ \mu H$ is obtained for $C_l = 760$ mm and $C_l = 500$ mm using the $Rect_{air}$ and $Rect_{ferr}$, respectively. The self-inductance limit can be used as a metric in the selection of C_l. Therefore, $Rect_{air}$ geometry offers a larger charging area and it's more suitable for dynamic charging applications whereas $Rect_{ferr}$ geometry offers higher k_{12} with better applicability in static applications.

The wheel's rotation translates in a linear movement along x axis (m_x), as illustrated in Figure 5.11. In conventional IPT systems, this movement has a Gaussian shape pattern. However, in inWIPT systems the wheel's rotation angle (θ_r) affects the relative positioning of the receiver coil towards the transmitter coil, affecting the k_{12} profile. Figure 5.12 illustrates k_{12} as a function of θ_r in different m_x positions, for a $Rect_{ferr}$ geometry with the dimensions $(C_l, C_w) = (500, 450)$ mm. The results show that at different m_x values, k_{12} exhibit similar maximum values, depending on θ_r. When compared with conventional IPT systems ($\theta = 0°$), the optimal charging position can be achieved under different m_x displacements, depending on the θ_r value. For example, for a $m_x = 200$ mm, a traditional IPT system would exhibit $k_{12} = 0.86$ (purple line with $\theta = 0°$) whereas in an inWIPT system k_{12} has maximum value of 0.153 for $\theta = -45°$. Unfortunately, the opposite behavior also occurs, i.e, no coupling values with high values of θ_r, even when $m_x = 0$ mm. The coupling link is reinforced if the value of θ_r guarantees the receiver coil faces the transmitter coil area, otherwise the link is weakened, as illustrated in Figure 5.11 by the dashed reference lines.

The initial positioning of the receiver coil when entering the transmitter pad area is responsible for the optimal k_{12} along the x axis. A new parameter δ is introduced in this work and identifies the difference angle between the laterals of the transmitter and receiver coil, when the rim center point is aligned with the lateral of the transmitter coil. A $\delta = 0°$, assuming that both transmitter and receiver coils have the same size, corresponds to a perfect
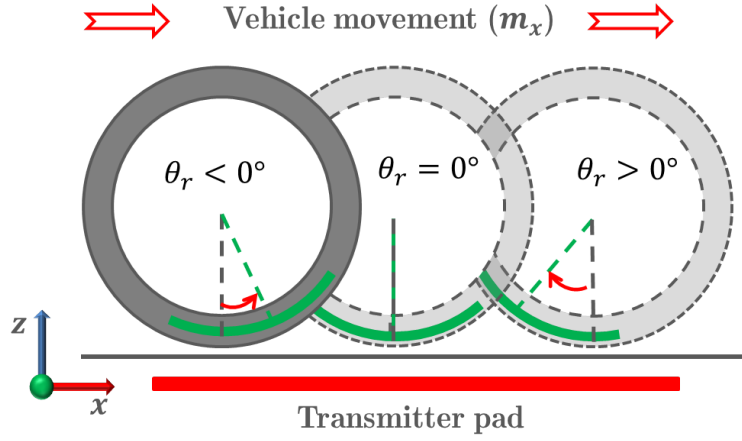
Figure 5.11: Illustration of the wheel's movement along the transmitter pad.
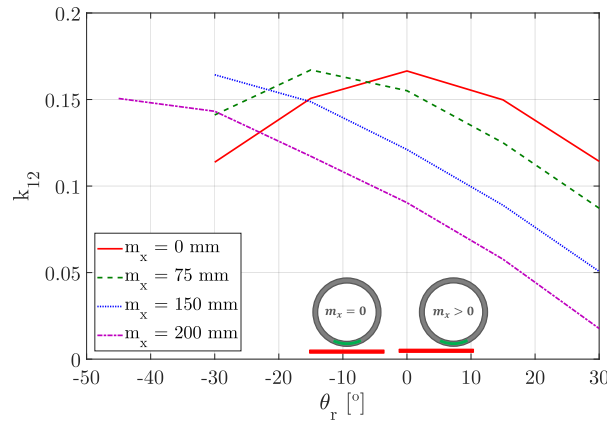
Figure 5.12: k_{12} as a function of θ_r for a $Rect_{ferr}$ in different m_x values.

alignment of both pads in the middle position. A positive δ, measured in clockwise direction, means that part of the receiver coil is out of the transmitter coil limits, as illustrated in Figure 5.13(a). Figures 5.13(b)-(c) show $k_{12_{cx}}$ in all 4 receiver coils of $Rect_{air}$ for δ equal to 82.5, 52.5 and 22.5°, respectively. The subscripts $c1$ to $c4$ in variables or electric quantities identify the receiver coil to whom they are associated with. The results show a shift of the optimum $k_{12_{c2}}$ (dashed green line) along the x axis while $k_{12_{c1}}$ (solid red line) exhibits different coupling patterns. The charging scenario with similar $k_{12_{c1}}$ and $k_{12_{c2}}$ patterns, illustrated in Figure 5.13(d), has lower coupling peaks when compared with other scenarios. The coupling variation (Δk_{12}) along the transmitter length is the difference between the maximum and minimum coupling values and in the studied configuration, the minimum corresponds, in most cases, to the intersection of two $k_{12_{cx}}$ patterns of adjacent receiver coils. For example, Δk_{12} is equal to 0.084 in Figure 5.13(b) and it corresponds to the difference between the maximum of $k_{12_{c2}}$ and the intersection of $k_{12_{c1}}$ with $k_{12_{c2}}$. This value is reduced to 0.039 if the charging conditions of Figure 5.13(d) are met.

The impact of C_l in the patterns of k_{12} with the same δ conditions is depicted in Figure

(a) δ measurement
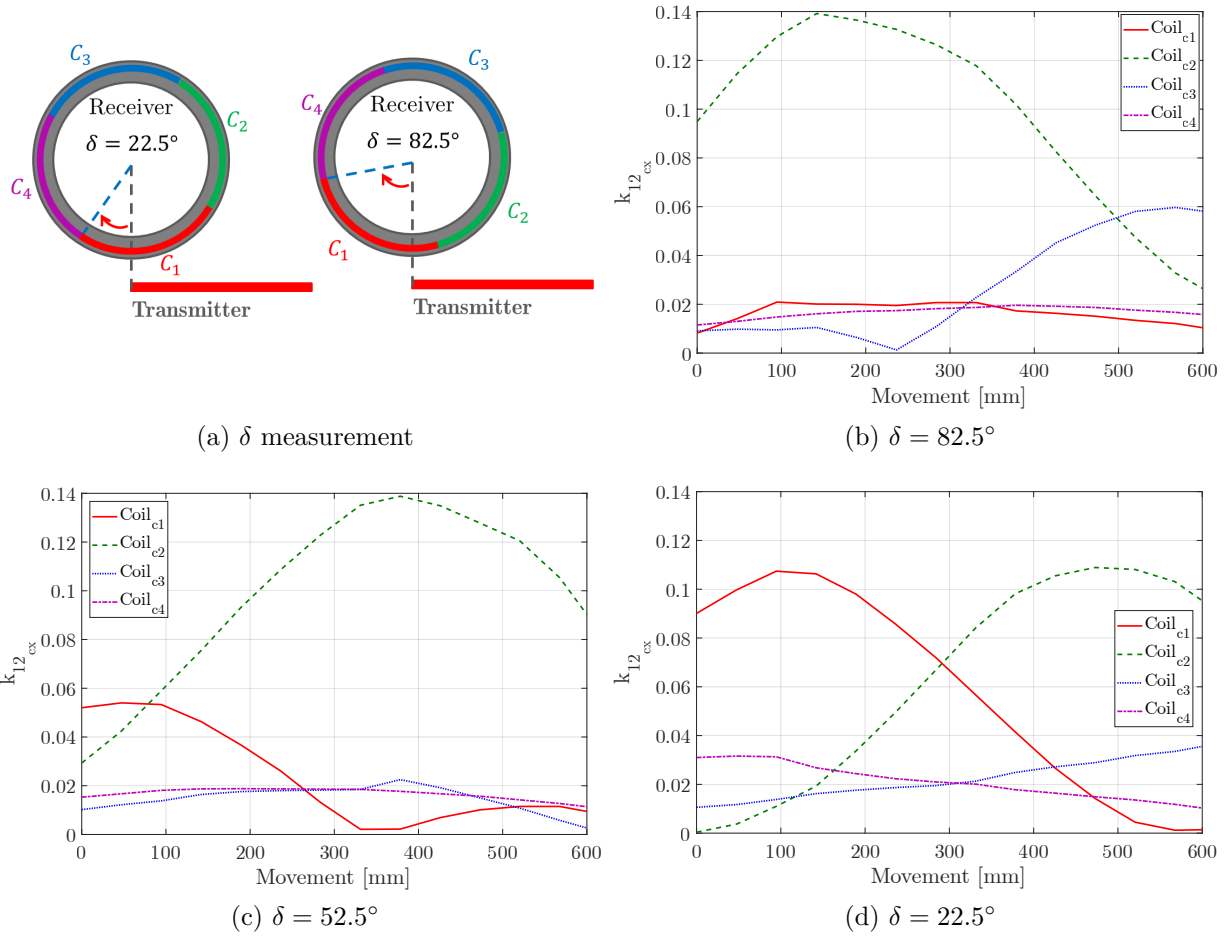
(b) $\delta = 82.5°$

(c) $\delta = 52.5°$

(d) $\delta = 22.5°$

Figure 5.13: Effect of different δ in k_{12} using a $Rect_{air}$ with the dimensions $(C_l, C_w)=(600,470)$ mm for: (a) δ illustration, (b)$\delta = 82.5°$, (c) $\delta = 52.5°$ and (d) $\delta = 22.5°$.

5.14 using $Rect_{air}$ transmitters with 500 and 800 mm. The results for the $Rect_{air}$ transmitter with $C_l = 600$ mm are already presented in Figure 5.13. Longer transmitter coils display higher Δk_{12} and k_{12} values below the minimum admissible coupling of 0.05. Therefore, depending on the δ value, the admissible charging length of the 800 mm $Rect_{air}$ is shorten up to 22 %. In contrast, the 500 mm $Rect_{air}$ offers k_{12} values above 0.1 between 41 and 86 % of C_l. This interval decreases for the 600 mm $Rect_{air}$ with a range from 48 to 60 %. In dynamic applications, this feature allows a higher energy transfer rate whereas in static applications it offers a wider parking tolerance since the top of k_{12} Gaussian shape is wider.

The coupling patterns of Figure 5.13 and Figure 5.14 are difficult to predict in static charging applications since δ depend on external factor like the driver and parking maneuvers. In dynamic applications it adds complexity in the placement of the transmitter pads along the road to avoid the worst the coupling patterns. Based on the presented simulation results, the sizing of $Rect$ transmitter geometries differ between static and dynamic applications as follows:

Figure 5.14: Effect of different δ in k_{12} using a $Rect_{air}$ with the dimensions (C_l, C_w)=(500,470) mm for: (a), (c) and (e) and with the dimensions (C_l, C_w)=(800,470) mm for: (b), (d) and (f).

- **Static Applications**

  - The ratio between C_w and the receiver coil width (which corresponds to the width of the tire) can be set from 1 to 1.45. This range was found by taking into account the results from Figure 5.9 and assuming a receiver coil width between 180 and 220 mm. Within this range, the ORMC offers k_{12} above 0.2 and lateral tolerances of ± 50 mm.

  - The ratio of C_l with the receiver coil length (which corresponds to $\theta = 180°$) is set between 1.16 and 1.33. This range was determined using the results from Figure 5.10 and ensures the maximum k_{12} admissible with the widest parking tolerance.

- **Dynamic Applications**

– Similarly to static applications, the ratio between C_w and the receiver coil width takes into account the green areas from Figure 5.9 and assuming a receiver coil width between 180 and 220 mm. A range between 1.9 and 2.36 was found and ensures a lateral displacement tolerance of 150 mm with similar k_{12} within the interval;

– The ratio of C_l with the receiver coil length is set from 1.33 to 1.64. This range fully utilizes the transmitter coil length with k_{12} values above 0.05.

The aforementioned ratios provide a ballpark set of sizing rules for $Rect$ transmitter with Sad_1 receiver geometries.

5.2.2   Double D transmitter

The base dimensions of the DDP_{ferrx} are identified in Table 5.5. The width of each transmitter coil (C_w) and length (C_l) are varied proportionally while the receiver coils that form the Sad_{2x} geometry remain constant. Each receiver coil has a $\theta = 65°$ with an overlap of 20° and they are inserted in an 18 inches rim with a width of 220 mm.

Table 5.5: Dimensions of the DDP_{ferrx} transmitter geometry.

Parameter	Value [mm]
C_w	200
C_{wint}	136
C_l	460
F_l	380
F_w	20

Figure 5.15(a) illustrates k_{12} as a function of C_w in multiple lateral displacement values. A distinctive advantage of the DDP geometry in comparison with non-polarized geometries like the rectangular pad is the better tolerance that offers to lateral displacements (along the y axis). This benefit is evident when the purple dashed lines ($my = 150$ mm) of both Figure 5.9(a) and Figure 5.15(a) are compared. In the $Rect$ geometry the value of k_{12} is 0.012 whereas in the DDP geometry this value increases to 0.076. The maximum k_{12} value, under perfect aligned positions ($my = 0$ mm), increases by almost 24 % in the DDP when compared with the $Rect$ geometry. The increase of C_w in DDP boosts the values of k_{12} under lateral
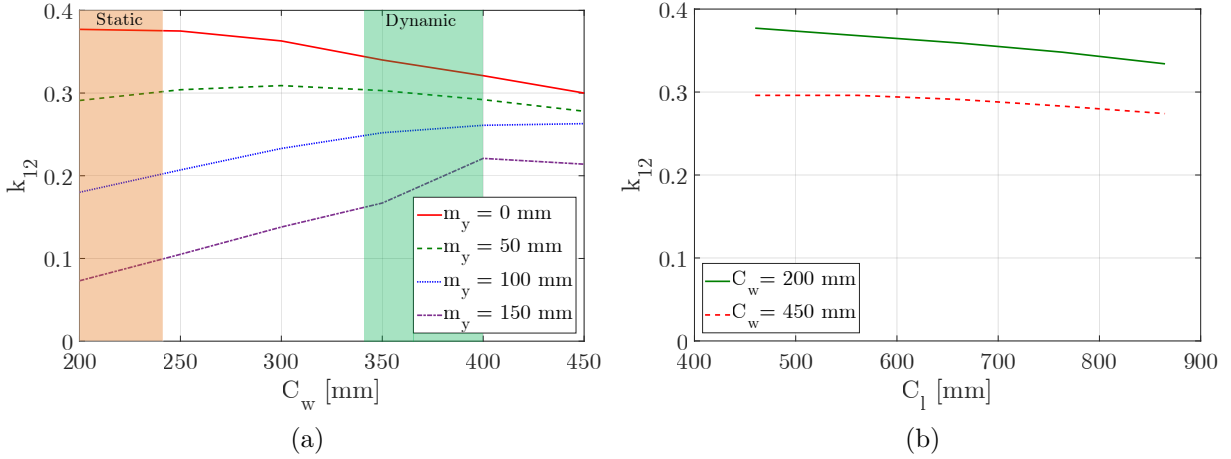
Figure 5.15: k_{12} as a function of: (a) C_w and (b) C_l.

displacements to values above 0.2. However, in perfect aligned positions (red line in Figure 5.15(a)), the value of k_{12} decreases in a second order polynomial pattern. Consequently, the value of k_{12} decreases 15 % if the ratio between the width of the transmitter and receiver coils increases by a factor of 2 (Cw increases from 220 to 440 mm). Therefore, and similarly to the *Rect* geometry analysis, two zones can be identified for static and dynamic applications. For static applications, the value of C_w is comprised between 200 and 240 mm when using a receiver coil with a width of 220 mm. This range ensures a coupling above 0.295 within the lateral tolerance of $\pm$ 50 mm with little variations. These results translate in a ratio between C_w and the receiver coil width comprised in the range of 0.91 and 1.1. On the other hand, the value of C_w is set between 340 and 400 mm for dynamic applications, resulting in a ratio between C_w and the receiver coil width in the range of 1.55 and 1.82.

Figure 5.15(b) shows k_{12} as a function of C_l with two DDP geometries with different C_w values in a perfect aligned position (my =0 mm). Both geometries have similar second order polynomial patterns with smooth decays. In both geometries, the variation of k_{12} is inferior to 8 % for C_l values between 460 and 880 mm. This behavior contrasts with the rapid exponential decay of *Rect* geometries, illustrated in Figure 5.10. These results show the *DDP* geometry as the preferable option for dynamic applications, as it offers higher k_{12} values for longer transmitter coils when compared with the *Rect* geometry.

The entry point of the wheel in the transmitter DDP geometry affects the value of k_{12}. Figure 5.16 illustrates the coupling profiles in the three *Sad2* geometries placed around the wheel with a $\delta = 55°$. The selected δ corresponds to the middle position of the $Sad2_{c1}$, as illustrated in Figure 5.16(a). The k_{12} profiles, shown in Figure 5.16(b), have similar patterns to the *Rect* geometry, illustrated in Figure 5.13(c). The value of k_{12} from $Sad2_{c1}$ (red solid

(a) δ measurement

(b) $\delta = 55°$
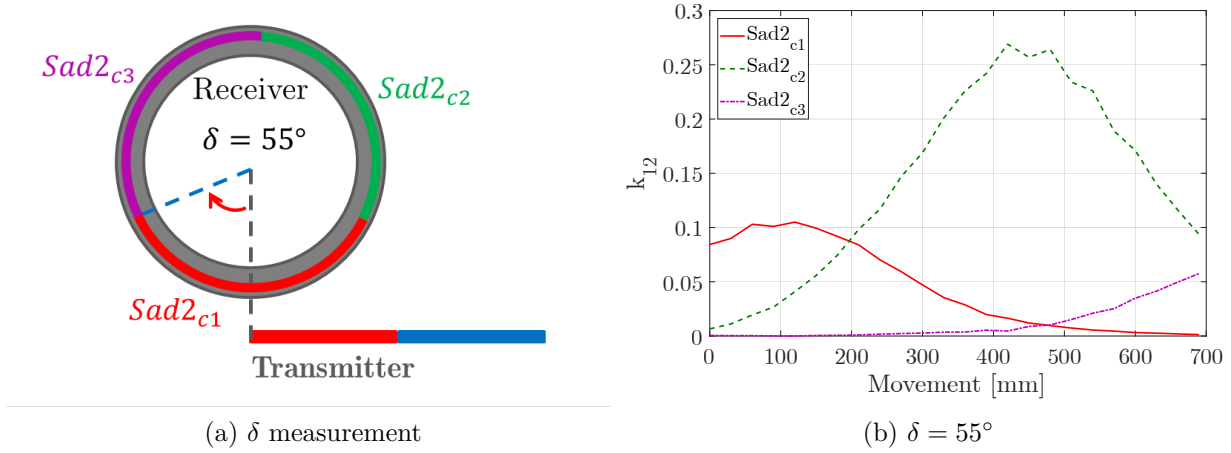
Figure 5.16: Effect of different δ in k_{12} using a DDP with the dimensions $(C_l, C_w)=(660,400)$ mm for: (a) illustration of δ and (b) $\delta = 55°$.

line) is low as a consequence of the total decoupling of one of the coils that form $Sad2_{c1}$. Around 200 mm, the contribution from $Sad2_{c2}$ exceeds the value from $Sad2_{c1}$ until the end of the transmitter pad length, resulting in a k_{12} variation between 0.088 and 0.267. This variation can, however, be comprised between a very low value (≈ 0.02) and 0.148 when the value of δ increases above the center of the $Sad2_{c1}$ coils (the value of δ depends on the ratio between C_l and the length of the receiver coils). In this scenario, $Sad2_{c1}$ is partially above one of the transmitter coils but they are almost decoupled from one another, resulting in very low k_{12} values. In static applications, this limitation is overcome by a small shift along the transmitter pad length during the park of the vehicle (this process is explained in detailed in Section 5.5). For dynamic applications, it is more challenging to avoid this scenario entirely, since it is impossible to predict the entry point of a vehicle along the roadway. A possible solution would be the shift of β degrees between the $Sad2_{c1}$ installed in each wheel (this solution assumes that inWIPT capabilities are installed in both rear or front axle wheels). In this way, in the event of a total decoupling in a wheel is compensated by the other one.

Based on the presented simulation results, the sizing of DDP transmitter geometries differ between static and dynamic applications as follows:
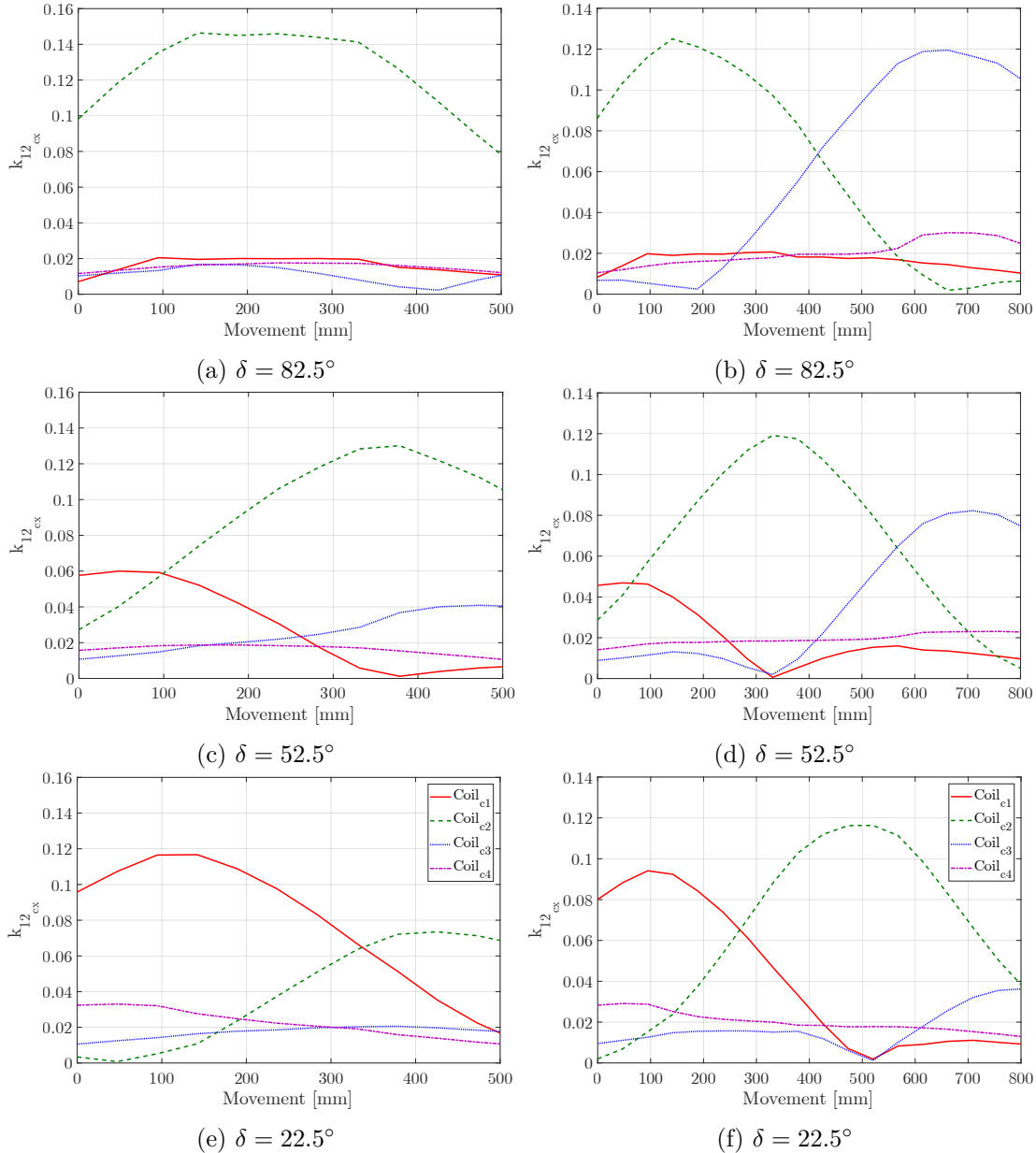
- **Static Applications**
    - The ratio between C_w and the receiver coil width is set between 0.95 to 1.16. This range was found by taking into account the results from Figure 5.15(a) and assuming a receiver coil width between 180 and 220 mm. Within this range, the ORMC offers k_{12} above 0.28 and lateral tolerances of ± 50 mm.
    - The ratio of C_l with the receiver coil length (which corresponds to $\theta = 180°$) is unitary. This value ensures the maximum k_{12}, as illustrated by Figure 5.15(b).

- **Dynamic Applications**
    - Similarly to static applications, the ratio between C_w and the receiver coil width takes into account the green area from Figure 5.15(a) and assuming a receiver coil width between 180 and 220 mm. A range between 1.62 and 1.92 was found and ensures a lateral displacement tolerance of 150 mm with minimum k_{12} above 0.15;
    - The ratio of C_l with the receiver coil length is affected by the δ angle and the rim size to reduce the existence of no coupling scenarios. Nevertheless, this ratio can be set between 1 and 1.9 as it ensures k_{12} values above 0.26 in perfect aligned conditions.

5.3   Inner Rim Magnetic Coupler

The inclusion of the IRMC in a inWIPT system enables the energy transfer between the wheel and the on-board side without contacts. This means that the IRMC has a rotary pad, fixed in the wheel, and a fixed pad in the on-board side, using the same structure that supports the disk brakes. The literature proposes several coupling solutions as replacements of traditional slip rings systems or in charging underwater autonomous vehicles [314–318] that also require a contactless energy transfer between movable parts [319–322]. The solutions presented in [319–321] use pot type configurations that are unsuitable for the proposed inWIPT since the placement of the IRMC must be between the inner side of the rim and the disk brakes of the vehicle. The authors in [322] investigate several solenoid geometries with different core and coil optimizations. The solenoid configuration, illustrated in Figure 5.4, is a viable IRMC design due to its hollow cylindrical shape. The transmitter and receiver pads are separated by a small air gap, and each pad is formed by a ferromagnetic core, a coil and an aluminum enclosure. It was found in [322] that a segmented core, like the one represented in Figure 5.17, has a better ferrite usage than a full cylindrical ferrite core. Furthermore, the use of longer ferrite strips is preferable since they have lower saturation levels and the coils have slightly larger self-inductance values. Therefore, it was selected the geometry in Figure 5.17 as a starting point in the IRMC design, but additional optimizations are required to assess the effect of different ferrite bars depths and dimension relations between the coils and the ferrite bars. Furthermore, the ICNIRP guidelines to human exposure of magnetic fields must be met, hence the aluminum enclosure must be included in the design optimization of the IRMC.
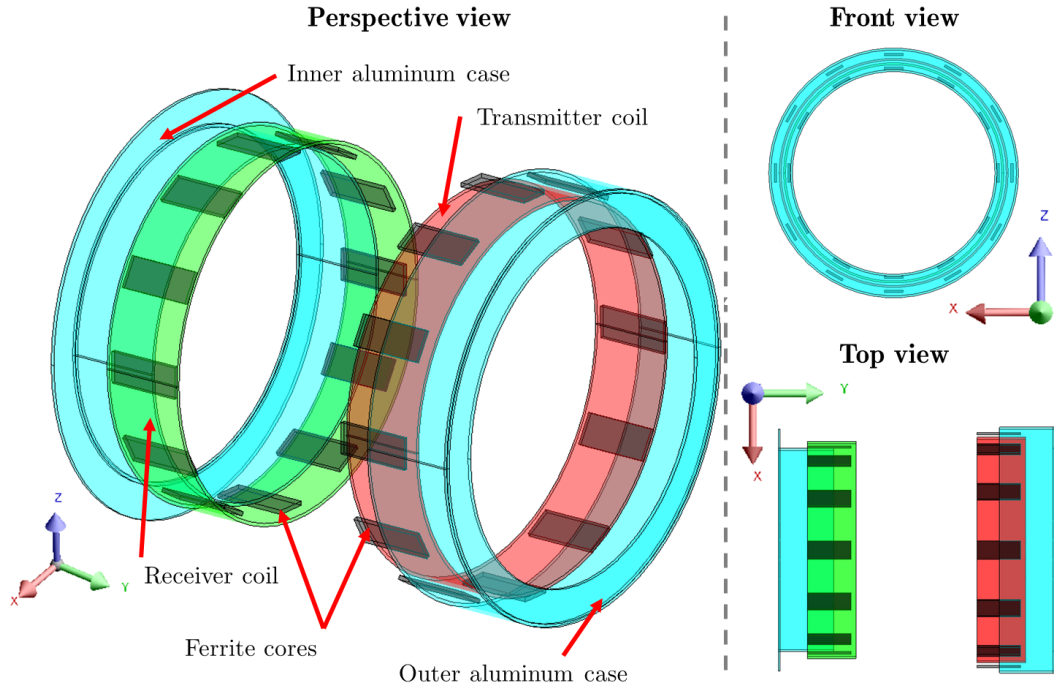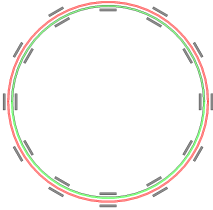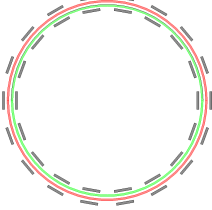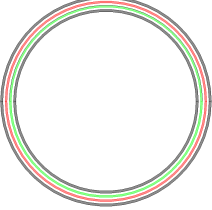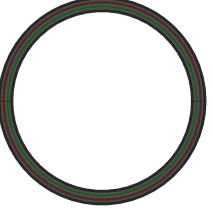
Figure 5.17: Geometry of the IRMC (including shield) in different views.

5.3.1 Core arrangement

The optimization process starts with the study of different core arrangements, followed by the investigation of optimal size relations between the core and coil. As discussed in Chapter 3, one way to evaluate magnetic couplers is through its coupling coefficient (k_{34}) and uncompensated power (P_{su}). The value P_{su} corresponds to the product of open-circuit voltage ($|\overline{V}_{oc}| = \omega.L_{34}.|\overline{I}_3|$) and short-circuit current ($|\overline{I}_{sc}| = L_{34}/L_4.|\overline{I}_3|$). Table 5.6 shows four IRMC designs, each with a different core layout and labeled from Type I to Type IV. The first two types have segmented cores with 12 and 18 ferrite bars in each side, respectively. Type III has two cylindrical ferromagnetic cores while Type IV enclosures completely the transmitter and receiver coils in a ferromagnetic case. All designs exhibit k_{34} above 0.93 and a maximum coupling of 0.98 is achieved using Type IV core arrangement. In terms of P_{su}, all designs show power transfer capabilities above 17 kVA, when driven by a constant current in the transmitter pad of 20 A_{RMS}. Additionally, Type IV has a P_{su} that exceeds Type I by a factor larger than 3.3, in the same working conditions. This difference is a consequence of the larger increase in the self-inductance values of both the transmitter and receiver coils caused by the additional ferrite. However, the ratio of ferrite versus P_{su} is higher in Type I configuration. This means, a segmented ferromagnetic core makes a better use of the ferrite than a full ferromagnetic core.

Table 5.6: Comparison of different core arrangements.

	Type I	Type II	Type III	Type IV
k_{34}	0.934	0.945	0.958	0.98
P_{su} [kVA]	17.867	21.385	28.708	59.413
Ferrite [cm^3]	456	684	1322	1759.1
Use (VA/cm^3)	39.18	31.26	21.72	33.78
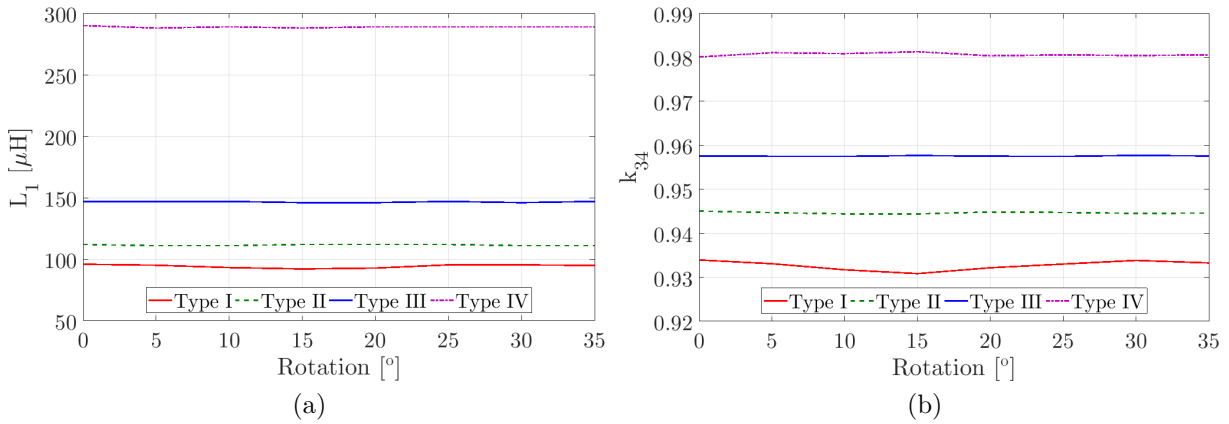
Figure 5.18: Magnetic parameters as a function of the transmitter rotation for different core arrangements: (a) self-inductance and (b) mutual coupling.

Figure 5.18 depicts the self-inductance and mutual coupling profiles as a function of the transmitter rotation for the different core arrangements. A single interval of 30° was considered for analysis since it corresponds to the overlap between two consecutive ferrite bars in the Type I configuration (360°/6 = 30°). The results show a coupling profile almost independent of the transmitter rotation for Type III and IV. On the other hand, segmented cores will undoubtedly exhibit small variations due to the relative positioning of the transmitter and receiver cores. These variations are, in the worst case scenario, inferior to 0.24 % with Type I configuration.

Compliance with the ICNIRP guideline limits to human exposure of magnetic fields must also be verified for IRMC designs. Figure 5.19 shows the simulated flux density from the center of designs and along the y axis (movement away from the vehicle, as illustrated in Figure 5.17) for the four studied designs without shields and for Type I with shield. Figure 5.19(a) shows the simulated flux density from a height of $z = 0$ mm whereas Figure 5.19(b) shows the simulated flux density for $z = 300$ mm. The height $z = 0$ mm corresponds to the

bottom of the IRMC while $z = 300$ mm is slightly the geometric center of the IRMC. The results show that designs without shield have similar flux patterns and amplitudes, especially for $z = 0$ mm. However, neither designs comply with the 27.3 μT limit at a distance of 0.5 m, making it impractical for inWIPT applications. Thereby, an aluminum shield must be integrated in the IRMC. The results from Figure 5.19 also show the flux density for a Type I with shield. The shield attenuates the flux density by a factor of almost 200 for $z = 0$ mm and 10 for $z = 300$ mm. This means a total compliance at a distance of about 0.12 m from the center of the design. Considering that the IRMC is placed in the inner side of aluminum rims, the stray fields are further reduced and compliance is achieved at lower distances. In conclusion, by taking into account all aforementioned results, the Type I geometry was selected as a work basis for further optimization.
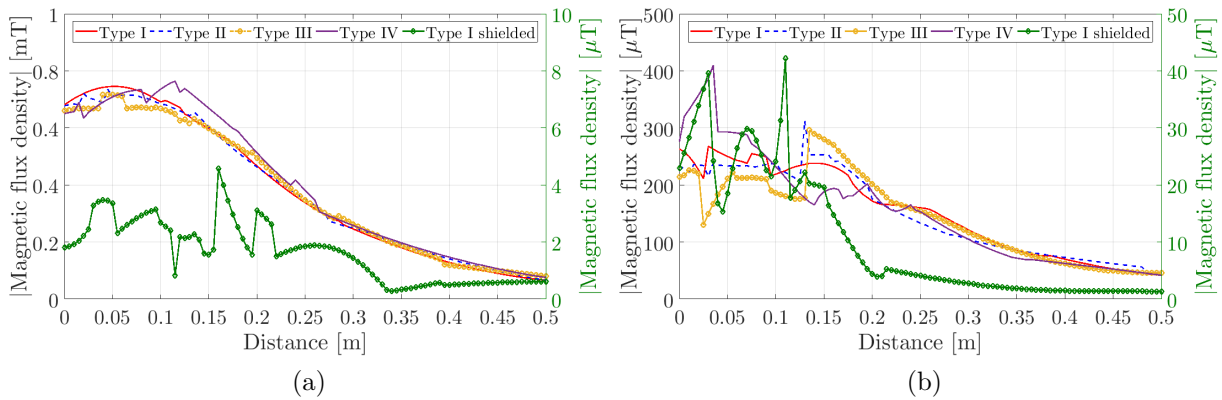
Figure 5.19: Simulated flux density along the y axis with $|\overline{I}_3| = 20$ A for heights of: (a) $z = 0$ mm and (b) $z = 300$ mm .

5.3.2   Coil sizing

The impact of coil width against a ferromagnetic core in the self and mutual inductance values is shown in Figure 5.20(a). The ferrite bars have a width of 100 mm while the coil width is varied between 50 and 100 mm, with 10 turns in each pad and a transmitter current of 20 A_{RMS}. The results show a decrease in the self-inductance of almost 20 % between the coil width of 50 and 100 mm. This reduction is justified by the wider distance between two consecutive turns that leads to higher reluctance values. In contrast, wider coils provide better coupling and optimum results are found for pads with the ratio between coil and core width in the range of 0.95 to 1. Figure 5.20(b) shows the self-inductance and mutual coupling profile for different pad sizes, while the ratio between coil and core width remains constant with a unitary value. The gradient of the mutual coupling curve indicates that wider pads offer better coupling with values above 0.92 for widths above 75 mm. Additionally, and
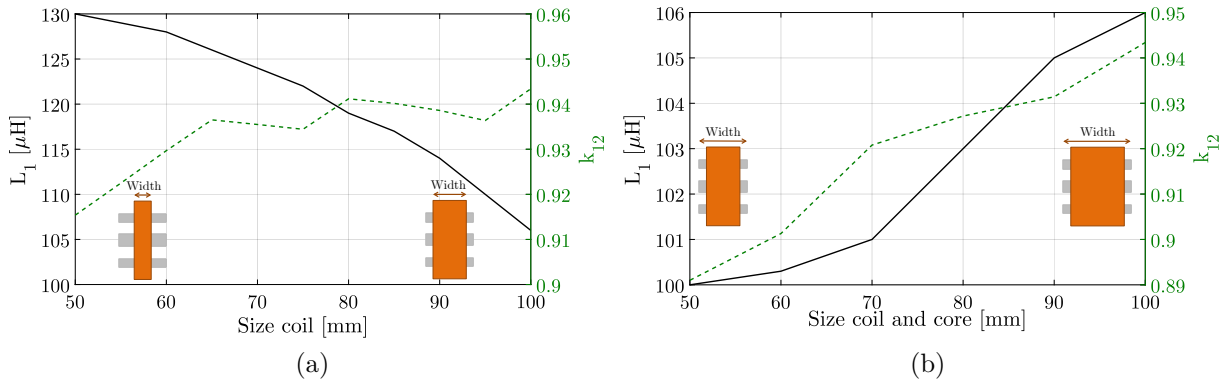
Figure 5.20: Self-inductance and mutual coupling profile as a function of: (a) coil width with a fixed ferrite core and (b) coil and ferrite core width.

comparing both Figure 5.20(a) and Figure 5.20(b), is visible the coupling benefits of wider ferromagnetic cores rather than wider coils. By comparing the first coupling values in each figure, is clearly preferable to have a wider core with a concentrated coil than a smaller core with a wider coil.

The results from coil sizing, shown in Figure 5.20, indicate that designs with smaller core sizes have poorer coupling profiles. Furthermore, concentrated coils reduce even further the mutual coupling than wider coils, as illustrated by the results in Figure 5.20(a). Therefore, from this point on, the optimization process for the IRMC will consider designs with a unitary ratio between the core and coil width.

5.3.3   Ferrite strips

The use of ferromagnetic material improves the coupling factor, the uncompensated power and it can be added to the MC by making the ferrite strips wider or thicker, assuming a constant MC size. Figure 5.21(a) and Figure 5.21(b) show the effect of adding ferromagnetic material in k_{34} and P_{su}, respectively. The width of the ferrite strips was varied between 20 and 60 mm, in intervals of 5 mm whereas the thickness was varied between 3 and 13 mm, in intervals of 2 mm. The intersection point corresponds to the same volume of the initial MC. The width parameter shows the steeper variation, which translates in a better ferromagnetic material utilization. This result is in line with the results from Table 5.6 where core arrangements with higher coil coverage offered better coupling values. The value of k_{34} shows increments around 2.2 % when the volume of ferrite increases by a factor of 3. The thickness parameter, on the other hand, shows coupling increments of only 0.9 % when the volume of ferrite increases by a factor of almost 6. Therefore, the ferromagnetic core should be wider rather than thicker to improve the coupling factor.
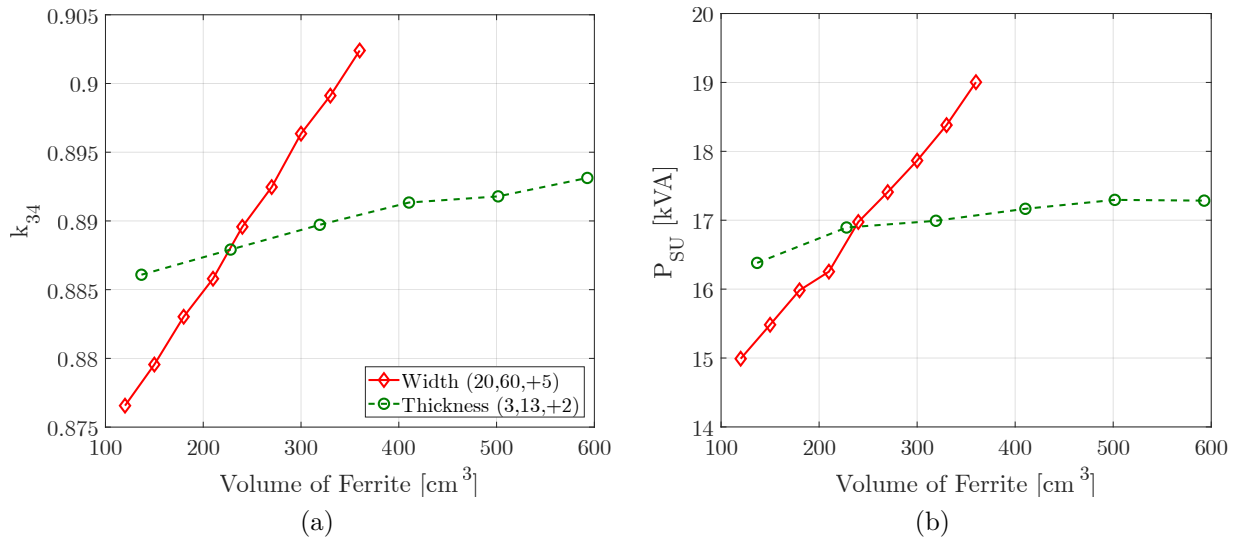
Figure 5.21: Volumetric comparison of pads with different ferrite dimensions for:(a) k_{34} and (b) P_{su} with an air gap of 5 mm.
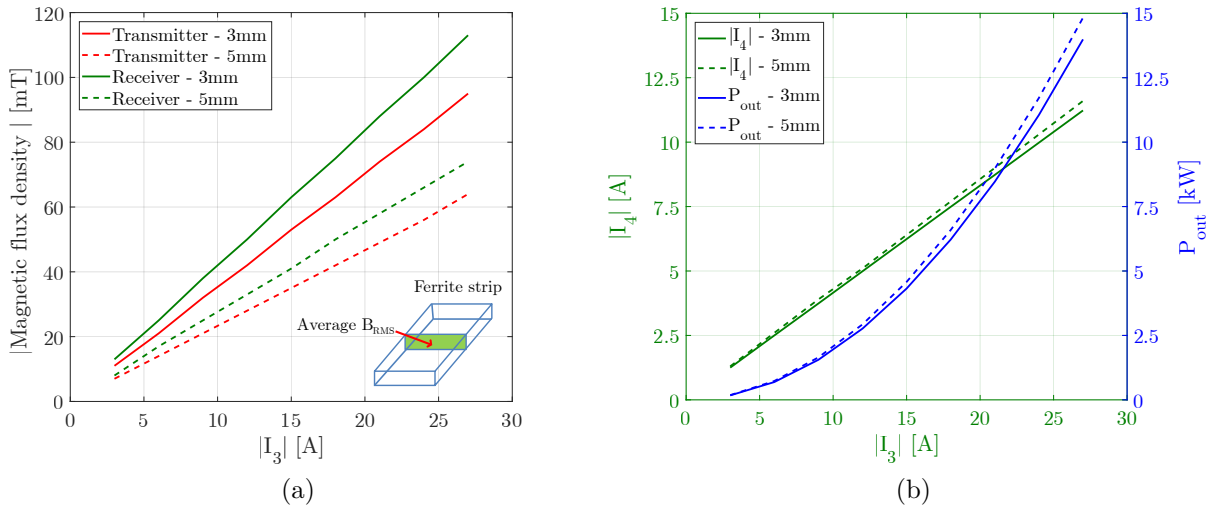
Figure 5.22: Analysis of different ferrite core thicknesses as a function of $|\overline{I}_3|$ in terms of: (a) Average RMS magnetic flux density and (b) P_{out} considering a series resonant configuration.

The use of thinner ferrite strips increases the chances of saturation and, consequently the iron losses. Figure 5.22(a) depicts the average RMS magnetic flux density in a cross section of a ferrite strip as a function of the transmitter current and with the receiver pad short-circuited. The maximum RMS values obtained via 3D FEA simulations occurred in the edges of the ferrite strips and never exceeded 200 mT with a $|\overline{I}_3| = 27$ A. The average magnetic flux density has a linear variation with $|\overline{I}_3|$. Moreover, and as expected, the ferrite core with a 3 mm thickness exhibits higher flux density values than the 5 mm ferrite core. The difference in flux density is 17 % for a $|\overline{I}_3| = 27$ A, as depicted in the solid green and red lines from Figure 5.22(a). In terms of power transfer capabilities, the use of thinner ferrite cores slightly reduces the self and mutual inductance values and consequently, the value of
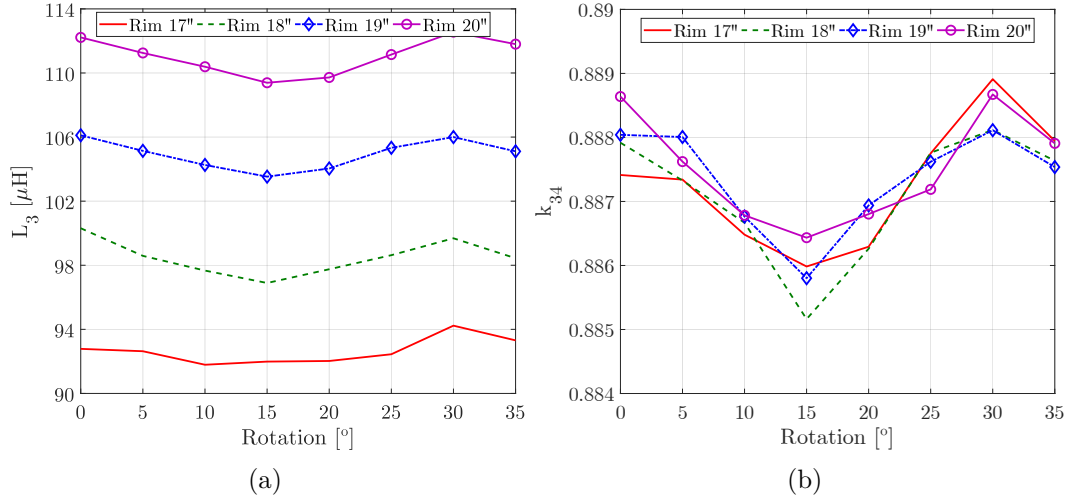
Figure 5.23: Magnetic parameters as a function of the transmitter rotation for different rim sizes: (a) L_3 and (b) k_{34}.

P_{out}. This difference is more significant for higher values of $|\overline{I}_3|$, with a maximum difference of 9 % when $|\overline{I}_3| = 27$ A, by comparing the blue dashed and solid lines in Figure 5.22(b). Similar results are obtained between the transmitter and receiver currents.

5.3.4   Rim size

One dimension that affects the magnetic properties of the IRMC is the wheel's radius. Figure 5.23 illustrates L_3 and k_{34} as a function of the wheel's rotation with different rim sizes and assuming the same number of turns. The EV models commercially available have rim sizes comprised between 17 and 20 inches and for that reason were selected for evaluation. As expected, coils with larger diameters have higher L_3 values. The increase, however, is proportional and identical between consecutive size tires, with increments of approximately 8 %. In contrast, k_{34} exhibits identical profiles, regardless of the wheel's size and position. This behavior is expected since the comparison is made with the same number of turns in each transmitter and receiver coils of each rim.

The air gap between the transmitter and receiver pads also affects the magnetic properties of the IRMC. Under normal operation, this value remains constant and is only affected by external factors like unbalance between the wheel and the wheel's hub, or by an eccentricity in the wheel. Figure 5.24 depicts L_3 and k_{34} as a function of the air gap with different rim sizes. The self-inductance value is slightly reduced for high air gap values since the effect of the receiver ferromagnetic core is reduced. This behavior is verified for all evaluated rims. The coupling factor k_{34}, on the other hand, shows coupling reductions of 16 % when the air gap increases from 2 to 12 mm. In addition, this reduction is identical for all evaluated rims.
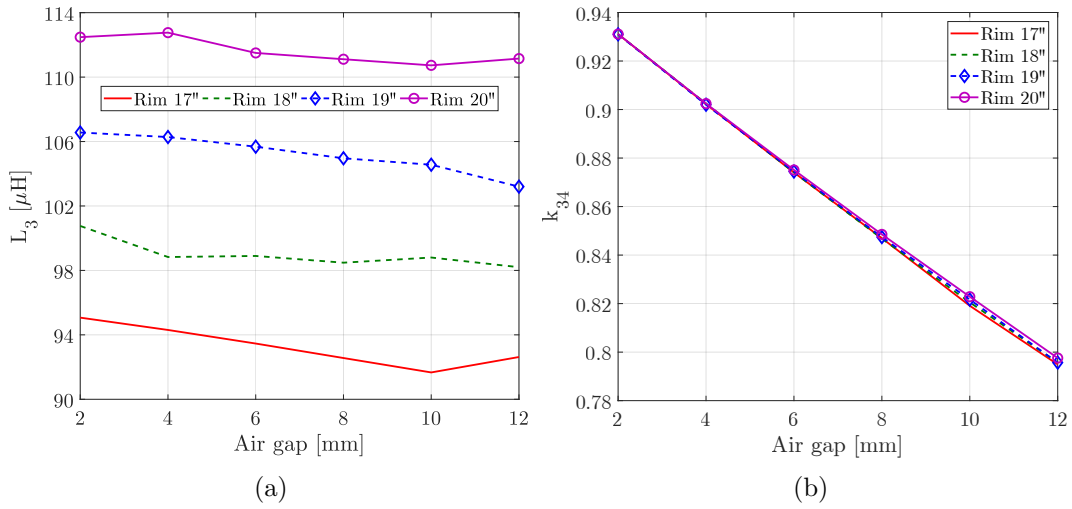
Figure 5.24: Magnetic parameters as a function of the air gap for different rim sizes: (a) L_3 and (b) k_{34}.
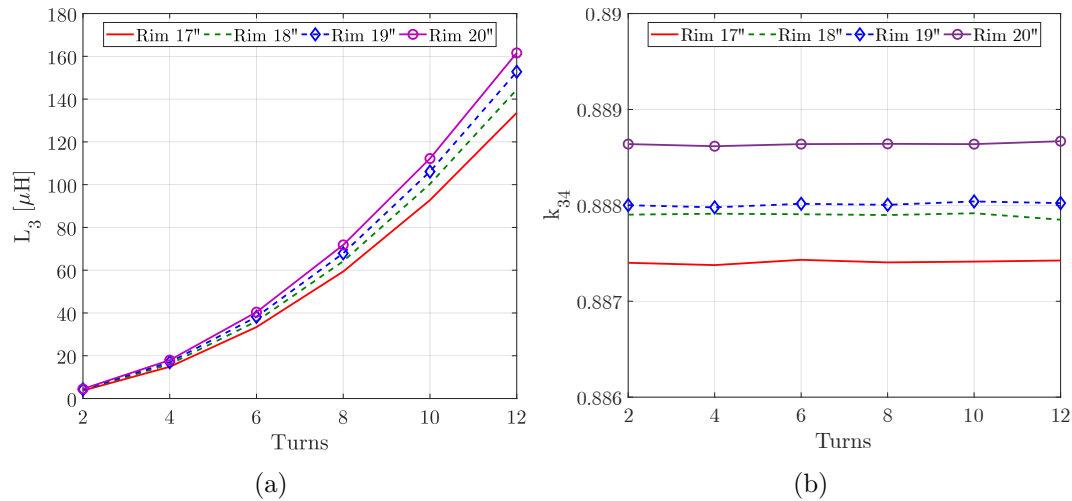
Figure 5.25: Magnetic parameters as a function of turns in both coils for different rim sizes: (a) L_3 and (b) k_{34}.

The large variation of the coupling factor is a consequence of the solenoid geometry and impact of having two solenoids with different radius. Therefore, the air gap of the IRMC should be comprised between 4 and 6 mm in order to keep k_{34} above 0.87 and minimize the leakage magnetic fields.

The number of turns in each pad also has different results based on the rim size. Figure 5.25 illustrates L_3 and k_{34} as a function of the number of turns. As expected, L_3 exhibits a second order polynomial pattern. Also, the 20 inches rim has slightly higher L_3 values, with the same number of turns, due to the larger diameter of the coil. The value of k_{34}, on the other hand, remains approximately constant and independent of the number of turns.
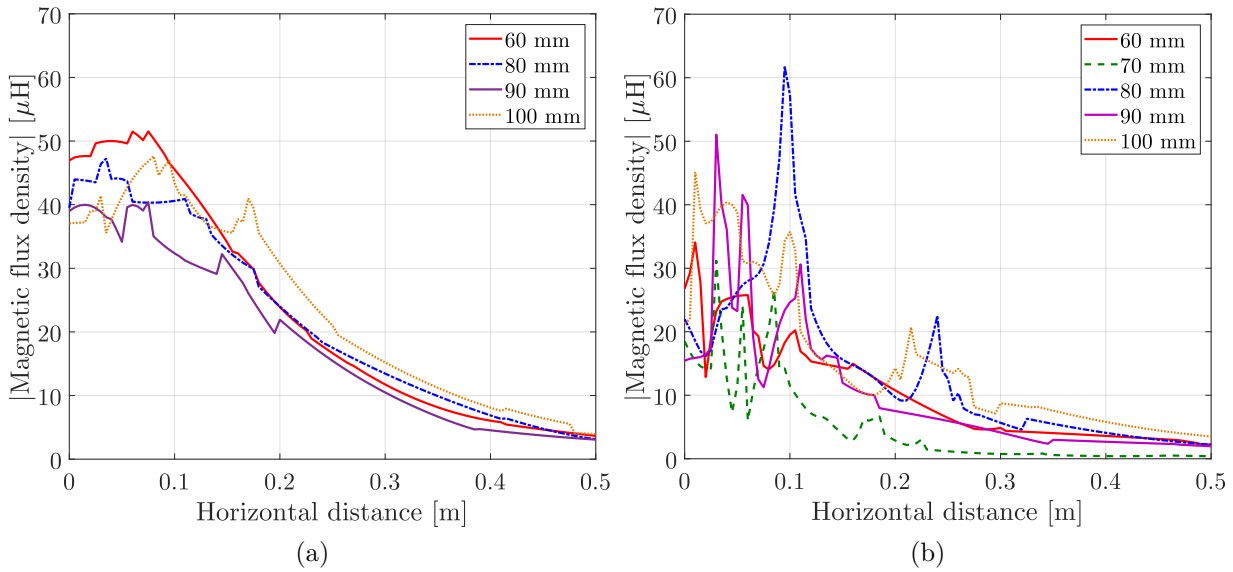
Figure 5.26: Simulated magnetic flux density along the z axis as a function of different aluminum case widths, considering $|\overline{I}_3| = 20$ A, $|\overline{I}_4| = 10$ A at heights of (a) y= 0 mm and, (b) y= 300 mm.

5.3.5   Aluminum case

The aluminum enclosure offers protection against external elements like dust or water but also to magnetic stray fields. The shield effect depends on the thickness of the aluminum walls but also in the size of the enclosure. Figure 5.26 illustrates the RMS magnetic flux density for aluminum enclosures with different widths, in two different heights: $z = 0$ mm and $z = 300$ mm. The 3D FEA simulations considered an air gap of 5 mm and constant currents values of $|\overline{I}_3| = 20$ A and $|\overline{I}_4| = 10$ A. The results show little difference in the pattern of the magnetic flux density for $z = 0$ mm after the first 100 mm. A similar behavior occur for $z = 300$ mm after the first 120 mm. In terms of compliance with ICNIRP guideline, a distance of 190 mm from the center of the IRMC ensures a maximum RMS magnetic flux density below the $27\mu T$ limit. Consequently, if the IRMC is placed closer to inner extremity of the rim (closer to the vehicle) and assuming a rim with a 200 mm width, the minimum safe distance could be as small as 90 mm from the wheel. The simulation results in Figure 5.26 do not take into account the shield effect of the rim itself including the rim spokes. All this additional shield material will decrease even further the 90 mm safe distance, most likely to values closer to 0 mm.

The compliance with the ICNIRP guidelines can be met at different distances depending mainly in the RMS value of the transmitter current. Figure 5.27 illustrates the RMC magnetic flux density with different $|\overline{I}_3|$ values, in two different heights: $z = 0$ mm and $z = 300$
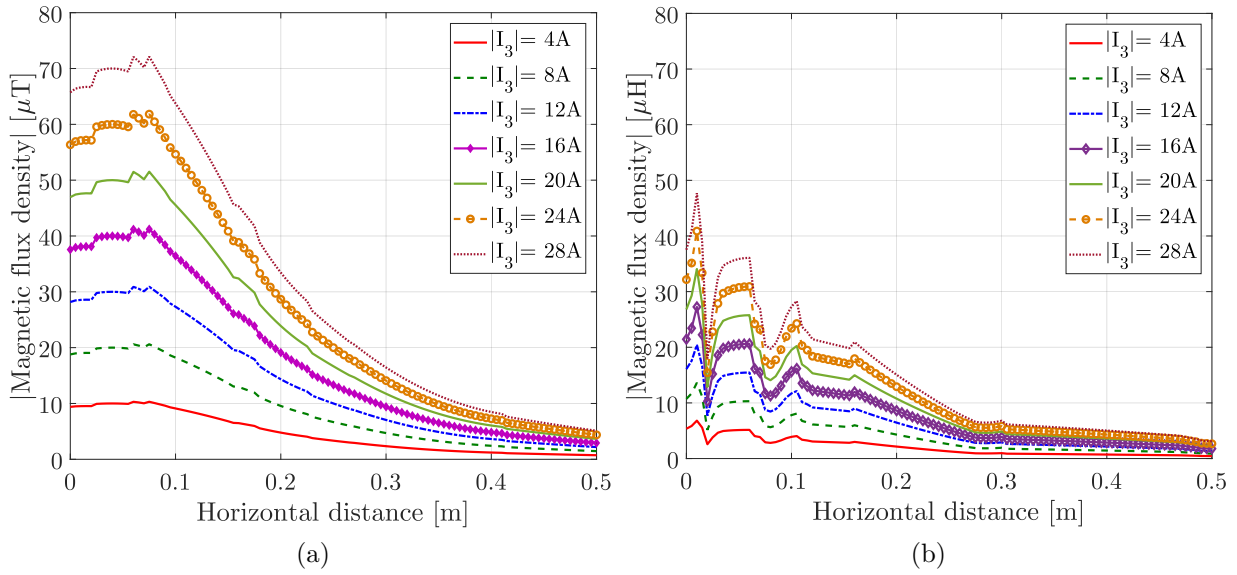
Figure 5.27: Simulated magnetic flux density along the z axis as a function of different $|\overline{I}_3|$ values, at heights of (a) y= 0 mm and, (b) y= 300 mm.
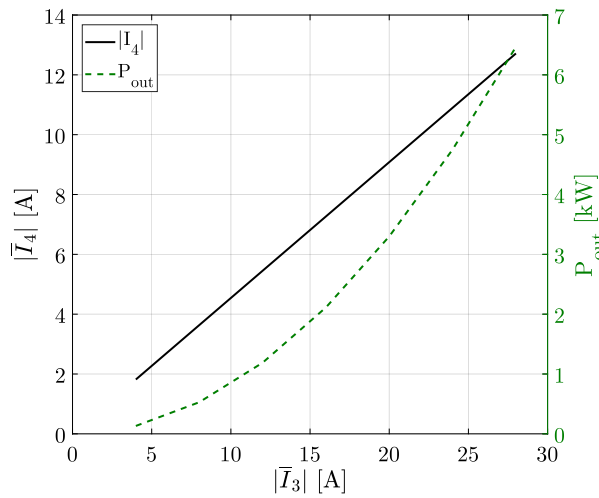
Figure 5.28: P_{out} and $|\overline{I}_4|$ as a function of $|\overline{I}_3|$ of the simulated results shown in Fig. 5.27.

mm. The 3D FEA simulation results considered a 60 mm aluminum enclosure and an air gap of 5 mm. The results show identical patterns that only differ in amplitude, regardless of the $|\overline{I}_3|$ value. The aluminum enclosure ensures a complete shield effect for $|\overline{I}_3|$ values up to 11 A, in the plane $z = 0$ mm. In the worst condition, for $|\overline{I}_3| = 28$ A, the compliance is met at a distance of 234 mm. Once again, the minimum safe charging distance will be comprised between 0 and 150 mm (considering a middle positioning of the IRMC). In the plane $z = 300$ mm, the safe distance is met around 100 mm, meaning the compliance is achieve within the rim width.

One downside of passive shielding is the reduction of the effective self and mutual inductance values and, consequently the power transfer capability of the system. Figure 5.28

depicts the output power of the IRMC with an aluminum enclosure of 60 mm as a function of the transmitter and receiver currents. One clear difference when compared with the results without an aluminum shield (depicted in Figure 5.22) is the drastic reduction of the output power capability (more than 55 %). This reduction is caused by a reduction of the self and mutual inductance values of approximately 40 % and 35 %, respectively. In addition, Eddy losses in the aluminum enclosure can account between 4 and 9 % of the inWIPT overall losses. Therefore, the design of the IRMC has to consider the impact of aluminum shielding in the self and mutual inductance values and desired output power.

5.4 inWIPT Double Coupling System Operational Conditions

The proposed double coupling inWIPT system differs from conventional IPT systems and the existing designing rules for IPT can not be applied. Thereby, two inWIPT configurations that ensure a 360° wheel coverage are presented and discussed. A circuit model analysis is carried out for different resonant network configurations. Then, a design methodology derived from the selected resonant configuration is presented and its outputs include optimal operation frequency, load independent output voltage conditions and range of admissible mutual inductance profiles.

5.4.1 ORMC and IRMC connection configurations

The 360° wheel coverage with inWIPT capabilities requires three Sad_2 ORMC receivers, according to the analysis carried out in section 5.3. Figure 5.29 shows two possible inWIPT configurations with different connections for the Sad_2 ORMC receivers. The first configuration, illustrated in Figure 5.29(a), connects the three Sad_2 receivers in series whereas the second configuration, illustrated in Figure 5.29(b), has a distinctive IRMC for each Sad_2 receiver. The first option is easier to implement and uses less components. However, the stray magnetic fields around the no-coupled coils is high due to the current that passes through all receiver coils.

The second configuration has a dedicated IRMC with respective resonant tanks plus rectifier with filter for each Sad_2 ORMC receiver. This configuration ensures that only ORMC receivers coupled with the transmitter pad have circulating currents. Therefore, the stray magnetic fields are contained to the lower part of the wheel. Additionally, the use of dedicated systems with each ORMC receiver offers fault tolerance capabilities in the event of
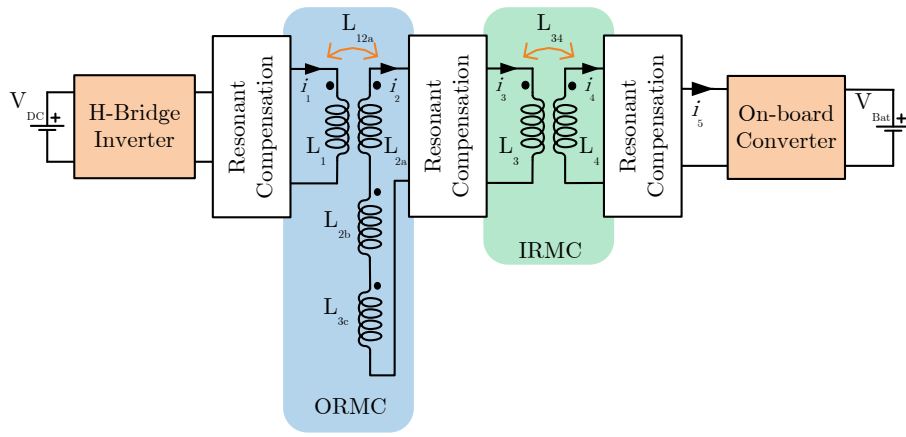
(a)
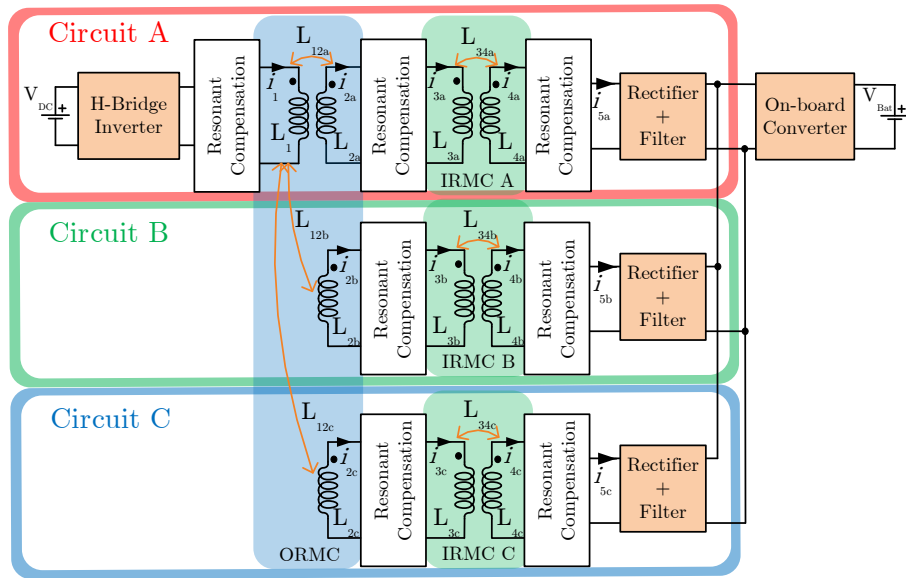
(b)

Figure 5.29: Possible inWIPT configurations that ensure a 360° wheel coverage.

problems in the IRMCs or resonant capacitors. The downside is the employment of additional components (rectifiers and capacitors) as well as two IRMC structures. This work chooses the second configuration and the circuitry model analysis as well as the design methodology will only take into account Circuit A, illustrated in Figure 5.29 (b), since Circuits B and C are merely duplicates of Circuit A. Therefore, it is only necessary to consider the coupling profiles of a single DDP-Sad_2 ORMC and solenoid IRMC geometries, since all magnetic components (ORMCs and IRMCs) are decoupled from one another.

5.4.2 System Specifications and Constraints

Typically, the design of a battery charger has to meet electric specifications such as maximum output power (P_{out}), output voltage and/or current range and, hardware operational limits like the rated current of the semiconductors ($|\bar{I}_{inv}|$) used in the converters. Other elec-
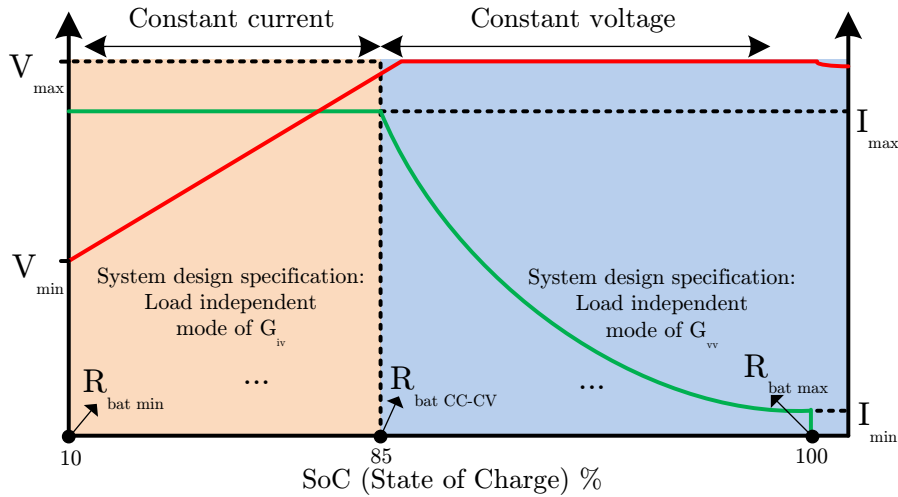
Figure 5.30: Charging profile of a Lithium battery.

tric specifications, however, are imposed by government restrictions, such as the maximum voltage of 1000 V across the transmitter and receiver coils, or by guidelines of the Society of Automotive Engineers (SAE) like the operating frequency (f_s) range between 81.2 kHz and 90 kHz.

The charging process of a Lithium battery pack is made in two stages: constant current (CC) and constant voltage (CV) modes, as depicted in Figure 5.30. Constant current mode is applied until the batteries state of charge (SOC) reaches 85-90 %, whereas voltage mode is applied to the remaining 10-15 % with the main function of equalization. Therefore, the selected resonant configuration must exhibit load-independent current and/or voltage source characteristics.

In addition to the electric specifications, inWIPT battery chargers also need to comply with operational requirements, like air gap and lateral displacements, to offer the driver some driving/parking mobility. These operational requirements have direct impact in the coupling profiles of the ORMC. Besides the electric and operational requirements, inWIPT have physical constraints, namely the dimensions of the rim which dictate the size of the receiver coils in the ORMC, as discussed in Section 5.3.

The energy transfer capability in both static and dynamic conditions is also an important design specification. Dynamic IPT systems require an on-board battery controller since is not feasible, in a large scale, to regulate the batteries of each vehicle using the off-board inverter controller. One way to avoid duplication of on-board converters is by taking advantage of the plug-in battery charger already available in most commercial EVs. This means that the proposed inWIPT system has to provide a voltage source characteristic with similar amplitude values of the grid.

5.4.3   Double Coupling System Electrical Analysis

The inclusion of a second MC adds a new resonant compensation between the ORMC and the IRMC and changes the resonant characteristics of the conventional IPT configurations, described in Chapter 2. Figure 5.31(a) illustrates the fundamental harmonic equivalent circuit model of Circuit A, illustrated in Figure 5.29(b), using series-series-series (SSS) whereas Figure 5.31(b) illustrates a series-series-parallel (SSP) double coupling resonant configuration. The series compensation was chosen as a work basis for the off-board and wheel sides while both S or P compensations are implemented in the on-board side.

The circuit from Figure 5.31 comprises the equivalent voltage supply $(\overline{V}_1)$ of the off-board inverter (not depicted in figure), the off-board and wheel sides series compensation networks interconnected by the ORMC, both S or P compensation networks on the on-board side and interconnected to the wheel side by the IRMC. The main difference between SSS and SSP is in the definition of the on-board equivalent resonant impedance and corresponding current formulation. The equivalent on-board impedance for a series compensation is given by (5.1) whereas for a parallel compensation takes the form of (5.2).

$$Z_{4_S,1} = Z_4 + R_{eq} = r_{4,1} + j.\omega.L_4(1 - 1/b_4^2) + R_{eq} \tag{5.1}$$

$$Z_{4_P,1} = r_{4,1} + j.\omega L_4 + \frac{R_{eq} - j.\omega.R_{eq}.C_4}{1 + (\omega.R_{eq}.C_4)^2} \tag{5.2}$$

The parameters L_4 and $r_{4,1}$ correspond to the self-inductance and equivalent resistance of the on-board pad. The parameter C_4 corresponds to the capacitor placed in series or parallel with the load and it is defined as $C_4 = 1/ (\omega_4^2.L_4)$. The variable b_4 is the relation factor between the system angular frequency (ω) and the on-board (ω_4) angular frequency. The parameter Z_4 is the equivalent impedance of the inductor in series with the capacitor. The variable R_{eq} is the equivalent resistance of the batteries (R_{bat}) before rectifier action and it is given by

$$R_{eq} = \frac{8.R_{bat}}{\pi^2} = \frac{8.V_{bat}}{\pi^2.I_{bat}}, \tag{5.3}$$

where V_{bat} and I_{bat} are the voltage and current values in the batteries, respectively.

The root mean square (RMS) output voltage $(|\overline{V}_{1,1}|)$ of the inverter, at the fundamental harmonic, is described as a function of the phase-shift (α) control angle using

$$|\overline{V}_{1,1}| = V_{DC}\frac{2\sqrt{2}}{\pi}cos\left(\frac{\alpha}{2}\right), \tag{5.4}$$
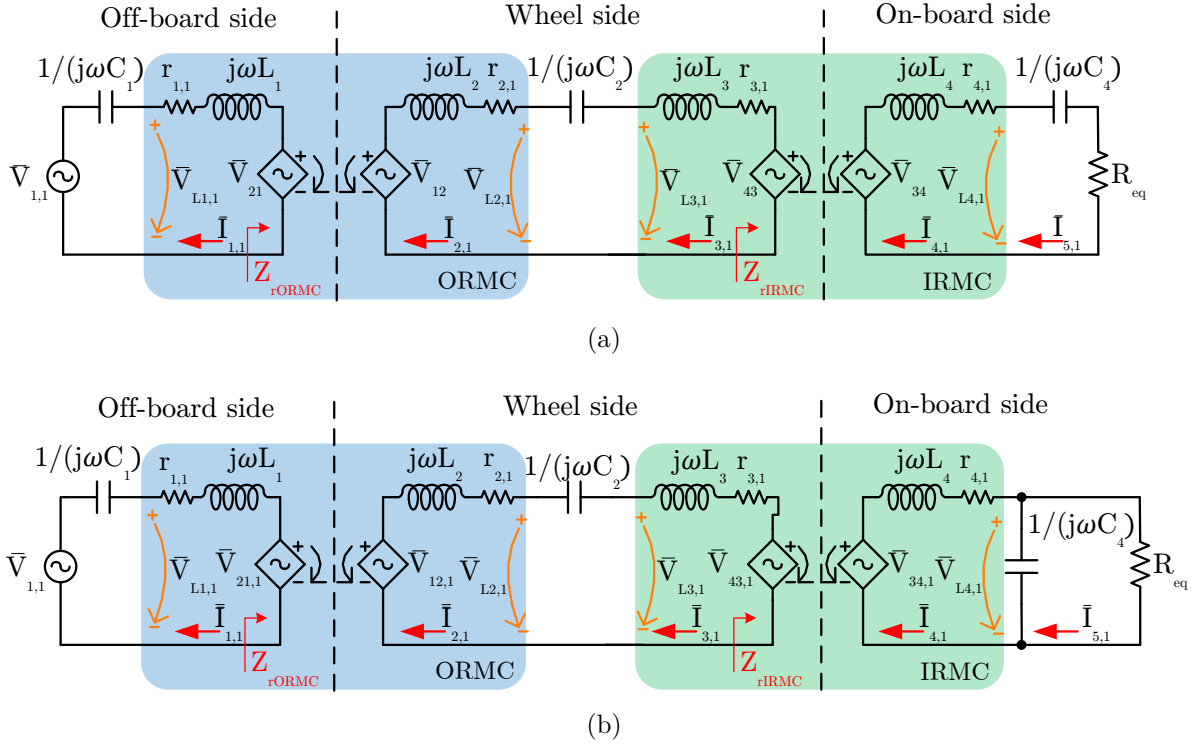
Figure 5.31: Equivalent circuit of a double coupling system for: (a) SSS and (b) SSP.

where V_{DC} is the average DC link voltage.

By applying the Kirchhoff laws to the circuit, the following equations are obtained:

$$\overline{V}_{1,1} = r_{1,1}.\overline{I}_{1,1} + j.\omega((L_1 - 1/(\omega^2.C_1))\overline{I}_{1,1} - L_{12}.\overline{I}_{2,1}) \tag{5.5}$$

$$0 = (r_{2,1} + r_{3,1}).\overline{I}_{2,1} + j.\omega((L_2 + L_3 - 1/(\omega^2.C_2))\overline{I}_{2,1} - L_{12}.\overline{I}_{,11} - L_{34}.\overline{I}_{4,1}), \tag{5.6}$$

$$0 = (R_{eq} + r_{4,1})\overline{I}_{4,1} + j.\omega((L_4 - 1/(\omega^2.C_4))\overline{I}_{4,1} - L_{34}.\overline{I}_{2,1}), \tag{5.7}$$

where L_1 and L_2 are the self-inductances of ORMC and, L_3 and L_4 are the self-inductances of the IRMC. The subscript numbers in the variables indicate to which side the variable is related to, where 1 and 4 stands for off-board and on-board sides, while numbers 2 and 3 stands for wheel side. L_{12} and L_{34} quantify the mutual inductance between the transmitter and receiver pads of the ORMC and IRMC, respectively. The parameters $r_{1,1}$, $r_{2,1}$, $r_{3,1}$ and $r_{4,1}$ denote the equivalent resistance of each pad and they include the Joule and Iron (if applicable) losses. The capacitors values are given by $C_1 = 1/(\omega_1^2.L_1)$ and $C_2 = 1/(\omega_2^2.(L_2 + L_3))$, where ω_1 and ω_2 are the natural angular resonant frequencies of the resonant compensation networks.

Solving (5.5) to (5.7) provides the current equations that accurately define the SSS model:

$$\overline{I}_{1,1} = \frac{\overline{V}_{1,1}}{Z_{in,1}} = \frac{\overline{V}_{1,1}}{(Z_{1,1} + Z_{r_{ORMC},1})} \tag{5.8}$$

$$\overline{I}_{2,1} = \overline{I}_{1,1} \frac{j.\omega.L_{12}}{Z_{2,1} + Z_{r_{IRMC},1}} \tag{5.9}$$

$$\overline{I}_{4,1} = \overline{I}_{2,1} \frac{j.\omega.L_{34}}{Z_{4S,1}}, \tag{5.10}$$

where $Z_{in,1}$ is the equivalent impedance seen by the inverter. The parameters $Z_{1,1}$ and $Z_{2,1}$ are the equivalent impedance values of the resonant tanks in the transmitter and wheel sides and they are given by

$$Z_{1,1} = r_{1,1} + j.\omega.L_1(1 - 1/b_1^2) \tag{5.11}$$

$$Z_{2,1} = (r_{2,1} + r_{3,1}) + j.\omega.(L_2 + L_3)(1 - 1/b_2^2) \tag{5.12}$$

$$\tag{5.13}$$

The variables b_1, b_2 and b_4, described in (5.14), are relation factors between the system angular operating frequency ω and the natural angular frequencies of the transmitter (ω_1), wheel (ω_2) and receiver (ω_4) resonant tanks. A unitary relation factor at the fundamental frequency means $\omega = \omega_x$.

$$b_1 = \omega/\omega_1, \quad b_2 = \omega/\omega_2, \quad b_4 = \omega/\omega_4. \tag{5.14}$$

The concept of reflected impedance in IPT systems refers to the equivalent impedance of one side referred to the opposite side. The proposed circuit has two reflected impedance values, as illustrated in Figure 5.31. The reflected impedance from the on-board side onto the wheel side ($Z_{r_{IRMC}}$) is defined in (5.15), while the reflected impedance from the wheel side onto the transmitter side ($Z_{r_{ORMC}}$) is described in (5.16).

$$Z_{r_{IRMC},1} = \frac{\overline{V}_{43,1}}{\overline{I}_{3,1}} = \frac{\omega^2.L_{34}^2}{Z_{4X,1}} \tag{5.15}$$

$$Z_{r_{ORMC},1} = \frac{\overline{V}_{21,1}}{\overline{I}_{1,1}} = \frac{\omega^2.L_{12}^2.Z_{4X,1}}{Z_{2,1}.Z_{4X,1} + \omega^2.L_{34}^2}. \tag{5.16}$$

The analysis of $Z_{r_{IRMC},1}$ has been extensively made in the literature for perfectly tuned systems ($\omega_1 = \omega_2 = \omega_4 = \omega$) [98] and in its generic form [107]. One advantage of series compensation in the receiver side is the absence of reactive component in $Z_{r_{IRMC},1}$ under perfectly tuned systems, as seen in (5.17). This feature guarantees, in a typical IPT system, a zero voltage switch (ZVS) of the inverter placed in the transmitter with a fixed f_s, even

Table 5.7: Reflected impedance formulas of $Z_{r_{IRMC},1}$ and $Z_{r_{ORMC},1}$ for series and parallel compensation on the on-board side.

	Real	Imaginary	Real	Imaginary
	Series compensation		Parallel compensation	
$Z_{r_{IRMC},1}$	$\dfrac{\omega^2 . L_{34}^2}{R_{eq}}$	0	$\dfrac{R_{eq} . L_{34}^2}{L_4^2}$	$-\dfrac{j . \omega . L_{34}^2}{L_4}$
$Z_{r_{ORMC},1}$	$\dfrac{R_{eq} . L_{12}^2}{L_{34}^2}$	0	$\dfrac{L_{12}^2 . R_{eq}}{\frac{R_{eq}^2 . L_{34}^2}{\omega . L_4^2} + L_{34}^2}$	$\dfrac{\omega . L_{12}^2}{\frac{R_{eq}^2 . L_{34}^2}{\omega . L_4^2} + L_{34}^2}$

in the event of air gap and lateral displacements.

$$Z_{r_{IRMC_{tun}},1} = \frac{\omega^2 . L_{34}^2}{R_{eq}} + j0. \tag{5.17}$$

The value of $Z_{r_{ORMC},1}$, on the other hand, is investigated in this work and it depends on the resonant configuration of the wheel side but also in $Z_{r_{IRMC},1}$. Assuming an ideal and perfect tuned system, (5.16) can be simplified into the equations described in Table. 5.7. The value of $Z_{r_{ORMC},1}$ for a series configuration in both wheel and on-board sides is purely resistive and the value of R_{eq} is affected by a factor of L_{12}^2/L_{34}^2. This mutual inductance factor dictates the nominal voltage and current requirements of the power supply and it must be taken into account during the design of both MCs.

The equivalent mathematical model of the SSP configuration is determined using a similar analysis as the one used for the SSS configuration. The equivalent circuits of the off-board and wheel sides are the same for both SSS and SSP configurations, hence, equations (5.8) and (5.9) are valid for both configurations. The equations that describe the on-board currents $\bar{I}_{4,1}$ and $\bar{I}_{5,1}$ for the SSP configuration are found using (5.2) and correspond to

$$\bar{I}_{4,1} = \bar{I}_{2,1} \frac{j . \omega . L_{34}}{Z_{4_P,1}}, \tag{5.18}$$

$$\bar{I}_{5,1} = \bar{I}_{4,1} \frac{1 - j . \omega . R_{eq} . C_4}{1 + (\omega . R_{eq} . C_4)^2}, \tag{5.19}$$

The parallel compensation in the on-board side also modifies the reflected impedance when compared with the series compensation. Table 5.7 summarizes $Z_{r_{IRMC},1}$ and $Z_{r_{ORMC},1}$ in tuned conditions. The first has a real part that depends on the load value but also the self and mutual inductance values of the IRMC. The imaginary part, contrary to series

configuration, is not null and it originates a reflected capacitance that depends on the self and mutual inductance of the IRMC. As a consequence, the imaginary part in the wheel side is not fully compensated and causes $Z_{r_{ORMC},1}$ to also have an imaginary part, as seen in Table 5.7.

The operation point with constant voltage (CV) characteristics is discover using the voltage (G_{vv}) transfer function that correlates the output voltage ($\overline{V}_{R_{eq},1}$) with the input voltage ($\overline{V}_{1,1}$). The transfer function G_{vv_S} is found by rearranging (5.8)-(5.10) into

$$G_{vv_S} = \frac{-\omega^2.L_{34}.L_{12}.R_{eq}}{Z_{1,1}\left(Z_{2,1}\left(Z_{4,1} + R_{eq}\right) + \omega^2.L_{34}^2\right) + \omega^2.L_{12}^2\left(Z_{4,1} + R_{eq}\right)}. \tag{5.20}$$

Equation (5.20) can be further manipulate into the form

$$G_{vv_S} = \frac{1}{\frac{Z_{1,1}.Z_{2,1}.Z_{4,1} + \omega^2.L_{34}^2.Z_1 + \omega^2L_{12}^2.Z_{4,1}}{-\omega^2.L_{12}.L_{34}.R_{eq}} + \frac{Z_{1,1}.Z_{2,1} + \omega^2.L_{12}^2}{\omega^2.L_{12}.L_{34}}}. \tag{5.21}$$

If the system losses are neglected ($r_{1,1} = r_{2,1} = r_{3,1} = r_{4,1} = 0$), (5.21) is independent of R_{eq} for an operating frequency defined by

$$Z_{1,1}.Z_{2,1}.Z_{4,1} + \omega^2.L_{34}^2.Z_{1,1} + \omega^2L_{12}^2.Z_{4,1} = 0. \tag{5.22}$$

The condition in (5.22) is verify, at least, when the transmitter and receiver resonant frequencies match the operating frequency ($b_1 = b_4 = 1$) and the impedance values of $Z_{1,1}$ and $Z_{4,1}$ become null. At this frequency, $|G_{vv_S}|$ is independent of variations that may occur in $Z_{2,1}$ and is equal to L_{34}/L_{12}. The switching losses in the transmitter inverter, in such conditions, are low since both reactive components of $Z_{r_{IRMC},1}$ and $Z_{r_{ORMC},1}$ are null and the inverter operates in ZVS mode. Additionally, the ZVS mode is guaranteed independently of the relative position between the transmitter and receiver pads of both ORMC and IRMC.

The transconductance function (G_{iv}) correlates the output current ($\overline{I}_{5,1}$) with $\overline{V}_1$ and for the SSS is given by

$$G_{iv_S} = \frac{-\omega^2.L_{12}.L_{34}}{(Z_{1,1} + Z_{r_{ORMC},1}).(Z_{2,1} + Z_{r_{IRMC},1}).(Z_{4,1} + R_{eq})}. \tag{5.23}$$

Equation (5.23) can be further manipulated into

$$G_{iv_S} = \frac{-\omega^2.L_{12}.L_{34}}{(Z_{4,1} + R_{eq}).(Z_{1,1}.Z_{2,1} + \omega^2.L_{12}^2) + \omega^2.L_{34}^2.Z_{1,1}}. \tag{5.24}$$

In a lossless system, (5.24) is independent of the load conditions when

$$Z_{1,1}.Z_{2,1} + \omega^2.L_{12}^2 = 0 \tag{5.25}$$

Equation (5.25) can be expanded using (5.11), (5.12) and (5.1) into

$$L_1.(L_2 + L_3).\left(-\omega^4.L_{12}^2 + \omega^2.(\omega_1^2 + \omega_2^2) - \omega_1^2.\omega_2^2\right) = 0. \tag{5.26}$$

The roots of (5.26) in order to ω define the operating frequency where the transconductance gain ($|G_{iv_S}|$) is independent of the load. These ω values, however, will not match the resonance frequency of the overall system and the impedance seen by the inverter will have a reactive component and the switching losses will increase. In short, the operation of the inverter in ZVS or Zero Current Switch (for a capacitive reactive component), when the frequency matches the load independent $|G_{iv_S}|$, will vary with the selected reactive components in all resonant compensation networks.

The unconstrained sizing of both ORMC and IRMC offers total control in the system design. The inWIPT system can, however, be supplied by an existing transmitter pad that also supplies a conventional IPT system. In this context, it is important to define guidelines of compatibility between a transmitter pad and both conventional or inWIPT receiver pads. The transfer function $G_{i_2v_S}$ can be used as requirement in the transmitter pad design and it is described as

$$G_{i_2v_S} = \frac{\overline{I}_{2,1}}{\overline{V}_{1,1}} = \frac{j.\omega L_{12}}{Z_{1,1}.(Z_{2,1} + Z_{r_{IRMC},1}) + \omega^2.L_{12}^2}. \tag{5.27}$$

The transfer function in (5.27) has load independent characteristic, neglecting the system losses, when the system operates at the natural frequency of the transmitter resonant tank $b_1 = 1$. The transfer function gain ($|G_{i_2v_S}|$) is then simply the magnetizing susceptance of the ORMC ($1/(\omega.L_{12})$). Therefore, (5.27) can be used as a design parameter of transmitter pads that supply both inWIPT and conventional IPT systems, without losing any power transfer capabilities.

A similar analysis can be conducted for the SSP configuration. The voltage gain function

is determined by arranging (5.8), (5.18) and (5.19) into

$$G_{vv_P} = \frac{-\omega^2.R_{eq}.L_{34}.L_{12}}{(R_{eq} + r_4 + j\omega.(L_4 + C_4.R_{eq}.r_4)).V_1} \tag{5.28}$$

where $V_1 = (Z_{2,1} + Z_{r_{IRMC},1})(Z_{1,1} + Z_{r_{ORMC},1})$.

The transconductance gain (G_{iv_P}) is given by

$$G_{iv_P} = \frac{-\omega^2.L_{34}.L_{12}}{(R_{eq} + r_4 + j\omega(L_4 + r_4.C_4.R_{eq})).V_1} \tag{5.29}$$

The analysis of (5.28) and (5.29) is not as straightforward as for the SSS configuration, being harder to identify possible load independent conditions directly from the equations. Therefore, in order to compare the most suitable configuration for the inWIPT system, the resonant compensation behavioral study will be conducted through a graphical function analysis in the next subsection.

5.4.3.1 Resonant Compensation Behavioral Analysis

The voltage and transconductance functions are analyzed under different load and coupling values to validate or identify the intrinsic CC and CV modes. An output power of 2 kW was consider for both SSS and SSP configurations at resonant operation. In addition, the input impedance, module and phase, is also analyzed to assess ZPA, ZVS or ZCS mode capabilities and impact on overall system efficiency.

Figure 5.32 illustrates $Z_{in,1}$ module and phase as a function of the switching frequency for different load and k_{12} values. In the proposed inWheel system, k_{34} is kept constant for all plots, since the IRMC design has a constant air gap. In the defined operating conditions (for the adopted mutual inductance profile), for low k_{12} and SOC values, SSS needs a higher primary side current to transfer the same amount of power (lower Z_{in}) than SSP, as illustrated by the lower $|Z_{in}|$ in Figure 5.32 (a). Nonetheless, with an increasing k_{12} this effect is reversed and, the SSS presents a lower input current variation. As the battery charges (higher SOC values) the previous behavior is reversed again, and SSS allows lower input currents than SSP. On the other hand, the results in Figure 5.32(b) regarding the phase of Z_{in} show that both SSS and SSP configurations have a ZPA at resonant frequency ($f_s = f_r = 85$ kHz) and this happens independent of SOC and k_{12} variations. Outside this frequency, both configurations can operate either in ZCS or ZVS depending on SOC and k_{12} values.

Figure 5.33 illustrates the voltage and transconductance gain as a function of the switch-
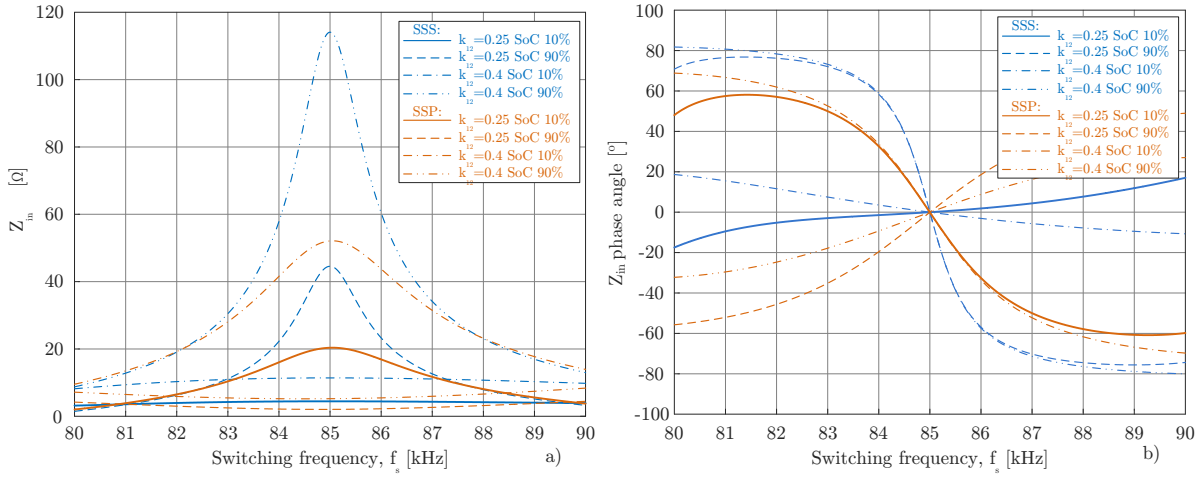
Figure 5.32: a) Module and b) Phase of Z_{in} as function of switching frequency.
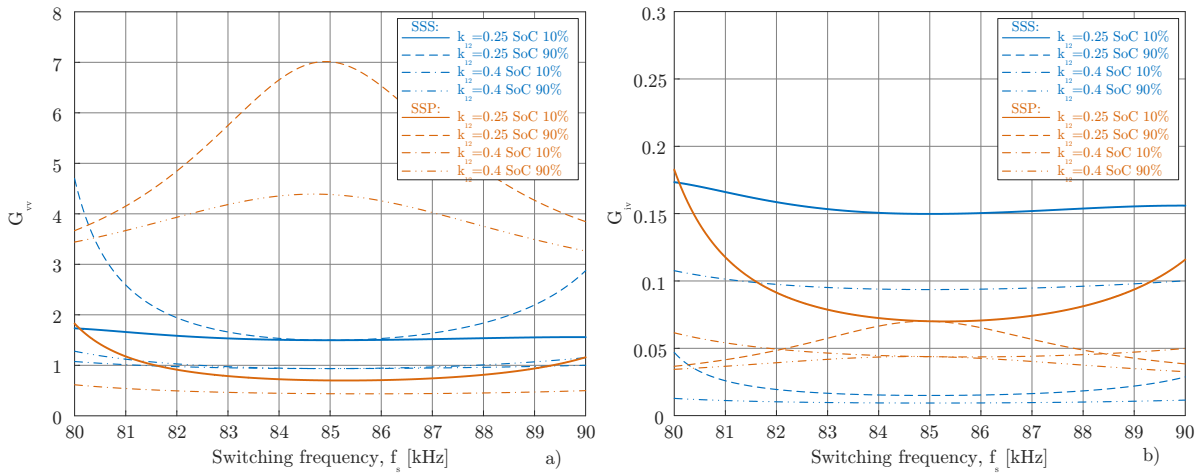
Figure 5.33: (a) Voltage gain and (b) Transconductance, as function of the switching frequency.

ing frequency for different load and coupling values. As expected from the theoretical analysis and proven by Figure 5.33 (a), the SSS has a load independent voltage gain function at resonance (85 kHz), allowing CV mode. Furthermore, for different k_{12}, the $|G_{vv_S}|$ is solely determined, at resonance, by the ratio L_{34}/L_{12}. This behavior is not replicated in the SSP configuration and load independent mode is not achieved in the considered frequency range.

As for the transconductance gain, depicted in Figure 5.33 (b), SSP exhibits CC independent operation at resonance regardless of k_{12} values. This behavior is not verified for the SSS configuration. Consequently, the SSP is preferable for a dedicated inWIPT whereas the SSS configuration is ideal for plug-in integration.

5.4.4   Design Steps

This subsection combines, in the form of steps, the specifications and constraints defined in Section 5.4.2 with the SSS equivalent electrical model devised in Section 5.4.3, to find

f_s, L_{12} and L_{34} that ensure a constant G_{vv} at the on-board converter input terminals. The steps are defined as follows:

1) Frequency selection: According to Section 5.4.3, $|G_{vv_S}|$ exhibits a load independent characteristic when the natural frequency of the resonant tanks matches the operating frequency of the inverter (f_s). Assuming the self inductance values are known, the capacitor values can then be determined using

$$f = \frac{1}{2.\pi.\sqrt{L_1.C_1}} = \frac{1}{2.\pi.\sqrt{(L_2+L_3).C_2}} = \frac{1}{2.\pi.\sqrt{L_4.C_4}}. \tag{5.30}$$

The value of f_s, under normal IPT conditions, is set to 85 kHz but can vary in the range defined in Section 5.4.2.

2) Voltage gain limits: In the conditions of Step 1 and assuming a lossless system, (5.21) is simplified into a ratio of mutual inductances, described as

$$|G_{vv_S}| = \frac{|\overline{V}_{Req}|}{|\overline{V}_1|} = \frac{L_{34}}{L_{12}}. \tag{5.31}$$

The value of L_{12} depends on the relative positioning of the wheel towards the transmitter placed under the road whereas L_{34} remains approximately constant. Since $|\overline{V}_{Req}|$ is a design specification, any deviation of L_{12} must be compensated with a new value of $|\overline{V}_1|$. The minimum value of $|\overline{V}_1|$ ($|\overline{V}_{1_{min}}|$) ensures P_{out} at $|\overline{I}_{inv_{rated}}|$. On the other hand, the maximum value ($|\overline{V}_{1_{max}}|$) is set for $\alpha = 0$, according to (5.4). Therefore, the range of $|\overline{V}_1|$ is given by

$$\frac{P_{out}}{|\overline{I}_{inv_{rated}}|} \leq |\overline{V}_1| \leq V_{DC}\frac{2\sqrt{2}}{\pi}. \tag{5.32}$$

This works assumes the VA rating of the inverter ($|\overline{I}_{inv_{rated}}|.|\overline{V}_{1_{max}}|$) to be larger than P_{out}, otherwise, the inverter can't regulate $|\overline{V}_1|$. A range of admissible L_{34}/L_{12} sets can be found through the manipulation of (5.31) and (5.32) into

$$\frac{|\overline{V}_{Req}|}{|\overline{V}_{1_{max}}|} \leq \frac{L_{34}}{L_{12}} \leq \frac{|\overline{V}_{Req}|}{|\overline{V}_{1_{min}}|}. \tag{5.33}$$

3) Admissible L_{12} and L_{34} sets: The range for the L_{34}/L_{12} ratio, defined in Step 2, have infinite combinations between L_{12} and L_{34}. As stated in Step 2, L_{34} remains almost constant and $|G_{vv_S}|$ is only affected by variations in L_{12}. The selection of L_{34} must then ensure the widest range of L_{12} (ΔL_{12}) possible while, at the same time, minimizes the value of $|\overline{I}_2|$. The minimization of $|\overline{I}_2|$ allows compact and lighter designs for the transmitter and receiver
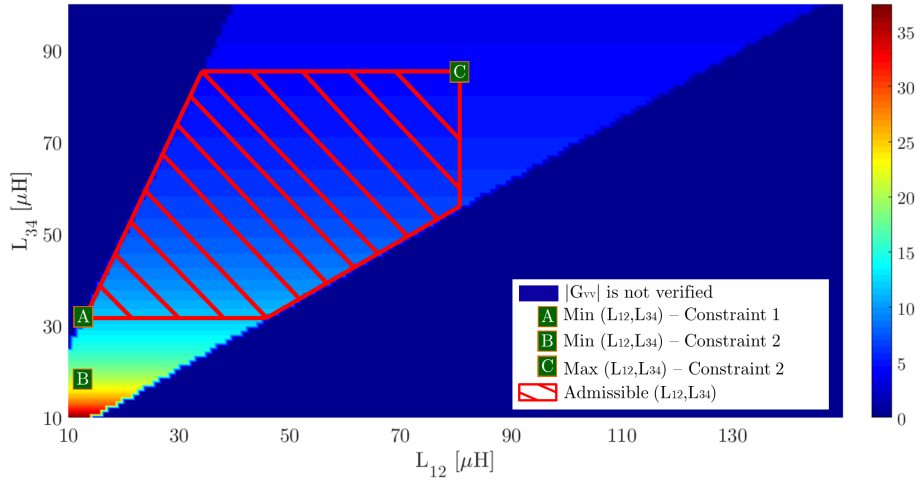
Figure 5.34: Intensity plot of $|\overline{I}_2|$ as function of L_{12} and L_{34} with the admissible sets of (L_{12}, L_{34}).

pads of the IRMC and ORMC, respectively, with lower cross-section conductors and thinner cores. The selection of best admissible L_{12} and L_{34} set can be expressed as a multi-objective optimization problem

$$max \quad \Delta L_{12} \quad \&\& \quad min \quad |\overline{I}_2|. \tag{5.34}$$

The relation between $|\overline{I}_2|$ and $|\overline{I}_4|$, given by (5.10), in the conditions of Step 1 is simplify into

$$|\overline{I}_2| = \frac{|\overline{V}_{Req}|}{\omega . L_{34}}. \tag{5.35}$$

Equation (5.35) shows that $|\overline{I}_2|$ is inversely proportional to L_{34} therefore, the minimization of $|\overline{I}_2|$ is related to the selection of L_{34}.

The admissible sets of L_{12} and L_{34} that verify (5.34) are found using the limits (5.33) and (5.35).

4) Selection of L_{12} and L_{34}: The limits determined in Step 3 for L_{12} and L_{34} take into account all feasible values that meet the requirements, identified in Section 5.4.2.

Figure 5.34 illustrattes, in the form of an intensity plot, $|\overline{I}_2|$ as function of L_{12} and L_{34}. The admissible coupling sets, that verify (5.33), are identified by a colored scale, while all non-admissible coupling sets are identified by the dark blue areas ($|\overline{I}_2| = 0$ A). Furthermore, the shape illustrated in Figure 5.34 is inherent to $|\overline{I}_2|$ and $|G_{vv}|$ equations and not to the coupling profiles of the ORMC and IRMC. The results show that (5.34) is verified for higher L_{34} values. This behavior is beneficial with the working principle of the proposed inWIPT, since L_{34} has approximately a constant value. However, the combination sets of L_{12} and L_{34}
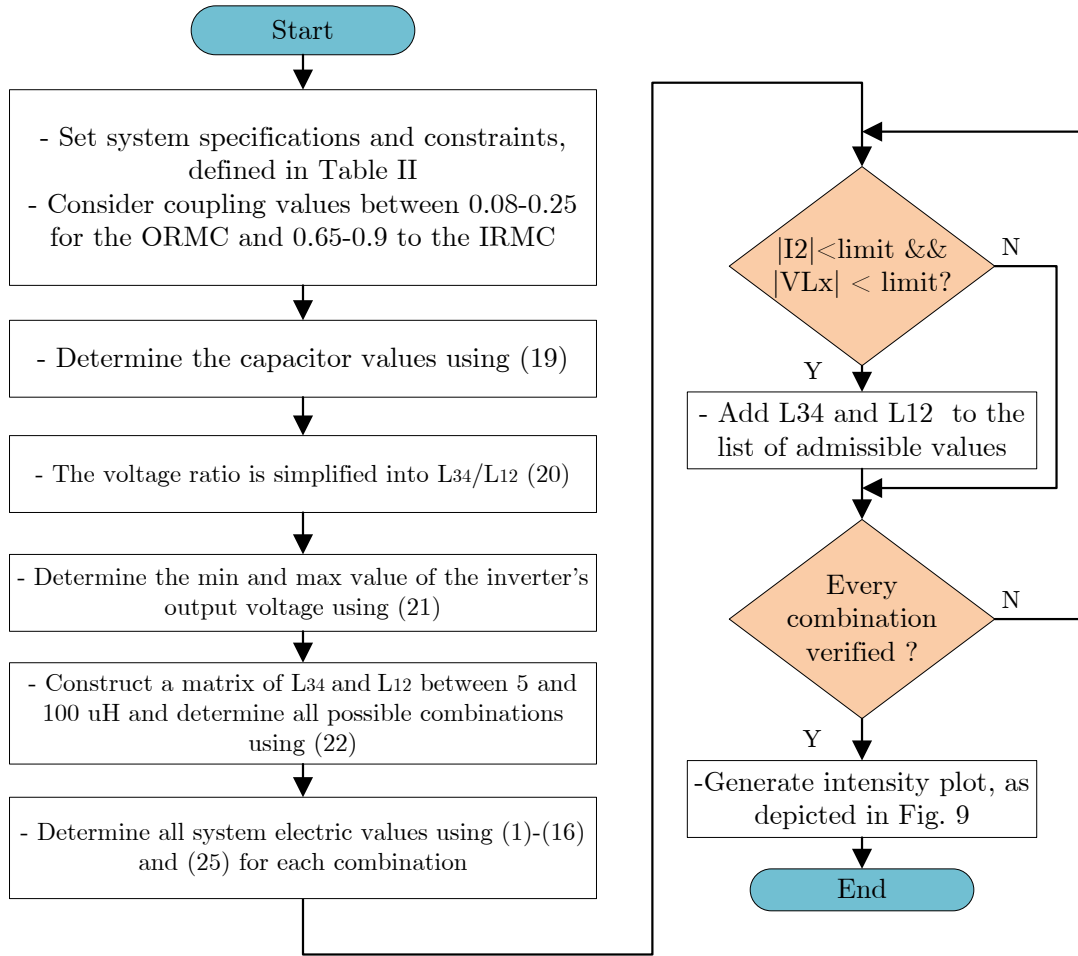
Figure 5.35: Flowchart of the design procedure.

that satisfy the requirements are virtually infinite and constraint rules are needed to narrow down the number of possibilities. The following list enumerates a set possible constraints based on electrical quantities and governmental directives:

Constraint 1: Rated $|\overline{I}_2|$: The rule can be applied in systems where $|\overline{I}_2|$ is a constraint in the system design to avoid large Joule losses in the receiver of the ORMC. In addition, the minimization of $|\overline{I}_2|$ reduces the required cross-section of the conductors that form the receiver coils of the ORMC and the transmitter coils of the IRMC to form a more lightweight inWIPT system. On either case, it sets the minimum combination possible for L_{12} and L_{34} and it is marked in Figure 5.34 by the labeled green square with the letter A.

Constraint 2: Induced voltages: Current regulations limit the induced voltages across the IRMC and ORMC coils to 1000 Vrms in Europe and 400 Vrms in Asia. The use of capacitors in series with the coils overcomes this limitations but at the cost of additional components. Thus, these parameters can be used as constraints to find the limit combinations of L_{12} and
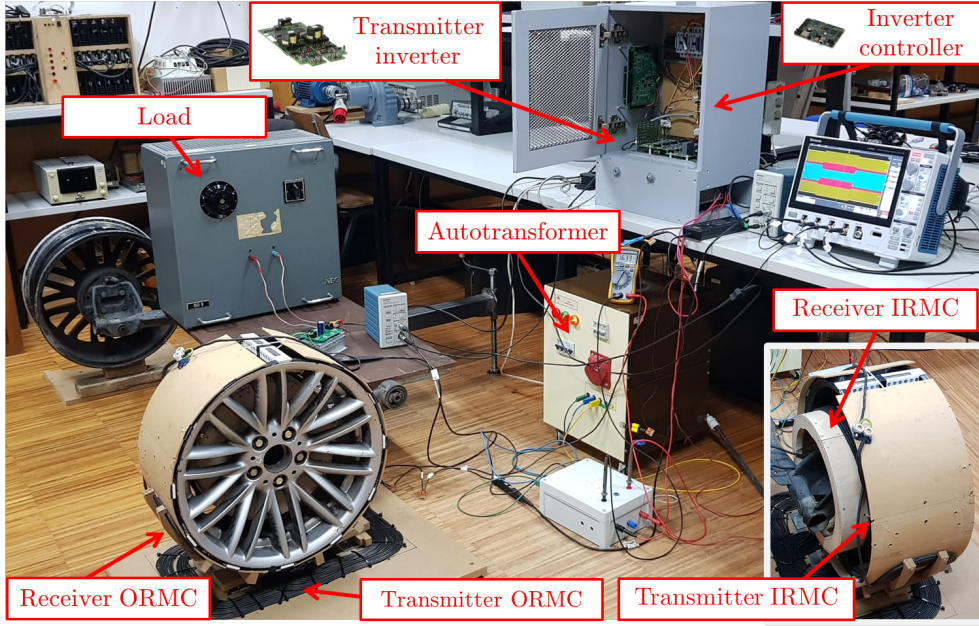
Figure 5.36: Experimental setup.

L_{34}. The induced voltages across the coils of the proposed inWIPT are given by

$$
\begin{aligned}
|\overline{V}_{L_1}| &= |\overline{I}_1.(r_1 + j\omega L_1 + Z_{r_{ORMC}})| \\
|\overline{V}_{L_2}| &= |\overline{I}_2.(r_3 + j\omega L_3 + 1/(j\omega.C_2) + Z_{r_{IRMC}})| \\
|\overline{V}_{L_3}| &= |\overline{I}_2.(r_3 + j\omega L_3 + Z_{r_{IRMC}})| \\
|\overline{V}_{L_4}| &= |\overline{I}_4.(R_{eq} + 1/(j\omega.C_4))|.
\end{aligned}
\tag{5.36}
$$

The equations listed in (5.36) may depend on the values of the system components like capacitors, load and, above all, the self inductance values of the coils. However, this last parameter depends on the geometry of the MC pad, number of turns and current that passes through the coil. Such profile is plotted during the sizing of the MC along with the coupling profiles between the transmitter and receiver pads as a function of different physical parameters, like air gap and lateral displacements. As such, the labeled green squares with the letters B and C in Figure 5.34, illustrate the down and up admissible sets for L_{12} and L_{34} using the induced voltage constraint.

The combine use of the rated $|\overline{I}_2|$ and induced voltages constraint rules provide an interval range for L_{12} and L_{34}. In the example of Figure 5.34, this interval is comprised between squares A and C and marked with red lines. Finally, the selection of L_{34} corresponds to the value that better suits inequation (5.34). Figure 5.35 summarizes the steps of the design methodology.

Table 5.8: Experimental specifications and coupling measurements.

Parameter	Value
Specifications and constraints	
V_{DC}	325 V (from 1ϕ grid)
$|\overline{V}_{1_{min}}|$-$|\overline{V}_{1_{max}}|$	40-290 V
$|\overline{V}_{Req}|$	160 V
P_{out}	2.6 kW
f	85 kHz
$|\overline{I}_{inv_{rated}}|$	35 A
$|\overline{V}_{L_1}|,|\overline{V}_{L_2}|,|\overline{V}_{L_3}|,|\overline{V}_{L_4}|$	1500 V
$|\overline{I}_2|$	20 A
ORMC: DDP-sad_2	
Size DDP (length*width)	460*320 mm
Size sad_2 (r_{radius},θ,width)	234 mm, 65°, 215 mm
Air gap	30-40 mm
Lateral displacement (m_x and m_y)	± 50 mm
Q_1, Q_2	218, 230
Δk_{12}	0.12-0.22
IRMC	
Size (radius*width)	234*70 mm
Air gap	14 mm
Q_3, Q_4	201, 189
Δk_{34}	0.64-0.69
Components	
R_{eq}	6.8-50.5 Ω

5.5 Experimental validation

The proposed double coupling system and operational conditions were validated experimentally using a 18 inches wheel prototype, illustrated in Figure 5.36. The system specifications and constraints are listed in Table 5.8 together with the physical characteristics and magnetic measurements of the ORMC and IRMC. A single configuration DDP-sad_2 with $\theta = 65°$ was selected for experimental validation. The DDP transmitter pad has the same length of rim (18 inches) and a width of 320 mm. A wider width of the transmitter pad reduces the impact of the ± 50 mm lateral tolerance defined for inWIPT systems. The solenoid geometry with a width of 93 mm in both ferrite core and coils was selected for the IRMC with a fixed air gap of 14 mm. The higher air gap value is an additional safe precaution to prevent contacts between both transmitter and receiver sides caused by small eccentricities in the prototype. As a consequence, the value of k_{34} drops to values in the range of 0.62 to 0.63. The coils were made with Litz wire with 1060 strands and a cross section of 5 mm^2. The quality factors of four coils are between 180 and 240. A total of 12 ferrite strips were equally displaced around the outer surface of the rim, each formed by two I N87 ferrite bars with the dimensions of 93x28x16 mm.

(a)   (b)
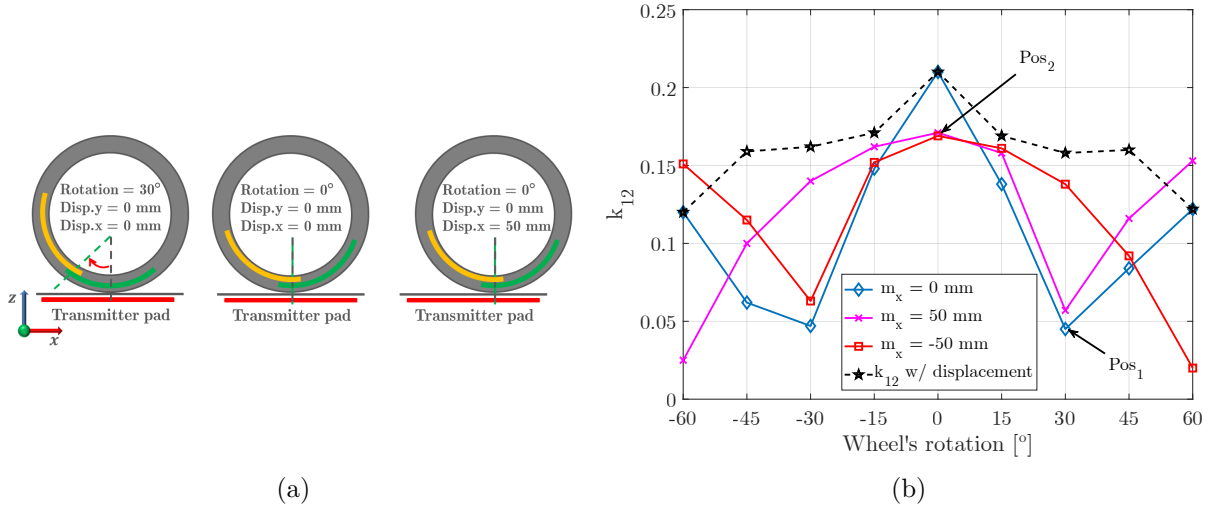
Figure 5.37:   (a) Illustration of the wheel position over the off-board transmitter pad and (b)experimental k_{12} profiles as a function of the wheel's movement with different lateral displacements.

The identification of the admissible intervals for L_{12} and L_{34} is carried out using the designs steps described in Section 5.4.4. The first step identifies the natural frequencies of the resonant tanks which matches the operating frequency of 85 kHz. The capacitors C_1, C_2 and C_4 are then determined accordingly using (5.30) and the self-inductance values from Table 5.8. The interval of $|G_{vv_S}|$ is determined in step 2 using (5.31) for $|\overline{V}_{1_{min}}|$ and $|\overline{V}_{1_{max}}|$, resulting in the range between 0.492 and 2.162. This range also corresponds to the ratio of L_{34}/L_{12} and it is an input parameter of the multi-objective optimization problem, described in step 3. The use of constraint rules, enumerated in step 4, narrow the admissible sets for L_{12} and L_{34}. The rated $|\overline{I}_2|$ constraint limits a minimum set of (L_{12}, L_{34})=(8 μH, 6 μH), which corresponds to the green square A in Figure 5.34. The maximum induced voltage values across the coils, on the other hand, provide a minimum and maximum sets equal to (5 μH, 7 μH) and (67 μH, 34 μH), respectively. These sets correspond to the green squares B and C in Figure 5.34. The above limit sets were found using (5.35) and (5.36) with the worst coupling values listed in Table 5.8. Finally, the combination of both constraints provides the eligible sets interval between (8 μH, 6 μH) and (67 μH, 34 μH).

One intrinsic degree of freedom of inWIPT systems is the wheel's rotation. This movement affects the relative positioning of the receiver coils towards the transmitter coils, as illustrated in Figure 5.37(a) using different wheel rotation angles and different displacements along the x axis. Figure 5.37(b) shows the measured k_{12} as a function of the wheel's rotation in different lateral displacements along the x axis (m_x). In a perfect aligned position ($m_x = 0$ mm), there is a drastic k_{12} drop between 0° and $\pm$ 30°. This is a consequence
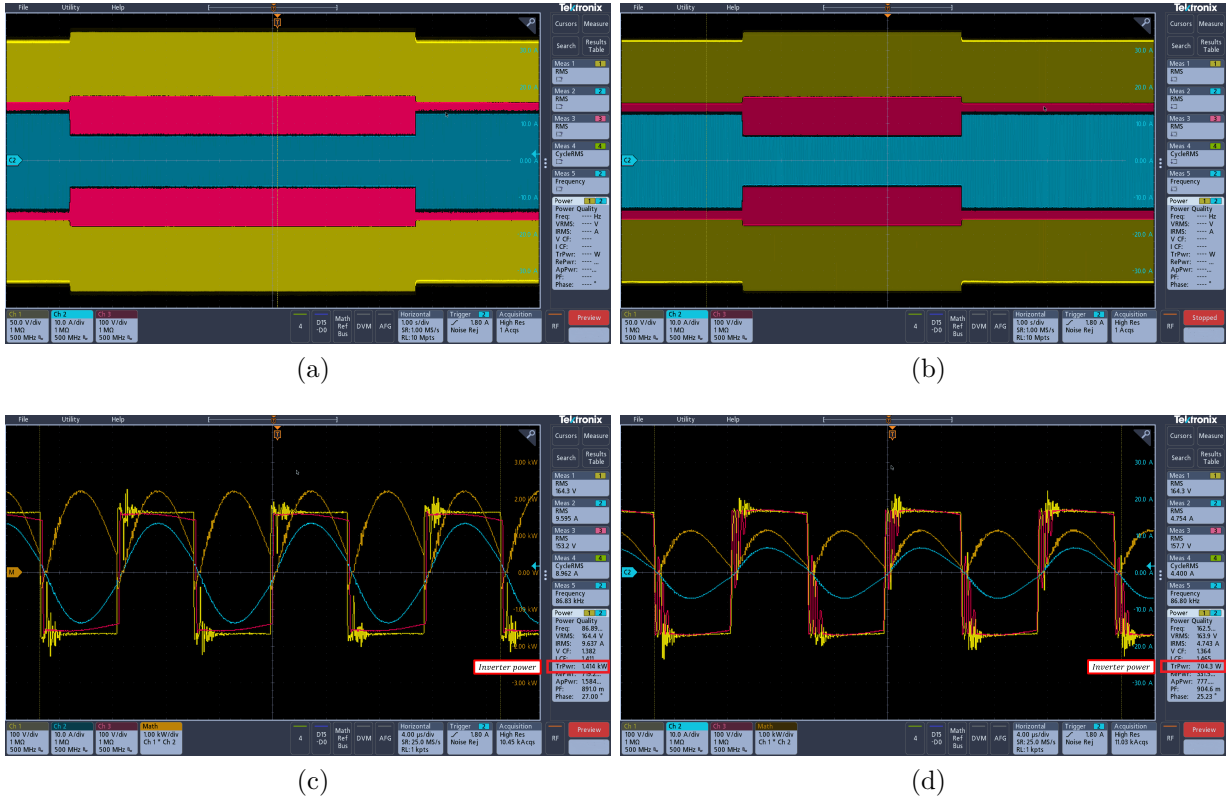
Figure 5.38: Waveforms of v_1, i_1 and v_{Req} for: (a) load response with $L_{12} = 16$ μH, (b) load response with $L_{12} = 13$ μH, (c) $L_{12} = 16$ μH with inverter power of 1.4 kW and (d) $L_{12} = 16$ μH with inverter power of 700 W.

of a decoupling of the receiver coils with both transmitter coils. In this charging position, the system behaves similarly to a DDP with a quadrature coil (Q) in a typical IPT system, hence the no coupling scenario depicted in Figure 5.37(b). One way to avoid this no-coupling scenario is to move the vehicle ±50 mm along the x axis to improve k_{12} to admissible values. Figure 5.37(b) also shows k_{12} as a function of the wheel's rotation for displacement scenarios along the x axis of ± 50 mm (pink and red lines). The displacement of 50 mm corresponds to approximately 30° wheel's rotation. Therefore, an initial 30° wheel's rotation (charging point marked as $Pos1$ in Figure 5.37(b) for $m_x = 0$ mm) will correspond to $Pos2$ after a vehicle movement of 50 mm along the x axis. This translates in an increase of k_{12} from 0.05 to 0.17. The worst k_{12} variation occurs between 45° and 60°. In such scenarios, the inclination of the receiver coil in respect to the transmitter coil causes a reduction of almost 22% to a minimum value of 0.12, corresponding to $L_{12} = 7.8$ μH. Therefore, the specifications from Table 5.8 are met within a tolerance of ± 50 mm along the x axis from the aligned position ($m_x = 0$ mm), regardless of the relative positioning of the receiver coils. The resulting k_{12} with displacement adjustment is depicted in Figure 5.37(b) by the black dashed line.

The results of Figure 5.38(a) and Figure 5.38(b) show the dynamic response to R_{eq}
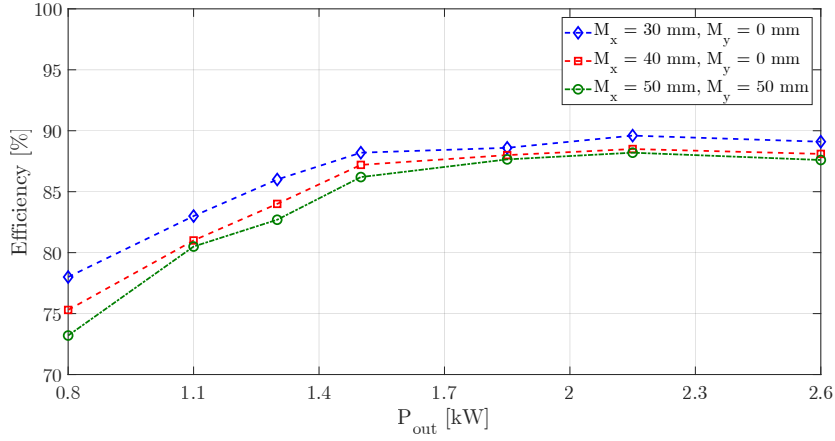
Figure 5.39: Experimental efficiency curves as a function of P_{out} under different air gap and lateral displacements.

variations between 20 and 55 Ω in an aligned ($L_{12} = 16$ μH) and a 50 mm misaligned ($L_{12} = 13$ μH) position of the ORMC. The yellow and blue signals represent v_1 and i_1, respectively, whereas v_{Req} corresponds to the red signal. The red lines indicate the load transitions. The amplitudes of both v_1 and v_{Req} increase in proportion by 7.6 % when the inverter power passes from 1.4 kW to 0.7 kW. Nevertheless, the voltage gain remains approximately constant with a error difference between both load conditions inferior to 2 %. The results from Figure 5.38(b) have a smaller voltage gain due to the increase of the switching frequency from 85.2 kHz to 86.8 kHz in order to avoid free-wheeling currents in the inverter due to the fixed 250 ns dead time zone of the PT62SCMD120 gate drivers.

Figure 5.38(c) and Figure 5.38(d) show the waveforms of v_1, i_1, v_{Req} and inverter instantaneous output power (orange signal) for the charging position with 50 mm lateral displacement, illustrated in Figure 5.38(b). The amplitude value of v_1 remains the same in both scenarios whereas v_{Req} has a small variation of 2.4 %. Moreover, both voltage signals remain approximately in phase with similar square pattern. The phase angle between the rising edge of v_1 and i_1 differs 1.7° between the two load conditions. The value of $|\overline{I}_2|$ has also maximum values around 16 A with low harmonic content. Another characteristic of the SSS double coupling system is also the low harmonic content in i_1 (blue waveform). Additionally, under no-load operation, the double coupling system limits $|\overline{I}_1|$, in the worst L_{12} case, to 12.5 A. In contrast, $|\overline{I}_1|$ would largely exceed $|\overline{I}_{inv_{rated}}|$ in a conventional series-series IPT configuration.

Figure 5.39 shows the efficiency as a function of P_{out} under different air gap and lateral displacements and a null wheel's rotation angle. A maximum efficiency of 89.6 % is achieved when transferring 2.2 kW with an air gap of 30 mm. In the worst charging position the

efficiency decreases to 88.2 % for the same 2.2 kW. The low difference between the optimal and worst charging positions is a consequence of the smaller k_{12} variations when the wheel's rotation angle is null. In the worst rotation angle position (60° as depicted in Figure 5.37(b)), k_{12} drops to 0.12 and the efficiency decreases 86.3 % when transferring 2.2 kW.

Table 5.9 compares the experimental results of the proposed work with recent literature in IPT systems. The majority of works conducted experimental tests with air gaps between 150 and 200 mm. In terms of lateral displacements, they range between 0 and 150 mm. One clear distinction between different works is the absence of shielding in the receiver side. The works with passive shielding (aluminum sheets) tend to have slightly lower overall efficiency values ($\approx$ 90 %). A global appreciation of the all efficiencies show, with the exception of [133], all recent works have comparable efficiency values.

Table 5.9: Comparison of experimental results with the existing literature

Work	Air gap [mm]	Displacement [mm]	Shield	Freq [kHz]	P_{out} [kW]	η_{sys}
[302]	200	0	No	85	0.7	93.14
[302]	200	100	No	85	0.7	89
[139]	150	0	No	85	1.09	89.86
[133]	150	0	No	85	3.3	95.2
[133]	150	240	No	85	3.3	93.1
[187]	175	0	Yes	85	6.7	90.8
[187]	175	75	Yes	85	6.7	89.9
[323]	140	0	Yes	85	3.3	91.6
[323]	140	120	Yes	85	3.3	88
-	40	0	Yes	86	2.2	89.6
-	40	50	Yes	86	2.2	88.2

5.6   Summary

This chapter presents a novel double coupling in-wheel IPT system. The inclusion of a second magnetic coupler enables the energy transfer between the wheel and the vehicle without the need of slip rings. In this way, the air gap between the off-board and the vehicle sides is kept to a minimum and almost independent of the vehicle class. Furthermore, inWIPT avoids the use of vehicle positioning systems and mitigates the risk of exposure to large magnetic fields.

The wheel curvature and rotation modify the coupling profiles in existing non-polarized and polarized geometries for the first magnetic coupler. Consequently, a comparative study using known geometries like the RP, DDP and BPP in the off-board transmitter pad against a single-coil non-polarized and a double-coil polarized geometries in the wheel receiver pad.

The maximum coupling is achieved when the correlation between the coil size and the wheel's perimeter is 18 % and 30 % for polarized and non-polarized geometries, respectively. The low air gap between the transmitter and receiver pads offers coupling profiles above 0.2, even under lateral displacements, for static applications with a unitary size ratio. For dynamic applications, the width of the transmitter pad is 2-2.2 times larger than the width of the receiver pad in order to cope with the larger required lateral displacement values (± 150 mm). In these scenarios, the coupling profiles are lower, in the range of 0.12-0.16, but with low variation regardless of the lateral displacement.

A hollow cylindrical design for the new magnetic coupler is also presented based on the solenoid geometry. The use of a segmented ferromagnetic core with 12 ferrite strips offers the best use of ferromagnetic material versus uncompensated power. The geometry exhibits coupling profiles almost independent of the wheel rotation, with variations inferior to 2 %.

The magnetic couplers are connected by a new resonant compensation network, and the existing designing rules can not be applied to the double coupling configuration. The intrinsic characteristics like operation with current and/or voltage source characteristics were examined for a series-series-series (SSS) and series-series-parallel (SSP) configurations. The SSS configuration exhibits load independent voltage source characteristics when the operating frequency matches the natural resonance frequency of the three compensation networks. In addition, the impedance seen at the inverter terminals is purely resistive in the entire load range, thus ensuring ZPA operation. The SSS configuration also avoids high circulating currents in the inverter under no-load operation. On the other hand, the SSP exhibits a load independent transconductance transfer function with ZPA operation when the operating frequency matches the natural resonance frequency of the three compensation networks.

The selection of the operating frequency and mutual inductance ranges vary with the system specifications and constraints. A design methodology that ensures a constant load independent voltage source characteristic is presented for plug-in integration with the existing on-board converter. The design combines the desired voltage gain with maximum induced voltage values across the coils in both magnetic couplers to retrieve the solution that offers the maximum lateral tolerance with minimum current in the intermediary compensation network. The presented methodology is validated experimentally in a real-size 18 inches aluminum rim with a maximum efficiency of 89.6 % when transferring 2.2 kW.

Chapter 6

Conclusions and Future Work

6.1 Conclusions

The greatest benefit of IPT systems is their ability to transfer energy between two sides without any contacts. It is also responsible for the limiting power transfer capability over large displacements. This thesis focused on mitigating the effects of vertical and lateral displacements by proposing new design methodologies, optimized magnetic designs or new IPT configurations.

Resonant compensation networks were firstly employed in IPT systems to overcome the low coupling factors caused by vertical and lateral displacements. Still, early magnetic designs had poor tolerance to displacements and a great effort was made in the literature to find better magnetic designs. Current magnetic couplers have their magnetic properties honed to the maximum but IPT power transfer capabilities are still limited for high displacements. A new IPT configuration appeared with intermediate resonators placed between both sides to boost the effective magnetic coupling. The full capabilities of this configuration, however, are not achievable as the intermediate resonator is placed closer to the transmitter side. The work conducted in this thesis made contributions in all the aforementioned solutions, but these are only half-measures for the displacement constraint. A new double coupling configuration is presented in this work that keeps vertical displacements to a minimum and independent of the vehicle class. The main contributions of the thesis are listed below by chapter.

- Chapter 2 explores IPT concept and past, current and future trends. Here the elongated versus the segmented transmitter pad configurations for dynamic IPT applications are analyzed. A special emphasis is given to power transfer capabilities under large air gap and lateral displacements. From here, IPT systems are classified into four main research areas: circuit analysis, resonant configurations, magnetic coupler and

controllers & control. The intrinsic characteristics of the basic configurations using a single coupling are highlighted. The generic reflected impedance equations are derived to assess the impact of frequency deviations from the resonant point. High order resonant configurations for single and multiple couplings are also presented and their main benefits detailed. Following this, key aspects of magnetic coupler designs were presented including the most suitable geometries for static charging applications like the Circular, Solenoid, Double-D and Bipolar pads. Finally, the most common off-board and on-board converter topologies and respective control strategies are presented and compared.

- Chapter 3 presents a vertical double receiver static IPT system based on the solenoid geometry. The use of a vertical transmitter pad reduces the vertical and lateral displacements to the receiver pad. In addition, such configuration avoids the use of Foreign Object Detection (FOD) systems to detect metallic objects between the transmitter and receiver pads. Several solenoid core arrangements were investigated using a 3D Finite Element Analysis (FEA) tool. The interoperability with both polarized and non-polarized geometries was also assessed as well as the compliance with ICNIRP rules of human exposure to stray magnetic fields. The magnetic properties of the selected geometries were validated experimentally.

- A comparative study of different non-polarized and polarized geometries with ferromagnetic cores, "pipe" coils and intermediate coils was also carried out in Chapter 3 for roadway applications. The goal of this study was the procurement of viable geometry alternatives that avoided the need of a ferromagnetic core. A new Ferrite-less Circular Pad (FLCP) geometry is proposed. The FLCP uses a cone shaped "pipe" coil to conduct the magnetic flux lines in the back-end of a Circular Pad (CP) geometry. The FLCP was optimized using a 3D FEA tool and compared with the remaining geometries. The simulation results were validated experimentally and showed similar coupling profiles to the CP but avoiding entirely the use of ferrites.

- Chapter 3 culminates in a new mapping methodology of the self and mutual inductance profiles as a function of the number of turns, air gap and lateral displacements with reduced computational effort. The methodology models the effect of vertical and lateral displacements with decay exponential and Gaussian functions, respectively. The effects of the number of turns in each coil are modeled using linear and second order functions for mutual and self-inductance values, respectively.

The mapping methodology avoids new FEA simulations if the charging positioning

or power requirements are modified. Additionally, the use of fitting functions convert discrete FEA simulation points in a continuous mapped volume. The methodology is applicable to non-polarized and polarized geometries including geometries with an intermediate coupler. A total of 60 FEA simulations are required to fully map circular geometries whereas non-circular pads like the DDP and the BPP require a total of 180 FEA simulations. A mapping example of the FLCP was carried out and compared with both FEA simulations and experimental measurements.

- Chapter 4 presents a design methodology to obtain a load-independent constant current charging mode using an intermediate coupler. The design methodology derives the fundamental equations for a series-series configuration with an intermediate coupler to find all capacitor values that guarantee a null reflected reactance from the receiver side. This condition also ensures an almost ZPA operation, regardless of the mutual and load values. A set of selection metrics are also presented based on system specifications like frequency range operation, maximum efficiency, minimum cost or weighted weigh cost-effectiveness function.

  The battery charging process is controlled using the transmitter side inverter. An estimation algorithm is proposed using only the output inverter voltage and current signals together with intermediate current signal to estimate the equivalent load resistance and mutual inductance values. Since the algorithm uses only measurements from the transmitter side the communication link to the vehicle can be avoided. The estimation algorithm was analyzed against the aging effect in the system capacitors and the non-linearity of voltage and current sensors, presenting a good performance even in the worst conditions. Both the design methodology and estimation algorithm were validated in simulation and experimentally in a converted electric vehicle.

- Chapter 5 introduces a novel double coupling in-Wheel IPT (inWIPT) system. The proposed system configuration ensures a minimum air gap between the off-board and the vehicles sides despite the vehicle class. In addition, given the known positioning of the system in the wheels, the lateral displacement tolerances are also reduced and the use of vehicle positioning systems are avoided. A set of curve based non-polarized and polarized geometries are presented and optimized using 3D FEA tools. The optimized geometries show better coupling profiles than a typical IPT system even under lateral displacement conditions. In addition, the compliance with ICNIRP guidelines is met at shorter distances.

  A design methodology that determines the operating frequency and mutual induc-

tance ranges is also presented in Chapter 5 for double coupling IPT configurations. The design combines the desired voltage gain with the maximum induced voltage values across the coils in both magnetic couplers to retrieve the solution that offers the maximum lateral tolerance with minimum current in the wheel side. The method considers a series-series-series resonant configuration but the series-series-parallel was also analyzed for constant current applications. The inWIPT system is validated experimentally in a real size aluminum rim.

6.2   Future Work

The contributions made in this thesis create new research opportunities. The following areas of research are considered:

- The literature review showed the existence of numerous resonant network configurations in two-coil, three-coil and double coupling systems. Unfortunately, the selection of the must suitable configuration for a particular IPT application is not linear and often inappropriate. Therefore, the existence of a framework that combines the intrinsic characteristics of each resonant configuration and selects the best one, based on a given set of specifications and constraints, would ensure optimal operation far any IPT application.

- The mapping of the self and mutual inductance profiles provides useful surface areas to correlate with vehicle positioning algorithms that use off-board measurements. The presented methodology addresses vertical and lateral displacements for a fixed MC size. The expansion of the methodology to cope with different MC sizes with minimum number of FEA simulations would allow the optimal sizing of a MC geometry based on the system requirements. Initial FEA simulations showed a linear behavior of the magnetic parameters of a MC in different sizes, if the size ratio of both transmitter and receiver pads are kept constant. This conclusion together with the work presented in [305] would serve as a starting point for a generic sizing and mapping methodology.

- Three-coil systems hold benefits over two-coil coil systems, especially under large displacement charging scenarios. The presented methodology in Chapter 4 ensures a CC mode, regardless of load and coupling values. The same series-series with an IC configuration also exhibits voltage source characteristics. Unfortunately, the frequency operation is different from the CC mode at a much higher value, falling outside the operating range defined by the SAE J2954. The use of a variable inductor [107] or

variable capacitor [247] in the intermediate resonant network would adjust the natural resonant frequency to fall within acceptable operating frequency range. Therefore, the study of this new configuration would offer both CC and CV modes using only the off-board inverter and without communication link to the vehicle.

- The proposed double coupling inWIPT was analyzed with different resonant configurations and different geometries in both MCs. Still, the system presents room for improvement in the following areas:
  - The presented work investigated two possible resonant configurations, the series-series-series and the series-series-parallel. Still, the use of the parallel configuration in the intermediary side could offer benefits not presently known. The same occurs for the use of other configurations, including an intermediate coupler, in the transmitter side. Therefore, a comparative analysis of different resonant configurations in double coupling systems would provide invaluable knowledge in the selection process of the best suitable configuration for a given IPT system.
  - The presented work also discussed two possible configurations to interconnect the ORMC receiver coils with the IRMC transmitter coil(s), and ensure a 360° wheel coverage. In these configurations, the IRMC is assumed to have a solenoid geometry, thus the coupling of the IRMC is constant, regardless of the wheel rotation. Still, if both ORMC and IRMC geometries are the same, the pattern of both couplings will be identical. In such working conditions, the system voltage gain, assuming a series-series-series resonant configuration, would be identical regardless of the system positioning. Therefore, such configuration could potentially ensure a constant voltage gain in dynamic applications.
  - The ORMC geometry was optimized in this work using different coil arrangements. Still, the same ferromagnetic core geometry, formed by ferrite strips, was considered for all coil arrangements in the receiver pad. The investigation of different core arrangements could boost the magnetic link even further between the transmitter and receiver pads. New 3D printing techniques allow the combine use of resins with other materials, namely ferromagnetic powder. Consequently, new receiver core geometries could be investigated including a honeycomb shape to assess the coupling profiles in different charging positions.
  - The presented inWIPT system was investigated in static charging conditions, but its applicability can be extended to dynamic IPT applications. The optimal approach for the dynamic off-board transmitter configuration, either segmented

or elongated, is not clear since each option has merits and limitations. One major drawback in using the elongated track configuration is the lower coupling and stray magnetic fields during the vehicle absence. The inWIPT system could potentially reduce the stray magnetic fields assuming the use of inWIPT in all wheels. In addition, lower air gaps may translate in longer tracks with similar coupling factors as in traditional IPT systems. The segmented configuration, on the other hand, offers better coupling profiles and the magnetic stray fields are better contained. This approach creates, however, a power fluctuation at the load terminals since the segmented pads are installed apart from one another. One solution is reducing the distance between pads to the point where the receiver pad is coupled simultaneously to two transmitter pads (during the transition between two consecutive pads). In this way, the total coupling scenario is avoided entirely and the power fluctuation is mitigated. The downside of moving transmitter pads closer is the appearance of a mutual coupling between them which will affect the coupling to the receiver pad. A distributed inWIPT solution could potentially minimize the power fluctuation with an asymmetric displacement of the transmitter pads to ensure that the power from all four wheels is almost constant.

– One of the major steps forward would be the implementation of inWIPT technology in multiple wheels with field trials in speeds closer to real EV applications (around 80 km/h). In this way, the benefits of inWIPT system with both elongated and segmented pads could be investigated.

References

[1] C. C. Chan, "The state of the art of electric, hybrid, and fuel cell vehicles," *Proceedings of the IEEE*, vol. 95, no. 4, pp. 704–718, April 2007.

[2] A. Khaligh and S. Dusmez, "Comprehensive topological analysis of conductive and inductive charging solutions for plug-in electric vehicles," *IEEE Transactions on Vehicular Technology*, vol. 61, no. 8, pp. 3475–3489, 2012.

[3] A. Khaligh and M. D'Antonio, "Global trends in high-power on-board chargers for electric vehicles," *IEEE Transactions on Vehicular Technology*, vol. 68, no. 4, pp. 3306–3324, 2019.

[4] M. Yilmaz and P. T. Krein, "Review of battery charger topologies, charging power levels, and infrastructure for plug-in electric and hybrid vehicles," *IEEE Transactions on Power Electronics*, vol. 28, no. 5, pp. 2151–2169, May 2013.

[5] J. Dai and D. C. Ludois, "A survey of wireless power transfer and a critical comparison of inductive and capacitive coupling for small gap applications," *IEEE Transactions on Power Electronics*, vol. 30, no. 11, pp. 6017–6029, 2015.

[6] S. Y. R. Hui, "Past, present and future trends of non-radiative wireless power transfer," *CPSS Transactions on Power Electronics and Applications*, vol. 1, no. 1, pp. 83–91, 2016.

[7] X. Lu, P. Wang, D. Niyato, D. I. Kim, and Z. Han, "Wireless charging technologies: Fundamentals, standards, and network applications," *IEEE Communications Surveys Tutorials*, vol. 18, no. 2, pp. 1413–1452, 2016.

[8] C.-H. Lin, M. Amir, M. Tariq, M. Shahvez, B. Alamri, A. Alahmadi, M. Siddiqui, and A. R. Beig, "Comprehensive analysis of ipt v/s cpt for wireless ev charging and effect of capacitor plate shape and foreign particle on cpt," *Processes*, vol. 9, no. 9, 2021. [Online]. Available: https://www.mdpi.com/2227-9717/9/9/1619

[9] J. Sallan, J. L. Villa, A. Llombart, and J. F. Sanz, "Optimal design of icpt systems applied to electric vehicle battery charge," *IEEE Transactions on Industrial Electronics*, vol. 56, no. 6, pp. 2140–2149, 2009.

[10] J. Dai and D. C. Ludois, "Single active switch power electronics for kilowatt scale capacitive power transfer," *IEEE Journal of Emerging and Selected Topics in Power Electronics*, vol. 3, no. 1, pp. 315–323, 2015.

[11] A. Kumar, S. Pervaiz, C. Chieh-Kai, S. Korhummel, Z. Popovic, and K. K. Afridi, "Investigation of power transfer density enhancement in large air-gap capacitive wireless power transfer systems," in *Wireless Power Transfer Conference (WPTC), 2015 IEEE*, pp. 1–4.

[12] F. Lu, H. Zhang, H. Hofmann, and C. Mi, "A double-sided <italic>lclc</italic>-compensated capacitive power transfer system for electric vehicle charging," *IEEE Transactions on Power Electronics*, vol. 30, no. 11, pp. 6011–6014, 2015.

[13] S. D. Barman, A. W. Reza, N. Kumar, M. E. Karim, and A. B. Munir, "Wireless powering by magnetic resonant coupling: Recent trends in wireless power transfer system and its applications," *Renewable and Sustainable Energy Reviews*, vol. 51, pp. 1525–1552, 2015. [Online]. Available: https://www.sciencedirect.com/science/article/pii/S1364032115006784

[14] S. R. Hui, "Magnetic resonance for wireless power transfer [a look back]," *IEEE Power Electronics Magazine*, vol. 3, no. 1, pp. 14–31, 2016.

[15] H. Li, K. Wang, L. Huang, W. Chen, and X. Yang, "Dynamic modeling based on coupled modes for wireless power transfer systems," *IEEE Transactions on Power Electronics*, vol. 30, no. 11, pp. 6245–6253, 2015.

[16] S. Y. R. Hui, W. Zhong, and C. K. Lee, "A critical review of recent progress in mid-range wireless power transfer," *IEEE Transactions on Power Electronics*, vol. 29, no. 9, pp. 4500–4511, 2014.

[17] C. Park, S. Lee, G. H. Cho, and C. T. Rim, "Innovative 5-m-off-distance inductive power transfer systems with optimally shaped dipole coils," *IEEE Transactions on Power Electronics*, vol. 30, no. 2, pp. 817–827, 2015.

[18] B. H. Choi, V. X. Thai, E. S. Lee, J. H. Kim, and C. T. Rim, "Dipole-coil-based wide-range inductive power transfer systems for wireless sensors," *IEEE Transactions on Industrial Electronics*, vol. 63, no. 5, pp. 3158–3167, 2016.

[19] B. H. Choi, E. S. Lee, J. Huh, and C. T. Rim, "Lumped impedance transformers for compact and robust coupled magnetic resonance systems," *IEEE Transactions on Power Electronics*, vol. 30, no. 11, pp. 6046–6056, 2015.

[20] W. Zhong, C. K. Lee, and S. Y. R. Hui, "General analysis on the use of tesla's resonators in domino forms for wireless power transfer," *IEEE Transactions on Industrial Electronics*, vol. 60, no. 1, pp. 261–270, 2013.

[21] A. P. Sample, D. T. Meyer, and J. R. Smith, "Analysis, experimental results, and range adaptation of magnetically coupled resonators for wireless power transfer," *IEEE Transactions on Industrial Electronics*, vol. 58, no. 2, pp. 544–554, 2011.

[22] C. Jungwon, D. Tsukiyama, Y. Tsuruda, and J. Rivas, "13.56 mhz 1.3 kw resonant converter with gan fet for wireless power transfer," in *Wireless Power Transfer Conference (WPTC), 2015 IEEE*, pp. 1–4.

[23] N. C. Kuo, B. Zhao, and A. M. Niknejad, "Bifurcation analysis in weakly-coupled inductive power transfer systems," *IEEE Transactions on Circuits and Systems I: Regular Papers*, vol. PP, no. 99, pp. 1–12, 2016.

[24] Z. Chunbo, L. Kai, Y. Chunlai, M. Rui, and C. Hexiao, "Simulation and experimental analysis on wireless energy transfer based on magnetic resonances," in *2008 IEEE Vehicle Power and Propulsion Conference*, pp. 1–4.

[25] M. Abou Houran, X. Yang, and W. Chen, "Magnetically coupled resonance wpt: Review of compensation topologies, resonator structures with misalignment, and emi diagnostics," *Electronics*, vol. 7, no. 11, 2018. [Online]. Available: https://www.mdpi.com/2079-9292/7/11/296

[26] A. Ahmad, M. S. Alam, and R. Chabaan, "A comprehensive review of wireless charging technologies for electric vehicles," *IEEE Transactions on Transportation Electrification*, vol. 4, no. 1, pp. 38–63, 2018.

[27] V. Cirimele, M. Diana, F. Freschi, and M. Mitolo, "Inductive power transfer for automotive applications: State-of-the-art and future trends," *IEEE Transactions on Industry Applications*, vol. 54, no. 5, pp. 4069–4079, Sep. 2018.

[28] J. Huang, Y. Zhou, Z. Ning, and H. Gharavi, "Wireless power transfer and energy harvesting: Current status and future prospects," *IEEE Wireless Communications*, vol. 26, no. 4, pp. 163–169, 2019.

[29] J. T. Boys and G. A. Covic, "The inductive power transfer story at the university of auckland," *IEEE Circuits and Systems Magazine*, vol. 15, no. 2, pp. 6–27, 2015.

[30] A. A. Mohamed, A. A. Shaier, H. Metwally, and S. I. Selem, "A comprehensive overview of inductive pad in electric vehicles stationary charging," *Applied Energy*, vol. 262, p. 114584, 2020. [Online]. Available: https://www.sciencedirect.com/science/article/pii/S0306261920300969

[31] H. Feng, R. Tavakoli, O. C. Onar, and Z. Pantic, "Advances in high-power wireless charging systems: Overview and design considerations," *IEEE Transactions on Transportation Electrification*, vol. 6, no. 3, pp. 886–919, 2020.

[32] N. Mohamed, F. Aymen, T. E. A. Alharbi, C. Z. El-Bayeh, S. Lassaad, S. S. M. Ghoneim, and U. Eicker, "A comprehensive analysis of wireless charging systems for electric vehicles," *IEEE Access*, vol. 10, pp. 43 865–43 881, 2022.

[33] J. M. Miller, O. C. Onar, and M. Chinthavali, "Primary-side power flow control of wireless power transfer for electric vehicle charging," *IEEE Journal of Emerging and Selected Topics in Power Electronics*, vol. 3, no. 1, pp. 147–162, 2015.

[34] O. C. Onar, J. M. Miller, S. L. Campbell, C. Coomer, C. P. White, and L. E. Seiber, "A novel wireless power transfer for in-motion ev/phev charging," in *2013 Twenty-Eighth Annual IEEE Applied Power Electronics Conference and Exposition (APEC)*, 2013, pp. 3073–3080.

[35] O. R. N. L. is managed by UT-Battelle LLC for the US Department of Energy, "Ornl demonstrates 120-kilowatt wireless charging for vehicles: Ornl," Oct 2018. [Online]. Available: https://www.ornl.gov/news/ornl-demonstrates-120-kilowatt-wireless-charging-vehicles

[36] S. Y. Choi and C. T. Rim, "Recent progress in developments of on-line electric vehicles," in *2015 6th International Conference on Power Electronics Systems and Applications (PESA)*, pp. 1–8.

[37] J. Huh, S. Lee, C. Park, G. H. Cho, and C. T. Rim, "High performance inductive power transfer system with narrow rail width for on-line electric vehicles," in *2010 IEEE Energy Conversion Congress and Exposition*, pp. 647–651.

[38] S. Lee, J. Huh, C. Park, N. S. Choi, G. H. Cho, and C. T. Rim, "On-line electric vehicle using inductive power transfer system," in *2010 IEEE Energy Conversion Congress and Exposition*, pp. 1598–1601.

[39] S. Lee, W. Lee, J. Huh, H. J. Kim, C. Park, G. H. Cho, and C. T. Rim, "Active emf cancellation method for i-type pickup of on-line electric vehicles," in *2011 Twenty-Sixth Annual IEEE Applied Power Electronics Conference and Exposition (APEC)*, March 2011, pp. 1980–1983.

[40] S. Choi, J. Huh, W. Y. Lee, S. W. Lee, and C. T. Rim, "New cross-segmented power supply rails for roadway-powered electric vehicles," *IEEE Transactions on Power Electronics*, vol. 28, no. 12, pp. 5832–5841, 2013.

[41] R. Bosshard, J. W. Kolar, J. Mühlethaler, I. Stevanović, B. Wunsch, and F. Canales, "Modeling and -pareto optimization of inductive power transfer coils for electric vehicles," *IEEE Journal of Emerging and Selected Topics in Power Electronics*, vol. 3, no. 1, pp. 50–64, 2015.

[42] R. Bosshard, U. Iruretagoyena, and J. W. Kolar, "Comprehensive evaluation of rectangular and double-d coil geometry for 50 kw/85 khz ipt system," *IEEE Journal of Emerging and Selected Topics in Power Electronics*, vol. 4, no. 4, pp. 1406–1415, Dec 2016.

[43] R. Bosshard and J. W. Kolar, "Multi-objective optimization of 50 kw/85 khz ipt system for public transport," *IEEE Journal of Emerging and Selected Topics in Power Electronics*, vol. 4, no. 4, pp. 1370–1382, 2016.

[44] S. Jayalath and A. Khan, "Design, challenges, and trends of inductive power transfer couplers for electric vehicles: A review," *IEEE Journal of Emerging and Selected Topics in Power Electronics*, vol. 9, no. 5, pp. 6196–6218, 2021.

[45] A. Mahesh, B. Chokkalingam, and L. Mihet-Popa, "Inductive wireless power transfer charging for electric vehicles–a review," *IEEE Access*, vol. 9, pp. 137 667–137 713, 2021.

[46] Z. Zhang, H. Pang, A. Georgiadis, and C. Cecati, "Wireless power transfer-an overview," *IEEE Transactions on Industrial Electronics*, vol. 66, no. 2, pp. 1044–1058, Feb 2019.

[47] T. M. Fisher, K. B. Farley, Y. Gao, H. Bai, and Z. T. H. Tse, "Electric vehicle wireless charging technology: a state-of-the-art review of magnetic coupling systems," *Wireless Power Transfer*, vol. 1, no. 2, p. 87–96, 2014.

[48] A. A. S. Mohamed, C. R. Lashway, and O. Mohammed, "Modeling and feasibility analysis of quasi-dynamic wpt system for ev applications," *IEEE Transactions on Transportation Electrification*, vol. 3, no. 2, pp. 343–353, 2017.

[49] A. C. Bagchi, A. Kamineni, R. A. Zane, and R. Carlson, "Review and comparative analysis of topologies and control methods in dynamic wireless charging of electric vehicles," *IEEE Journal of Emerging and Selected Topics in Power Electronics*, vol. 9, no. 4, pp. 4947–4962, 2021.

[50] J. T. Boys, G. A. Covic, and A. W. Green, "Stability and control of inductively coupled power transfer systems," *IEE Proceedings - Electric Power Applications*, vol. 147, no. 1, pp. 37–43, 2000.

[51] O. H. Stielau and G. A. Covic, "Design of loosely coupled inductive power transfer systems," in *Power System Technology, 2000. Proceedings. PowerCon 2000. International Conference on*, vol. 1, 2000, pp. 85–90 vol.1.

[52] G. A. Covic and J. T. Boys, "Inductive power transfer," *Proceedings of the IEEE*, vol. 101, no. 6, pp. 1276–1289, 2013.

[53] L. J. Chen, J. T. Boys, and G. A. Covic, "Power management for multiple-pickup ipt systems in materials handling applications," *IEEE Journal of Emerging and Selected Topics in Power Electronics*, vol. 3, no. 1, pp. 163–176, 2015.

[54] M. Budhia, G. Covic, and J. Boys, "Magnetic design of a three-phase inductive power transfer system for roadway powered electric vehicles," in *2010 IEEE Vehicle Power and Propulsion Conference*, Sept 2010, pp. 1–6.

[55] J.-Y. Lee, H.-Y. Shen, and K.-C. Chan, "Design and implementation of removable and closed-shape dual-ring pickup for contactless linear inductive power track system," *IEEE Transactions on Industry Applications*, vol. 50, no. 6, pp. 4036–4046, 2014.

[56] A. Shekhar, V. Prasanth, P. Bauer, and M. Bolech, "Generic methodology for driving range estimation of electric vehicle with on-road charging," in *Transportation Electrification Conference and Expo (ITEC), 2015 IEEE*, pp. 1–8.

[57] C. C. Mi, G. Buja, S. Y. Choi, and C. T. Rim, "Modern advances in wireless power transfer systems for roadway powered electric vehicles," *IEEE Transactions on Industrial Electronics*, vol. 63, no. 10, pp. 6533–6545, Oct 2016.

[58] D. M. Nguyen, M. A. Kishk, and M.-S. Alouini, "Modeling and analysis of dynamic charging for evs: A stochastic geometry approach," *IEEE Open Journal of Vehicular Technology*, vol. 2, pp. 17–44, 2021.

[59] S. Lee, B. Choi, and C. T. Rim, "Dynamics characterization of the inductive power transfer system for online electric vehicles by laplace phasor transform," *IEEE Transactions on Power Electronics*, vol. 28, no. 12, pp. 5902–5909, 2013.

[60] S. Y. Choi, B. W. Gu, S. Y. Jeong, and C. T. Rim, "Advances in wireless power transfer systems for roadway-powered electric vehicles," *IEEE Journal of Emerging and Selected Topics in Power Electronics*, vol. 3, no. 1, pp. 18–36, 2015.

[61] J. Shin, S. Shin, Y. Kim, S. Ahn, S. Lee, G. Jung, S.-J. Jeon, and D.-H. Cho, "Design and implementation of shaped magnetic-resonance-based wireless power transfer system for roadway-powered moving electric vehicles," *IEEE Transactions on Industrial Electronics*, vol. 61, no. 3, pp. 1179–1192, 2014.

[62] S. Y. Choi, S. Y. Jeong, B. W. Gu, G. C. Lim, and C. T. Rim, "Ultraslim s-type power supply rails for roadway-powered electric vehicles," *IEEE Transactions on Power Electronics*, vol. 30, no. 11, pp. 6456–6468, 2015.

[63] S. Cui, Z. Wang, S. Han, C. Zhu, and C. C. Chan, "Analysis and design of multiphase receiver with reduction of output fluctuation for ev dynamic wireless charging system," *IEEE Transactions on Power Electronics*, vol. 34, no. 5, pp. 4112–4124, 2019.

[64] B. Song, S. Cui, Y. Li, and C. Zhu, "A narrow-rail three-phase magnetic coupler with uniform output power for ev dynamic wireless charging," *IEEE Transactions on Industrial Electronics*, vol. 68, no. 8, pp. 6456–6469, 2021.

[65] W. Zhang, S. C. Wong, C. K. Tse, and Q. Chen, "An optimized track length in roadway inductive power transfer systems," *IEEE Journal of Emerging and Selected Topics in Power Electronics*, vol. 2, no. 3, pp. 598–608, 2014.

[66] W. Chen, F. Lin, G. A. Covic, and J. T. Boys, "Evaluation of a meandering track primary topology for ev roadway charging," *IEEE Journal of Emerging and Selected Topics in Industrial Electronics*, vol. 1, no. 1, pp. 26–35, 2020.

[67] F. Lu, H. Zhang, H. Hofmann, and C. C. Mi, "A dynamic charging system with reduced output power pulsation for electric vehicles," *IEEE Transactions on Industrial Electronics*, vol. 63, no. 10, pp. 6580–6590, 2016.

[68] J. M. Miller, P. Jones, J.-M. Li, and O. C. Onar, "Ornl experience and challenges facing dynamic wireless power charging of ev's," *IEEE Circuits and Systems Magazine*, vol. 15, no. 2, pp. 40–53, 2015.

[69] K. Lee, Z. Pantic, and S. M. Lukic, "Reflexive field containment in dynamic inductive power transfer systems," *IEEE Transactions on Power Electronics*, vol. 29, no. 9, pp. 4592–4602, 2014.

[70] T. Fujita, T. Yasuda, and H. Akagi, "A dynamic wireless power transfer system applicable to a stationary system," *IEEE Transactions on Industry Applications*, vol. 53, no. 4, pp. 3748–3757, 2017.

[71] S. Zhou, C. Zhu, S. Cui, Z. Wang, S. Zhou, and C. C. Chan, "Dynamic wireless power transfer system for electric vehicles employing multiplexing lcc modules with individual transmitters," *IEEE Access*, vol. 6, pp. 62 514–62 527, 2018.

[72] L. Xiang, X. Li, J. Tian, and Y. Tian, "A crossed dd geometry and its double-coil excitation method for electric vehicle dynamic wireless charging systems," *IEEE Access*, vol. 6, pp. 45 120–45 128, 2018.

[73] H. Wang, U. Pratik, A. Jovicic, N. Hasan, and Z. Pantic, "Dynamic wireless charging of medium power and speed electric vehicles," *IEEE Transactions on Vehicular Technology*, vol. 70, no. 12, pp. 12 552–12 566, 2021.

[74] R. Tavakoli and Z. Pantic, "Analysis, design, and demonstration of a 25-kw dynamic wireless charging system for roadway electric vehicles," *IEEE Journal of Emerging and Selected Topics in Power Electronics*, vol. 6, no. 3, pp. 1378–1393, 2018.

[75] Y. Guo, L. Wang, Q. Zhu, C. Liao, and F. Li, "Switch-on modeling and analysis of dynamic wireless charging system used for electric vehicles," *IEEE Transactions on Industrial Electronics*, vol. 63, no. 10, pp. 6568–6579, 2016.

[76] L. Chen, G. R. Nagendra, J. T. Boys, and G. A. Covic, "Double-coupled systems for ipt roadway applications," *IEEE Journal of Emerging and Selected Topics in Power Electronics*, vol. 3, no. 1, pp. 37–49, 2015.

[77] A. Zaheer, M. Neath, H. Z. Z. Beh, and G. A. Covic, "A dynamic ev charging system for slow moving traffic applications," *IEEE Transactions on Transportation Electrification*, vol. 3, no. 2, pp. 354–369, 2017.

[78] V. Z. Barsari, D. J. Thrimawithana, G. A. Covic, and S. Kim, "A switchable inductively coupled connector for ipt roadway applications," in *2020 IEEE PELS Workshop on Emerging Technologies: Wireless Power Transfer (WoW)*, 2020, pp. 35–39.

[79] V. Z. Barsari, D. J. Thrimawithana, and G. A. Covic, "An inductive coupler array for in-motion wireless charging of electric vehicles," *IEEE Transactions on Power Electronics*, vol. 36, no. 9, pp. 9854–9863, Sep. 2021.

[80] V. Cirimele, F. Freschi, L. Giaccone, L. Pichon, and M. Repetto, "Human exposure assessment in dynamic inductive power transfer for automotive applications," *IEEE Transactions on Magnetics*, vol. 53, no. 6, pp. 1–4, June 2017.

[81] G. R. Nagendra, L. Chen, G. A. Covic, and J. T. Boys, "Detection of evs on ipt highways," *IEEE Journal of Emerging and Selected Topics in Power Electronics*, vol. 2, no. 3, pp. 584–597, 2014.

[82] A. N. Azad, A. Echols, V. A. Kulyukin, R. Zane, and Z. Pantic, "Analysis, optimization, and demonstration of a vehicular detection system intended for dynamic wireless charging applications," *IEEE Transactions on Transportation Electrification*, vol. 5, no. 1, pp. 147–161, 2019.

[83] D. Patil, J. M. Miller, B. Fahimi, P. T. Balsara, and V. Galigekere, "A coil detection system for dynamic wireless charging of electric vehicle," *IEEE Transactions on Transportation Electrification*, vol. 5, no. 4, pp. 988–1003, 2019.

[84] Y. Shin, K. Hwang, J. Park, D. Kim, and S. Ahn, "Precise vehicle location detection method using a wireless power transfer (wpt) system," *IEEE Transactions on Vehicular Technology*, vol. 68, no. 2, pp. 1167–1177, 2019.

[85] J. Zhao, T. Cai, S. Duan, H. Feng, C. Chen, and X. Zhang, "A general design method of primary compensation network for dynamic wpt system maintaining stable transmission power," *IEEE Transactions on Power Electronics*, vol. 31, no. 12, pp. 8343–8358, 2016.

[86] Y. Liu, R. Mai, D. Liu, Y. Li, and Z. He, "Efficiency optimization for wireless dynamic charging system with overlapped dd coil arrays," *IEEE Transactions on Power Electronics*, vol. 33, no. 4, pp. 2832–2846, 2018.

[87] Y. Li, J. Hu, T. Lin, X. Li, F. Chen, Z. He, and R. Mai, "A new coil structure and its optimization design with constant output voltage and constant output current for electric

vehicle dynamic wireless charging," *IEEE Transactions on Industrial Informatics*, vol. 15, no. 9, pp. 5244–5256, 2019.

[88] K. Shi, C. Tang, H. Long, X. Lv, Z. Wang, and X. Li, "Power fluctuation suppression method for ev dynamic wireless charging system based on integrated magnetic coupler," *IEEE Transactions on Power Electronics*, vol. 37, no. 1, pp. 1118–1131, 2022.

[89] A. Kamineni, M. J. Neath, G. A. Covic, and J. T. Boys, "A mistuning-tolerant and controllable power supply for roadway wireless power systems," *IEEE Transactions on Power Electronics*, vol. 32, no. 9, pp. 6689–6699, Sept 2017.

[90] G. R. Nagendra, G. A. Covic, and J. T. Boys, "Sizing of inductive power pads for dynamic charging of evs on ipt highways," *IEEE Transactions on Transportation Electrification*, vol. 3, no. 2, pp. 405–417, June 2017.

[91] Z. Zhang, H. Pang, C. H. T. Lee, X. Xu, X. Wei, and J. Wang, "Comparative analysis and optimization of dynamic charging coils for roadway-powered electric vehicles," *IEEE Transactions on Magnetics*, vol. 53, no. 11, pp. 1–6, 2017.

[92] I. Karakitsios, F. Palaiogiannis, A. Markou, and N. D. Hatziargyriou, "Optimizing the energy transfer, with a high system efficiency in dynamic inductive charging of evs," *IEEE Transactions on Vehicular Technology*, vol. 67, no. 6, pp. 4728–4742, 2018.

[93] X. Dai, J.-C. Jiang, and J.-Q. Wu, "Charging area determining and power enhancement method for multiexcitation unit configuration of wirelessly dynamic charging ev system," *IEEE Transactions on Industrial Electronics*, vol. 66, no. 5, pp. 4086–4096, 2019.

[94] G. Di Capua and N. Femia, "Optimal coils and control matching in wireless power transfer dynamic battery chargers for electric vehicles," *IEEE Access*, vol. 9, pp. 166 542–166 551, 2021.

[95] L. Tan, W. Zhao, H. Liu, J. Li, and X. Huang, "Design and optimization of ground-side power transmitting coil parameters for ev dynamic wireless charging system," *IEEE Access*, vol. 8, pp. 74 595–74 604, 2020.

[96] S. Jeong, Y. J. Jang, and D. Kum, "Economic analysis of the dynamic charging electric vehicle," *IEEE Transactions on Power Electronics*, vol. 30, no. 11, pp. 6368–6377, 2015.

[97] C.-S. Wang, G. A. Covic, and O. H. Stielau, "Power transfer capability and bifurcation phenomena of loosely coupled inductive power transfer systems," *IEEE Transactions on Industrial Electronics*, vol. 51, no. 1, pp. 148–157, Feb 2004.

[98] V. Shevchenko, O. Husev, R. Strzelecki, B. Pakhaliuk, N. Poliakov, and N. Strzelecka, "Compensation topologies in ipt systems: Standards, requirements, classification, analysis, comparison and application," *IEEE Access*, vol. 7, pp. 120 559–120 580, 2019.

[99] R. K. Jha, G. Buja, M. Bertoluzzo, S. Giacomuzzi, and K. N. Mude, "Performance comparison of the one-element resonant ev wireless battery chargers," *IEEE Transactions on Industry Applications*, vol. 54, no. 3, pp. 2471–2482, 2018.

[100] W. Chwei-Sen, O. H. Stielau, and G. A. Covic, "Design considerations for a contactless electric vehicle battery charger," *IEEE Transactions on Industrial Electronics*, vol. 52, no. 5, pp. 1308–1314, 2005.

[101] J. L. Villa, J. Sallan, J. F. Sanz Osorio, and A. Llombart, "High-misalignment tolerant compensation topology for icpt systems," *IEEE Transactions on Industrial Electronics*, vol. 59, no. 2, pp. 945–951, 2012.

[102] W. Zhang, S.-C. Wong, C. K. Tse, and Q. Chen, "Design for efficiency optimization and voltage controllability of series–series compensated inductive power transfer systems," *IEEE Transactions on Power Electronics*, vol. 29, no. 1, pp. 191–200, 2014.

[103] M. Lu and K. D. T. Ngo, "Systematic design of coils in series-series inductive power transfer for power transferability and efficiency," *IEEE Transactions on Power Electronics*, vol. 33, no. 4, pp. 3333–3345, April 2018.

[104] B. Ni, C. Y. Chung, and H. L. Chan, "Design and comparison of parallel and series resonant topology in wireless power transfer," in *2013 IEEE 8th Conference on Industrial Electronics and Applications (ICIEA)*, 2013, pp. 1832–1837.

[105] D. Patil, M. K. McDonough, J. M. Miller, B. Fahimi, and P. T. Balsara, "Wireless power transfer for vehicular applications: Overview and challenges," *IEEE Transactions on Transportation Electrification*, vol. 4, no. 1, pp. 3–37, March 2018.

[106] R. L. Steigerwald, "A comparison of half-bridge resonant converter topologies," *IEEE Transactions on Power Electronics*, vol. 3, no. 2, pp. 174–182, Apr 1988.

[107] E. G. Marques, S. V. da Silva, C. Marques, J. V. N. Silva, M. S. Perdigão, and A. M. S. Mendes, "A new ipt transmitter configuration tolerant to magnetic coupler displacements," in *IECON 2017 - 43rd Annual Conference of the IEEE Industrial Electronics Society*, 2017, pp. 5307–5312.

[108] W. Zhang and C. C. Mi, "Compensation topologies of high-power wireless power transfer systems," *IEEE Transactions on Vehicular Technology*, vol. 65, no. 6, pp. 4768–4778, June 2016.

[109] Y. H. Sohn, B. H. Choi, E. S. Lee, G. C. Lim, G. H. Cho, and C. T. Rim, "General unified analyses of two-capacitor inductive power transfer systems: Equivalence of current-source ss and sp compensations," *IEEE Transactions on Power Electronics*, vol. 30, no. 11, pp. 6030–6045, 2015.

[110] X. Qu, H. Han, S. C. Wong, C. K. Tse, and W. Chen, "Hybrid ipt topologies with constant current or constant voltage output for battery charging applications," *IEEE Transactions on Power Electronics*, vol. 30, no. 11, pp. 6329–6337, 2015.

[111] A. A. S. Mohamed, A. Berzoy, F. G. N. de Almeida, and O. Mohammed, "Modeling and assessment analysis of various compensation topologies in bidirectional iwpt system for ev applications," *IEEE Transactions on Industry Applications*, vol. 53, no. 5, pp. 4973–4984, 2017.

[112] J. Lu, G. Zhu, H. Wang, F. Lu, J. Jiang, and C. C. Mi, "Sensitivity analysis of inductive power transfer systems with voltage-fed compensation topologies," *IEEE Transactions on Vehicular Technology*, vol. 68, no. 5, pp. 4502–4513, 2019.

[113] H. T. Nguyen, J. Y. Alsawalhi, K. A. Hosani, A. S. Al-Sumaiti, K. A. A. Jaafari, Y.-J. Byon, and M. S. E. Moursi, "Review map of comparative designs for wireless high-power transfer systems in ev applications: Maximum efficiency, zpa, and cc/cv modes at fixed resonance frequency independent from coupling coefficient," *IEEE Transactions on Power Electronics*, vol. 37, no. 4, pp. 4857–4876, 2022.

[114] S. Samanta and A. K. Rathore, "A new current-fed clc transmitter and lc receiver topology for inductive wireless power transfer application: Analysis, design, and experimental results," *IEEE Transactions on Transportation Electrification*, vol. 1, no. 4, pp. 357–368, 2015.

[115] X. Tan and X. Ruan, "Equivalence relations of resonant tanks: A new perspective for selection and design of resonant converters," *IEEE Transactions on Industrial Electronics*, vol. 63, no. 4, pp. 2111–2123, 2016.

[116] M. Borage, S. Tiwari, and S. Kotaiah, "Analysis and design of an lcl-t resonant converter as a constant-current power supply," *IEEE Transactions on Industrial Electronics*, vol. 52, no. 6, pp. 1547–1554, 2005.

[117] M. B. Borage, K. V. Nagesh, M. S. Bhatia, and S. Tiwari, "Characteristics and design of an asymmetrical duty-cycle-controlled lcl-t resonant converter," *IEEE Transactions on Power Electronics*, vol. 24, no. 10, pp. 2268–2275, 2009.

[118] J. U. W. Hsu and A. P. Hu, "Determining the variable inductance range for an lcl wireless power pick-up," in *Electron Devices and Solid-State Circuits, 2007. EDSSC 2007. IEEE Conference on*, pp. 489–492.

[119] H. H. Wu, A. Gilchrist, K. Sealy, P. Israelsen, and J. Muhs, "Design of symmetric voltage cancellation control for lcl converters in inductive power transfer systems," in *2011 IEEE International Electric Machines Drives Conference (IEMDC)*, pp. 866–871.

[120] Y. Wang, Y. Yao, X. Liu, D. Xu, and L. Cai, "An lc/s compensation topology and coil design technique for wireless power transfer," *IEEE Transactions on Power Electronics*, vol. 33, no. 3, pp. 2007–2025, 2018.

[121] A. A. S. Mohamed, A. A. Shaier, H. Metwally, and S. I. Selem, "An overview of dynamic inductive charging for electric vehicles," *Energies*, vol. 15, no. 15, 2022. [Online]. Available: https://www.mdpi.com/1996-1073/15/15/5613

[122] C. Y. Huang, J. T. Boys, G. A. Covic, and S. Ren, "Lcl pick-up circulating current controller for inductive power transfer systems," in *2010 IEEE Energy Conversion Congress and Exposition*, pp. 640–646.

[123] N. Keeling, G. A. Covic, F. Hao, L. George, and J. T. Boys, "Variable tuning in lcl compensated contactless power transfer pickups," in *2009 IEEE Energy Conversion Congress and Exposition*, Sept 2009, pp. 1826–1832.

[124] Y. Li, J. Hu, X. Li, and K. E. Cheng, "A flexible load-independent multi-output wireless power transfer system based on cascaded double t-resonant circuits: Analysis, design and experimental verification," *IEEE Transactions on Circuits and Systems I: Regular Papers*, vol. 66, no. 7, pp. 2803–2812, July 2019.

[125] T. Kan, T. D. Nguyen, J. C. White, R. K. Malhan, and C. C. Mi, "A new integration method for an electric vehicle wireless charging system using lcc compensation topology: Analysis and design," *IEEE Transactions on Power Electronics*, vol. 32, no. 2, pp. 1638–1650, Feb 2017.

[126] Z. Pantic, S. Bai, and S. M. Lukic, "Zcs lcc-compensated resonant inverter for inductive-power-transfer application," *IEEE Transactions on Industrial Electronics*, vol. 58, no. 8, pp. 3500–3510, Aug 2011.

[127] G. Ke, Q. Chen, L. Xu, X. Ren, and Z. Zhang, "Analysis and optimization of a double-sided s-lcc hybrid converter for high misalignment tolerance," *IEEE Transactions on Industrial Electronics*, vol. 68, no. 6, pp. 4870–4881, June 2021.

[128] M. Mohammad, J. L. Pries, O. C. Onar, V. P. Galigekere, G.-J. Su, and J. Wilkins, "Three-phase lcc-lcc compensated 50-kw wireless charging system with non-zero interphase coupling," in *2021 IEEE Applied Power Electronics Conference and Exposition (APEC)*, 2021, pp. 456–462.

[129] T. Campi, S. Cruciani, F. Maradei, and M. Feliziani, "Near-field reduction in a wireless power transfer system using lcc compensation," *IEEE Transactions on Electromagnetic Compatibility*, vol. 59, no. 2, pp. 686–694, April 2017.

[130] S. Li, W. Li, J. Deng, T. D. Nguyen, and C. C. Mi, "A double-sided lcc compensation network and its tuning method for wireless power transfer," *IEEE Transactions on Vehicular Technology*, vol. 64, no. 6, pp. 2261–2273, 2015.

[131] V.-B. Vu, D.-H. Tran, and W. Choi, "Implementation of the constant current and constant voltage charge of inductive power transfer systems with the double-sided lcc compensation topology for electric vehicle battery charge applications," *IEEE Transactions on Power Electronics*, vol. 33, no. 9, pp. 7398–7410, 2018.

[132] X. Qu, H. Chu, S.-C. Wong, and C. K. Tse, "An ipt battery charger with near unity power factor and load-independent constant output combating design constraints of input voltage and transformer parameters," *IEEE Transactions on Power Electronics*, vol. 34, no. 8, pp. 7719–7727, 2019.

[133] F. Wang, W. Zhang, L. Ye, J. Guo, K. Liu, and H. T. Do, "A design method to implement zvs for electric vehicle wireless charging system with double-side lcc compensation," *IEEE Journal of Emerging and Selected Topics in Power Electronics*, vol. 9, no. 3, pp. 3791–3801, 2021.

[134] J. Deng, W. Li, T. D. Nguyen, S. Li, and C. C. Mi, "Compact and efficient bipolar coupler for wireless power chargers: Design and analysis," *IEEE Transactions on Power Electronics*, vol. 30, no. 11, pp. 6130–6140, 2015.

[135] F. Lu, H. Zhang, H. Hofmann, W. Su, and C. C. Mi, "A dual-coupled lcc-compensated ipt system with a compact magnetic coupler," *IEEE Transactions on Power Electronics*, vol. 33, no. 7, pp. 6391–6402, 2018.

[136] W. Li, H. Zhao, S. Li, J. Deng, T. Kan, and C. C. Mi, "Integrated lcc compensation topology for wireless charger in electric and plug-in electric vehicles," *IEEE Transactions on Industrial Electronics*, vol. 62, no. 7, pp. 4215–4225, 2015.

[137] Z. Yan, Y. Zhang, K. Zhang, B. Song, S. Li, T. Kan, and C. C. Mi, "Fault-tolerant wireless power transfer system with a dual-coupled lcc-s topology," *IEEE Transactions on Vehicular Technology*, vol. 68, no. 12, pp. 11 838–11 846, 2019.

[138] W. Li, H. Zhao, J. Deng, S. Li, and C. C. Mi, "Comparison study on ss and double-sided lcc compensation topologies for ev/phev wireless chargers," *IEEE Transactions on Vehicular Technology*, vol. 65, no. 6, pp. 4429–4439, June 2016.

[139] Z. Dai and J. Wang, "A dual-frequency wpt based on multilayer self-decoupled compact coil and dual <italic>clcl</italic> hybrid compensation topology," *IEEE Transactions on Power Electronics*, vol. 37, no. 11, pp. 13 955–13 965, 2022.

[140] J. Hou, Q. Chen, S.-C. Wong, C. K. Tse, and X. Ruan, "Analysis and control of series/series-parallel compensated resonant converter for contactless power transfer," *IEEE Journal of Emerging and Selected Topics in Power Electronics*, vol. 3, no. 1, pp. 124–136, 2015.

[141] Y. Yao, Y. Wang, X. Liu, K. Lu, and D. Xu, "Analysis and design of an s/sp compensated ipt system to minimize output voltage fluctuation versus coupling coefficient and load variation," *IEEE Transactions on Vehicular Technology*, vol. 67, no. 10, pp. 9262–9272, 2018.

[142] X. Qu, Y. Jing, H. Han, S.-C. Wong, and C. K. Tse, "Higher order compensation for inductive-power-transfer converters with constant-voltage or constant-current output combating transformer parameter constraints," *IEEE Transactions on Power Electronics*, vol. 32, no. 1, pp. 394–405, 2017.

[143] J. Lu, G. Zhu, D. Lin, S.-C. Wong, and J. Jiang, "Load-independent voltage and current transfer characteristics of high-order resonant network in ipt system," *IEEE Journal of Emerging and Selected Topics in Power Electronics*, vol. 7, no. 1, pp. 422–436, 2019.

[144] Y. Wang, Y. Yao, X. Liu, and D. Xu, "S/clc compensation topology analysis and circular coil design for wireless power transfer," *IEEE Transactions on Transportation Electrification*, vol. 3, no. 2, pp. 496–507, June 2017.

[145] Y. Yao, Y. Wang, X. Liu, Y. Pei, D. Xu, and X. Liu, "Particle swarm optimization-based parameter design method for s/clc-compensated ipt systems featuring high tolerance to misalignment and load variation," *IEEE Transactions on Power Electronics*, vol. 34, no. 6, pp. 5268–5282, 2019.

[146] M. Kiani, U. M. Jow, and M. Ghovanloo, "Design and optimization of a 3-coil inductive link for efficient wireless power transmission," *IEEE Transactions on Biomedical Circuits and Systems*, vol. 5, no. 6, pp. 579–591, Dec 2011.

[147] D. Ahn and S. Hong, "A study on magnetic field repeater in wireless power transfer," *IEEE Transactions on Industrial Electronics*, vol. 60, no. 1, pp. 360–371, 2013.

[148] S. Moon, B. C. Kim, S. Y. Cho, C. H. Ahn, and G. W. Moon, "Analysis and design of a wireless power transfer system with an intermediate coil for high efficiency," *IEEE Transactions on Industrial Electronics*, vol. 61, no. 11, pp. 5861–5870, 2014.

[149] A. Kamineni, G. A. Covic, and J. T. Boys, "Analysis of coplanar intermediate coil structures in inductive power transfer systems," *IEEE Transactions on Power Electronics*, vol. 30, no. 11, pp. 6141–6154, 2015.

[150] A. Bilal, S. Kim, F. Lin, and G. A. Covic, "Analysis of ipt intermediate coupler system for vehicle charging over large air gaps," *IEEE Journal of Emerging and Selected Topics in Industrial Electronics*, pp. 1–1, 2021.

[151] K. Lee and S. H. Chae, "Power transfer efficiency analysis of intermediate-resonator for wireless power transfer," *IEEE Transactions on Power Electronics*, vol. 33, no. 3, pp. 2484–2493, March 2018.

[152] M. Machnoor, E. S. Gomez Rodriguez, P. Kosta, J. Stang, and G. Lazzi, "Analysis and design of a 3-coil wireless power transmission system for biomedical applications," *IEEE Transactions on Antennas and Propagation*, vol. 67, no. 8, pp. 5012–5024, Aug 2019.

[153] J. Zhang, X. Yuan, C. Wang, and Y. He, "Comparative analysis of two-coil and three-coil structures for wireless power transfer," *IEEE Transactions on Power Electronics*, vol. 32, no. 1, pp. 341–352, Jan 2017.

[154] E. G. Marques, A. M. S. Mendes, M. S. Perdigão, and V. S. Costa, "Design methodology of a three coil ipt system with parameters identification for evs," *IEEE Transactions on Vehicular Technology*, vol. 70, no. 8, pp. 7509–7521, Aug 2021.

[155] Y. Li, Q. Xu, T. Lin, J. Hu, Z. He, and R. Mai, "Analysis and design of load-independent output current or output voltage of a three-coil wireless power transfer system," *IEEE Transactions on Transportation Electrification*, vol. 4, no. 2, pp. 364–375, June 2018.

[156] D. H. Tran, V. B. Vu, and W. Choi, "Design of a high-efficiency wireless power transfer system with intermediate coils for the on-board chargers of electric vehicles," *IEEE Transactions on Power Electronics*, vol. 33, no. 1, pp. 175–187, Jan 2018.

[157] R. Mai, B. Yang, Y. Chen, N. Yang, Z. He, and S. Gao, "A misalignment tolerant ipt system with intermediate coils for constant-current output," *IEEE Transactions on Power Electronics*, vol. 34, no. 8, pp. 7151–7155, Aug 2019.

[158] U. K. Madawala and D. J. Thrimawithana, "Modular-based inductive power transfer system for high-power applications," *IET Power Electronics*, vol. 5, no. 7, pp. 1119–1126, 2012.

[159] C. Cheng, F. Lu, Z. Zhou, W. Li, C. Zhu, H. Zhang, Z. Deng, X. Chen, and C. C. Mi, "Load-independent wireless power transfer system for multiple loads over a long distance," *IEEE Transactions on Power Electronics*, vol. 34, no. 9, pp. 9279–9288, Sep. 2019.

[160] E. G. Marques, V. S. Costa, M. Torres, B. Rios, A. Mendes, and M. S. Perdigão, "Double coupling ipt systems for ev charging applications," in *2021 IEEE Vehicle Power and Propulsion Conference (VPPC)*, 2021, pp. 1–6.

[161] C. Joffe, S. Ditze, A. Ro, x00Df, and kopf, "A novel positioning tolerant inductive power transfer system," in *Electric Drives Production Conference (EDPC), 2013 3rd International*, pp. 1–7.

[162] V. Prasanth and P. Bauer, "Distributed ipt systems for dynamic powering: Misalignment analysis," *IEEE Transactions on Industrial Electronics*, vol. 61, no. 11, pp. 6013–6021, 2014.

[163] C. Zheng, H. Ma, J. S. Lai, and L. Zhang, "Design considerations to reduce gap variation and misalignment effects for the inductive power transfer system," *IEEE Transactions on Power Electronics*, vol. 30, no. 11, pp. 6108–6119, 2015.

[164] B. H. Choi, E. S. Lee, Y. H. Sohn, G. C. Jang, and C. T. Rim, "Six degrees of freedom mobile inductive power transfer by crossed dipole tx and rx coils," *IEEE Transactions on Power Electronics*, vol. 31, no. 4, pp. 3252–3272, 2016.

[165] D. Lin, C. Zhang, and S. Y. R. Hui, "Mathematical analysis of omnidirectional wireless power transfer two-dimensional systems," *IEEE Transactions on Power Electronics*, vol. 32, no. 1, pp. 625–633, Jan 2017.

[166] H. Wang, C. Zhang, Y. Yang, H. W. R. Liang, and S. Y. R. Hui, "A comparative study on overall efficiency of two-dimensional wireless power transfer systems using rotational and directional methods," *IEEE Transactions on Industrial Electronics*, vol. 69, no. 1, pp. 260–269, 2022.

[167] M. Budhia, G. A. Covic, and J. T. Boys, "Design and optimisation of magnetic structures for lumped inductive power transfer systems," in *2009 IEEE Energy Conversion Congress and Exposition*, 2009, pp. 2081–2088.

[168] R. Bosshard, J. W. Kolar, and B. Wunsch, "Accurate finite-element modeling and experimental verification of inductive power transfer coil design," in *2014 IEEE Applied Power Electronics Conference and Exposition - APEC 2014*, 2014, pp. 1648–1653.

[169] M. Moghaddami, A. Anzalchi, A. Moghadasi, and A. Sarwat, "Pareto optimization of circular power pads for contactless electric vehicle battery charger," in *2016 IEEE Industry Applications Society Annual Meeting*, Oct 2016, pp. 1–6.

[170] T. D. Nguyen, S. Li, W. Li, and C. C. Mi, "Feasibility study on bipolar pads for efficient wireless power chargers," in *2014 IEEE Applied Power Electronics Conference and Exposition - APEC 2014*, pp. 1676–1682.

[171] S. Bandyopadhyay, P. Venugopal, J. Dong, and P. Bauer, "Comparison of magnetic couplers for ipt-based ev charging using multi-objective optimization," *IEEE Transactions on Vehicular Technology*, vol. 68, no. 6, pp. 5416–5429, June 2019.

[172] R. Oliveira and P. Lehn, "An improved mutual inductance electromagnetic model for inductive power transfer systems under misalignment conditions," *IEEE Transactions on Vehicular Technology*, vol. 69, no. 6, pp. 6079–6093, 2020.

[173] A. Zaheer, H. Hao, G. A. Covic, and D. Kacprzak, "Investigation of multiple decoupled coil primary pad topologies in lumped ipt systems for interoperable electric vehicle charging," *IEEE Transactions on Power Electronics*, vol. 30, no. 4, pp. 1937–1955, 2015.

[174] M. Budhia, G. A. Covic, and J. T. Boys, "Design and optimization of circular magnetic structures for lumped inductive power transfer systems," *IEEE Transactions on Power Electronics*, vol. 26, no. 11, pp. 3096–3108, 2011.

[175] Y. Zhang, S. Chen, X. Li, and Y. Tang, "Design of high-power static wireless power transfer via magnetic induction: An overview," *CPSS Transactions on Power Electronics and Applications*, vol. 6, no. 4, pp. 281–297, 2021.

[176] W. Zhang, J. C. White, A. M. Abraham, and C. C. Mi, "Loosely coupled transformer structure and interoperability study for ev wireless charging systems," *IEEE Transactions on Power Electronics*, vol. 30, no. 11, pp. 6356–6367, 2015.

[177] U. M. Jow and M. Ghovanloo, "Geometrical design of a scalable overlapping planar spiral coil array to generate a homogeneous magnetic field," *IEEE Transactions on Magnetics*, vol. 49, no. 6, pp. 2933–2945, 2013.

[178] Y. Zhang, S. Chen, X. Li, and Y. Tang, "Design methodology of free-positioning nonoverlapping wireless charging for consumer electronics based on antiparallel windings," *IEEE Transactions on Industrial Electronics*, vol. 69, no. 1, pp. 825–834, 2022.

[179] M. Budhia, G. Covic, and J. Boys, "A new ipt magnetic coupler for electric vehicle charging systems," in *IECON 2010 - 36th Annual Conference on IEEE Industrial Electronics Society*, pp. 2487–2492.

[180] M. Chigira, Y. Nagatsuka, Y. Kaneko, S. Abe, T. Yasuda, and A. Suzuki, "Small-size lightweight transformer with new core structure for contactless electric vehicle power transfer system," in *2011 IEEE Energy Conversion Congress and Exposition*, pp. 260–266.

[181] F. Y. Lin, G. A. Covic, and J. T. Boys, "Evaluation of magnetic pad sizes and topologies for electric vehicle charging," *IEEE Transactions on Power Electronics*, vol. 30, no. 11, pp. 6391–6407, 2015.

[182] R. Shimizu, Y. Kaneko, and S. Abe, "A new he core transmitter of a contactless power transfer system that is compatible with circular core receivers and h-shaped core receivers," in *Electric Drives Production Conference (EDPC), 2013 3rd International*, pp. 1–7.

[183] M. Budhia, J. T. Boys, G. A. Covic, and C. Y. Huang, "Development of a single-sided flux magnetic coupler for electric vehicle ipt charging systems," *IEEE Transactions on Industrial Electronics*, vol. 60, no. 1, pp. 318–328, 2013.

[184] W. jing Li, J. hua Lu, G. rong Zhu, W. Zhang, and J. Jiang, "Design and research of a double-sided flux coupler in inductive power transfer system," in *IECON 2016 - 42nd Annual Conference of the IEEE Industrial Electronics Society*, Oct 2016, pp. 6033–6037.

[185] G. R. Kalra, M. G. S. Pearce, S. Kim, D. J. Thrimawithana, and G. A. Covic, "A power loss measurement technique for inductive power transfer magnetic couplers," *IEEE Journal of Emerging and Selected Topics in Industrial Electronics*, vol. 1, no. 2, pp. 113–122, 2020.

[186] F. Y. Lin, A. Zaheer, M. Budhia, and G. A. Covic, "Reducing leakage flux in ipt systems by modifying pad ferrite structures," in *2014 IEEE Energy Conversion Congress and Exposition (ECCE)*, pp. 1770–1777.

[187] K. Song, G. Yang, Y. Guo, Y. Lan, S. Dong, J. Jiang, and C. Zhu, "Design of dd coil with high misalignment tolerance and low emf emissions for wireless electric vehicle charging systems," *IEEE Transactions on Power Electronics*, vol. 35, no. 9, pp. 9034–9045, 2020.

[188] D. Kraus and H.-G. Herzog, "Magnetic design of a q-coil for a 10 kw ddq system for inductive power transfer," in *2019 IEEE PELS Workshop on Emerging Technologies: Wireless Power Transfer (WoW)*, 2019, pp. 140–143.

[189] A. Zaheer, M. Budhia, D. Kacprzak, and G. A. Covic, "Magnetic design of a 300 w under-floor contactless power transfer system," in *IECON 2011 - 37th Annual Conference on IEEE Industrial Electronics Society*, Nov 2011, pp. 1408–1413.

[190] A. Zaheer, D. Kacprzak, and G. A. Covic, "A bipolar receiver pad in a lumped ipt system for electric vehicle charging applications," in *2012 IEEE Energy Conversion Congress and Exposition (ECCE)*, pp. 283–290.

[191] A. Zaheer, G. A. Covic, and D. Kacprzak, "A bipolar pad in a 10-khz 300-w distributed ipt system for agv applications," *IEEE Transactions on Industrial Electronics*, vol. 61, no. 7, pp. 3288–3301, July 2014.

[192] U. Pratik, B. J. Varghese, A. Azad, and Z. Pantic, "Optimum design of decoupled concentric coils for operation in double-receiver wireless power transfer systems," *IEEE Journal of Emerging and Selected Topics in Power Electronics*, vol. 7, no. 3, pp. 1982–1998, 2019.

[193] S. Kim, A. Zaheer, G. Covic, and J. Boys, "Tripolar pad for inductive power transfer systems," in *IECON 2014 - 40th Annual Conference of the IEEE Industrial Electronics Society*, pp. 3066–3072.

[194] S. Y. Choi, J. Huh, W. Y. Lee, and C. T. Rim, "Asymmetric coil sets for wireless stationary ev chargers with large lateral tolerance by dominant field analysis," *IEEE Transactions on Power Electronics*, vol. 29, no. 12, pp. 6406–6420, 2014.

[195] A. Tejeda, G. A. Covic, and J. T. Boys, "Novel single-sided ferrite-less magnetic coupler for roadway ev charging," in *2015 IEEE Energy Conversion Congress and Exposition (ECCE)*, pp. 3148–3153.

[196] M. G. S. Pearce, G. A. Covic, and J. T. Boys, "Robust ferrite-less double d topology for roadway ipt applications," *IEEE Transactions on Power Electronics*, vol. 34, no. 7, pp. 6062–6075, 2019.

[197] A. Tejeda, C. Carretero, J. T. Boys, and G. A. Covic, "Ferrite-less circular pad with controlled flux cancelation for ev wireless charging," *IEEE Transactions on Power Electronics*, vol. 32, no. 11, pp. 8349–8359, Nov 2017.

[198] E. G. Marques and A. M. S. Mendes, "Optimization of transmitter magnetic structures for roadway applications," in *2017 IEEE Applied Power Electronics Conference and Exposition (APEC)*, March 2017, pp. 959–965.

[199] P. K. S. Jayathurathnage, A. Alphones, and D. M. Vilathgamuwa, "Optimization of a wireless power transfer system with a repeater against load variations," *IEEE Transactions on Industrial Electronics*, vol. 64, no. 10, pp. 7800–7809, Oct 2017.

[200] Y. Chen, R. Mai, Y. Zhang, M. Li, and Z. He, "Improving misalignment tolerance for ipt system using a third-coil," *IEEE Transactions on Power Electronics*, vol. 34, no. 4, pp. 3009–3013, April 2019.

[201] S. Moon and G. Moon, "Wireless power transfer system with an asymmetric four-coil resonator for electric vehicle battery chargers," *IEEE Transactions on Power Electronics*, vol. 31, no. 10, pp. 6844–6854, Oct 2016.

[202] J. Kim, J. Kim, S. Kong, H. Kim, I. S. Suh, N. P. Suh, D. H. Cho, J. Kim, and S. Ahn, "Coil design and shielding methods for a magnetic resonant wireless power transfer system," *Proceedings of the IEEE*, vol. 101, no. 6, pp. 1332–1342, June 2013.

[203] "Wireless power transfer for light-duty plug-in/ electric vehicles and alignment methodology," vol. 3, no. 2, pp. 321–331, 2019.

[204] F. Lin, G. A. Covic, and M. Kesler, "Design of a sae compliant multicoil ground assembly," *IEEE Journal of Emerging and Selected Topics in Industrial Electronics*, vol. 1, no. 1, pp. 14–25, 2020.

[205] M. G. S. Pearce, G. A. Covic, and J. T. Boys, "Reduced ferrite double d pad for roadway ipt applications," *IEEE Transactions on Power Electronics*, vol. 36, no. 5, pp. 5055–5068, 2021.

[206] P. A. J. Lawton, F. J. Lin, and G. A. Covic, "Magnetic design considerations for high-power wireless charging systems," *IEEE Transactions on Power Electronics*, vol. 37, no. 8, pp. 9972–9982, 2022.

[207] L. Tan, J. Li, C. Chen, C. Yan, J. Guo, and X. Huang, "Analysis and performance improvement of wpt systems in the environment of single non-ferromagnetic metal plates," *Energies*, vol. 9, no. 8, 2016. [Online]. Available: https://www.mdpi.com/1996-1073/9/8/576

[208] F. Y. Lin, G. A. Covic, and J. T. Boys, "Leakage flux control of mismatched ipt systems," *IEEE Transactions on Transportation Electrification*, vol. 3, no. 2, pp. 474–487, June 2017.

[209] C. Liang, G. Yang, F. Yuan, X. Huang, Y. Sun, J. Li, and K. Song, "Modeling and analysis of thermal characteristics of magnetic coupler for wireless electric vehicle charging system," *IEEE Access*, vol. 8, pp. 173 177–173 185, 2020.

[210] M. G. S. Pearce, J. D. D. Gawith, A. Tejeda, J. T. Boys, and G. A. Covic, "Shaped passive magnetic field shaping for roadway ipt," in *2016 IEEE 2nd Annual Southern Power Electronics Conference (SPEC)*, Dec 2016, pp. 1–6.

[211] S. Ahn, J. Pak, T. Song, H. Lee, J.-G. Byun, D. Kang, C.-S. Choi, E. Kim, J. Ryu, M. Kim, Y. Cha, Y. Chun, C.-T. Rim, J.-H. Yim, D.-H. Cho, and J. Kim, "Low frequency electromagnetic field reduction techniques for the on-line electric vehicle (olev)," in *2010 IEEE International Symposium on Electromagnetic Compatibility*, 2010, pp. 625–630.

[212] Y. H. Sohn, B. H. Choi, E. S. Lee, and C. T. Rim, "Comparisons of magnetic field shaping methods for ubiquitous wireless power transfer," in *Emerging Technologies: Wireless Power (WoW), 2015 IEEE PELS Workshop on*, pp. 1–6.

[213] Y. Xiong, S. Sun, H. Jia, P. Shea, and Z. John Shen, "New physical insights on power mosfet switching losses," *IEEE Transactions on Power Electronics*, vol. 24, no. 2, pp. 525–531, Feb 2009.

[214] E. G. Marques and A. M. S. Mendes, "Constant current controller for electric vehicles chargers based on ipt systems," in *2014 IEEE Vehicle Power and Propulsion Conference (VPPC)*, 2014, pp. 1–6.

[215] D. J. Thrimawithana, U. K. Madawala, and S. Yu, "Design of a bi-directional inverter for a wireless v2g system," in *2010 IEEE International Conference on Sustainable Energy Technologies (ICSET)*, pp. 1–5.

[216] M. J. Neath, U. K. Madawala, and D. J. Thrimawithana, "A new controller for bi-directional inductive power transfer systems," in *2011 IEEE International Symposium on Industrial Electronics*, pp. 1951–1956.

[217] U. K. Madawala and D. J. Thrimawithana, "A bidirectional inductive power interface for electric vehicles in v2g systems," *IEEE Transactions on Industrial Electronics*, vol. 58, no. 10, pp. 4789–4796, 2011.

[218] D. J. Thrimawithana and U. K. Madawala, "A generalized steady-state model for bidirectional ipt systems," *IEEE Transactions on Power Electronics*, vol. 28, no. 10, pp. 4681–4689, 2013.

[219] B. Esteban, M. Sid-Ahmed, and N. C. Kar, "A comparative study of power supply architectures in wireless ev charging systems," *IEEE Transactions on Power Electronics*, vol. 30, no. 11, pp. 6408–6422, Nov 2015.

[220] B. X. Nguyen, D. M. Vilathgamuwa, G. H. B. Foo, P. Wang, A. Ong, U. K. Madawala, and T. D. Nguyen, "An efficiency optimization scheme for bidirectional inductive power transfer systems," *IEEE Transactions on Power Electronics*, vol. 30, no. 11, pp. 6310–6319, 2015.

[221] A. A. S. Mohamed, A. A. Marim, and O. A. Mohammed, "Magnetic design considerations of bidirectional inductive wireless power transfer system for ev applications," *IEEE Transactions on Magnetics*, vol. 53, no. 6, pp. 1–5, June 2017.

[222] D. J. Thrimawithana and U. K. Madawala, "A three-phase bi-directional ipt system for contactless charging of electric vehicles," in *2011 IEEE International Symposium on Industrial Electronics*, June 2011, pp. 1957–1962.

[223] D. J. Thrimawithana, U. K. Madawala, A. Francis, and M. Neath, "Magnetic modeling of a high-power three phase bi-directional ipt system," in *IECON 2011 - 37th Annual Conference on IEEE Industrial Electronics Society*, Nov 2011, pp. 1414–1419.

[224] H. Feng, T. Cai, S. Duan, J. Zhao, X. Zhang, and C. Chen, "An lcc-compensated resonant converter optimized for robust reaction to large coupling variation in dynamic wireless power transfer," *IEEE Transactions on Industrial Electronics*, vol. 63, no. 10, pp. 6591–6601, 2016.

[225] M. Kim, D. Joo, and B. K. Lee, "Design and control of inductive power transfer system for electric vehicles considering wide variation of output voltage and coupling coefficient," *IEEE Transactions on Power Electronics*, vol. 34, no. 2, pp. 1197–1208, Feb 2019.

[226] V. Vu, V. Phan, M. Dahidah, and V. Pickert, "Multiple output inductive charger for electric vehicles," *IEEE Transactions on Power Electronics*, vol. 34, no. 8, pp. 7350–7368, Aug 2019.

[227] W. Chwei-Sen, G. A. Covic, and O. H. Stielau, "Investigating an lcl load resonant inverter for inductive power transfer applications," *IEEE Transactions on Power Electronics*, vol. 19, no. 4, pp. 995–1002, 2004.

[228] H. Hao, G. A. Covic, and J. T. Boys, "An approximate dynamic model of lcl based inductive power transfer power supplies," *IEEE Transactions on Power Electronics*, vol. 29, no. 10, pp. 5554–5567, 2014.

[229] N. Xuan Bac, D. M. Vilathgamuwa, and U. K. Madawala, "A sic-based matrix converter topology for inductive power transfer system," *IEEE Transactions on Power Electronics*, vol. 29, no. 8, pp. 4029–4038, Aug 2014.

[230] S. Weerasinghe, U. K. Madawala, and D. J. Thrimawithana, "A matrix converter-based bidirectional contactless grid interface," *IEEE Transactions on Power Electronics*, vol. 32, no. 3, pp. 1755–1766, 2017.

[231] M. Moghaddami and A. I. Sarwat, "Single-phase soft-switched ac–ac matrix converter with power controller for bidirectional inductive power transfer systems," *IEEE Transactions on Industry Applications*, vol. 54, no. 4, pp. 3760–3770, 2018.

[232] H. Cai, L. Shi, and Y. Li, "Harmonic-based phase-shifted control of inductively coupled power transfer," *IEEE Transactions on Power Electronics*, vol. 29, no. 2, pp. 594–602, 2014.

[233] T. Diekhans, F. Stewing, G. Engelmann, H. v. Hoek, and R. W. D. Doncker, "A systematic comparison of hard- and soft-switching topologies for inductive power transfer systems," in *Electric Drives Production Conference (EDPC), 2014 4th International*, pp. 1–8.

[234] D. J. Thrimawithana, U. K. Madawala, and M. Neath, "A synchronization technique for bidirectional ipt systems," *IEEE Transactions on Industrial Electronics*, vol. 60, no. 1, pp. 301–309, 2013.

[235] A. Berger, M. Agostinelli, S. Vesti, J. A. Oliver, J. A. Cobos, and M. Huemer, "A wireless charging system applying phase-shift and amplitude control to maximize efficiency and extractable power," *IEEE Transactions on Power Electronics*, vol. 30, no. 11, pp. 6338–6348, 2015.

[236] A. K. Swain, M. J. Neath, U. K. Madawala, and D. J. Thrimawithana, "A dynamic multivariable state-space model for bidirectional inductive power transfer systems," *IEEE Transactions on Power Electronics*, vol. 27, no. 11, pp. 4772–4780, 2012.

[237] U. K. Madawala, M. Neath, and D. J. Thrimawithana, "A power frequency controller for bidirectional inductive power transfer systems," *IEEE Transactions on Industrial Electronics*, vol. 60, no. 1, pp. 310–317, 2013.

[238] K. Colak, E. Asa, M. Bojarski, D. Czarkowski, and O. C. Onar, "A novel phase-shift control of semibridgeless active rectifier for wireless power transfer," *IEEE Transactions on Power Electronics*, vol. 30, no. 11, pp. 6288–6297, 2015.

[239] T. Diekhans and R. W. D. Doncker, "A dual-side controlled inductive power transfer system optimized for large coupling factor variations and partial load," *IEEE Transactions on Power Electronics*, vol. 30, no. 11, pp. 6320–6328, 2015.

[240] J. T. Boys, C. Y. Huang, and G. A. Covic, "Single-phase unity power-factor inductive power transfer system," in *2008 IEEE Power Electronics Specialists Conference*, pp. 3701–3706.

[241] H. H. Wu, A. Gilchrist, K. D. Sealy, and D. Bronson, "A high efficiency 5 kw inductive charger for evs using dual side control," *IEEE Transactions on Industrial Informatics*, vol. 8, no. 3, pp. 585–595, 2012.

[242] K. Colak, E. Asa, and D. Czarkowski, "A novel phase control of single switch active rectifier for inductive power transfer applications," in *2016 IEEE Applied Power Electronics Conference and Exposition (APEC)*, 2016, pp. 1767–1772.

[243] A. Abdolkhani, A. P. Hu, and J. Tian, "Autonomous polyphase current-fed pushpull resonant converter based on ring coupled oscillators," *IEEE Journal of Emerging and Selected Topics in Power Electronics*, vol. 3, no. 2, pp. 568–576, 2015.

[244] E. Asa, K. Colak, M. Bojarski, and D. Czarkowski, "A novel multi-level phase-controlled resonant inverter with common mode capacitor for wireless ev chargers," in *Transportation Electrification Conference and Expo (ITEC), 2015 IEEE*, pp. 1–6.

[245] K. Colak, E. Asa, D. Czarkowski, and H. Komurcugil, "A novel multi-level bi-directional dc/dc converter for inductive power transfer applications," in *Industrial Electronics Society, IECON 2015 - 41st Annual Conference of the IEEE*, pp. 003 827–003 831.

[246] X. Ju, L. Dong, X. Liao, and Y. Jin, "An ac-ac energy injection resonant converter for wireless power transfer applications," in *Future Energy Electronics Conference (IFEEC), 2015 IEEE 2nd International*, pp. 1–5.

[247] J. Tian and A. P. Hu, "A dc-voltage-controlled variable capacitor for stabilizing the zvs frequency of a resonant converter for wireless power transfer," *IEEE Transactions on Power Electronics*, vol. 32, no. 3, pp. 2312–2318, 2017.

[248] E. G. Marques, S. V. da Silva, and A. Mendes, "A new magnetic coupler for evs chargers based on plug-in and ipt technologies," in *2017 IEEE Energy Conversion Congress and Exposition (ECCE)*, 2017, pp. 2760–2766.

[249] R. Bosshard, U. Badstübner, J. W. Kolar, and I. Stevanović, "Comparative evaluation of control methods for inductive power transfer," in *2012 International Conference on Renewable Energy Research and Applications (ICRERA)*, Nov 2012, pp. 1–6.

[250] x. Despotovix0107;, D. Reljix0107;, V. Vasix0107;, and D. Oros, "Steady-state multiple parameters estimation of the inductive power transfer system," *IEEE Access*, vol. 10, pp. 46 878–46 894, 2022.

[251] D. Ahn, S. Kim, J. Moon, and I. K. Cho, "Wireless power transfer with automatic feedback control of load resistance transformation," *IEEE Transactions on Power Electronics*, vol. 31, no. 11, pp. 7876–7886, Nov 2016.

[252] B. Song, S. Cui, Y. Li, and C. Zhu, "A fast and general method to calculate mutual inductance for ev dynamic wireless charging system," *IEEE Transactions on Power Electronics*, vol. 36, no. 3, pp. 2696–2709, 2021.

[253] J. P. W. Chow and H. S. H. Chung, "Use of primary-side information to perform online estimation of the secondary-side information and mutual inductance in wireless inductive link," in *2015 IEEE Applied Power Electronics Conference and Exposition (APEC)*, pp. 2648–2655.

[254] J. Yin, D. Lin, T. Parisini, and S. Y. Hui, "Front-end monitoring of the mutual inductance and load resistance in a series–series compensated wireless power transfer system," *IEEE Transactions on Power Electronics*, vol. 31, no. 10, pp. 7339–7352, 2016.

[255] Y. Su, L. Chen, X. Wu, A. P. Hu, C. Tang, and X. Dai, "Load and mutual inductance identification from the primary side of inductive power transfer system with parallel-tuned secondary power pickup," *IEEE Transactions on Power Electronics*, vol. 33, no. 11, pp. 9952–9962, Nov 2018.

[256] W. Xiao, R. Shen, B. Zhang, D. Qiu, Y. Chen, and F. Xie, "Multiple parameters estimation based on transmitter side information in wireless power transfer system," *IEEE Access*, vol. 7, pp. 164 835–164 843, 2019.

[257] J. Yin, D. Lin, C.-K. Lee, and S. Y. R. Hui, "A systematic approach for load monitoring and power control in wireless power transfer systems without any direct output measurement," *IEEE Transactions on Power Electronics*, vol. 30, no. 3, pp. 1657–1667, 2015.

[258] Z. Zhang and W. Yu, "Communication/model-free constant current control for wireless power transfer under disturbances of coupling effect," *IEEE Transactions on Industrial Electronics*, vol. 69, no. 5, pp. 4587–4595, 2022.

[259] C. Xia, Q. Sun, X. Li, and A. P. Hu, "Robust u-synthesis control of dual lcl type ipt system considering load and mutual inductance uncertainty," *IEEE Access*, vol. 7, pp. 72 770–72 782, 2019.

[260] S.-C. Tan, Y. Lai, M. Cheung, and C. Tse, "On the practical design of a sliding mode voltage controlled buck converter," *IEEE Transactions on Power Electronics*, vol. 20, no. 2, pp. 425–437, 2005.

[261] H. S. Marques, B. V. Borges, and A. V. Anunciada, "Transient behavior and frequency response of constant frequency one cycle charge control modulator (o3c)," *IEEE Transactions on Power Electronics*, vol. 23, no. 5, pp. 2507–2515, 2008.

[262] W. Shi, J. Deng, Z. Wang, and X. Cheng, "The start-up dynamic analysis and one cycle control-pd control combined strategy for primary-side controlled wireless power transfer system," *IEEE Access*, vol. 6, pp. 14 439–14 450, 2018.

[263] X. Dai, J. Jiang, Z. Xu, and Y. Li, "Cooperative control for multi-excitation units wpt system with multiple coupling parameter identification and area adaptation," *IEEE Access*, vol. 8, pp. 38 728–38 741, 2020.

[264] A. Trigui, S. Hached, F. Mounaim, A. C. Ammari, and M. Sawan, "Inductive power transfer system with self-calibrated primary resonant frequency," *IEEE Transactions on Power Electronics*, vol. 30, no. 11, pp. 6078–6087, Nov 2015.

[265] J. R. E. G. Prazeres, V. Prasanth, and P. Bauer, "Multi-coil multi-frequency inductive power transfer," in *Transportation Electrification Conference and Expo (ITEC), 2015 IEEE*, pp. 1–8.

[266] U. K. Madawala and D. J. Thrimawithana, "New technique for inductive power transfer using a single controller," *IET Power Electronics*, vol. 5, no. 2, pp. 248–256, 2012.

[267] F. Grazian, T. B. Soeiro, P. van Duijsen, and P. Bauer, "Auto-resonant detection method for optimized zvs operation in ipt systems with wide variation of magnetic coupling and load," *IEEE Open Journal of the Industrial Electronics Society*, vol. 2, pp. 326–341, 2021.

[268] C. Chen, H. Zhou, Q. Deng, W. Hu, Y. Yu, X. Lu, and J. Lai, "Modeling and decoupled control of inductive power transfer to implement constant current/voltage charging and zvs operating for electric vehicles," *IEEE Access*, vol. 6, pp. 59 917–59 928, 2018.

[269] H. Hu, T. Cai, S. Duan, X. Zhang, J. Niu, and H. Feng, "An optimal variable frequency phase shift control strategy for zvs operation within wide power range in ipt systems," *IEEE Transactions on Power Electronics*, vol. 35, no. 5, pp. 5517–5530, 2020.

[270] A. Babaki, S. Vaez-Zadeh, A. Zakerian, and G. A. Covic, "Variable-frequency retuned wpt system for power transfer and efficiency improvement in dynamic ev charging with fixed voltage characteristic," *IEEE Transactions on Energy Conversion*, vol. 36, no. 3, pp. 2141–2151, 2021.

[271] E. Gati, G. Kampitsis, and S. Manias, "Variable frequency controller for inductive power transfer in dynamic conditions," *IEEE Transactions on Power Electronics*, vol. 32, no. 2, pp. 1684–1696, Feb 2017.

[272] Y. Jiang, L. Wang, Y. Wang, J. Liu, X. Li, and G. Ning, "Analysis, design, and implementation of accurate zvs angle control for ev battery charging in wireless high-power transfer," *IEEE Transactions on Industrial Electronics*, vol. 66, no. 5, pp. 4075–4085, 2019.

[273] S. Y. Jeong, J. H. Park, G. P. Hong, and C. T. Rim, "Autotuning control system by variation of self-inductance for dynamic wireless ev charging with small air gap," *IEEE Transactions on Power Electronics*, vol. 34, no. 6, pp. 5165–5174, 2019.

[274] A. Dayerizadeh, H. Feng, and S. M. Lukic, "Dynamic wireless charging: Reflexive field containment using saturable inductors," *IEEE Transactions on Industry Applications*, vol. 56, no. 2, pp. 1784–1792, 2020.

[275] U. D. Kavimandan, S. M. Mahajan, and C. W. Van Neste, "Analysis and demonstration of a dynamic zvs angle control using a tuning capacitor in a wireless power transfer system," *IEEE Journal of Emerging and Selected Topics in Power Electronics*, vol. 9, no. 2, pp. 1876–1890, 2021.

[276] J. E. I. James, A. Chu, D. Robertson, A. Sabitov, and G. A. Covic, "A series tuned high power ipt stage lighting controller," in *2011 IEEE Energy Conversion Congress and Exposition*, pp. 2843–2849.

[277] Y. Shen, H. Wang, A. Al-Durra, Z. Qin, and F. Blaabjerg, "A bidirectional resonant dc–dc converter suitable for wide voltage gain range," *IEEE Transactions on Power Electronics*, vol. 33, no. 4, pp. 2957–2975, 2018.

[278] D. Kobayashi, T. Imura, and Y. Hori, "Real-time coupling coefficient estimation and maximum efficiency control on dynamic wireless power transfer for electric vehicles," in *Emerging Technologies: Wireless Power (WoW), 2015 IEEE PELS Workshop on*, pp. 1–6.

[279] N. A. Keeling, G. A. Covic, and J. T. Boys, "A unity-power-factor ipt pickup for high-power applications," *IEEE Transactions on Industrial Electronics*, vol. 57, no. 2, pp. 744–751, 2010.

[280] R. Mai, Y. Liu, Y. Li, P. Yue, G. Cao, and Z. He, "An active-rectifier-based maximum efficiency tracking method using an additional measurement coil for wireless power transfer," *IEEE Transactions on Power Electronics*, vol. 33, no. 1, pp. 716–728, 2018.

[281] D. J. Thrimawithana, U. K. Madawala, M. Neath, and T. Geyer, "A sense winding based synchronization technique for bi-directional ipt pick-ups," in *2011 IEEE Energy Conversion Congress and Exposition*, pp. 1405–1410.

[282] W. Zhong and S. Y. R. Hui, "Charging time control of wireless power transfer systems without using mutual coupling information and wireless communication system," *IEEE Transactions on Industrial Electronics*, vol. 64, no. 1, pp. 228–235, 2017.

[283] M. J. Neath, A. K. Swain, U. K. Madawala, and D. J. Thrimawithana, "An optimal pid controller for a bidirectional inductive power transfer system using multiobjective genetic algorithm," *IEEE Transactions on Power Electronics*, vol. 29, no. 3, pp. 1523–1531, 2014.

[284] C. Qi, Z. Lang, L. Su, X. Chen, and H. Miao, "Model predictive control for a bidirectional wireless power transfer system with maximum efficiency point tracking," in *2019 IEEE International Symposium on Predictive Control of Electrical Drives and Power Electronics (PRECEDE)*, May 2019, pp. 1–5.

[285] R. P. Twiname, D. J. Thrimawithana, U. K. Madawala, and C. A. Baguley, "A dual-active bridge topology with a tuned clc network," *IEEE Transactions on Power Electronics*, vol. 30, no. 12, pp. 6543–6550, 2015.

[286] U. K. Madawala and D. J. Thrimawithana, "Current sourced bi-directional inductive power transfer system," *IET Power Electronics*, vol. 4, no. 4, pp. 471–480, 2011.

[287] M. Wu, X. Yang, W. Chen, L. Wang, Y. Jiang, C. Zhao, and Z. Yan, "A dual-sided control strategy based on mode switching for efficiency optimization in wireless power transfer system," *IEEE Transactions on Power Electronics*, vol. 36, no. 8, pp. 8835–8848, 2021.

[288] W. X. Zhong, C. Zhang, X. Liu, and S. Y. R. Hui, "A methodology for making a three-coil wireless power transfer system more energy efficient than a two-coil counterpart for extended transfer distance," *IEEE Transactions on Power Electronics*, vol. 30, no. 2, pp. 933–942, Feb 2015.

[289] Y. Nagatsuka, N. Ehara, Y. Kaneko, S. Abe, and T. Yasuda, "Compact contactless power transfer system for electric vehicles," in *Power Electronics Conference (IPEC), 2010 International*, pp. 807–813.

[290] "Guidelines for limiting the exposure to time-varying electric, magnetic and electromagnetic fields(up to 300 ghz)," *Health Physics*, vol. 74, no. 4, pp. 494–522.

[291] M. L. G. Kissin, H. Hao, and G. A. Covic, "A practical multiphase ipt system for agv and roadway applications," in *2010 IEEE Energy Conversion Congress and Exposition*, Sept 2010, pp. 1844–1850.

[292] F. Lu, Y. Zhang, H. Zhang, C. Zhu, L. Diao, M. Gong, W. Zhang, and C. Mi, "A low-voltage and high-current inductive power transfer system with low harmonics for automatic guided vehicles," *IEEE Transactions on Vehicular Technology*, vol. 68, no. 4, pp. 3351–3360, 2019.

[293] M. R. Sonapreetha, S. Y. Jeong, S. Y. Choi, and C. T. Rim, "Dual-purpose non-overlapped coil sets as foreign object and vehicle location detections for wireless stationary ev chargers," in *Emerging Technologies: Wireless Power (WoW), 2015 IEEE PELS Workshop on*, pp. 1–7.

[294] L. Xiang, Z. Zhu, J. Tian, and Y. Tian, "Foreign object detection in a wireless power transfer system using symmetrical coil sets," *IEEE Access*, vol. 7, pp. 44 622–44 631, 2019.

[295] V. Jiwariyavej, T. Imura, and Y. Hori, "Coupling coefficients estimation of wireless power transfer system via magnetic resonance coupling using information from either side of the

system," *IEEE Journal of Emerging and Selected Topics in Power Electronics*, vol. 3, no. 1, pp. 191–200, 2015.

[296] J. P. W. Chow, H. S. H. Chung, and C. S. Cheng, "Use of transmitter-side electrical information to estimate mutual inductance and regulate receiver-side power in wireless inductive link," *IEEE Transactions on Power Electronics*, vol. 31, no. 9, pp. 6079–6091, 2016.

[297] J. Acero, C. Carretero, I. Lope, R. Alonso, x00D, Lucia, and J. M. Burdio, "Analysis of the mutual inductance of planar-lumped inductive power transfer systems," *IEEE Transactions on Industrial Electronics*, vol. 60, no. 1, pp. 410–420, 2013.

[298] V. Prasanth, P. Bauer, and J. A. Ferreira, "A sectional matrix method for ipt coil shape optimization," in *2015 9th International Conference on Power Electronics and ECCE Asia (ICPE-ECCE Asia)*, 2015, pp. 1684–1691.

[299] G. Wei, X. Jin, C. Wang, J. Feng, C. Zhu, and M. I. Matveevich, "An automatic coil design method with modified ac resistance evaluation for achieving maximum coil coil efficiency in wpt systems," *IEEE Transactions on Power Electronics*, vol. 35, no. 6, pp. 6114–6126, 2020.

[300] A. Delgado, G. Di Capua, K. Stoyka, L. Shi, N. Femia, A. Maffucci, S. Ventre, P. Alou, J. A. Oliver, and J. A. Cobos, "Self and mutual inductance behavioral modeling of square-shaped ipt coils with air gap and ferrite core plates," *IEEE Access*, vol. 10, pp. 7476–7488, 2022.

[301] X. Gao, C. Liu, H. Zhou, W. Hu, Y. Huang, Y. Xiao, Z. Lei, and J. Chen, "Design and analysis of a new hybrid wireless power transfer system with a space-saving coupler structure," *IEEE Transactions on Power Electronics*, vol. 36, no. 5, pp. 5069–5081, 2021.

[302] A. Hossain, P. Darvish, S. Mekhilef, K. S. Tey, and C. W. Tong, "A new coil structure of dual transmitters and dual receivers with integrated decoupling coils for increasing power transfer and misalignment tolerance of wireless ev charging system," *IEEE Transactions on Industrial Electronics*, vol. 69, no. 8, pp. 7869–7878, 2022.

[303] W. Shi, J. Dong, T. B. Soeiro, C. Riekerk, F. Grazian, G. Yu, and P. Bauer, "Design of a highly efficient 20-kw inductive power transfer system with improved misalignment performance," *IEEE Transactions on Transportation Electrification*, vol. 8, no. 2, pp. 2384–2399, 2022.

[304] G. R. Nagendra, G. A. Covic, and J. T. Boys, "Determining the physical size of inductive couplers for ipt ev systems," in *2014 IEEE Applied Power Electronics Conference and Exposition - APEC 2014*, pp. 3443–3450.

[305] F. Y. Lin, C. Carretero, G. A. Covic, and J. T. Boys, "A reduced order model to determine the coupling factor between magnetic pads used in wireless power transfer," *IEEE Transactions on Transportation Electrification*, vol. 3, no. 2, pp. 321–331, 2017.

[306] M. Mohammad, S. Choi, M. Z. Islam, S. Kwak, and J. Baek, "Core design and optimization for better misalignment tolerance and higher range wireless charging of phev," *IEEE Transactions on Transportation Electrification*, vol. PP, no. 99, pp. 1–1, 2017.

[307] R. P. Twiname, D. J. Thrimawithana, U. K. Madawala, and C. A. Baguley, "A new resonant bidirectional dc-dc converter topology," *IEEE Transactions on Power Electronics*, vol. 29, no. 9, pp. 4733–4740, Sept 2014.

[308] "Yasa limited", accessed on: Nov 25, 2021. [online].available:https://www.yasa.com/," 2021.

[309] M. Sato, G. Yamamoto, D. Gunji, T. Imura, and H. Fujimoto, "Development of wireless in-wheel motor using magnetic resonance coupling," *IEEE Transactions on Power Electronics*, vol. 31, no. 7, pp. 5270–5278, 2016.

[310] H. Fujimoto, O. Shimizu, S. Nagai, T. Fujita, D. Gunji, and Y. Ohmori, "Development of wireless in-wheel motors for dynamic charging: From 2nd to 3rd generation," in *2020 IEEE PELS Workshop on Emerging Technologies: Wireless Power Transfer (WoW)*, 2020, pp. 56–61.

[311] C. Panchal, S. Stegen, and J. Lu, "Review of static and dynamic wireless electric vehicle charging system," *Engineering Science and Technology, an International Journal*, vol. 21, no. 5, pp. 922–937, 2018. [Online]. Available: https://www.sciencedirect.com/science/article/pii/S221509861830154X

[312] Y. J. Hwang and J. Y. Jang, "Design and analysis of a novel magnetic coupler of an in-wheel wireless power transfer system for electric vehicles," *Energies*, vol. 13, no. 2, 2020. [Online]. Available: https://www.mdpi.com/1996-1073/13/2/332

[313] O. Shimizu, T. Utsu, H. Fujimoto, D. Gunji, and I. Kuwayama, "Dynamic wpt transmitting through fiber-belt tire and cfrp wheel to in-wheel arc-shaped coil," *IEEE Journal of Emerging and Selected Topics in Industrial Electronics*, vol. 2, no. 2, pp. 113–121, 2021.

[314] J. Zhou, P. Yao, Y. Chen, K. Guo, S. Hu, and H. Sun, "Design considerations for a self-latching coupling structure of inductive power transfer for autonomous underwater vehicle," *IEEE Transactions on Industry Applications*, vol. 57, no. 1, pp. 580–587, Jan 2021.

[315] M. A. Houran, X. Yang, and W. Chen, "Two-degree-of-freedom wpt system using cylindrical-joint structure for applications with movable parts," *IEEE Transactions on Circuits and Systems II: Express Briefs*, vol. 68, no. 1, pp. 366–370, Jan 2021.

[316] Z. Yan, Y. Zhang, K. Zhang, B. Song, and C. Mi, "Underwater wireless power transfer system with a curly coil structure for auvs," *IET Power Electronics*, vol. 12, no. 10, pp. 2559–2565, 2019. [Online]. Available: https://ietresearch.onlinelibrary.wiley.com/doi/abs/10.1049/iet-pel.2018.6090

[317] Z. Yan, B. Song, Y. Zhang, K. Zhang, Z. Mao, and Y. Hu, "A rotation-free wireless power transfer system with stable output power and efficiency for autonomous underwater vehicles," *IEEE Transactions on Power Electronics*, vol. 34, no. 5, pp. 4005–4008, May 2019.

[318] T. Kan, Y. Zhang, Z. Yan, P. P. Mercier, and C. C. Mi, "A rotation-resilient wireless charging system for lightweight autonomous underwater vehicles," *IEEE Transactions on Vehicular Technology*, vol. 67, no. 8, pp. 6935–6942, Aug 2018.

[319] A. Abdolkhani, A. P. Hu, and N.-K. C. Nair, "A double stator through-hole type contact-less slipring for rotary wireless power transfer applications," *IEEE Transactions on Energy Conversion*, vol. 29, no. 2, pp. 426–434, June 2014.

[320] J. Smeets, L. Encica, and E. Lomonova, "Comparison of winding topologies in a pot core rotating transformer," in *2010 12th International Conference on Optimization of Electrical and Electronic Equipment*, May 2010, pp. 103–110.

[321] R. Trevisan and A. Costanzo, "A 1-kw contactless energy transfer system based on a rotary transformer for sealing rollers," *IEEE Transactions on Industrial Electronics*, vol. 61, no. 11, pp. 6337–6345, Nov 2014.

[322] K. Song, B. Ma, G. Yang, J. Jiang, R. Wei, H. Zhang, and C. Zhu, "A rotation-lightweight wireless power transfer system for solar wing driving," *IEEE Transactions on Power Electronics*, vol. 34, no. 9, pp. 8816–8830, Sep. 2019.

[323] L. Zhao, D. J. Thrimawithana, U. K. Madawala, A. P. Hu, and C. C. Mi, "A misalignment-tolerant series-hybrid wireless ev charging system with integrated magnetics," *IEEE Transactions on Power Electronics*, vol. 34, no. 2, pp. 1276–1285, 2019.